

Validation of a Thermo-mechanical Finite element model of an Onshore WindTurbine Foundation

Pragya Mukherjee

Student number:5431751
Master Thesis:CIE 5060-09

Cover image: ©Can Stock Photo/ssuaphoto,
url: <https://www.windsystemsmag.com/fundamentals-of-wind-turbines/>



Validation of a thermo-mechanical finite element model of an Onshore Wind Turbine Foundation

by

Pragya Mukherjee

to obtain the degree of Master of Science in Structural Engineering at the
Delft University of Technology, to be defended publicly on
22 August 2023

Student number: 5431751

Project duration: October 3, 2022- August 22, 2023

Thesis committee: Dr.ir.E.O.L.Lantsoght, TU Delft and USFQ, Chairperson-Concrete Structures

Prof.dr.ir. Max Hendriks, TU Delft, Committee member

Ir. Paul Korswagen, TU Delft, Committee member

Ir. Joost Reijers, ABT BV, Company Supervisor

An electronic version of this thesis is available at <http://repository.tudelft.nl/>.



Copyright © Pragma Mukherjee, 2023
All rights reserved.

Preface

The following report is the representation of the final chapter of my Masters in structural engineering at the Faculty of Civil Engineering and Geosciences at TU Delft. I am grateful to the engineering and consultancy firm ABT BV for providing me the opportunity to execute this research which is an integral part of my Masters studies curriculum. The project was performed under the supervision of the graduation committee of TU Delft and ABT. This research delves into the validation of steel stresses in onshore wind turbine foundations through advanced finite element simulations. Its primary objective is to enhance confidence in using FEA as a predictive tool for analyzing the behavior of wind turbine foundations under diverse loading conditions. Particular emphasis is placed on incorporating the effect of hydration heat during concrete curing, which has significant implications for early-age concrete development and subsequent steel stress distributions.

I would like to express my sincere gratitude to all of my committee members who helped me throughout the research thesis in every possible way. To begin with, I would appreciate the help and guidance provided by my Chair, Dr. Ir. Eva Lantsoght. Her ideas and comments throughout the process really helped in shaping the research thesis. I want to thank Prof. Max Hendriks for his invaluable guidance throughout the process. He played a crucial role in ensuring the scientific relevance of this project and provided valuable advice on how to effectively communicate the message of this thesis. Also, I would like to express my gratitude to Ir. Paul Korswagen, for the valuable input and expertise in FE modeling, which has greatly helped me to improve my project. The constructive feedback and insights were immensely helpful.

I am grateful to Joost Reijers and Mark Verbaten at ABT, who provided me with the opportunity to work on such an amazing project at their firm. I would like to take this chance to thank Joost Reijers who was also my daily supervisor in this project. His knowledge and experience really helped me in achieving my final goal. I would like to mention Lex van der Meer, who was a constant support during my whole thesis. I learned a lot from him about the FE software during the research. I can't forget about how he cleared my every doubt in FE modeling despite having a busy schedule of himself. Next, I would like to sincerely thank Krishna A. Pillai who helped me in every aspect during the whole research journey. In the end, I want to thank everyone at ABT, for always supporting me and helping me in every possible way.

I take this opportunity to express my regards to my parents Mrs. Susmita Mukherjee and Mr. Prasenjit Mukherjee. I am grateful for the unwavering love and support I have received from my family members. It will always hold a special place in my heart. I must express my utmost gratitude to my friends in India and The Netherlands. Despite the physical distance, Perna, Shivangi, and Aditya have always been a pillar of support for me. I am deeply appreciative of Swarnangshu, Sneha, Payal, Saurabh, Satvik, Pratyaksh, Karthick, Sayantan, and Leonid for their unwavering encouragement and unrelenting motivation.

*Pragya Mukherjee
Delft, August 2023*

Abstract

The growing demand for renewable energy sources has led to the deployment of wind turbines worldwide. One of the most critical parts of the wind turbine is the foundation which plays an important role in maintaining the structural integrity and reliability of the towers throughout the service life. This research project is a case study that focuses on validating the numerical model against the experimental values from an operational onshore wind turbine foundation present at Riemst, Belgium while considering the effect of hydration heat during the concrete curing process.

The main aim of this research is to study and compare the behavior of the steel stresses in the on-site foundation with that of the numerical analysis and to see whether an adequate match can be obtained. The study begins with the development of a three-dimensional symmetrical finite element model that captures its intricate geometrical and material properties. The structure's behavior is simulated under realistic loading conditions to assess its structural performance and identify potential areas of concern.

To validate the accuracy of numerical analysis, experimental data obtained from fiber optic sensors are used. After converting the measured strains into stresses, they are carefully compared with the finite element analysis results to identify any variations and fine-tune the model. The validation of the FE model is performed using a 2D plate model in SCIA engineering.

The research investigates the effects of hydration heat along with the structural analysis in FEA on the stresses experienced by the steel elements in the mass structure. This further extends to the effects of bedding and inclined piles combined with the thermo-mechanical analysis where properties such as stiffness are varied in the simulations to study their influence on the structural response.

It is imperative to note that utilizing the FE model with solely non-linear structural analysis can lead to a significant overestimation of the expected field results, up to a whopping 87 times. To mitigate this issue, the variant with thermo-mechanical analysis is implemented, reducing this estimation to a maximum factor of 58 compared to the field data. It is crucial to achieve a satisfactory level of the project through iterative modifications. Implementing soil bedding on all sides in the thermo-mechanical model is one such step to effectively reduce steel stress to an acceptable level. The model showed steel stresses that are approximately 26 times higher than the actual experimental values. Along with reducing the steel stresses, the crack widths have decreased considerably from 3.4mm to 2.35mm. Hence, the effective way to perform the numerical simulation is to consider thermal-mechanical coupling along with minimizing assumptions and ensuring sufficient stiffness to the structure for reliable assessments of steel stresses and structural integrity of onshore wind turbine foundations.

The findings contribute valuable insights into the foundation's structural behavior under varying operational conditions, highlighting areas of strength and potential advancement. Moreover, the outcomes from this investigation can assist engineers and designers in making informed decisions during the planning and construction phases of wind turbine foundations, leading to more cost-effective and robust structures. Additionally, the methodologies present here may serve as a framework for future research in this field.

Contents

Abstract	v
List of Figures	ix
List of Tables	xv
1 Introduction	1
1.1 Background	1
1.2 Scope	4
1.3 Research Questions	5
1.4 Methodology	5
1.5 Thesis Outline	7
2 Literature Review	8
2.1 Existing studies conducted on onshore wind turbine foundations	8
2.2 Fiber Optics Measurement	14
2.3 Determination of concrete cracks	15
2.4 Theory behind Uncracked concrete	16
2.5 Heat of Hydration	17
2.6 Temperature distribution in hardening concrete	18
3 Field monitoring of strain measurements	22
3.1 Description of the setup	22
3.2 Methodology for the measured data from 2017	24
3.3 Methodology for the measured data 2022	29
3.4 Methodology for the measured data from 2023	31
3.5 Determination of Cracks	33
4 SCIA engineering calculation	36
4.1 Description of the model	36
4.2 Methodology	38
4.3 Results	38
4.4 Conclusion	40
5 Structural Non-linear Finite element analysis	41
5.1 Dimensions and properties of the concrete body	41
5.2 DIANA FEA approach to model a wind turbine foundation	42
5.3 Maturity effects	52
5.4 Effects of Structural analysis	54
6 Thermo-mechanical Non-linear Finite element analysis	59
6.1 Heat Flow effects	59
6.2 Summary of the analysis performed	63
6.3 Effect of constant maturity	64
6.4 Effect of varying Maturity	97
6.5 Effect of reducing thermal gradient	105
6.6 Effect of Bedding	123
6.7 Effect of Inclined Piles	145
7 Results and Discussion	162
7.1 Field Monitoring of strain measurements	162
7.2 SCIA engineering calculations	163
7.3 Structural analysis in DIANA	164

7.4	Thermo-mechanical analysis on a wind turbine foundation	167
7.5	Discussion	180
8	Conclusion and Recommendations	182
8.1	Conclusion	182
8.2	Recommendations	184
	References	187
A	Appendix-A	188
A.1	Graphs for steel measurements from 2017	188
A.2	Graphs for steel measurements from 2022	193
A.3	Graphs for steel measurements from 2023	197
A.4	Determination of cracks	200
B	Appendix-B	201
B.1	Steel stresses due to the Nonlinear structural analysis only	201
B.2	Effects of Maturity effect	203
B.3	Steel stresses generated due to the Hydration heat effect	206
B.4	Steel stress due to the combined analysis	212
C	Appendix-C	232
C.1	SCIA Report	232

Nomenclature

List of Abbreviations

DAF	Dynamic Amplification factor	FEA	Finite Element Analysis
DOF	Degree of freedom	FEM	Finite Element Modeling
EOM	Equations of Motion	FO	Field Operating
FBG	Fiber Bragg Grating	HTC	Heat Transfer Coefficient
FE	Finite Element	SLS	Serviceability Limit State
		ULS	Ultimate Limit State

List of Figures

1.1	Components of Wind Turbine [1]	2
1.2	Rotation axis definition (ABT document)	2
1.3	Slab Wind Turbine Foundation (ABT document)	3
1.4	Pile Wind Turbine Foundation (ABT document)	4
1.5	Anchor cage (ABT document)	4
1.6	DIANA model components	6
1.7	Methodology	6
2.1	Layout drawing of stress gauges in the foundation [3]	8
2.2	Numerical Model of the wind turbine foundation [3]	9
2.3	Axial stresses of steel bars in the foundation [3]	9
2.4	Temperature of concrete samples in an adiabatic calorimeter [7]	10
2.5	Sensor layout [7]	10
2.6	Hardening temperature of the foundation [7]	11
2.7	Temperature comparison between two points [8]	12
2.8	Thermal FEM results: a) Average foundation temperature results, b)-d) Temperature profiles at different times [9]	13
2.9	Temperature variation along the vertical direction [8]	13
2.10	Fiber Bragg Grating system	14
2.11	Example of damping evaluation a) Ambient noise record, b) Amplitude spectrum, c) Damped response of the building [19]	15
2.12	Temperature difference in the foundation [29]	16
2.13	Different characteristic stages during hydration [31]	17
2.14	Adiabatic hydration process and rise in temperature [31]	20
2.15	Temperature distribution into 3 different components [31]	21
3.1	Glass Fiber optics sensor	22
3.2	L01 sensor	23
3.3	Position of sensors-Side view	24
3.4	Pictorial representation of the wind direction-2017	25
3.5	Natural frequency of the tower	25
3.6	Wind turbine foundation with directions and bending moment a) Top view, b) Section view	26
3.7	Steel stress for L01 position	27
3.8	Pictorial representation of the wind direction-2022	29
3.9	Pictorial representation of the wind direction-2023	31
3.10	Natural Frequencies for two measurements a) From 2017 data, b) From 2022 data c) From 2023 data	34
4.1	2D plate model	36
4.2	Applied Bending Moment	38
4.3	Principal stresses-Sigma 1+	39
4.4	Reaction forces	39
4.5	Reaction forces in DIANA	40
5.1	Cross-section of wind turbine foundation	41
5.2	Concrete foundation block	42
5.3	Reinforcements at different locations a) Top tangential, b) Bottom tangential, c) Vertical, d) Top radial, e) Bottom radial	43
5.4	Pretensioned anchors	44
5.5	Concrete in confinement layers	44

5.6	Elements with linear properties	44
5.7	Model with symmetrical support	45
5.8	Model with pile supports	45
5.9	Element types used in the FE model	47
5.10	Dead load in the FE model	48
5.11	Horizontal force in the FE model	49
5.12	Vertical force in the FE model	49
5.13	Moment in the FE model	50
5.14	Soil force in the FE model	50
5.15	Maturity-Young's modulus graph for C35/45	52
5.16	Maturity-Tensile strength graph for C35/45	53
5.17	Maturity-Tensile fracture energy graph for C35/45	53
5.18	Wind turbine foundation-Wind directions	54
5.19	Cross section of the foundation with the reinforcements in interest	54
5.20	Rebars in the top tangential position	55
5.21	Rebars in the bottom tangential position	55
5.22	Rebars in the bottom tangential position near the piles	55
5.23	Stirrup	56
5.24	Rebars in the top radial position	56
5.25	Rebars in the bottom radial position	56
6.1	Adiabatic curve for CEM III/A 42.5 N LH [31]	60
6.2	Wind turbine foundation-Wind directions	64
6.3	Temperature Evolution in concrete foundation a) Day 0, b) Day 1, c) Day 2, d) Day 3	65
6.3	Temperature Evolution in concrete foundation e) Day 7, f) Day 14, g) Day 28, h) Day 45	66
6.3	Temperature Evolution in concrete foundation i) Day 60	67
6.4	Wind turbine foundation-section layout	67
6.5	Temperature vs Time plots for different sections of the concrete foundation a) Left section-I-I, b) Middle section-II-II, c) Right section-III-III	68
6.6	Height vs Temperature plots for different sections of the concrete foundation a) Left section-I-I, b) Middle section-II-II, c) Right section-III-III	69
6.7	Steel stress wrt time at different locations in the rebar a) Inner node	70
6.7	Steel stress wrt time at different locations in the rebar b) Outer node	71
6.8	Steel stress wrt time for different positions in the foundation a) Radial, b) Tangential	71
6.9	Steel stress in the Top tangential rebars a) Day 0, b) Day 1, c) Day 2, d) Day 3	72
6.9	Steel stress in the Top tangential rebars e) Day 7, f) Day 14, g) Day 28, h) Day 45	73
6.9	Steel stress in the Top tangential rebars i) Day 60	74
6.10	Steel stress in the Bottom tangential rebars a) Day 0, b) Day 1	74
6.10	Steel stress in the Bottom tangential rebars c) Day 2, d) Day 3, e) Day 7, f) Day 14	75
6.10	Steel stress in the Bottom tangential rebars g) Day 28, h) Day 45, i) Day 60	76
6.11	Steel stress in the Bottom tangential rebars near the piles a) Day 0, b) Day 1, c) Day 2	77
6.11	Steel stress in the Bottom tangential rebars near the piles d) Day 3, e) Day 7, f) Day 14	78
6.11	Steel stress in the Bottom tangential rebars near the piles g) Day 28, h) Day 45, i) Day 60	79
6.12	Steel stress in the Top radial rebars a) Day 0, b) Day 1, c) Day 2	80
6.12	Steel stress in the Top radial rebars d) Day 3, e) Day 7, f) Day 14	81
6.12	Steel stress in the Top radial rebars g) Day 28, h) Day 45, i) Day 60	82
6.13	Steel stress in the Bottom radial rebars a) Day 0, b) Day 1, c) Day 2	83
6.13	Steel stress in the Bottom radial rebars d) Day 3, e) Day 7, f) Day 14	84
6.13	Steel stress in the Bottom radial rebars g) Day 28, h) Day 45, i) Day 60	85
6.14	Steel stress in the side stirrups a) Day 0, b) Day 1, c) Day 2	86
6.14	Steel stress in the side stirrups d) Day 3, e) Day 7, f) Day 14	87
6.14	Steel stress in the side stirrups g) Day 28, h) Day 45, i) Day 60	88
6.15	Steel stress in the Top tangential rebars a) After prestress, b) After vertical load	89
6.15	Steel stress in the Top tangential rebars c) After wind load	90
6.16	Steel stress in the Bottom tangential rebars a) After prestress, b) After vertical load	90
6.16	Steel stress in the Bottom tangential rebars c) After wind load	91

6.17 Steel stress in the Bottom tangential rebars near piles a) After prestress, b) After vertical load	91
6.17 Steel stress in the Bottom tangential rebars near piles c) After wind load	92
6.18 Steel stress in the stirrups a) After prestress, b) After vertical load	92
6.18 Steel stress in the stirrups c) After wind load	93
6.19 Steel stress in the Top radial rebars a) After prestress, b) After vertical load	93
6.19 Steel stress in the Top radial rebars c) After wind load	94
6.20 Steel stress in the Bottom radial rebars a) After prestress, b) After vertical load	94
6.20 Steel stress in the Bottom radial rebars c) After wind load	95
6.21 Crack patterns	95
6.22 Maturity-Young's modulus graph for C35/45	97
6.23 Maturity-Tensile strength graph for C35/45	97
6.24 Maturity-Tensile fracture energy graph for C35/45	98
6.25 Steel stress wrt time at each wind directions a) Top radial	98
6.25 Steel stress wrt time at each wind directions b) Bottom radial, c) Top tangential, d) Bottom tangential	99
6.26 Steel stress in the Top tangential rebars a) Model 1, b) Model 2	100
6.27 Steel stress in the Bottom tangential rebars a) Model 1, b) Model 2	101
6.28 Steel stress in the Bottom tangential rebars near piles a) Model 1, b) Model 2	101
6.29 Steel stress in the stirrups a) Model 1, b) Model 2	102
6.30 Steel stress in the Top radial rebars a) Model 1, b) Model 2	102
6.31 Steel stress in the Bottom radial rebars a) Model 1, b) Model 2	103
6.32 Temperature Evolution in concrete foundation a) Day 0	105
6.32 Temperature Evolution in concrete foundation b) Day 1, c) Day 2, d) Day 3	106
6.32 Temperature Evolution in concrete foundation e) Day 7, f) Day 14, g) Day 28	107
6.32 Temperature Evolution in concrete foundation h) Day 45, i) Day 60	108
6.33 Comparison of Temperature evolution a) Variant 1 at day 7, b) Variant 3 at day 7	109
6.34 Temperature-Time comparison between Model 1 and 3	109
6.35 Height vs Temperature plots for different sections of the concrete foundation a) Left section-I-I, b) Middle section-II-II	110
6.35 Height vs Temperature plots for different sections of the concrete foundation c) Right section-III-III	111
6.36 Steel stress wrt time at each wind directions a) Top radial	111
6.36 Steel stress wrt time at each wind directions b) Bottom radial, c) Top tangential, d) Bottom tangential	112
6.37 Steel stress in the Top tangential rebars a) After prestress, b) After vertical load	113
6.37 Steel stress in the Top tangential rebars c) After wind load	114
6.38 Steel stress in the Bottom tangential rebars a) After prestress	114
6.38 Steel stress in the Bottom tangential rebars b) After vertical load, c) After wind load	115
6.39 Steel stress in the Bottom tangential rebars near piles a) After prestress, b) After vertical load	116
6.39 Steel stress in the Bottom tangential rebars near piles c) After wind load	117
6.40 Steel stress in the stirrups a) After prestress	117
6.40 Steel stress in the stirrups b) After vertical load, c) After wind load	118
6.41 Steel stress in the Top radial rebars a) After prestress, b) After vertical load, c) After wind load	119
6.42 Steel stress in the Bottom radial rebars a) After prestress, b) After vertical load	120
6.42 Steel stress in the Bottom radial rebars c) After wind load	121
6.43 Crack patterns	121
6.44 Bedding underneath the foundation	123
6.45 Steel stress wrt time at each wind directions a) Top radial, b) Bottom radial, c) Top tangential	124
6.45 Steel stress wrt time at each wind directions d) Bottom tangential	125
6.46 Steel stress in the Top tangential rebars a) Model 3	125
6.46 Steel stress in the Top tangential rebars b) Model 4	126
6.47 Steel stress in the Bottom tangential rebars a) Model 3, b) Model 4	126
6.48 Steel stress in the Bottom tangential rebars near piles a) Model 3, b) Model 4	127
6.49 Steel stress in the stirrups a) Model 3	127
6.49 Steel stress in the stirrups b) Model 4	128
6.50 Steel stress in the Top radial rebars a) Model 3, b) Model 4	128

6.51 Steel stress in the Bottom radial rebars a) Model 3, b) Model 4	129
6.52 Crack patterns	130
6.53 Steel stress in the Top tangential rebars a) Model 4, b) Model 5	133
6.54 Steel stress in the Bottom tangential rebars a) Model 4, b) Model 5	134
6.55 Steel stress in the Bottom tangential rebars near piles a) Model 4	134
6.55 Steel stress in the Bottom tangential rebars near piles b) Model 5	135
6.56 Steel stress in the stirrups a) Model 4, b) Model 5	135
6.57 Steel stress in the Top radial rebars a) Model 4, b) Model 5	136
6.58 Steel stress in the Bottom radial rebars a) Model 4	136
6.58 Steel stress in the Bottom radial rebars b) Model 5	137
6.59 Crack patterns	137
6.60 Bedding on all sides of the foundation	140
6.61 Top tangential rebar	141
6.62 Bottom tangential rebar	141
6.63 Bottom tangential rebar near the piles	141
6.64 Side stirrup	142
6.65 Top radial rebar	142
6.66 Bottom radial rebar	142
6.67 Crack patterns	143
6.68 Depiction of Piles in the Riemst wind turbine foundation	145
6.69 Inclined pile supports in the model	146
6.70 Illustration of the arching effect	147
6.71 Steel stress wrt time at each wind directions a) Top radial	147
6.71 Steel stress wrt time at each wind directions b) Bottom radial, c) Top tangential, d) Bottom tangential	148
6.72 Top tangential rebar	149
6.73 Bottom tangential rebar	149
6.74 Bottom tangential rebar near the piles	150
6.75 Side stirrup	150
6.76 Top radial rebar	150
6.77 Bottom radial rebar	151
6.78 Crack patterns	151
6.79 Top tangential rebar	153
6.80 Bottom tangential rebar	153
6.81 Bottom tangential rebar near the piles	154
6.82 Side stirrup	154
6.83 Top radial rebar	154
6.84 Bottom radial rebar	155
6.85 Crack patterns	155
6.86 Top tangential rebar	157
6.87 Bottom tangential rebar	157
6.88 Bottom tangential rebar near the piles	158
6.89 Side stirrup	158
6.90 Top radial rebar	158
6.91 Bottom radial rebar	159
6.92 Crack patterns	159
7.1 Comparison of bottom tangential piles in a) 2022, b) 2023	163
7.2 Steel stress at Top radial (L02) in North(A), East(B), South(C) directions	164
7.3 Steel stress at Top tangential (L03) in North(A), East(B), South(C) directions	165
7.4 Steel stress at Bottom radial (L05) in North(A), East(B), South(C) directions	165
7.5 Steel stress at Bottom tangential (L06) in North(A), East(B), South(C) directions	166
7.6 Steel stress at Bottom radial near piles (L07) in North(A), East(B), South(C) directions	166
7.7 Steel stress at Bottom tangential near piles (L08) in North(A), East(B), South(C) directions	167
7.8 Steel stress wrt time at each wind directions a) Top radial, b) Bottom radial	168
7.8 Steel stress wrt time at each wind directions c) Top tangential, d) Bottom tangential	169

7.9	Steel stress at Top radial (L02) in North(A), East(B), South(C) directions	170
7.10	Steel stress at Top tangential (L03) in North(A), East(B), South(C) directions	171
7.11	Steel stress at Bottom radial (L05) in North(A), East(B), South(C) directions	171
7.12	Steel stress at Bottom tangential (L06) in North(A), East(B), South(C) directions	172
7.13	Steel stress at Bottom radial near piles (L07) in North(A), East(B), South(C) directions	172
7.14	Steel stress at Bottom tangential near piles (L08) in North(A), East(B), South(C) directions	173
7.15	Steel stress at Top radial (L02) in North(A), East(B), South(C) directions	174
7.16	Steel stress at Top tangential (L03) in North(A), East(B), South(C) directions	174
7.17	Steel stress at Bottom radial (L05) in North(A), East(B), South(C) directions	175
7.18	Steel stress at Bottom tangential (L06) in North(A), East(B), South(C) directions	175
7.19	Steel stress at Bottom radial near piles (L07) in North(A), East(B), South(C) directions	176
7.20	Steel stress at Bottom tangential near piles (L08) in North(A), East(B), South(C) directions	176
7.21	Steel stress at Top radial (L02) in North(A), East(B), South(C) directions	177
7.22	Steel stress at Top tangential (L03) in North(A), East(B), South(C) directions	178
7.23	Steel stress at Bottom radial (L05) in North(A), East(B), South(C) directions	178
7.24	Steel stress at Bottom tangential (L06) in North(A), East(B), South(C) directions	179
7.25	Steel stress at Bottom radial near piles (L07) in North(A), East(B), South(C) directions	179
7.26	Steel stress at Bottom tangential near piles (L08) in North(A), East(B), South(C) directions	180
A.1	Steel stress for L01 position	188
A.2	Steel stress for L02 position	189
A.3	Steel stress for L03 position	189
A.4	Steel stress for L04 position	190
A.5	Steel stress for L05 position	190
A.6	Steel stress for L06 position	191
A.7	Steel stress for L07 position	191
A.8	Steel stress for L08 position	192
A.9	Steel stress for L01 position	193
A.10	Steel stress for L02 position	193
A.11	Steel stress for L03 position	194
A.12	Steel stress for L04 position	194
A.13	Steel stress for L05 position	195
A.14	Steel stress for L06 position	195
A.15	Steel stress for L07 position	196
A.16	Steel stress for L08 position	196
A.17	Steel stress for L01 position	197
A.18	Steel stress for L02 position	197
A.19	Steel stress for L03 position	198
A.20	Steel stress for L05 position	198
A.21	Steel stress for L06 position	199
A.22	Steel stress for L07 position	199
A.23	Frequency analytical calculation	200
B.1	Steel stress at top tangential-L3 position	201
B.2	Steel stress at bottom tangential-L6 position	201
B.3	Steel stress at bottom tangential near piles-L8 position	202
B.4	Steel stress at stirrup-L4 position	202
B.5	Steel stress at top radial-L2 position	202
B.6	Steel stress at bottom radial-L5 position	202
B.7	Top radial bars a) without maturity effect, b)with maturity effect	203
B.8	Bottom radial bars a) without maturity effect, b)with maturity effect	204
B.9	Top tangential bars a) without maturity effect, b)with maturity effect	204
B.10	Bottom tangential bars a) without maturity effect, b)with maturity effect	205
B.11	Steel stress in the Top tangential rebars a) Day 0, b) Day 1, c) Day 2, d) Day 3, e) Day 7, f) Day 14, g) Day 28, h) Day 45, i) Day 60	206

B.12 Steel stress in the Bottom tangential rebars a) Day 0, b) Day 1, c) Day 2, d) Day 3, e) Day 7, f) Day 14, g) Day 28, h) Day 45, i) Day 60	207
B.13 Steel stress in the Bottom tangential rebars near the piles a) Day 0, b) Day 1, c) Day 2, d) Day 3, e) Day 7, f) Day 14, g) Day 28, h) Day 45, i) Day 60	208
B.14 Steel stress in the Top radial rebars a) Day 0, b) Day 1, c) Day 2, d) Day 3, e) Day 7, f) Day 14, g) Day 28, h) Day 45, i) Day 60	209
B.15 Steel stress in the Bottom radial rebars a) Day 0, b) Day 1, c) Day 2, d) Day 3, e) Day 7, f) Day 14, g) Day 28, h) Day 45, i) Day 60	210
B.16 Steel stress in the side stirrups a) Day 0, b) Day 1, c) Day 2, d) Day 3, e) Day 7, f) Day 14, g) Day 28, h) Day 45, i) Day 60	211
B.17 Steel stress in the Top tangential rebars a) After prestress, b) After vertical load, c) After wind load	212
B.18 Steel stress in the Bottom tangential rebars a) After prestress, b) After vertical load, c) After wind load	212
B.19 Steel stress in the Bottom tangential rebars near piles a) After prestress, b) After vertical load, c) After wind load	213
B.20 Steel stress in the stirrups a) After prestress, b) After vertical load, c) After wind load	213
B.21 Steel stress in the Top radial rebars a) After prestress, b) After vertical load, c) After wind load	214
B.22 Steel stress in the Bottom radial rebars a) After prestress, b) After vertical load, c) After wind load	214
B.23 Steel stress in the Top tangential rebars a) Day 0, b) Day 1, c) Day 2, d) Day 3	215
B.23 Steel stress in the Top tangential rebars e) Day 7, f) Day 14, g) Day 28, h) Day 45	216
B.23 Steel stress in the Top tangential rebars i) Day 60	217
B.24 Steel stress in the Bottom tangential rebars a) Day 0, b) Day 1	217
B.24 Steel stress in the Bottom tangential rebars c) Day 2, d) Day 3, e) Day 7, f) Day 14	218
B.24 Steel stress in the Bottom tangential rebars g) Day 28, h) Day 45, i) Day 60	219
B.25 Steel stress in the Bottom tangential rebars near the piles a) Day 0, b) Day 1, c) Day 2	220
B.25 Steel stress in the Bottom tangential rebars near the piles d) Day 3, e) Day 7, f) Day 14	221
B.25 Steel stress in the Bottom tangential rebars near the piles g) Day 28, h) Day 45, i) Day 60	222
B.26 Steel stress in the Top radial rebars a) Day 0, b) Day 1, c) Day 2	223
B.26 Steel stress in the Top radial rebars d) Day 3, e) Day 7, f) Day 14	224
B.26 Steel stress in the Top radial rebars g) Day 28, h) Day 45, i) Day 60	225
B.27 Steel stress in the Bottom radial rebars a) Day 0, b) Day 1, c) Day 2	226
B.27 Steel stress in the Bottom radial rebars d) Day 3, e) Day 7, f) Day 14	227
B.27 Steel stress in the Bottom radial rebars g) Day 28, h) Day 45, i) Day 60	228
B.28 Steel stress in the side stirrups a) Day 0, b) Day 1, c) Day 2	229
B.28 Steel stress in the side stirrups d) Day 3, e) Day 7, f) Day 14	230
B.28 Steel stress in the side stirrups g) Day 28, h) Day 45, i) Day 60	231

List of Tables

3.1	Overview of the sensor directions	23
3.2	Timeline	24
3.3	Summary of wind speed and wind direction-2017	24
3.4	Measured maximum steel stresses at different locations and directions-2017	28
3.5	Summary of wind speed and wind direction-2022	29
3.6	Measured steel stresses at different locations and directions-2022	30
3.7	Summary of wind speed and wind direction-2023	31
3.8	Measured steel stresses at different locations and directions-2023	32
3.9	Estimated Frequency for all the years	33
3.10	Parameters	35
4.1	Dimensions of the structure	37
4.2	Material properties	37
4.3	Load cases	37
4.4	Steel stresses as a result of SCIA calculation	38
5.1	Concrete properties	41
5.2	Material models used in the FEA	46
5.3	Choices for the concrete constitutive model	46
5.4	Summary of load cases	51
5.5	Load combinations for favorable analysis	51
5.6	Load combinations for unfavorable analysis	51
5.7	Steel stresses as a result of structural analysis	57
5.8	Comparison between the Field measurement and DIANA structural analysis	58
6.1	Material Properties	59
6.2	Temperature variation wrt the number of days	60
6.3	Summarized values for the Heat transfer coefficient	62
6.4	Summary of the values	62
6.5	Summary of the variants	63
6.6	Comparison between the Field measurement and DIANA Model 1	96
6.7	Comparison between the Field measurement and DIANA Model 2	104
6.8	Comparison between the Field measurement and DIANA Model 3	122
6.9	Comparison between the DIANA Model 3 and DIANA Model 4	131
6.10	Comparison between the Field measurement and DIANA Model 4	132
6.11	Comparison between the DIANA Model 4 and DIANA Model 5	138
6.12	Comparison between the Field measurement and DIANA Model 5	139
6.13	Comparison between the Field measurement and DIANA Model 6	144
6.14	Comparison between the Field measurement and DIANA Model 7	152
6.15	Comparison between the Field measurement and the DIANA Model 8	156
6.16	Comparison between the Field measurement and the DIANA Model 9	160

Introduction

The first chapter comprises the basic description of the project. It begins with an introduction to the wind turbine followed by the scope of the study. It also deals with the research methodology which is going to be followed during the course of the project along with the thesis outline.

1.1. Background

The energy sources worldwide have been dominated by fossil fuels since industrialization. Conventional energy sources such as coal and oil are used for everything. Nevertheless, they are not only finite resources but they also emit carbon dioxide, which negatively impacts the Earth. Hence, there has been a shift to move from conventional energy sources to alternative energy sources. They function the same way as traditional sources of energy but almost all alternative sources do not emit carbon dioxide as a byproduct. Wind energy is one of the most sustainable and renewable sources of energy. The first electricity-producing wind turbine was invented in 1887. Since then a lot of development has occurred in the wind farm industries. The wind farms can be both onshore as well as offshore. Wind farms in onshore are comparatively cheaper than any coal or gas plants but fossil fuel subsidies are hindering the expansion of wind energy. Nowadays, the total wind energy capacity is almost 733 gigawatts worldwide. In order to meet the energy requirements, an increasingly large number of turbines with high capacity are being developed.

To build such huge wind turbines, special care has to be taken while designing its foundation since it is one of the most important components of the wind turbine. It not only transfers and spread the load into the soil but also provides overall stability to the structure. They are cast in place, leaving the concrete to mature under environmental conditions which vary in time and space. Thus, there is uncertainty about the initial performance of concrete, which can result in costly over-design and inaccurate prognoses of structural health. In order to design the reinforced concrete foundation, conventional design methods are used which make use of static and quasi-static analyses. These kinds of analyses often lead to over-designed structures. When more effort is put into analyses, for instance, the finite element analysis, the construction, and its failure mechanisms can be better understood. The optimizations can also be possible in this case. Knowing the real structure behavior and implementing the results in the finite element analyses can be beneficiary since it can provide support to the design optimization along with the modeling techniques used in FE software. With the ambition to keep innovating the design, the company aims to optimize the designs with less waste of materials and to understand the behavior of the foundation block and compare it with the theoretical approach. Successful conduction of the research thesis can be helpful in the proper designing of wind turbine foundations.

1.1.1. Wind Turbine

The conversion of wind energy to electrical energy at a large height is a concept of mechanical and civil engineering. The basic components of wind turbines and their mechanics are explained in this section.

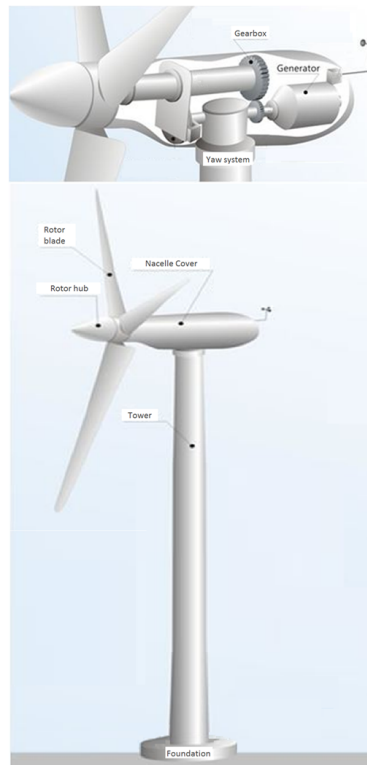


Figure 1.1: Components of Wind Turbine [1]

Rotor

The rotor is composed of the blades and the hub, which are connected together with the help of controllable interfaces.

- **Blades** Blades are one of the most important parts of the wind turbine. Its function is to harvest the energy of the wind. The energy production is directly related to the area the blades sweep. The interaction between the motion of the air, with solid objects, is analyzed in the aerodynamic design. Also, the weight distribution, the stiffness, and the varying moment of inertia of the rotor are important properties required in structural analysis.
- **Hub** The hub connects the blades to the main shaft. It also houses the controls of the blades. Pitch is the rotation around the lateral axis, which can be altered in the hub.

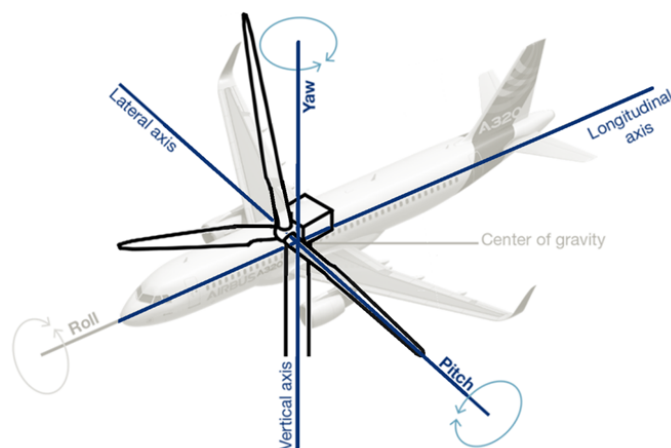


Figure 1.2: Rotation axis definition (ABT document)

Nacelle

The Nacelle is the main frame of the power transporting and producing parts of the wind turbine. It is protected from environmental elements. The main shaft leads the mechanical power from the rotor, guide with bearings, to the gearbox. The wind turbine generator functions at 1800 rpm or 1500 rpm. It converts mechanical power into electrical power.

Yaw system

Yaw is the rotation around the perpendicular vertical axis. The yaw system rotates the nacelle with the attached rotor into the wind.

Tower structure

The purpose of the tower structure is to elevate the power-producing parts. Wind speeds climb and turbulences reduce at increasing altitudes. The height of the tower is determined by a trade-off between rising building costs and increasing energy capture.

Foundation

The main objective of a wind turbine foundation is to keep the tower upright. Besides the required strength of the foundation, limits have been set for minimal rotation, translation, and overall stability. Loads acting on the foundation are- a downward vertical force due to the weight of the tower, wind generating a horizontal force, and an overturning moment and prestressing force due to the pretensioning of the anchor. Additionally, there are forces originating from the surrounding soil. The type of foundation slab also depends on the size of the tower and the blades. At higher altitudes, the wind is mostly stronger, hence larger towers with longer blades are required. When the dimensions of the tower and blades increase, the magnitude of forces acting on the foundation also increases. Therefore, resulting in the need for big foundation slabs. They are generally circular in shape due to the change in wind direction and must be strong in every direction to sustain the overturning moment. Two types of foundations:

- **Slab Foundation** A slab or spread foundation consists of a reinforced concrete plate with a significant area. This area must be large enough to spread the load to the ground without exceeding the maximum ground pressure. This type is most suitable for strong and stiff soils. Slab foundations reduce the settlements which are critical for the minimal rotation limit.

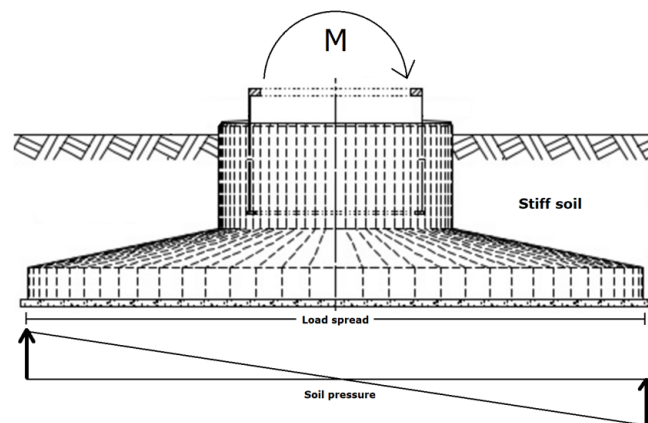


Figure 1.3: Slab Wind Turbine Foundation (ABT document)

- **Pile Foundation** When weak and loose soils are present, excavation has to be executed to reach stronger soil. A common technique is piling. Due to the large bending moment, these piles will be subjected to tension loads. Pile reinforcing steel is needed to transfer the tensile stresses from the tower flange to the ground surrounding the pile shaft. An example of the piled foundation is shown Figure 1.4.

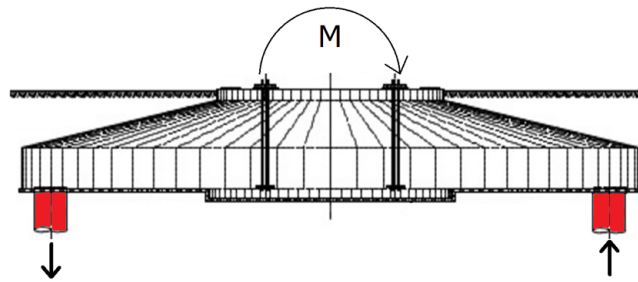


Figure 1.4: Pile Wind Turbine Foundation (ABT document)

Anchor Cage

The forces acting on the tower need to be transferred to the foundation slab. Generally, two designs are applied: the steel insert ring and the anchor cage. The anchor cage design is mainly used for the wind turbine foundation. In this case, the bottom flange of the cage and the rods are embedded in the foundation, the top flange is left sticking out. These rods are prestressed ensuring the connection between the tower and the foundation slab.

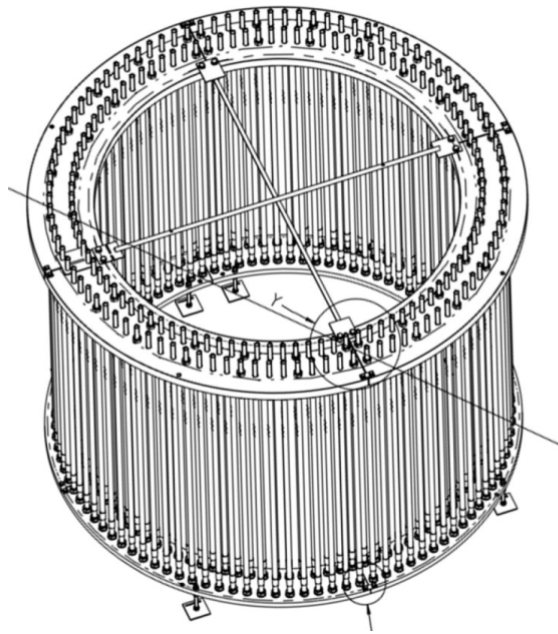


Figure 1.5: Anchor cage (ABT document)

1.2. Scope

The project's focus will be on validating the stresses in the steel bars inside the concrete foundation by health monitoring using FBG sensors and implementing the structural behavior in the finite element analysis. The strength of concrete is not only used as a direct measure of its ability to support load but also an indirect measure of its elasticity and durability [2]. Since designing such foundations is a complex method, it is much more difficult to understand the behavior of the concrete and the reinforcements under loading conditions. It has been observed that mass structures release heat due to the hydration effect which results in thermal cracks in the structure. In order to determine the stresses in the reinforcement many studies such as [3], [4] etc. were conducted, which only focused on linear FE analysis making the conclusions obtained from them vaguely. Some assumptions are generally made while designing any structure but it is also fascinating to know how much the assumptions align with the actual structural behavior. Hence, it becomes important to monitor existing structures' structural behavior and implement

the changes in FE software. The emphasis will be on the rebar stresses at the occurrence of maximum bending moment due to the wind load and to accommodate the observations in the Finite Element software to achieve adequate accuracy.

1.3. Research Questions

To achieve the objective, two main research questions have been formulated-

1. How do the steel stresses measured in the on-site concrete foundation vary from the FE model's numerical analysis?
2. What is the best way to model the wind turbine foundation in the DIANA which will represent the real structure adequately?

While answering the above main questions, the following sub-research questions should be answered which are as follows:

1. How does the hydration heat develop over time?
2. To what extent does the hydration heat emission, which provides the prestressing to the foundation affect the steel stresses?

1.4. Methodology

The research thesis will be subdivided into the following tasks, which are presented in detail in the following:

i. Background study and research on the results obtained from the past studies: To get a clear understanding of the project, it is necessary to be familiar with the previous project conducted on the same wind turbine foundation and do an analysis of the conclusions obtained from it. The analysis involves validation of the strain data along with the preliminary check of the FE model which includes verification of the stresses obtained from it. A background study is also required to be conducted on the effects of hydration heat emission in the foundation, since it is acting like a prestress, affecting the steel stresses.

ii. Analyses of the experimental strain measurement data: To obtain strain data from the foundation, glass fiber optics have been used. Since the focus of the research thesis is on comparing the steel stresses in the real foundation and the FE model, it is necessary to obtain the stresses from the strain measurements before visualizing them in Power BI. After the analyses, maximum steel stresses at various positions can be obtained which can be further compared with the stress obtained in the DIANA calculation at the same position. After this step, the actual behavior of rebars in the concrete foundation can be known. From the measurement data, it is possible to find the stiffness of the foundation with the help of the natural frequency. In case the frequency is within the range provided by the wind turbine company, it is safe to conclude that the foundation is still uncracked.

iii. Finite Element Analysis: A FE model has to be set up for the project considering the current design methods. The current method used by the company is the 3D FEA model. This will be the reference for further studies in the project. The finite element software used for the analysis is DIANA. An implicit check of the reinforcement and concrete stress can be performed by modeling the actual reinforcement configuration and concrete properties in the software. The model comprises concrete nonlinear solid shapes with embedded reinforcement elements. The shaft is connected to the top anchor flange. At this location, high-strength concrete is applied in order to resist high compressive stresses. The interaction between the pile and the concrete is modeled as the linear elastic strip of material since the pile reinforcement is not modeled.

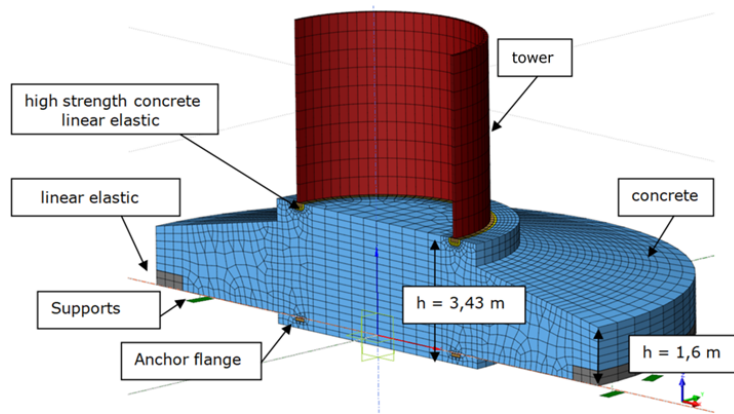


Figure 1.6: DIANA model components

iv. Numerical analyses and modification of the DIANA model: After modeling the DIANA model, the maximum bending moment that occurred during the measurement is put in the model in order to know the stresses occurring from the FE calculation. When there is a difference between the measured and the numerical data, the possible cause for the variations will be examined. Since mass concrete structures also release heat during hydration, it is necessary to add the heat flow properties into the model and examine how much the hydration heat is affecting the steel stresses. While combining both the structural and heat flow analysis, a proper representation of the concrete foundation can be mimicked. The next step would be to analyze the variations in the obtained result and how these variations can be minimized.

v. Second structural calculation : Another structural calculation has to be performed using a different method or preferably software (SCIA Engineering). Later, a comparison has to be made between the modified DIANA model and the SCIA model.

vi. Results and analysis: After obtaining the results from the field monitoring, and numerical and structural calculations, the results will be discussed in this step.

vii. Discussions and Recommendations for future work: This step will mostly consist of discussions based on the obtained results and some recommendations for future work.

vii. Conclusions: Next to analyzing and updating the DIANA model, the conclusions will be drawn and the research questions will be answered.

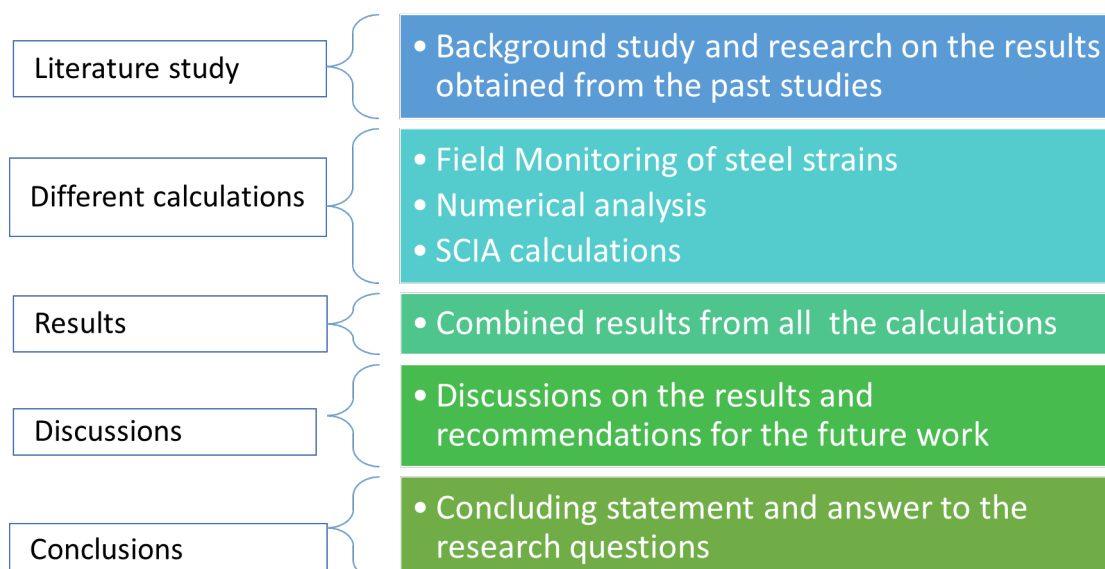


Figure 1.7: Methodology

1.5. Thesis Outline

To achieve the main objective of this research project, it is necessary to distribute the workflow into distinct parts. Hence, the chapters are categorized as follows:

- **Chapter 1** consists of the overall introduction of the Master Thesis. This chapter will not only provide the definitions of the basic components but will also deal with the basic parameters of the research topic.
- **Chapter 2** contains the State-of-the-art (Literature review) for the Master thesis. This section highlights the previous research related to the stress-strain analysis of the onshore wind turbine foundations. It also includes the theory of the effects that need to be included in the FE model.
- **Chapter 3** consists of the strain measurements of the onshore wind turbine foundation. This data has been collected using FO sensors placed inside the foundation. A detailed analysis of the calculated stress results from the obtained measurements is presented in this part.
- **Chapter 4** deals with a secondary structural calculation with SCIA engineering.
- **Chapter 5** deals with the non-linear structural calculations and a comparison of the monitored steel stresses with that of the FE calculation.
- **Chapter 6** highlights the effects of the heat of hydration in the DIANA model and a comparison of the monitored steel stresses with that of the FE calculation. This chapter will also include a detailed report of other effects along with hydration heat.
- **Chapter 7** deals with the explanation of the results obtained from the different analyses.
- **Chapter 8** presents a set of conclusions and corresponding answers to the main and sub-research questions. The end of this chapter will include some recommendations for future research.

Literature Review

This chapter highlights past research based on the onshore wind turbine foundation. In the beginning, it highlights the behavior of the steel stresses inside the foundation when modeling with linear analysis. Along with this, the chapter also focuses on the suitable ways to determine cracks inside the mass structure and the effects which need to be considered during the modeling of the concrete foundation in the FE software. Hence, this part is an encapsulation of all the literature studies during the course of the project.

2.1. Existing studies conducted on onshore wind turbine foundations

2.1.1. Behavior of Steel stresses with linear analysis

Field monitoring of steel stresses has been performed in many wind turbine foundations to analyze the structural behavior of the foundation and to perform numerical analysis. Linear numerical analysis has been performed in order to estimate the steel stresses and then compare them with the measured values. He et al. [4] performed structural health monitoring of an onshore wind turbine foundation with an embedded ring. According to the author, it is necessary to monitor the concrete deformation for a long period of time to ensure safety. Gao et al. [5] and Deng et al. [6] conducted physical model tests and numerical simulations on a wind turbine that is subjected to arbitrary wind loads. It was concluded that the surrounding of the onshore wind turbine foundation is affected by the dynamic wind loads, and the DAF depends on the wind speed and the spatial position. Zhou et al. [3] measured the axial steel stresses with the help of stress gauges in various positions and directions of the shallow foundation. Figure 2.1 [3] shows the layout of the stress gauges fixed in the concrete foundation at different locations. The 3-D model is created in the ABAQUS finite element software which consists of the steel reinforcement cage, the steel ring, concrete, and the subsoil. The finite element modeling is shown in Figure 2.2 [3].

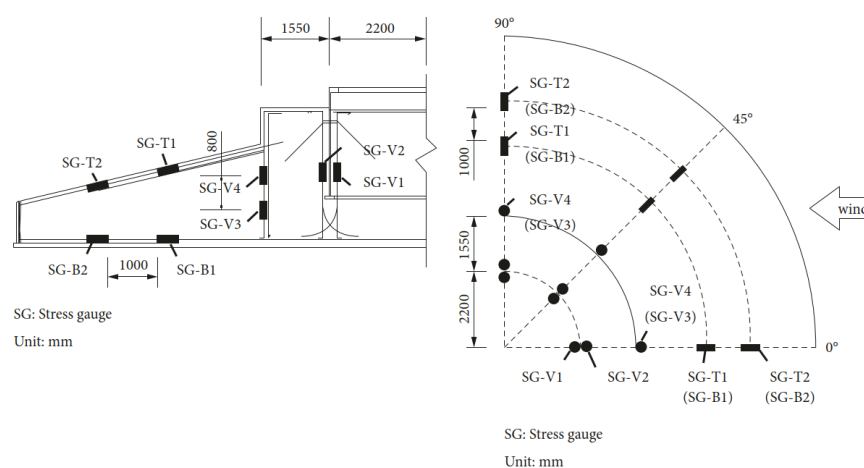


Figure 2.1: Layout drawing of stress gauges in the foundation [3]

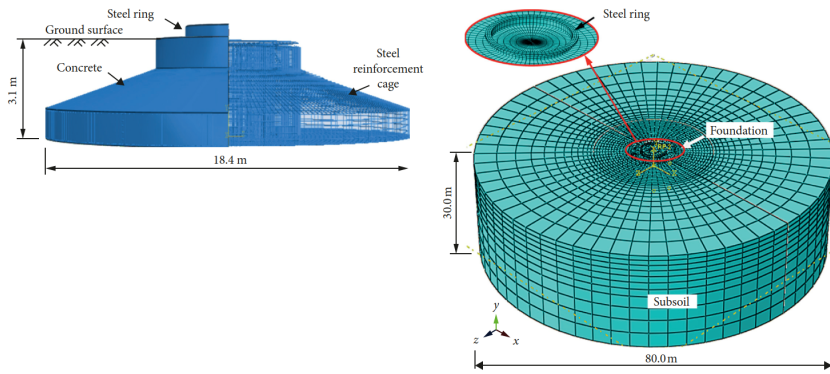


Figure 2.2: Numerical Model of the wind turbine foundation [3]

According to [3], the radial steel bars in the foundation were in tension whereas those near the top surface were in compression. Vertical steel bars were either in compressive or tensile stress depending on the position. Also, the axial stresses in the vertical steel bars were affected by the wind speed. In comparison to the radial and vertical bars, circumferential bars experience lower stress. Both the simulated and monitored results depicted similar variations and distributions despite being different values as shown in Figure 2.3 [3]. A possible reason for the disparity in the magnitude of the steel stresses could be the fact that material non-linearity is not included in the analysis. Hence, this leaves room for discussion about the effects of nonlinear analysis.

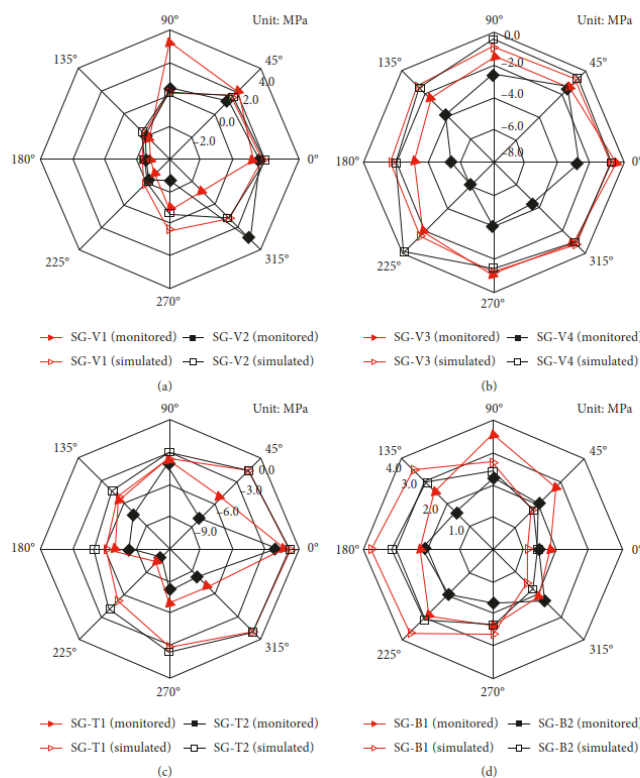


Figure 2.3: Axial stresses of steel bars in the foundation [3]

2.1.2. Monitoring of temperature evolution during concrete hardening

Massive concrete foundations require temperature control of concrete hardening during their construction. An experimental study was conducted in [7] for a wind turbine foundation. The study was conducted using two methods- calorimetric analysis and continuous temperature-time monitoring. The temperature of the operation should not be more than 70 °C. In the calorimetric analysis, the adiabatic method is used. The temperature variations for concrete hardening are recorded for 72 hours. The figure below depicts the results from the calorimeter for two concrete compositions of cement type CEM II/A-S 32.5-LH. A big difference is observed in the indicators of the initial temperature of both compositions. The absolute temperature during this period is 70.5 °C, and its excess relative to the initial value is 55 °C. Hence, it proves the possibility of a significant increase in the concrete temperature during hardening.

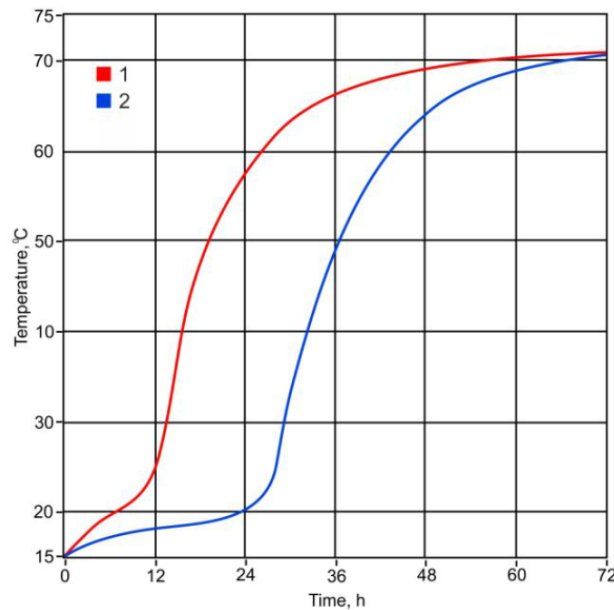


Figure 2.4: Temperature of concrete samples in an adiabatic calorimeter [7]

In another method, the temperature is measured using 8 temperature sensors. These sensors were installed at different points in the structure as shown in the below figure:

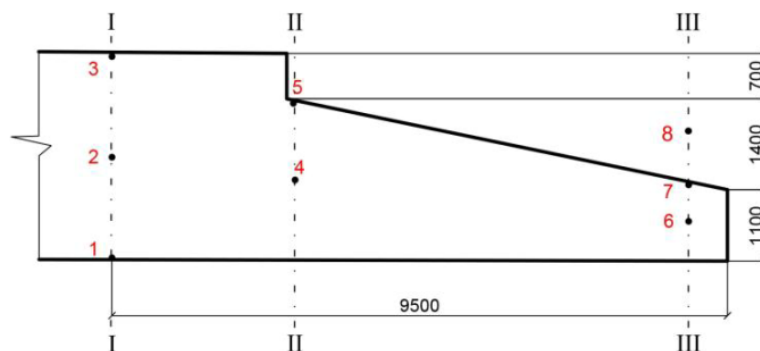


Figure 2.5: Sensor layout [7]

The following figure shows the results obtained from the sensors monitoring the hardening temperature inside the foundation slab after concreting:

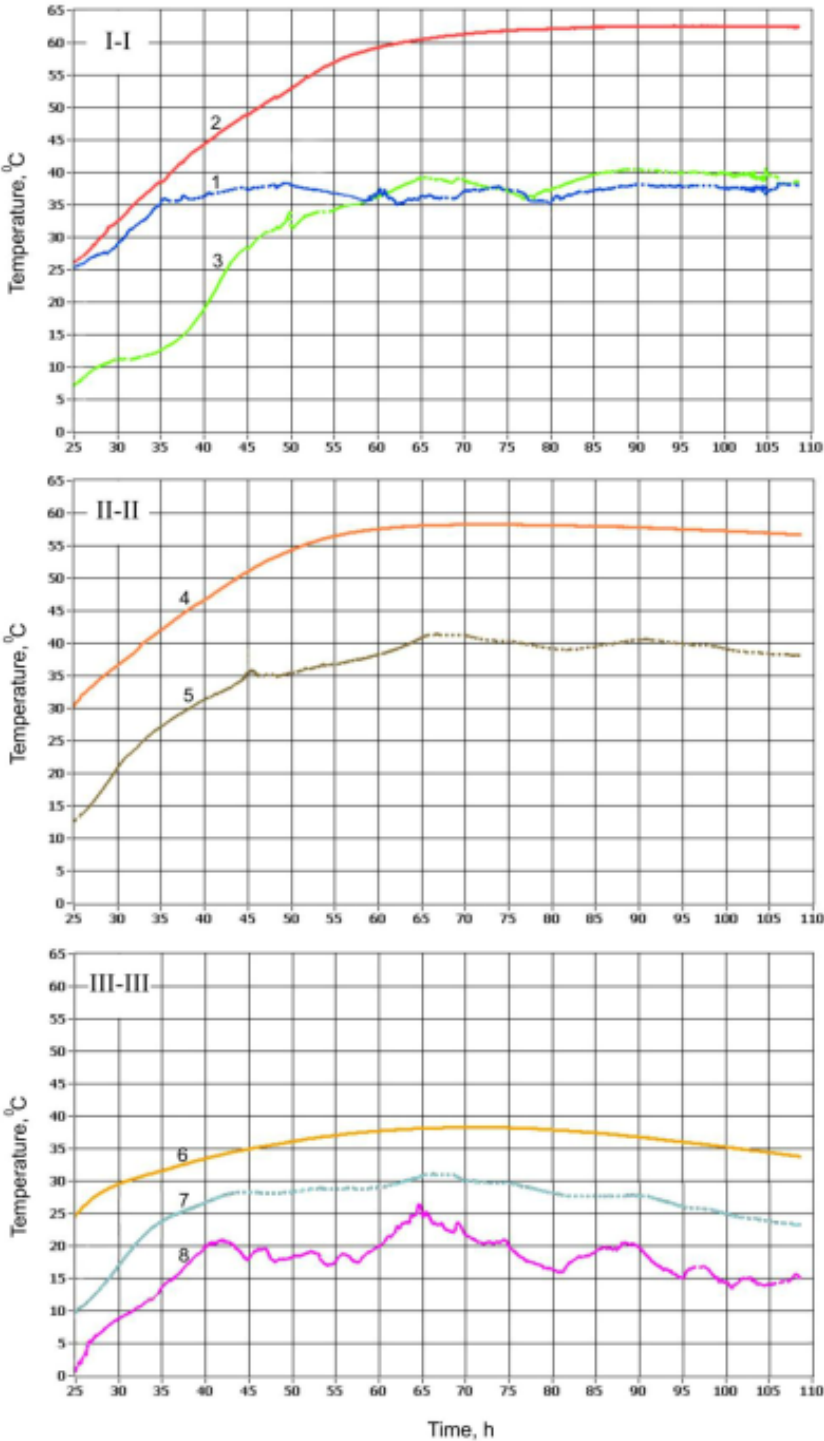


Figure 2.6: Hardening temperature of the foundation [7]

From the above Figure 2.6, the maximum temperature of 62.5 °C is observed at point 2 of section I-I, where the hardening condition approaches adiabatic ones. The initial temperature was 7.5 °C and the increase in temperature is 55 °C. Also, it is to be noted that due to the significant time interval of concreting of the lower and upper parts of the foundation, there is a significant lag in the rate of temperature rise over 60 hours, after which temperature values are equalized. The temperature gradient between the inner and outer parts of the foundation is significant. The maximum value of 27 °C is observed after 38 hours of hardening after which it reduces to 20-25 °C. While in II-II, the maximum temperature is 58 °C, and the temperature gradient is 16-18 °C. The minimum rate of temperature rise is recorded in III-III, where the maximum temperature is 38 °C, and the gradient was from 15 to 8-10 °C. The installation of the tents over the foundation creates favorable conditions for hardening to reduce the temperature gradient. At the same time, the temperature of concrete rises by 15-20 °C as compared to the temperature of the outside air. It can also be concluded from the obtained results that the heat accumulation phase lasted longer at the locations closer to the core of the foundation, leading to higher temperature peaks [8]. The temperature decreases after the heat transfer phase and a fluctuation at locations closer to the foundation surface has been observed. The Figure 2.7 depicts the temperature distribution between two points. The red curve shows the point closer to the foundation core whereas the blue curve is the result of the point away from the core.

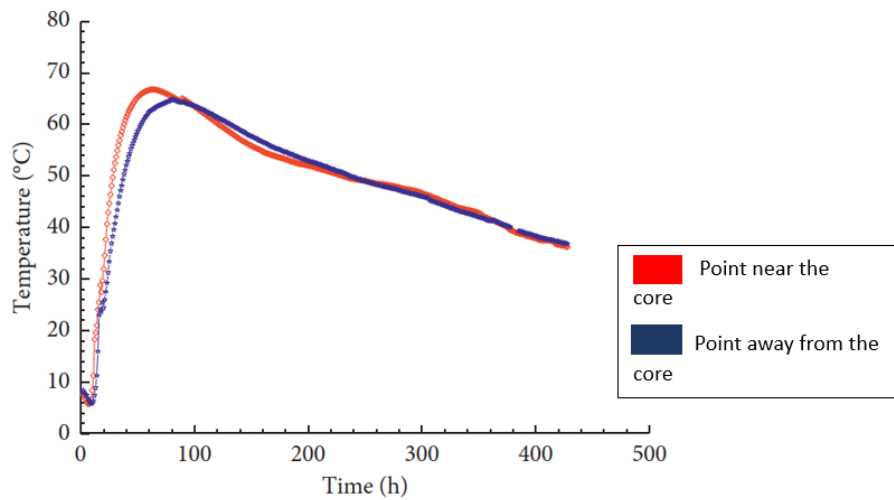


Figure 2.7: Temperature comparison between two points [8]

The temperature variations in FEM analysis of the foundation at different time periods are shown in Figure 2.8.

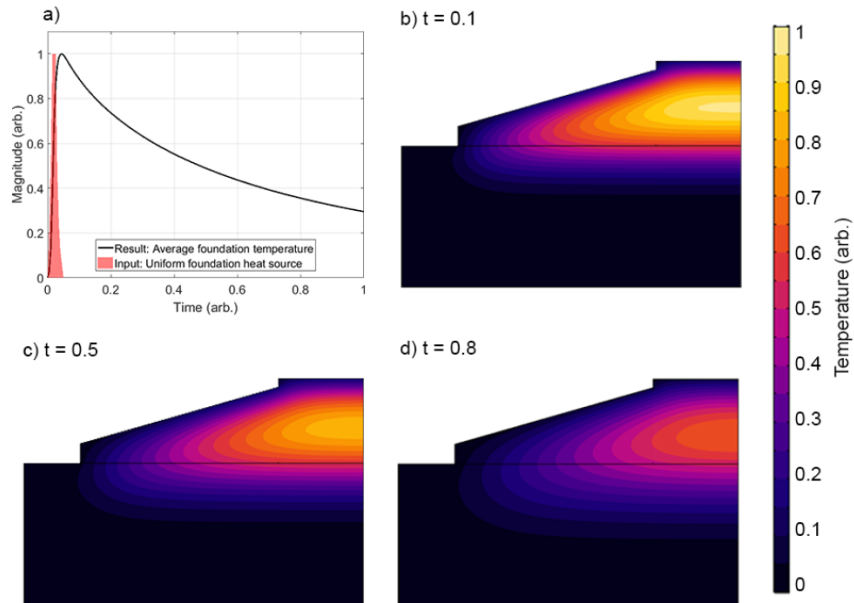


Figure 2.8: Thermal FEM results: a) Average foundation temperature results, b)-d) Temperature profiles at different times [9]

The temperature gradient is one of the significant reasons which leads to thermal cracking in mass structures [10]. Temperature gradients are obtained in the vertical direction. From the experiments of [8], the maximum gradient is obtained at an age of 9 days, when the temperature difference between the foundation core and the top surface is 35 °C.

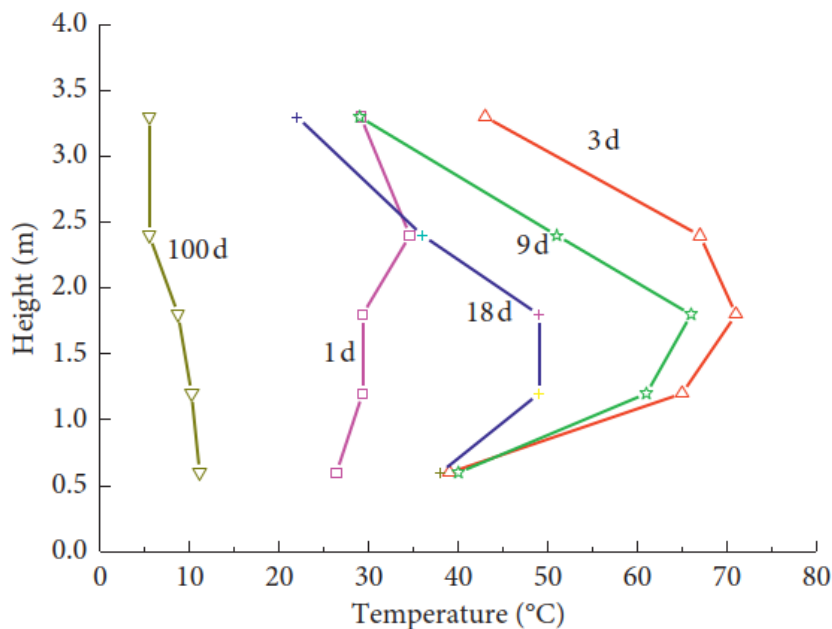


Figure 2.9: Temperature variation along the vertical direction [8]

Due to the presence of maximum temperature in the core, it also has a higher magnitude of temperature decay, which results in tensile stresses since the temperature decay is constrained during contraction by the region with a weak temperature decay [8]. A larger value of tensile stress is observed in this phase

because of the increasing Young's modulus. This counteracts the compressive stress inside the concrete which was generated during the temperature rise phase. A big temperature gradient between the core and the foundation surface leads to higher tensile stress, which results in cracks.

The temperature values presented in the paper will be as a reference point in order to verify the results of the DIANA calculation.

2.2. Fiber Optics Measurement

Strain is the deformation of the particles in a body due to the stress induced by force. In order to monitor the structural behavior of the turbine foundation, the strain measurements were carried out by using Fiber optics. In this case, Fibre Bragg Gratings are used which are basically glass fibers generally known for their light-emitting properties and ability to transport data over large distances. Fiber photosensitivity is the main principle involved in writing Bragg gratings into the core of the fiber. This measuring technique is based on a passive sensor with active monitoring. The monitoring unit emits light into the fiber. Intended distortions generate a reflection of a specific wavelength when the light refracts on the wavelength-dependent optical filter. This marks the location of the point with a high degree of precision. The light frequencies are tenable and the characteristics traveling within the fiber are modified as a function of the temperature and the strain. They are determined in the back-scattering light, which is later collected by the monitoring unit, analyzed, and then converted into strain and temperature data. The applied sensors are distributed sensors where strain is measured over the full length of the fiber. The fiber cable has to be looped to transmit the data to the receiver. With regards to the advantage, many FO sensors are developed to achieve specific challenges in the health monitoring of concrete structures, such as crack detection or crack monitoring [11]. Mass structures such as bridges and wind turbine foundations can be instrumented with sensors to assess and ensure ongoing structural health and safe operation of the structure [12, 9]. Not only that, in the FBG sensor, the measurand is encoded directly with the wavelength, which is an absolute parameter and does not suffer from the disturbances of the light paths [13]. Thus, the output signal is independent of the intensity of the source, and losses in the connecting fibers and couplers. The accuracy of the sensor depends on different factors such as linearity, resolution, temperature stability, long-term stability, and statistical error. The FBG is sensitive to both strain and temperature due to linear expansion affecting the grating period and the difference in refractive index from the photoelastic effect, and thermal expansion and thermo-optic effect of fiber material respectively [14]. Regardless, of the temperature sensitivity, the temperature is very stable in FBG sensors during short-term monitoring and usually, there are no differentials between the start and end of monitoring cycles. The strains measured due to the forces induced into the gauges are all differentials and the rebar gauges are not calibrated.

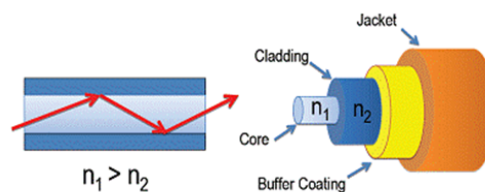


Figure 2.10: Fiber Bragg Grating system

2.3. Determination of concrete cracks

Wind turbines onshore or offshore often experience continuous cyclic loads [15, 16, 17]. The constituents of such structures are expected to support the existing repetitive and variable loads to maintain structural integrity. The concrete foundation that responds to a given set of dynamic loads with resonant vibrations at one or more natural periods is evaluated using dynamic analysis techniques [18]. Vibrations of small amplitude are mainly used to determine the dynamic parameters assuming a linear behavior of the structure. In case of the amplitude increases, non-linear behavior begins to alter the dynamic properties [19]. Omori et al. [20] was the first to build a relation between the fundamental period in buildings with damage. It has been observed that the damaging process due to seismic activities produces a permanent loss of stiffness and then a permanent increase of the fundamental period [21]. According to [22], using the natural period as a diagnostic parameter is based on the assumption that the natural frequencies are sensitive indicators for structural integrity and directly proportional to the strength of the structure. Various damage-detecting techniques assume that the development of cracks leads to nonlinear behavior in the structure [23, 24]. Therefore, to determine the cracks in the foundation, a comparison between the undamaged and damaged state of the structure is required. This can be determined based on formulas that are either empirical or numerical. Natural frequency is not only an essential parameter for designing new structures but also essential for the assessment of existing structures.

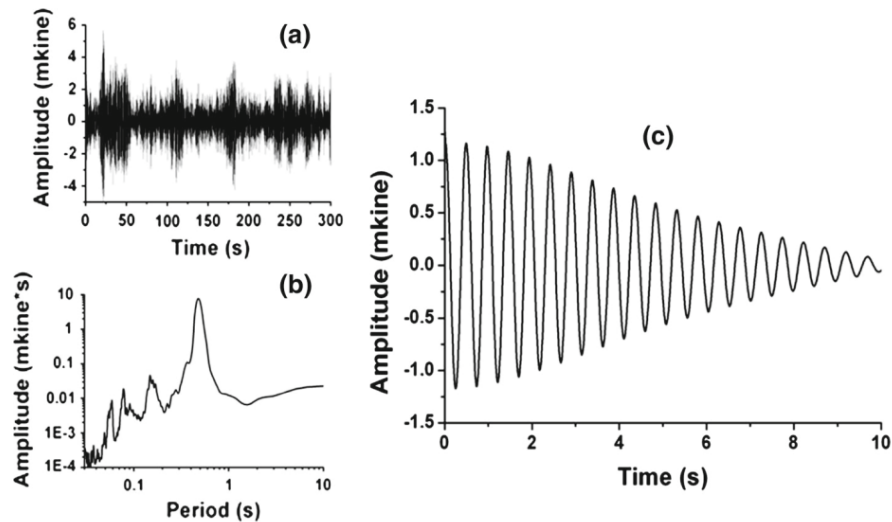


Figure 2.11: Example of damping evaluation a) Ambient noise record, b) Amplitude spectrum, c) Damped response of the building [19]

Jiao et al. [25] in their paper stated that the temperature changes in the mass structures could also lead to changes in modal parameters such as modal frequencies. Another important parameter is the damping ratio, which depends on the structure-soil interaction. From [19], it does not have any significant effect on the earthquake damage degree.

2.4. Theory behind Uncracked concrete

When the tensile stress of the concrete is less than the tensile strength of the concrete, there will be no cracking in the foundation. Often, some cracks are observed in the mass structures such as wind turbine foundations, but with proper design, this can be avoided. A wind turbine foundation often experiences dynamic loads due to the wind, self-weight of the structure, weight from the surrounding soil, and prestressing from the anchors. It depends on the structural engineer which load combinations they are considering while designing the structure. One reason for the occurrence of cracks can be due to the consideration of ULS while designing the structure instead of SLS as it may happen that the loads in SLS in combination with thermal stresses have caused the cracks [26]. Other possibilities include cracking near the connection of the tower and foundation with the insert ring, while some cracks may happen due to poor workmanship and inappropriate material selection. Foundations of wind turbines often experience fatigue due to the application of repetitive loads [18]. Hence, it is necessary to take fatigue into consideration while designing such mass structures. Under dynamic loads, the fatigue strength is estimated with the help of S-N curves. From [27], to ascertain the potential of cracking due to the hydration heat, a stress analysis is required to assess whether the thermally induced stresses are greater than the tensile strength of concrete at a given age.

There are many mass structures that remain uncracked over a period of time. The different parameters influence the strengthening of the structural element over time. Generally, thermal stresses are generated in the mass concrete structures which leads to thermal cracking [28]. Though this can be avoided with proper design, consideration of low-heat cement, and good workmanship. Furthermore, when the concrete is uncracked and the steel stresses are low as compared to the tensile strength, it is safe to assume that the structure is prestressed which does not allow cracks to form inside the foundation. This prestressing force can be generated from the heating inside the foundation due to the effect of hydration heat. In a reinforced mass concrete structure, when concrete is poured, the heating of the foundation due to the effect of hydration heat leads to a rise in temperature, and the internal volume expands whereas the external volume decreases due to ambient temperature. During the cooling period, the outer surface temperature decreases while the foundation temperature is still hot. This cooling in the outer surface leads to contraction whereas the inner surface is in tension. This results in the prestressing of the reinforcement in the foundation. A pictorial representation of the temperature difference and crack formation mechanism is shown in Figure 2.12.

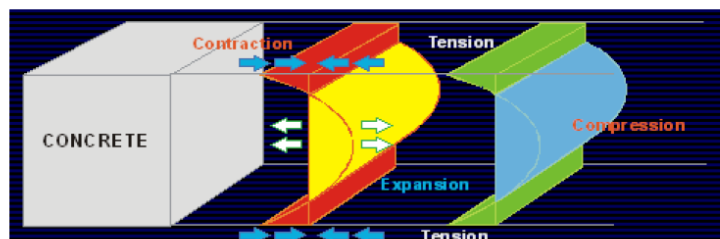
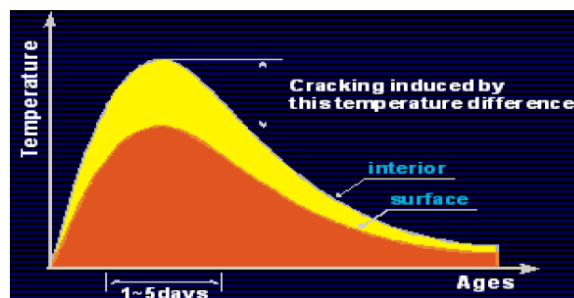


Figure 2.12: Temperature difference in the foundation [29]

According to [30], the cement paste blended with different substitution materials changes the hydration kinetics. This changes the release peak value significantly, but the main peak time does not fluctuate evidently. Also, from the experimental studies in [30], depending on the composition of the mixture, the 3-day, and 28-day compressive strength of the blended cement range from 19-40 MPa and 37-60 MPa. This blended cement contains a mixture of either silica fume or fly ash or quartz powder. The mixture containing silica fume has higher reactivity than ordinary cement whereas fly ash and quartz powder have lower reactivity. It is observed that the pozzolanic action of fly ash and quartz powder to compressive strength becomes more remarkable in the later period. The experimental results confirmed that cement replacement plays a significant role in the development of compressive strength.

2.5. Heat of Hydration

2.5.1. Process and Mechanism

When cement and water come in contact, a thin layer of reaction products forms at the surface of the cement particles. This is known as a phase-boundary reaction. After this stage, comes the dormant stage where hardly any observable reaction activity happens. At the end of the dormant stage, the reaction process leads to the acceleration period. In this process, the layer of the hydration products around the cement particles comes in contact with each other as they become thicker. By the end of this stage, the process becomes diffusion controlled [31]. A schematic representation is shown in Figure 2.13. The potential risk of early-age concrete, mainly massive concrete structures, cracking depends on the ability of hardening concrete to support thermal stresses caused by the exothermic nature of the hydration process [32]. Mass concrete structures generate a significant amount of temperature gradient between the inside and outside surfaces of the foundation. The exothermic reaction of the hydration process results in the rise of temperature in mass concrete structures which induces the possibility of early-age concrete cracking during cooling and of premature degradation of the structure [32].

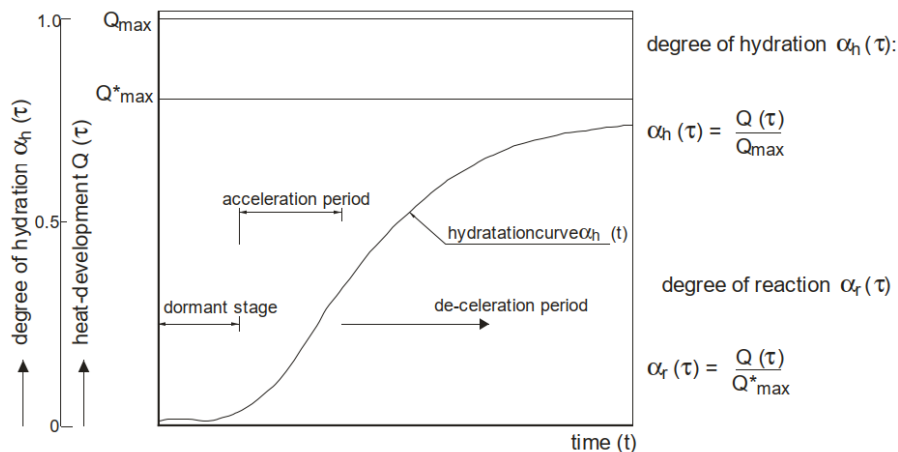


Figure 2.13: Different characteristic stages during hydration[31]

2.5.2. Degree of hydration

The degree of hydration is the ratio between the amount of cement that has changed into reaction products and the originally available amount of cement. It is also defined as the amount of heat liberated from the amount of cement that has reacted.

$$\alpha_h(\tau) = \frac{Q(\tau)}{Q_{max}} \quad (2.1)$$

where,

$Q(\tau)$ = the amount of liberated heat at time $t=\tau$

Q_{max} = the amount of liberated heat at complete hydration of all available cement

2.5.3. Degree of reaction

This is the ratio between the amount of heat liberated $Q(\tau)$ and the practical maximum amount of heat liberated $Q_{(max)}$ * [31].

$$\alpha_r(\tau) = \frac{Q(\tau)}{Q_{max}} \quad (2.2)$$

2.6. Temperature distribution in hardening concrete

2.6.1. Fourier Differential Equation

According to [31], an analysis of the heat fluxes and temperature distributions can be conducted if the source of heat is known. To calculate the temperature distributions in a structural element, the Fourier differential equation will be used. The equation is given below:

$$\frac{\partial T}{\partial t} = a_c \cdot \left[\frac{\partial^2 T}{\partial x^2} + \frac{\partial^2 T}{\partial y^2} + \frac{\partial^2 T}{\partial z^2} \right] + \frac{1}{\rho_c c_c} \cdot [q_c(x, y, z, t)] \quad (2.3)$$

where,

λ_c	= heat conduction coefficient[W/mK]
c_c	= specific heat of concrete[kJ/kgK]
ρ_c	= specific mass of concrete[kg/m ³]
$T(x, y, z)$	= temperature of the concrete[K]
$q_c(x, y, z, t)$	= heat source[kJ/m ³ h]
x, y, z	= coordinates
a_c	= temperature levelling coefficient[m ² /h]

$$a_c = \frac{\lambda_c}{\rho_c c_c} \quad (2.4)$$

The Fourier differential equation is solved using the finite element method.

2.6.2. Thermal Properties of Hardened concrete

The thermal characteristics of the concrete depend on the composition of the concrete mixture including the microstructure of the concrete.

Heat conduction coefficient, λ_c

It depends on the concrete's mix composition, especially on the type of aggregates. This value lies between 2.0 and 3.0 W/mK.

Specific heat, c_c

The specific heat of young normal concrete varies between 1.0 and 1.15 kJ/kg.K. It increases with increasing water content and slightly increases with an increase in temperature [31].

Heat diffusion coefficient, a_c

This coefficient will not be constant since the properties on which it depends, change during the hardening process [31].

Heat Capacity

From [31], the heat capacity is the product of the mass density of concrete and specific heat. It is assumed to be a constant value for practical applications but generally, it is a function of the degree of hydration. Heat capacity = specific heat of concrete * specific mass of concrete

2.6.3. Thermal boundary conditions

Heat-Transfer coefficient

From [33], the convective heat transfer coefficient, measures the amount of heat transfer between the concrete surface and ambient air. HTC depends on the factors such as wind velocity, curing condition, and thermal conductivity. At this surface, the heat flux will experience resistance which depends on the medium of the surroundings and on the temperature difference between the surface and the medium. The following relation Equation 2.5 states that at the concrete surface, the amount of heat supplied should be equal to the amount of heat exchanged with the environment [31]. The convective heat transfer coefficient also depends on the factors such as the roughness of the concrete surface, materials of the formwork, and flow characteristics [33]. Furthermore, the convective heat transfer coefficient depends on the boundary condition of the concrete surface in contact with the ambient air.

$$\lambda_c \cdot \left(\frac{\partial T}{\partial x} \right)_0 - \alpha \cdot (T_s - T_{om}) = 0 \quad (2.5)$$

where,

- λ_c = heat conduction coefficient [W/mK]
- T_s = temperature at the concrete surface [$^{\circ}C$]
- T_{om} = temperature of the surroundings [$^{\circ}C$]
- x = normal to the surface [m]
- α = heat-transfer coefficient [$W/m^2 \cdot ^{\circ}C$]

When a formwork or an insulating layer is present with a thickness d_i and a heat flow conductivity λ_i , and α_m as the heat transfer coefficient of formwork and the surrounding, then the resulting heat-transfer coefficient is calculated:

$$\frac{1}{\alpha_{res}} = \frac{1}{\alpha_m} + \sum_1^i \frac{d_i}{\lambda_i} \quad (2.6)$$

According to [34], the maturity of the concrete of the same composition has almost the same strength as the combination of temperature and age requires to make that maturity. Furthermore, the experiments conducted by [33], showed that when curing materials are used, the temperature difference between the center and the surface of the structure decreases since the rate of heat release decreases. It is also noted that the fast release of heat on the surface of the concrete structure causes excessive tensile stress at the early stage of concrete casting. In addition to the above-mentioned factors, it is observed that the effect of the wind velocity and curing condition on the coefficient is apparent. Also, it is noted that the convective heat transfer coefficient influences the temperature profile of the structure, and the resulting tensile stress results in cracking.

Adiabatic temperature rise

When the liberated heat is used for concrete heating, it is called the adiabatic process. The adiabatic temperature rise can be calculated using the formula below:

$$\Delta T_a(t) = \frac{\alpha_h(t) \cdot C \cdot Q_{max}}{\rho_c \cdot c_c} \quad (2.7)$$

where,

- $\Delta T_a(t)$ = adiabatic temperature rise at time t [$^{\circ}C$]
- C = cement content of the concrete [kg/m^3]
- ρ_c = specific mass of the concrete [kg/m^3]
- c_c = specific heat of the concrete [$kJ/kg \cdot ^{\circ}C$]

The schematic representation of the adiabatic hydration process and temperature rise is presented in Figure 2.14.

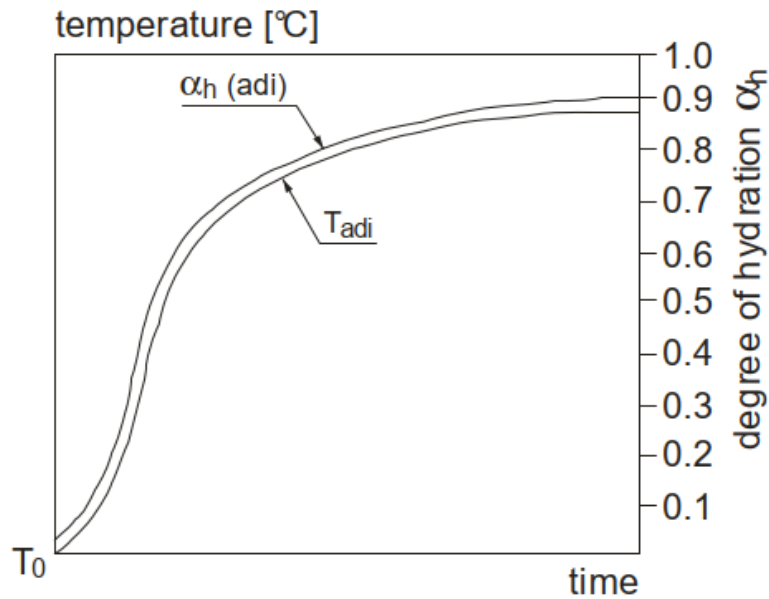


Figure 2.14: Adiabatic hydration process and rise in temperature [31]

2.6.4. Temperature deformations in hardened concrete

Thermal expansion coefficient

Thermal expansion depends on the expansion coefficient of the individual components inside a concrete. For the majority of the practical applications, a constant expansion coefficient is assumed.

2.6.5. Average temperature, temperature difference, and eigen temperature

The temperature calculation results in a temperature distribution over the cross-section of a structural element. The different temperature components are explained below in detail:

Average temperature

The average temperature depends on restrained or unrestrained conditions. In the case of the free deformations, ΔT_{ave} will lead to either elongation or shortening. Whereas, if the deformations are restrained, a normal force will develop.

$$\Delta T_{ave} = \frac{1}{A_c} \cdot \int_{x_1}^{x_2} \Delta T(x) \cdot b(x) dx \quad (2.8)$$

where,

- x_1 and x_2 = distances along the x-axis of the outer fiber
- $b(x)$ = width of the concrete cross-section
- A_c = area of the concrete cross-section

Temperature difference

The temperature gradient over the whole cross-section results in a linear temperature distribution. From [31], the temperature distribution due to an arbitrary thermal load is shown in Figure 2.15.

The equation for the temperature gradient is shown below:

$$\begin{aligned} \Delta T_b(x) &= \frac{\Delta T_b}{h} \cdot x \\ \Delta T_b &= \frac{h}{I} \int_{x_1}^{x_2} T(x) \cdot b(x) \cdot x dx \end{aligned} \quad (2.9)$$

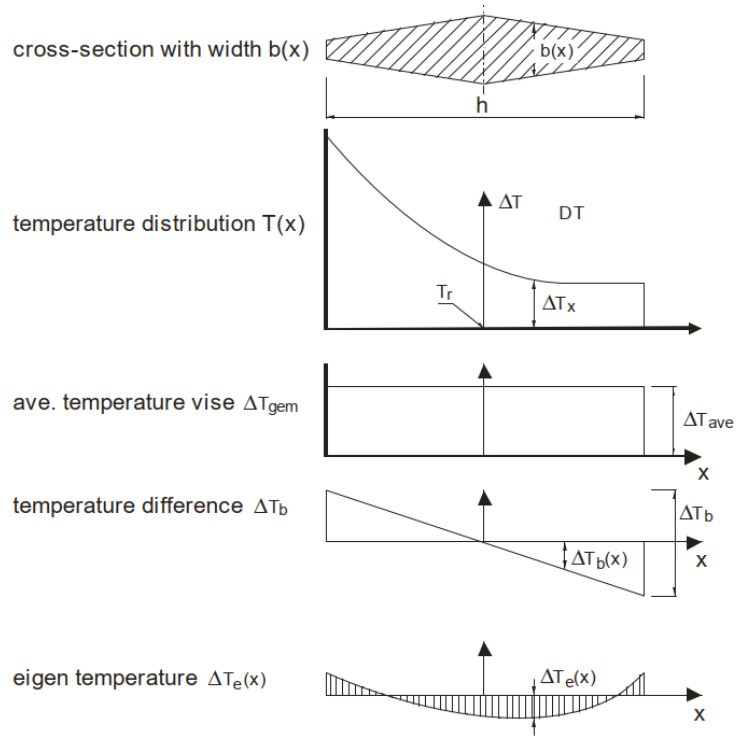


Figure 2.15: Temperature distribution into 3 different components [31]

where,

I = Moment of inertia

h = height of the element

When the structure is free to deform, the linear temperature gradient causes a curvature $\kappa(\Delta T_b)$.

$$\kappa(\Delta T_b) = \frac{\Delta T_b \cdot \alpha_c}{h} \quad (2.10)$$

Eigen temperatures

These temperatures result in eigen stresses. It is calculated using the following equation Equation 2.11. The summation of the eigen temperature over the whole cross-section of the structural elements should be zero. They generally do not lead to any kind of deformations of the cross-section as a whole, except at its outer ends [31].

$$\Delta T_e = \Delta T(x) - (\Delta T_{ave} + \Delta T_b(x)) \quad (2.11)$$

Reference Temperature

According to [31], the reference temperature is the basic temperature that is used to calculate the temperature variations relatively. T_r is mostly assumed to be equal to 20°C.

Field monitoring of strain measurements

This chapter encapsulates the field monitoring of the wind turbine foundation and discusses the basic description of the setup along with the methodology and the obtained results. This will also include the determination of the occurrence of cracks inside the mass structure.

3.1. Description of the setup

Health monitoring of the concrete foundation is conducted in order to determine the structural behavior of the mass structure. This is conducted using the FO sensors, typically an FBG sensor as described in section 2.2, which were placed inside the foundation before the concrete was poured into the wind turbine 01 in Riemst. The optical glass fibers are present in different locations to measure the strain data in the reinforcements present inside the structure. A typical glass fiber optics is shown in Figure 3.1. For this project, the sensors are located at 8 positions as shown in Figure 3.3. The setup is based on 4 axial orientations.



Figure 3.1: Glass Fiber optics sensor

3.1.1. Overview of the sensors

During the interpretation of the results, it is necessary to understand the function of each component of the sensor and hence, this section will highlight the terminologies used in the results.

- **Interrogators:** These are devices that obtain data from the sensors located in different directions. The interrogators present during the measurement are named I_x0 , I_x1 , and I_x2 .
- **Channels:** There are four channels present that help to figure out the position of the sensors.

- **Directions:** The directions in the sensors are interpreted in the following way:

Table 3.1: Overview of the sensor directions

Actual Wind Directions	Represented directions in sensors
North	A
East	B
South	C
West	D

- **Measuring locations:** There are 8 measuring locations inside the foundation. The description of each sensor at different locations is provided below:
 - **L01:** It detects the steel stress in the wind turbine tower's bottom section which in turn determines the maximum bending moment that goes inside the foundation. This is a crucial step for further analysis of the steel stresses in the DIANA since it determines the maximum tensile and compressive steel stresses inside the foundation. The sensor is located 1m above the concrete in the basement of the wind turbine tower.

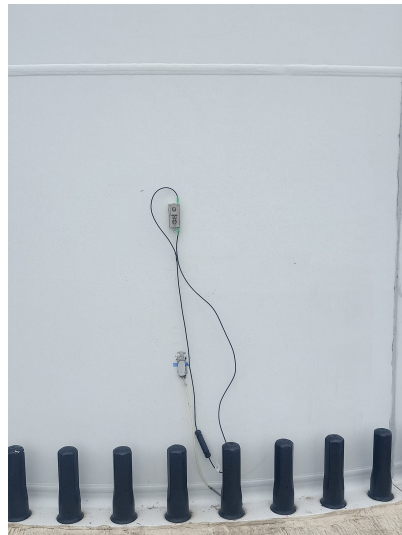


Figure 3.2: L01 sensor

- **L02:** Detects the longitudinal stress of the top radial reinforcing bar. All other sensors except L01 are encased in concrete and subjected to working loads during construction. The sensors can measure the strain of the rebar over 1m, consisting of 4 sections of each 250mm.
- **L03:** The sensor at this position determines the longitudinal stress of the top tangential reinforcing bar.
- **L04:** At this position, the sensor measures the longitudinal stress of the stirrup.
- **L05:** This is the inner part of the foundation bottom. Hence, the sensor at this position determines the longitudinal stress of the bottom radial reinforcing bar.
- **L06:** This measures the longitudinal stress of the bottom inner tangential reinforcing bar.
- **L07:** The outer part of the bottom side of the foundation measures the longitudinal stress of the radial reinforcing bar.
- **L08:** It measures the longitudinal stress of the bottom outer tangential reinforcing bar.

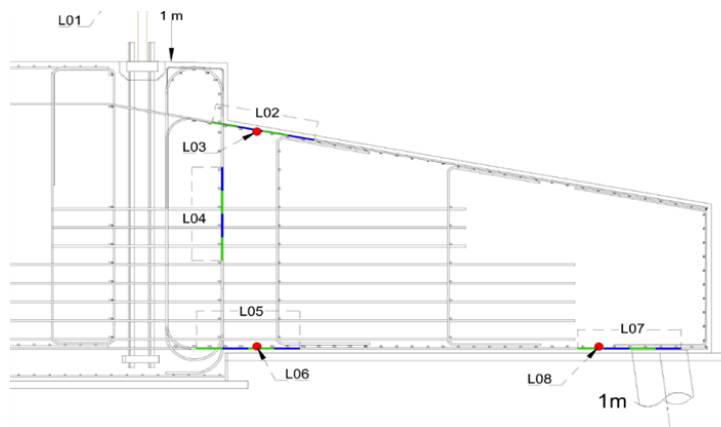


Figure 3.3: Position of sensors-Side view

- **Measuring points:** In order to get the strains from all the neighboring elements, the optical fiber has 4 measuring locations.

Table 3.2: Timeline

Date	Event
July 2017	Concrete pouring
August 2017	Prestressing of the foundation
September 2017	Erection of the tower
October 2017	Baseline measurement
November 2017	First measurement
May 2022	Second measurement
March 2023	Third measurement

3.2. Methodology for the measured data from 2017

3.2.1. Research Data

This is the first measurement conducted after two months of the tower's erection on the foundation. At that time, the foundation was newly constructed and the concrete was poured before 2 months of tower erection. Before performing the test, it is necessary to predict the wind speed and wind directions for a week since wind direction affects the direction of the bending moment and wind speed affects the amount of steel stress [3] in the foundation. On the day of the measurement, a basic check is performed in order to verify the proper functionality of the glass fiber optics. The monitored results were obtained during the emergency stop to achieve maximum bending moment in the foundation.

A summarised value for the wind speed and direction is provided below Table 3.3.

Table 3.3: Summary of wind speed and wind direction-2017

Date and time	Wind speed (m/s)	Wind direction (degrees)	Nacelle position (degrees)
22/11/2017; 14:25	6.5	185	190
22/11/2017; 14:30	7.1	185	188

The mean wind speed obtained is 6.8 m/s during the measurement and the wind direction is more towards the south from the measured angle as shown in Figure 3.4.

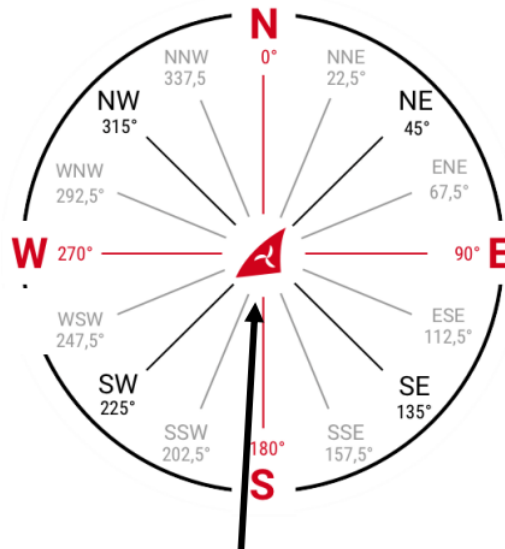


Figure 3.4: Pictorial representation of the wind direction-2017

3.2.2. Stiffness of the foundation

The presence of cracks is determined inside the foundation using the relation between the stiffness and the frequency [22]. The frequency of the foundation is calculated using the Fourier transform in MATLAB. Thus, the frequency obtained is 0.157Hz. According to the data obtained from the turbine company, the natural frequency of the tower must be within the frequency interval of 0.157 Hz-0.162 Hz. Since the calculated value is within the range, it can be concluded that the tower is performing in an expected way. In the later stages, another measurement will be conducted where a comparison can be built between the two natural frequencies in order to determine the structural health of the foundation.

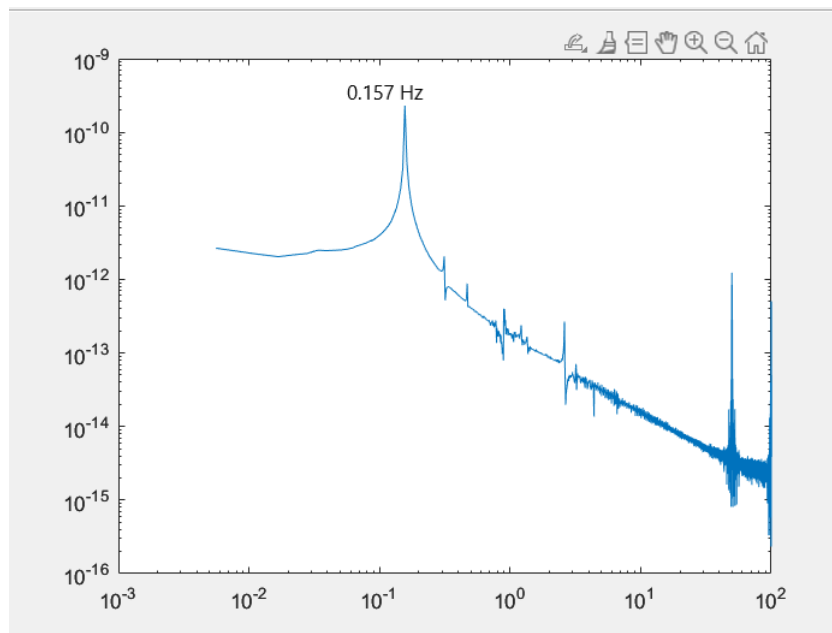


Figure 3.5: Natural frequency of the tower

3.2.3. Results

The results from the sensors are then processed in the interrogators present at the location. The obtained data from the measurements are in the form of strains. These strains are converted into steel stresses and then visualized in Power BI with respect to time for the given duration of the emergency stop. After obtaining graphs for the steel stresses, it is important to determine the prevailing wind direction during the measurement so as to obtain the direction for the bending moment. Since the wind direction is from south to north, the maximum bending moment will be from north to south. This is the primary bending moment while the secondary bending moment will act in the east-west direction due to the swaying back of the tower.

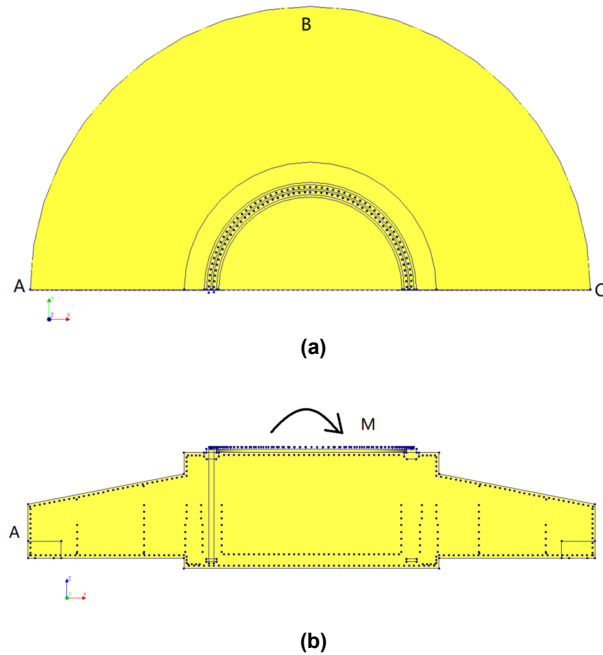


Figure 3.6: Wind turbine foundation with directions and bending moment a) Top view, b) Section view

From the obtained graphs in Power BI, the maximum tensile stress is found to be 182.21 MPa while the maximum compressive stress is 160.99 MPa obtained from the shaft sensor. From the steel stresses, the maximum bending moment is calculated to be 151.07 MNm. Figure 3.7 shows the maximum tensile and compressive stresses that go inside the foundation. The steel stresses at each position are presented in Appendix A for all directions.

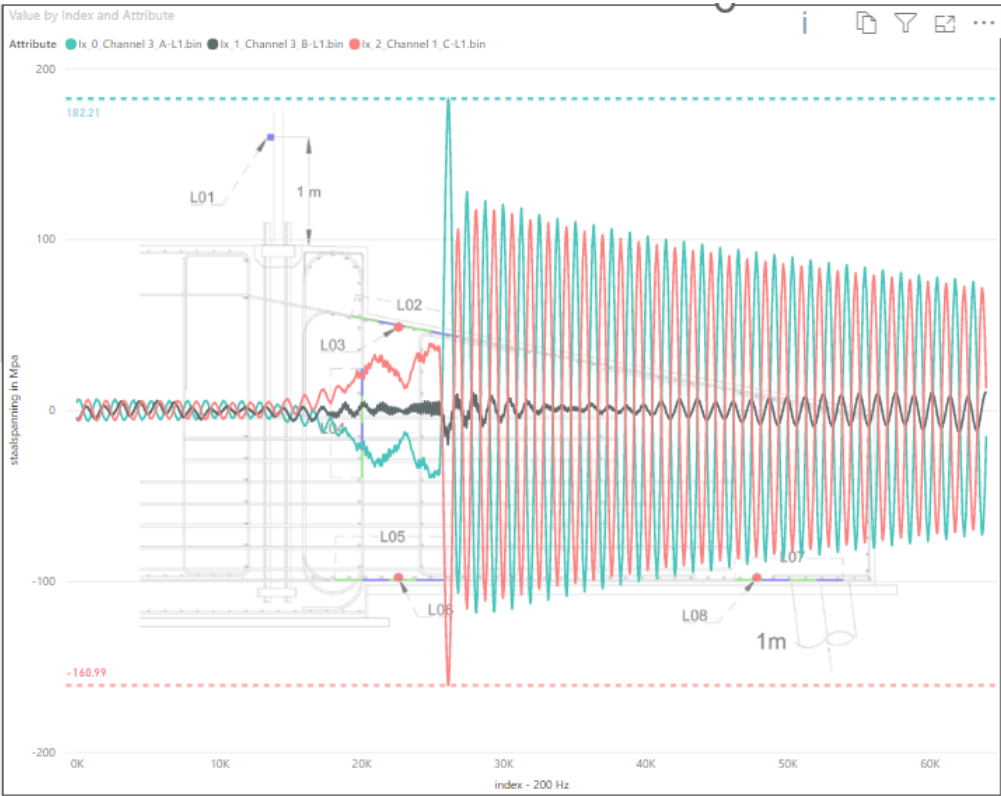


Figure 3.7: Steel stress for L01 position

The monitored stresses in the reinforcement groups located at different positions are obtained at a maximum level when the emergency stop has been applied and they are presented below in tabular form.

Table 3.4: Measured maximum steel stresses at different locations and directions-2017

Measuring Locations	Directions	Tensile Stress (MPa)	Compressive Stress (MPa)
L01	A	182.21	-118.53
	B	10.66	-20.16
	C	117.07	-160.99
	D	-	-
L02	A	21.97	-12.47
	B	5.1	-3.4
	C	15.4	-19.94
	D	3.06	-4.68
L03	A	3.13	-1.87
	B	1.08	-0.76
	C	3.13	-4.13
	D	0.75	-1.15
L04	A	4.64	-2.94
	B	1.32	-0.92
	C	3.7	-5.1
	D	0.96	-1.42
L05	A	5.04	-7.5
	B	1.67	-2.33
	C	8.96	6.04
	D	2.23	-1.55
L06	A	2.12	-2.9
	B	0.85	-1.19
	C	3.13	-1.99
	D	0.94	-0.68
L07	A	2.49	-1.13
	B	0.5	-0.38
	C	0.82	-0.73
	D	0.25	-0.33
L08	A	1.46	-2.17
	B	0.61	-0.81
	C	2.09	-1.39
	D	0.76	-0.5

At each location, the sensors measured the strains in all 4 directions. These strains are then converted into stress values which provide the generated stress due to the application of dynamic load. Each sensor measured both maximum tensile and compressive stresses at different moments. At the tower, the sensors are located in three directions instead of four. Hence, the obtained stresses are for North, East, and South direction only. From the table Table 3.4, it can be observed that the maximum tensile stress going in the foundation is 182.21 MPa measured in the North direction whereas, the maximum compressive stress is 160.99 MPa observed in the south direction. Since the wind is flowing from the South to the North and the bending moment is applied in the opposite direction, tensile stress occurring in the North and compressive stress occurring in the south seems logical. Also, the other directions East and West, experience lesser stress as compared to the prevailing directions since secondary bending moment is observed in both East and West. From the field measurements, the steel stresses in the top radial position were quite high compared to the steel stress in the top tangential direction. Whereas, in the case of the bottom radial and tangential rebars, the steel stresses are comparable.

3.3. Methodology for the measured data 2022

3.3.1. Research Data

In 2022, another measurement was conducted in order to monitor the structural health of the concrete foundation. Similar to the previous measurement, in this case as well the wind speeds and wind directions were predicted for a week before performing the field measurements. Below Table 3.5, gives the summary of the wind speed and wind directions during the time of the measurements:

Table 3.5: Summary of wind speed and wind direction-2022

Date and Time	Wind speed (m/s)	Wind direction (degrees)	Nacelle position (degrees)
24/05/2022,15:10	8	261.5	262.7
24/05/2022,15:15	8	261.5	262.7
24/05/2022,15:20	7.5	275.1	262.5
24/05/2022,15:25	7.5	275.1	262.5
24/05/2022,15:30	6.2	266.8	262.5

The mean wind speed is estimated to be 7.5 m/s flowing at a direction of 268° from the West to East direction. Since the wind direction is from west to east, the overturning moment that occurred will be from East to West. The pictorial representation of the wind direction is shown in Figure 3.8:

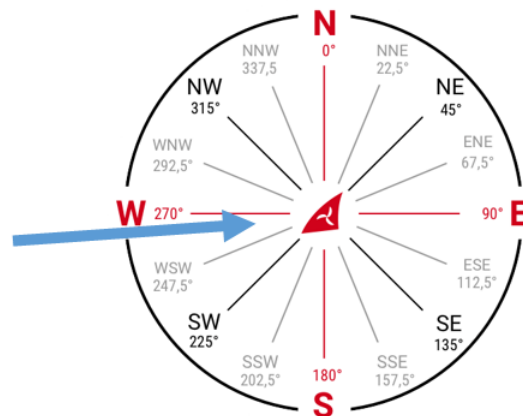


Figure 3.8: Pictorial representation of the wind direction-2022

3.3.2. Results

Unlike the measurements from 2017, the data from the prevailing directions of the shaft sensors are missing. Due to this, it becomes difficult to determine the amount of maximum steel stress that goes inside the foundation. The steel stresses from the measurement are presented in Table 3.6.

Table 3.6: Measured steel stresses at different locations and directions-2022

Measuring Locations	Directions	Tensile Stress (MPa)	Compressive Stress (MPa)
L01	A	0.51	-3.83
	B	-	-
	C	6.92	-5.02
	D	-	-
L02	A	2.66	-3.12
	B	7.6	-4.56
	C	-	-
	D	5.43	-8.52
L03	A	0.55	-0.63
	B	1.66	-1
	C	-	-
	D	1.51	-1.83
L04	A	0.69	-0.92
	B	2.18	-1.15
	C	-	-
	D	1.35	-2.23
L05	A	1.31	-1.08
	B	2.38	-3.99
	C	2	-1.62
	D	3.9	-2.3
L06	A	0.68	-0.52
	B	0.81	-1.39
	C	0.64	-0.57
	D	11.06	-11.29
L07	A	0.06	-0.11
	B	0.48	-0.33
	C	0.18	-0.26
	D	0.37	-0.42
L08	A	0.27	-0.33
	B	0.72	-1.23
	C	2.96	-2.58
	D	1.57	-0.99

Since the prevailing wind direction is from west to east, hence the applied overturning bending moment should be from East to West. From the above table, the maximum occurring steel stresses are in the primary directions i.e. East and West while the other two directions experience comparatively lower steel stress. As the wind speed is more in 2022 than the wind speed in 2017, according to subsection 2.1.1, the steel stress in 2022 has to be greater than the ones measured in 2017 but after comparing Table 3.4 and Table 3.6, that is not the case. Due to the lack of data, estimation is done with hand calculation otherwise it is difficult to find the exact maximum tensile and compressive stresses in the foundation. Along with the missing information from the shaft sensor, the data from the few other sensors are omitted during the

process in the interrogators. Thus, it becomes necessary to conduct another experiment on the same foundation in order to determine the accurate measurement results.

3.4. Methodology for the measured data from 2023

3.4.1. Research Data

Due to the missing information about the maximum steel stress present in the wind turbine foundation, a new measurement is performed for the same foundation in order to obtain the exact measurement results. This time the mean wind speed is 10 m/s and the prevailing wind direction is south-west as shown in

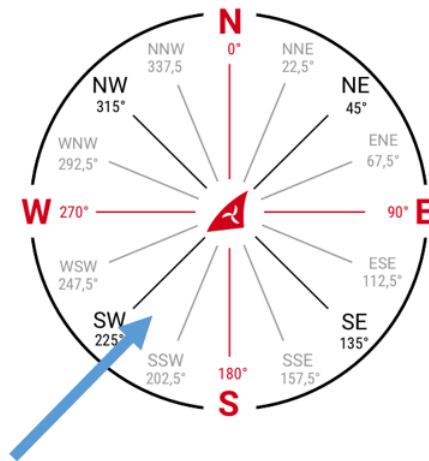


Figure 3.9: Pictorial representation of the wind direction-2023

Figure 3.9 and Table 3.7. Since the wind speed is greater than the other two measurements, it can be expected to have a larger tensile and compressive stress in the rebars.

Table 3.7: Summary of wind speed and wind direction-2023

Date and Time	Wind speed (m/s)	Wind direction (degrees)	Nacelle position (degrees)
23-03-2023;13:05	9.1	214.5	215.9
23-03-2023;13:10	10.9	214.5	215.9

3.4.2. Results

Despite conducting another measurement, the results obtained are not satisfactory due to the absence of measured values from the shaft sensor in the East-West direction. It is necessary to get readings from at least three sides in order to obtain accurate measurements, while in this case, only two readings are measured. The results are shown in the below Table 3.8.

Table 3.8: Measured steel stresses at different locations and directions-2023

Measuring Locations	Directions	Tensile Stress (MPa)	Compressive Stress (MPa)
L01	A	0.09	-0.11
	B	-	-
	C	0.24	-0.19
	D	-	-
L02	A	2.55	-5.16
	B	2.84	-6.62
	C	5.46	-2.43
	D	7.82	-4.8
L03	A	0.44	-0.92
	B	0.63	-1.4
	C	1.7	-0.77
	D	1.47	-0.64
L04	A	0.72	-1.44
	B	0.92	-2.07
	C	1.69	-0.8
	D	4.49	-4.01
L05	A	2.31	-1.11
	B	3.77	-1.65
	C	1.31	-2.89
	D	1.56	-3.61
L06	A	1.1	-0.58
	B	1.41	-0.63
	C	0.46	-0.99
	D	0.7	-1.57
L07	A	0.21	-0.11
	B	0.22	-0.45
	C	0.44	-0.24
	D	0.29	-0.35
L08	A	0.73	-0.33
	B	1.23	-0.55
	C	0.37	-0.68
	D	0.63	-1.44

In the 2023 measurement, the main wind direction is South-West, which results in maximum steel stresses in the East and West directions in most of the locations. Also, it is expected from the wind speed that this time the measured values will be greater than the previous field monitoring, but after comparing Table 3.4 and Table 3.8, the steel stresses are very low. Along with this, two sensors L04 and L08 showed strange values after post-processing which questions the accuracy of the current measurement. Hence, the DIANA model will be based on the measurements from 2017, and the rest two measurements will be used to detect the possible presence of cracks.

3.5. Determination of Cracks

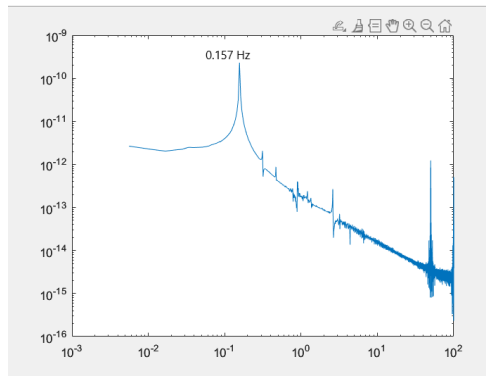
In order to determine the presence of cracks in the foundation after the tower's erection, field monitoring is conducted in different time periods. One measurement happened in 2017, which was just after the tower construction, and the other two happened in 2022 and 2023. The strain measurements from the current years are also preprocessed similarly to those of the 2017 measurements. Next, the stiffness of the foundation is determined by calculating the frequency at the moment of the emergency stop.

3.5.1. From Measurement

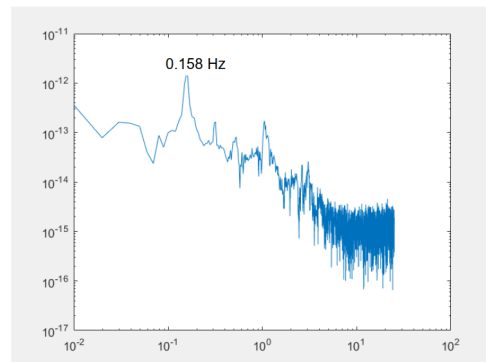
In order to determine the presence of possible cracks in the concrete foundation, the natural frequency of the tower is determined from one of its sensors using the strain data with the help of the Fourier transform. Based on the frequency from the previous data i.e. 2017, and the current data, a comparison is made to detect any cracks in the foundation [22]. After determining the frequency from all the years i.e. 2017, 2022, and 2023, it is concluded that the mass concrete structure is still uncracked since the frequency is more or less the same over the years. If the concrete is cracked, then the natural frequency of the tower would have reduced to below 0.156 Hz which is not the case in this foundation. The frequency of the measured strains from all the years is presented below:

Table 3.9: Estimated Frequency for all the years

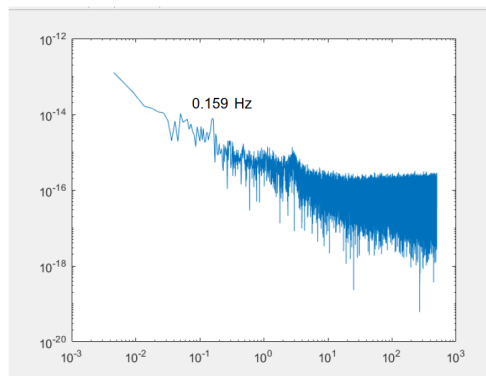
Year	Frequency (Hz)
2017	0.157
2022	0.158
2023	0.159



(a)



(b)



(c)

Figure 3.10: Natural Frequencies for two measurements a) From 2017 data, b) From 2022 data c) From 2023 data

3.5.2. Analytical calculation

In order to verify the above calculations, a simple analytical formulation is being performed where the frequency is calculated using Equation 3.1. The complete calculation is provided in Figure A.23, where the obtained frequency is 0.1592 Hz.

$$f_1 = \frac{1}{2\pi} * \sqrt{\frac{3.04EI}{(0.227m(L + L_f) + M_{top})(L + L_f)^3}} \quad (3.1)$$

where,

- f_1 = frequency of the tower (Hz)
 EI = bending stiffness of the tower (Nm^2)
 m = mass of the tower (kg/m)
 L = hub height (m)
 L_f = tower height below the ground (m)
 M_{top} = mass of the nacelle and rotor hub (kg)

Table 3.10: Parameters

Parameters	Description
L	150 m
L _f	22 m
EI	5.51544e+11 Nm ²
m	4710 kg/m
M _{top}	114000 kg

3.5.3. Conclusion

From both subsection 3.5.1 and subsection 3.5.2, it is evident that the tower frequency is more or less the same which implies that the wind turbine foundation is still uncracked. In case the tower frequencies of 2022 and 2023 have reduced as compared to the frequency of 2017, then it can be concluded that the stiffness of the foundation has decreased over the time period resulting in the possibility of cracks in the foundation.

SCIA engineering calculation

This chapter deals with the structural calculation of the wind turbine foundation. It includes the basic description of the model created in SCIA followed by the structural analyses. The purpose of this study is to verify the structural model in which the numerical analysis is performed.

4.1. Description of the model

The model is created as a 2D plate in the structural software. The two-dimensional plate is a homogeneous plate that acts as a whole. A simplified calculation will be performed on the circular plate and the results from such calculations will be compared with the numerical analyses. There are 28 piles underneath the foundation represented as nodes along with the spring properties in the model.

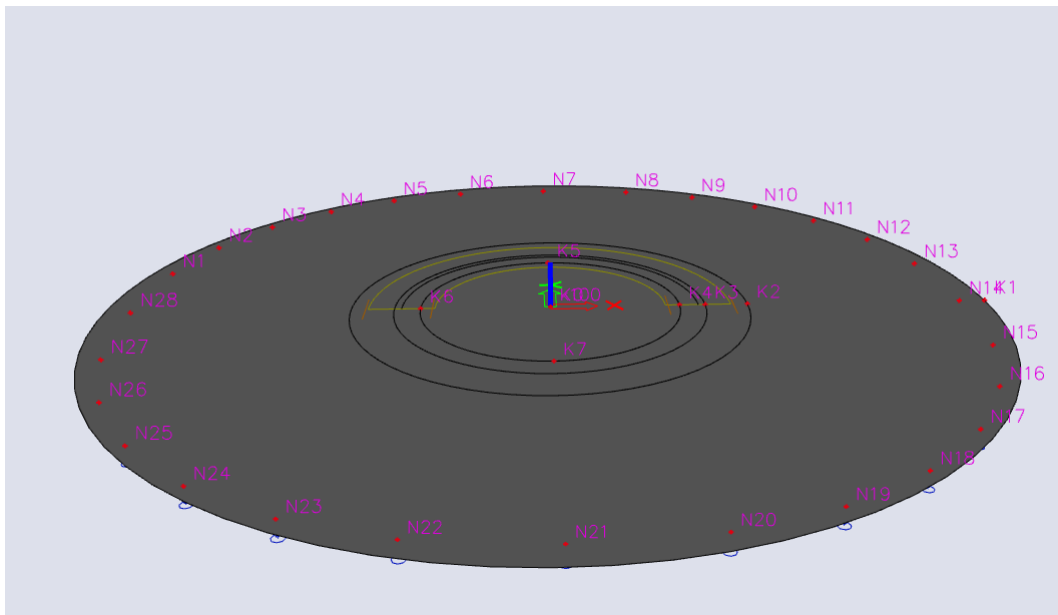


Figure 4.1: 2D plate model

4.1.1. Dimensions of the model

The plate dimensions are presented in the Table 4.1.

Table 4.1: Dimensions of the structure

Structure	Diameter (mm)	Center thickness (mm)
Foundation base_bottom	17000	3130 1600
Foundation base_top	7650	3430
Tower	6000	3430

4.1.2. Material properties

The following material properties have been used in the structural analysis. Due to the assumption in the structural analysis that the concrete foundation is cracked, Young's modulus of the concrete grade C30/37 is lower than the expected value. By applying a lesser Young's modulus of concrete, the larger force is transferred through the tangential reinforcements in order to have an equivalent distribution of forces.

Table 4.2: Material properties

Material	Density (kg/m^3)	$E_{mod}(MPa)$	$G_{mod}(MPa)$	μ	$\alpha(m/mK)$	$F_y(N/mm^2)$	$F_u(N/mm^2)$
S 235	7850	2.1e+05	8.08e+04	0.3	0	235	360
Material	Density (kg/m^3)	$E_{mod}(MPa)$	μ	$\alpha(m/mK)$	$f_{ck28}(MPa)$		
Concrete main	2500	8e+03	0.15	0	30		
Concrete middle	2500	3e+03	0.15	0	30		

4.1.3. Load combinations

Since this project is about the structural health monitoring of the existing foundation, the applied loads and bending moment are the values obtained during the measurement using fiber optics. Below Table 4.3 gives an overview of the applied loads into the structure:

Table 4.3: Load cases

Load cases	Coefficient
Self weight concrete	0.9
unit load vertical (1000kN)	2.31
unit load moment (100000kNm)	1.51

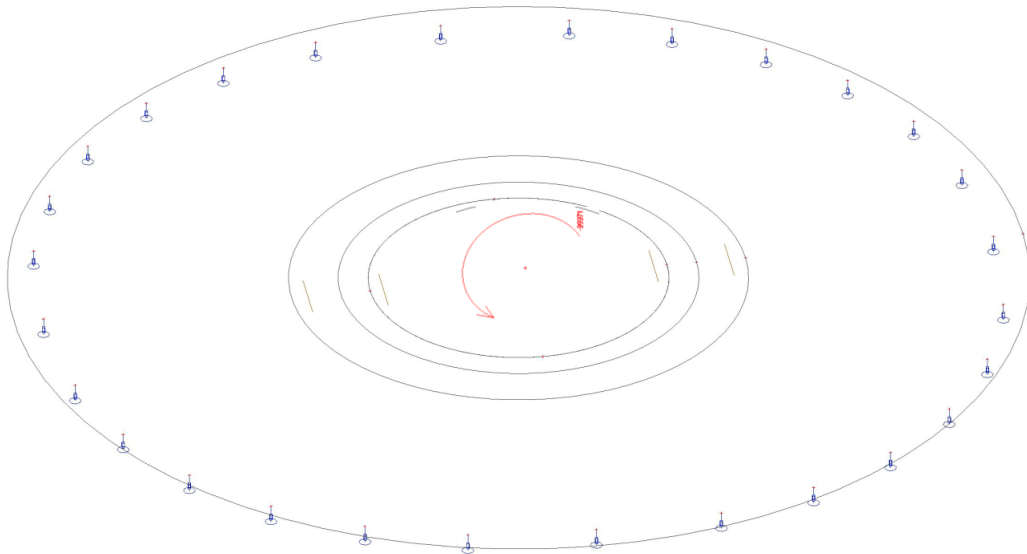


Figure 4.2: Applied Bending Moment

4.2. Methodology

In the SCIA calculations, a linear structural analysis is performed. Hence, there are many simplifications that are put into the model while performing SCIA analysis, hence it is a low-level approximation. One advantage of such an approach is that it is a fast and easy-to-understand method to gain insight into the distribution of forces. The measured bending moment is used in the model to verify the DIANA model used for the research project.

4.3. Results

The results obtained from SCIA analysis are provided in Appendix C and the stresses generated at a bending moment of 151 MNm for the plate are provided in the Table 4.4 below. The stresses in each direction are estimated from the position of nodes in the plate.

Table 4.4: Steel stresses as a result of SCIA calculation

Directions	Tensile stress (MPa)	Compressive stress (MPa)
A	10.98	-2.83
B	1.12	-0.09
C	21.83	-10.12
D	1.90	-0.09

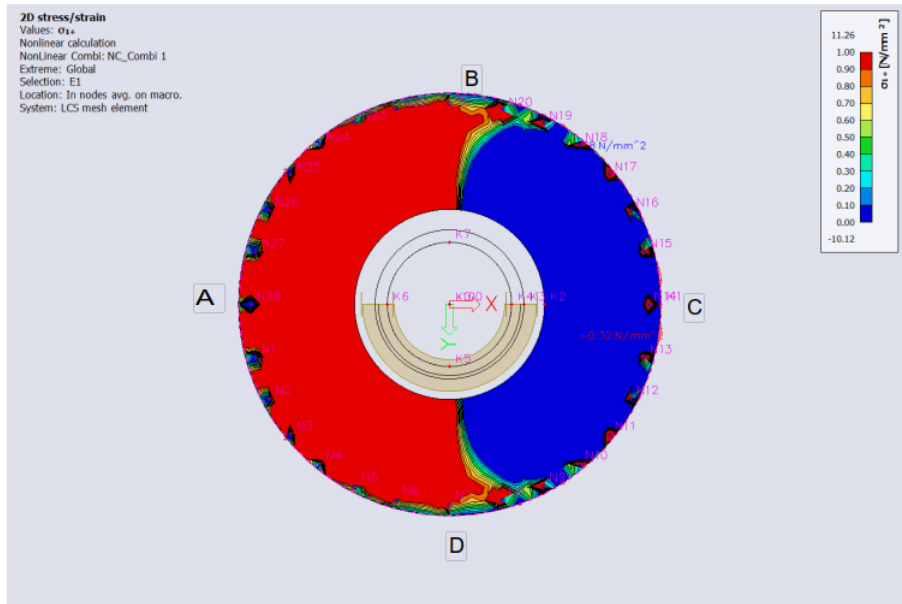


Figure 4.3: Principal stresses-Sigma 1+

Since it is a 2D plate model, it is difficult to show the stresses in every location. The bending moment acts counterclockwise in the plate model as shown in Figure 4.2. Hence the resultant vertical reaction forces are such that the compressive force acts on the A side while the tensile force is on the C position as described in Figure 4.4. Also, the maximum tensile and compressive stresses occur in the south (C) position, which is also the prevailing wind direction.

Reactions
 Nonlinear calculation
 NonLinear Combi: Load nonlinear combinations
 System: Global
 Extreme: Global
 Selection: All

Nodal reactions

Name	Case	R _z [kN]	M _x [kNm]	M _y [kNm]	e _x [mm]	e _y [mm]
Sn28/N28	Load nonlinear combinations	-1018	0	0	0.00	0.00
Sn14/N14	Load nonlinear combinations	2329	0	0	0.00	0.00

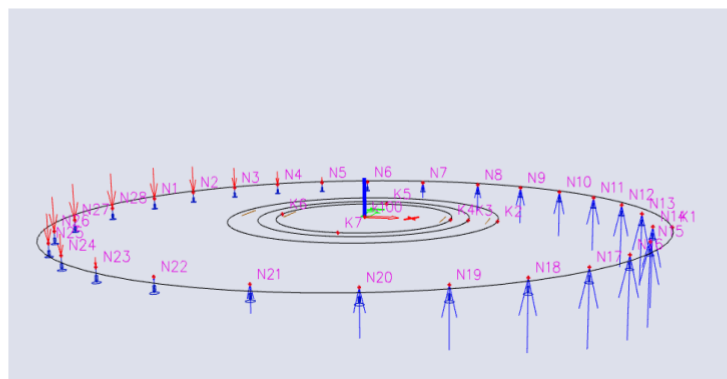


Figure 4.4: Reaction forces

The below Figure 4.5 shows a linear structural calculation in FE software. It is observed from both Figure 4.4 and Figure 4.5 that the compressive forces are around 2000 kN for both the calculations while the tensile force in the SCIA is 1018 kN and in DIANA, it is 616 kN. This variation could be due to several reasons such as the use of different numerical methods, boundary conditions, convergence criteria, etc. Considering the compressive forces, it can be concluded that both the models give similar results and the results of non-linear FE analysis are reliable.

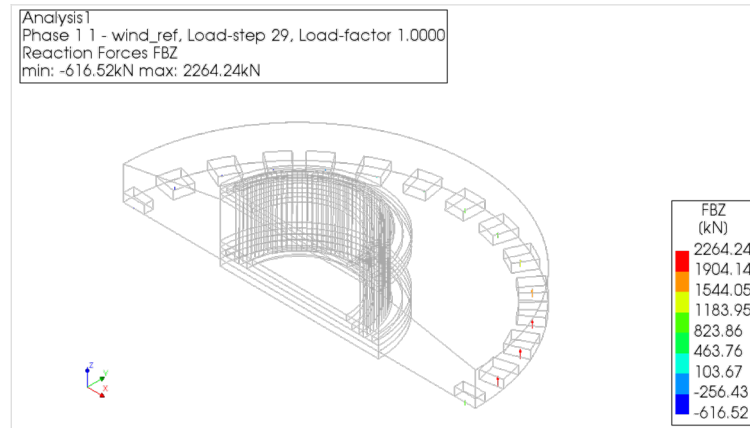


Figure 4.5: Reaction forces in DIANA

4.4. Conclusion

From the obtained reaction forces results of SCIA analysis, the model provides a good match with the FEM model at a given bending moment. Hence, the results obtained from the FE model are reliable. The stress results are within the range of the elastic limit due to the applied linear analysis in the calculations. This also matches the obtained results from the field measurement with a variation of up to a factor of 0.5.

5

Structural Non-linear Finite element analysis

This chapter is dedicated to the numerical analysis of the concrete foundation performed in DIANA. This includes the basic description of the model including the DIANA approach used in modeling and a summary of the analysis used. In the end, it will include all the FE calculations that are performed during the study.

5.1. Dimensions and properties of the concrete body

The concrete foundation comprises two different parts, a concrete base and a concrete pedestal, with different material properties. Below Figure 5.1 shows the cross-section of the foundation along with its dimensions. Table 5.1 depicts the strength class of each component.

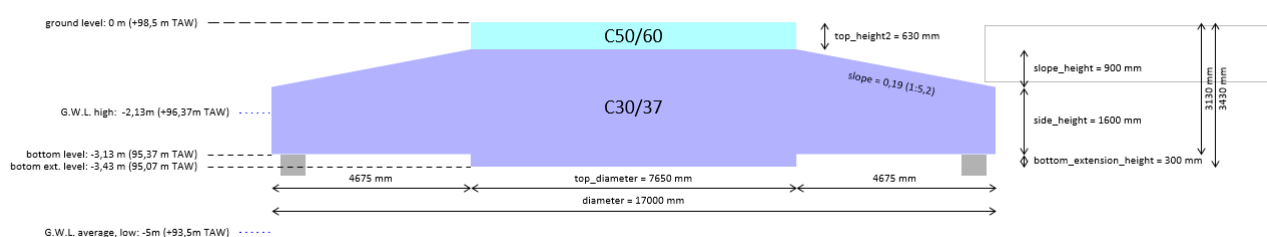


Figure 5.1: Cross-section of wind turbine foundation

Table 5.1: Concrete properties

Component	Strength Class
Concrete Base	C 30/37
Concrete Pedestal	C 50/60

5.2. DIANA FEA approach to model a wind turbine foundation

5.2.1. Description of the model

Wind turbine foundations are designed using a nonlinear finite element analysis approach in DIANA. The name DIANA is derived from DIsplacement ANALyzer. It is a nonlinear 3D finite element program that can perform analyses for both static and dynamic behavior. Modeling of damage initiation and propagation until failure of structure can be accurately carried out in DIANA by modeling the geometry and the material behavior, the composed elements individually, and their interconnection. The foundation is modeled as a 3D symmetric model. The physical nonlinear analysis is considered along with the cracking and crushing of concrete and the yielding and failure of reinforcement steel. In order to include all possible failure mechanisms of the RC foundation block, the structure is modeled with volume elements, and the reinforcement bars are modeled according to the drawings. The geometry of the whole model is presented in Figure 5.2 and the rebar groups are shown in Figure 5.3.

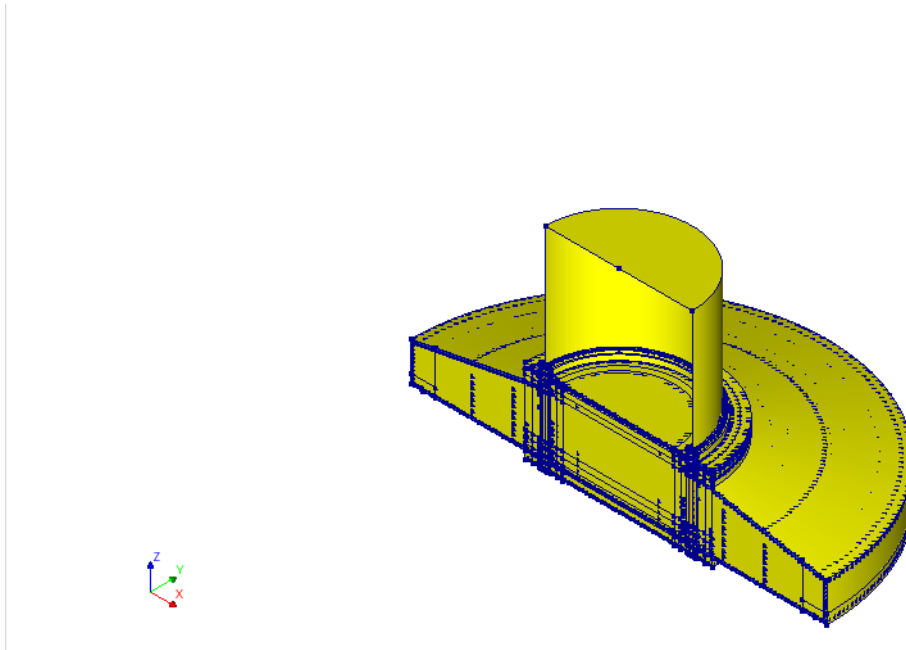


Figure 5.2: Concrete foundation block

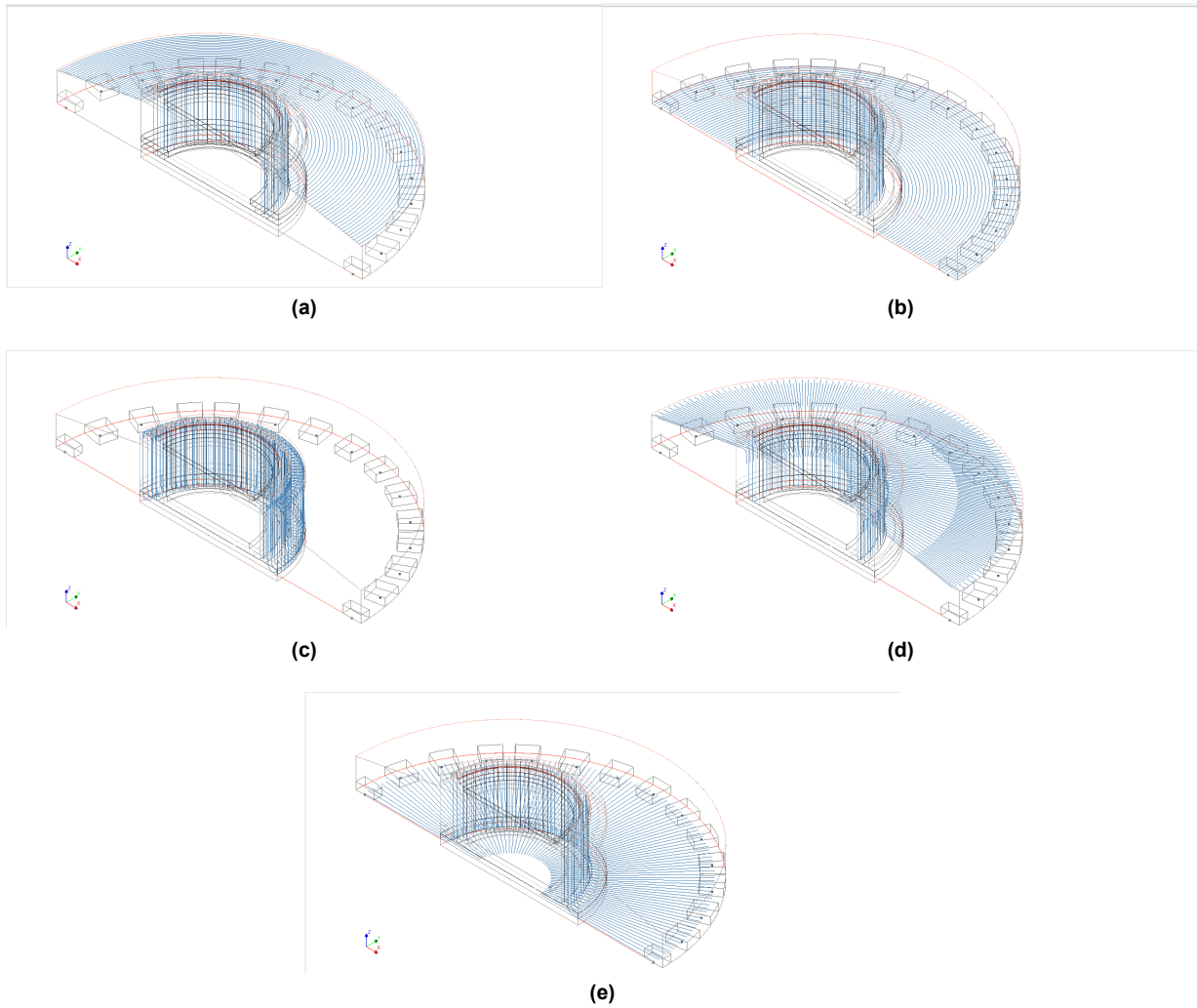


Figure 5.3: Reinforcements at different locations a) Top tangential, b) Bottom tangential, c) Vertical, d) Top radial, e) Bottom radial

Special care by introducing loads is taken in case of interaction between the foundation block and other elements such as anchor cages and soil or piles. In the model, the anchor cage is already included with linear elastic material properties to prevent it from failing all by itself. No tension and low shear surface interfaces separate the anchor plates from the concrete to make sure that the load is introduced primarily by compression into the concrete. Also, it is avoided that the anchor cage contributes to the resistance of the concrete. Above and below the anchor plates where the compression loads are introduced, layers of higher quality concrete are included to mimic the effect of confinement and prevent local failure shown in Figure 5.5. Linear elastic areas are included above the piles to introduce the concentrated loads into the foundation block depicted in Figure 5.6.

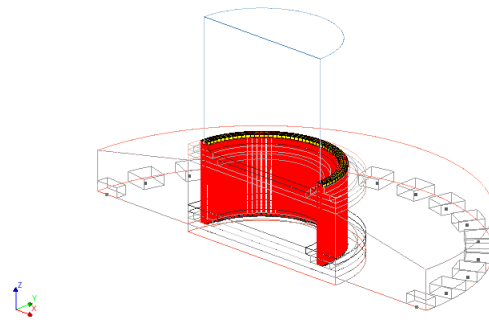


Figure 5.4: Pretensioned anchors

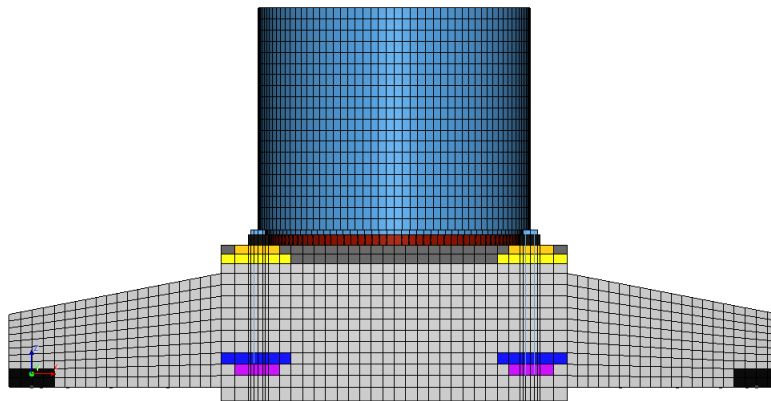


Figure 5.5: Concrete in confinement layers

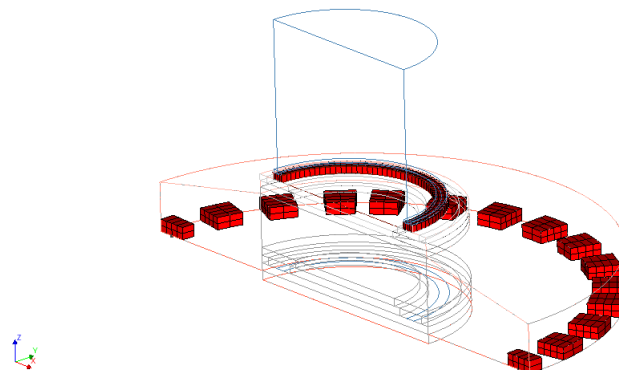


Figure 5.6: Elements with linear properties

A small piece of the shaft is included in the model in a phased manner. According to IEC61400-6 Annex N, until ULS load combination, the analysis is conducted force-controlled without a shaft since it states the distribution of loads in the foundation should not be disturbed by external factors. From ULS up to the failure, a piece of the shaft with a stiff end plate is used to introduce a prescribed rotation and conduct the remainder analysis in a rotation-controlled way. The shaft piece is only required to translate the rotation which is applied in a single point to a distributed load in the foundation. Its participation in the resistance of the foundation block is avoided by lowering the shear stiffness of the interaction between the shaft and the foundation block.

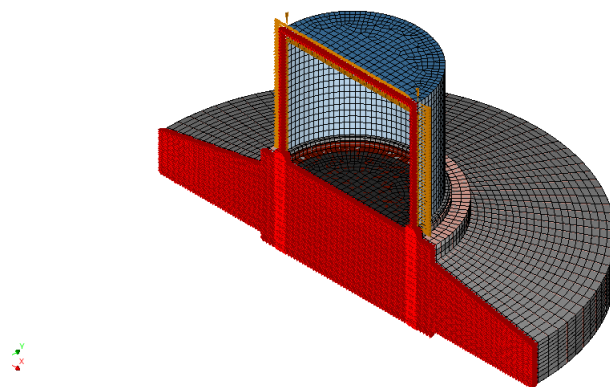


Figure 5.7: Model with symmetrical support

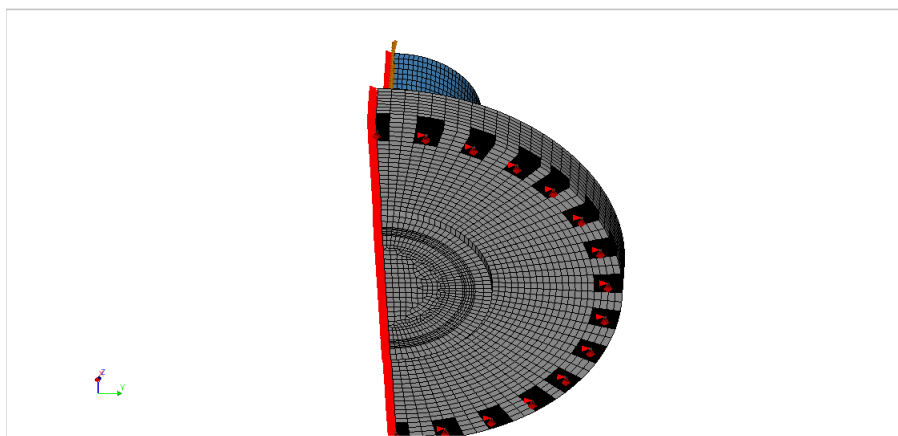


Figure 5.8: Model with pile supports

5.2.2. Current Design Method

According to the [15], there are three types of safety formats for nonlinear analysis. They are:

- Partial Factor (PF) method
- Global Resistance Factor (GRF) method
- Estimation of Coefficient of Variation (ECOV) method

In the current design approach, the ECOV method is taken into consideration. In this method, an estimate of the mean and characteristic values of resistance are calculated using material parameters of corresponding values. The models will be loaded up to failure. The safety factor is derived from the ratio of the mean and characteristic resistance. In the ECOV method, the uncertainties are evaluated at the global structural level and not at local material points. This methodology is only applicable when the failure mechanism is the same for both characteristic and mean material properties, and it can be assumed that both resistances are a part of the same lognormal distribution of resistance. The advantages of the ECOV method are as follows:

- Conducting analyses with both characteristic and mean material properties indicates if the structure is sensitive to variations in material properties of concrete and reinforcement.
- The safety factor and hence the design resistance can be derived directly from the characteristic and mean resistance.

5.2.3. Constitutive models

The constitutive models which are generally used in every project are presented below:

Table 5.2: Material models used in the FEA

Material	Model name	Reference
Concrete (Nonlinear)	Total strain rotating crack model	RTD1016-1:2020-2.4.1 [35] DIANA10.5-Manual-47.5 [36] Appendix 8
Rebar (Nonlinear)	Von mises plasticity	RTD1016-1:2020-2.4.2 [35] DIANA10.5-Manual-54.3 [36]
Rebar bond-slip	N.A.	
Steel Anchor bolts Mortar	Isotropic linear elasticity	
Pile springs (point interfaces)	Interface linear elasticity	DIANA10.5-Manual-53.1 [36]
Concrete-anchor plate or concrete-mortar interaction (surface interfaces)	Interface nonlinear elasticity	DIANA10.5-Manual-53.2 [36]

Concrete Model

A summary of different aspects is provided in the table below:

Table 5.3: Choices for the concrete constitutive model

Aspect	Choices
Concrete Model	Total strain rotating crack model [36]
Linear elastic properties	No reduction for sustained loading
Tensile behavior	Hordijk softening [36]
Shear behavior	-
Compressive behavior	Parabolic compression diagram [36]
Tension-Compression interaction	Vecchio & Collins 1993 [36]
Compression-Compression interaction	Selby and Vecchio [36]
Equivalent length	Govindjee [36]

Model for reinforcement

Von Mises plasticity model with strain hardening is used to model the reinforcements. The rupture of reinforcement is included by a steep softening branch in order to consider local rebar failure as part of a global failure.

Concrete-reinforcement interaction model

This is modeled with the assumption of the full bond between concrete and reinforcement i.e. embedded reinforcements.

5.2.4. Material properties**Concrete Linear elastic**

Linear elastic concrete is used for the mortar. For piled foundations, linear elastic concrete is used locally above the piles to introduce the pile reactions into the foundations. The young's modulus used is 10000 N/mm^2 .

Concrete nonlinear

In the case of the piled foundations, the ECOV method is applied, and hence mean and characteristic material properties are used for the models. Material properties for nonlinear concrete are derived from the

characteristic compressive strength of concrete. Usually, the top of the pedestal is executed with a higher strength concrete class than the remaining part of the foundation. To include the effects of confinement due to the applied prestress in the model, the layers below the mortar and above the bottom anchor plate are modeled with a high-strength concrete class.

Reinforcement

Material properties for nonlinear reinforcement are according to [35] and [cen20041992]. The ECOV method is used for piled foundations with mean and characteristic properties.

5.2.5. Element types

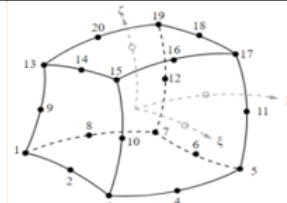
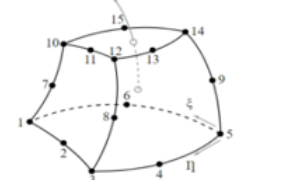
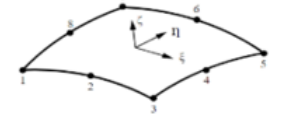
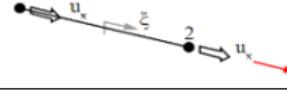
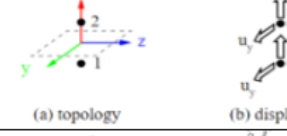
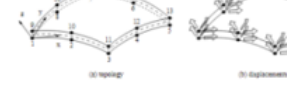
Element Type	Illustration	Description	Application
CHX60		20-node solid, brick shaped	All solid parts: concrete, top anchor plate, grout
CTP45		15-node solid, wedge shaped	A few concrete elements inside the anchor cage are of this type
CQ40S		8-node curved shell element	Bottom anchor plate, shaft
L2TRU		2-node regular truss element	Anchor bolts
N6IF		1+1 nodes point interface element	Pile springs
CQ48I		8+8 nodes surface interface element	Interfaces between bottom anchor plate and surrounding concrete, interface between mortar and concrete

Figure 5.9: Element types used in the FE model

5.2.6. Loads

Different types of loads and their combination is applied in the DIANA model. The applied loads are shown in the following section:

Dead Load

The dead load of the foundation is derived from DIANA using the density of the applied materials. The density of the reinforced concrete is assumed to be 2500 kg/m^3 and the density of steel bars is assumed to be 0 kg/m^3 since the dead load of the reinforcement is included in the density of the reinforced concrete. The total volume of the concrete is 518.4 m^3 . Hence, the total foundation dead load can be calculated to be 12961 kN .

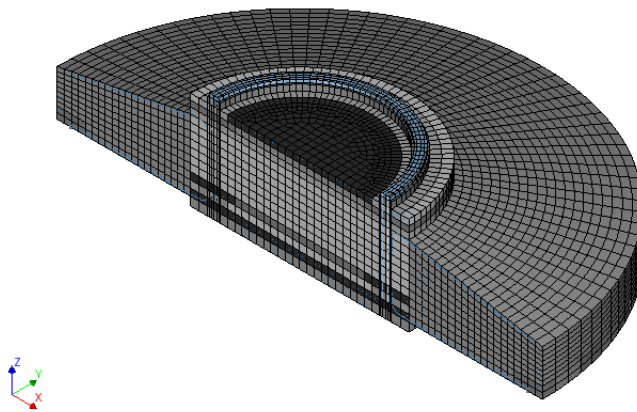


Figure 5.10: Dead load in the FE model

Horizontal Load

The horizontal load is applied by means of a surface load which is uniformly distributed over the top surface of the tower's bottom flange. The applied value of the horizontal load is 0.21351 MPa . This results in a total horizontal load equal to 1205.3 kN .

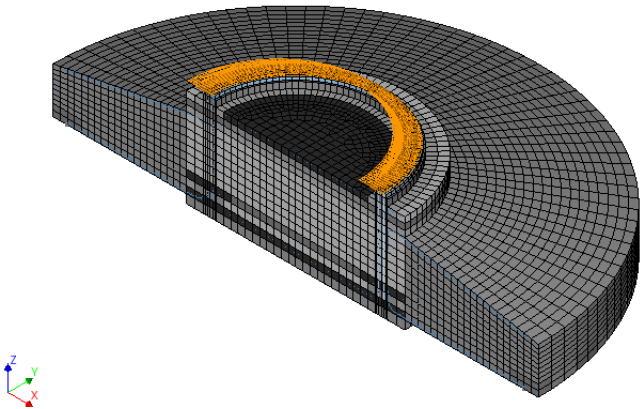


Figure 5.11: Horizontal force in the FE model

Vertical Load

The vertical load is applied by means of a surface load which is uniformly distributed over the top surface of the top anchor plate. The applied load is -1.023 MPa . This results in a total vertical load of -5789 kN .

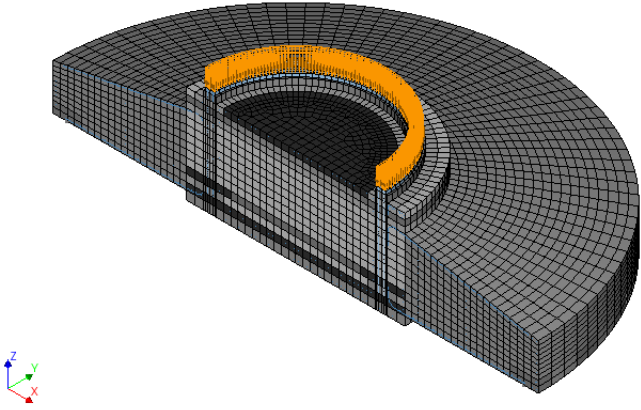


Figure 5.12: Vertical force in the FE model

Bending Moment

The bending moment is applied as a vertical surface load to the top surface of the top anchor plate. The moment is applied as a constant value of 17.4 MPa which is then multiplied by a linear function. The total design bending moment on the foundation is 141000 kNm . In the DIANA calculations, the measured bending moment equal to 151070 kNm is used.

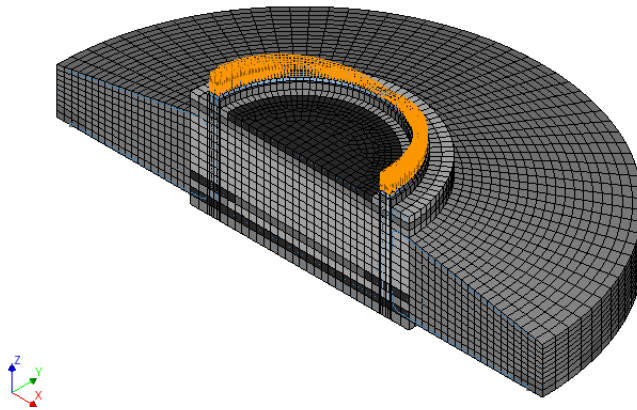


Figure 5.13: Moment in the FE model

Backfilling soil

The pressures on backfilling soil are taken into account as a constant surface pressure of -17 kPa (dry soil) and -19 kPa (saturated soil) which is multiplied by spatial function based on the soil depth. In total, the resultant forces are 3499 kN (dry soil) and 3910 kN (wet soil).

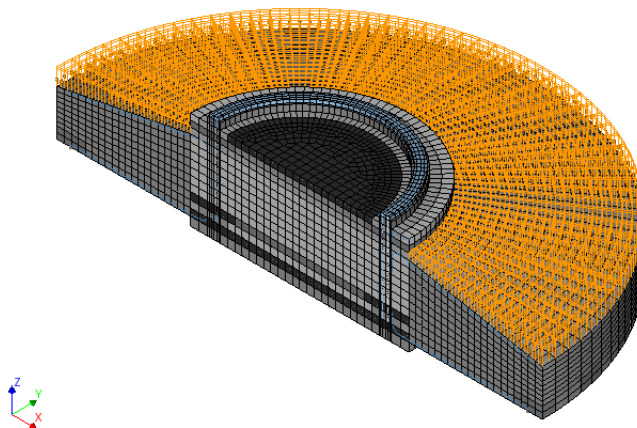


Figure 5.14: Soil force in the FE model

The below Table 5.4 provides a summary of the applied loads and Table 5.5 and Table 5.6 describe the load combinations:

Table 5.4: Summary of load cases

Load case	Description	Direction	Unit
LC 1	Dead load	Z	kN
LC 2	Anchor prestress	Z	N/mm ²
LC 3	Horizontal load	X	kN
LC 4	Vertical load	Z	kN
LC 5	Groundwater pressure	Z	kN
LC 6	Rotation deformation	Around Y	mrad
LC 7	Moment load	Around Y	kNm
LC 8	Backfilling load (high)	Z	kN
LC 9	Backfilling load (low)	Z	kN

Table 5.5: Load combinations for favorable analysis

Steps	Description	Load Factor	Stage
1-5	Prestress	1*LC2	
6-10	Vertical REF	1*LC1+1*LC4+1*LC5+1*LC9	REF
11-29	Wind REF	1*LC3+1*LC7	REF
30-31	Vertical ULS	-0.1*LC1-0.1*LC4-0.1*LC9	ULS
32-52	Wind ULS	0.35*LC3+0.35*LC7	ULS
53-102	Rotation	1*LC6	Failure

Table 5.6: Load combinations for unfavorable analysis

Steps	Description	Load Factor	Stage
1-5	Prestress	1*LC2	
6-10	Vertical REF	1*LC1+1*LC4+1*LC8	REF
11-29	Wind REF	1*LC3+1*LC7	REF
30-31	Vertical ULS	0.35*LC1+0.35*LC4+0.35*LC8	ULS
32-52	Wind ULS	0.35*LC3+0.35*LC7	ULS
53-102	Rotation	1*LC6	Failure

5.3. Maturity effects

Concrete material properties also included maturity effects in order to mimic the exact behavior of concrete right after pouring. From [15, 37], the relationship between maturity-young's modulus, maturity-tensile strength, and maturity-tensile fracture energy is calculated. The variation of modulus of elasticity with time can be calculated using the formula:

$$E_{cm}(t) = (f_{cm}(t)/f_{cm})^{0.3} E_{cm} \quad (5.1)$$

where,

$E_{cm}(t)$ = Young's modulus at t days [MPa]

$f_{cm}(t)$ = Mean compressive strength at t days [MPa]

f_{cm} = Mean compressive strength in 28 days [MPa]

E_{cm} = Young's modulus in 28 days [MPa]

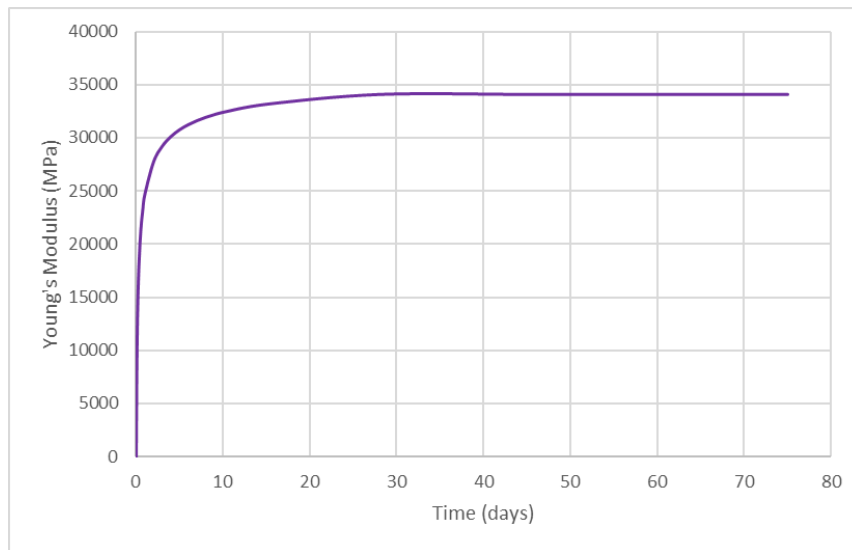


Figure 5.15: Maturity-Young's modulus graph for C35/45

The mean tensile strength of the concrete for t days can be estimated using the equation below:

$$f_{ctm}(t) = (\beta_{cc}(t))^\alpha \cdot f_{ctm} \quad (5.2)$$

where,

$f_{ctm}(t)$ = Mean tensile strength at t days [MPa]

f_{ctm} = Mean tensile strength in 28 days [MPa]

$$\beta_{cc}(t) = \exp \left\{ s \left[1 - \left(\frac{28}{t} \right)^{1/2} \right] \right\} \quad (5.3)$$

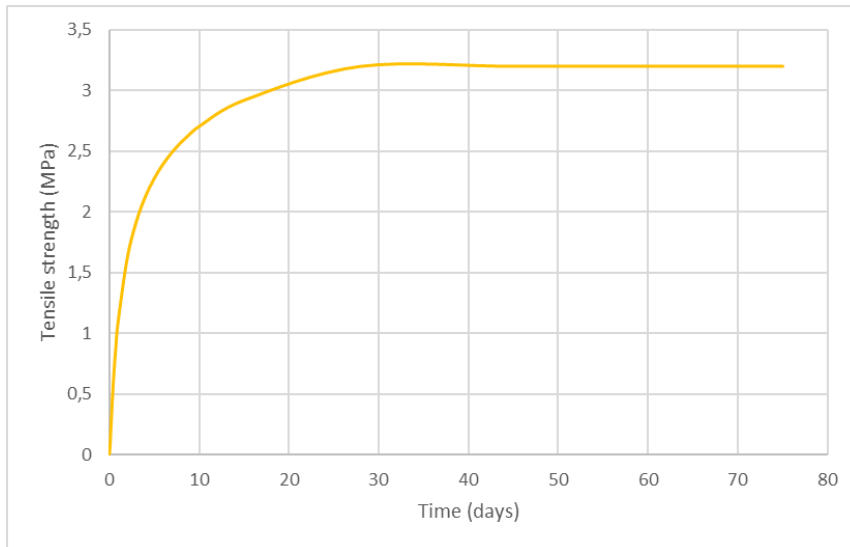


Figure 5.16: Maturity-Tensile strength graph for C35/45

The below Equation 5.4 estimates the tensile fracture energy of the concrete:

$$G_F = 73 \cdot f_{cm}^{0.18} \quad (5.4)$$

where,

G_F = Mode-I tensile fracture energy [N/m]

f_{cm} = Mean compressive strength [MPa]

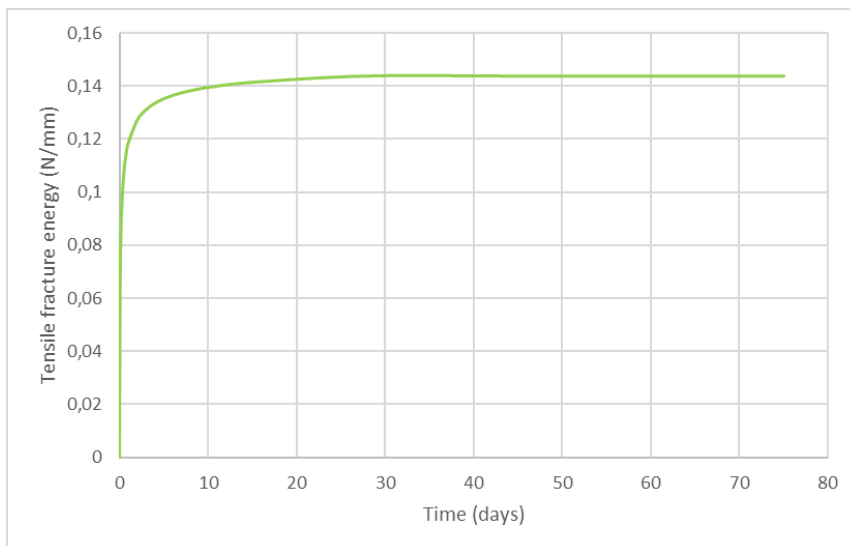


Figure 5.17: Maturity-Tensile fracture energy graph for C35/45

The temperature plays a significant role in the development of concrete strength [9] since heat is both a product and accelerator of the reactions responsible for producing CSH. To predict concrete strength development, cube strength tests are required at a controlled curing temperature.

5.4. Effects of Structural analysis

This section deals with the nonlinear analysis of the concrete foundation. In the beginning, a FE model is generated to check the effects of the various loads applied to the structure. For this purpose, a structural non-linear analysis is done for the generated overturning moment during the measurement, which is used instead of the original design value for the bending moment of the structure. The load steps in the foundation model are applied as mentioned in subsection 5.2.6. The non-linear analysis has been performed using the ECOV method but, the research thesis is mainly focused on the results of mean unfavorable load conditions since the study involves the investigation of the existing concrete foundation and with the consideration of the maturity effect it provides the result of strength development with respect to the time. The stresses in the reinforcements at different positions in the concrete foundation are depicted in the following Figure 5.20-Figure 5.25. The wind directions mentioned in the section are represented in the Figure 5.18

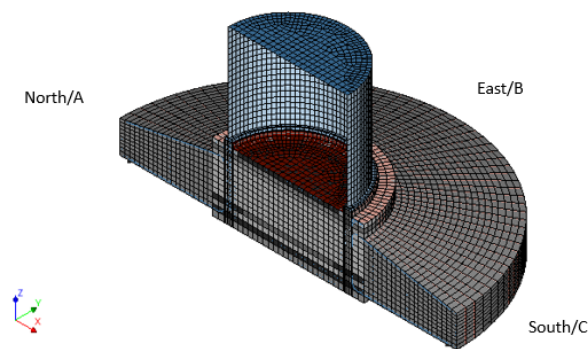


Figure 5.18: Wind turbine foundation-Wind directions

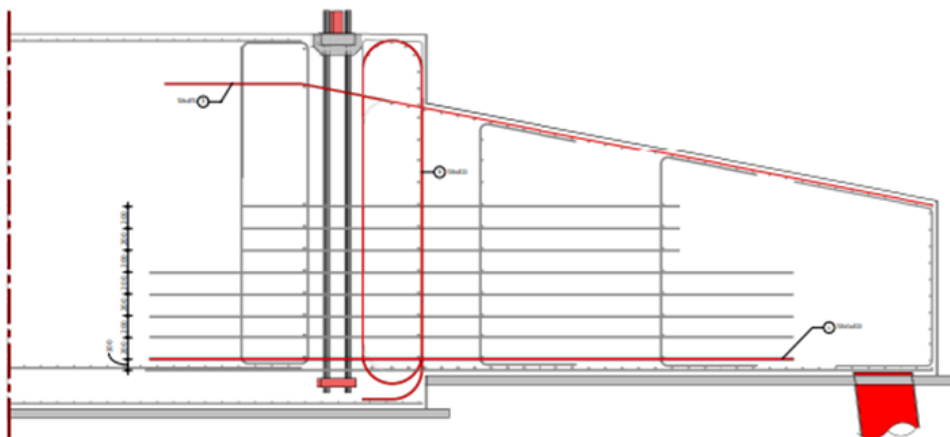


Figure 5.19: Cross section of the foundation with the reinforcements in interest

Analysis1
Phase 1 1 - wind_ref, Loadstep 29, LoadFactor 1.0000
Reinforcement Coeuchy Total Stresses: Sxx, layer 1
min: -29.64N/mm² max: 176.33N/mm²

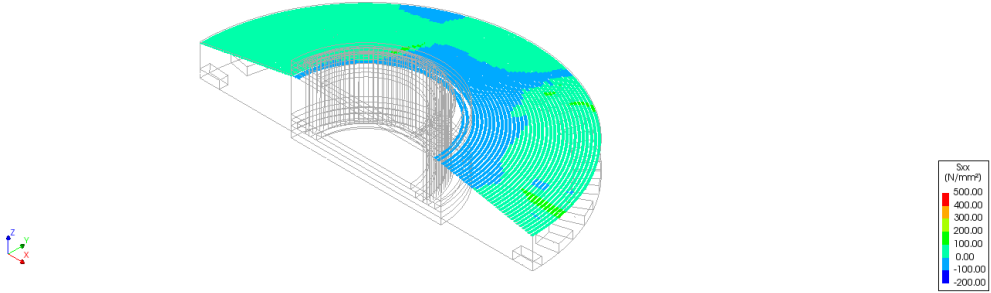


Figure 5.20: Rebars in the top tangential position

Analysis1
Phase 1 1 - wind_ref, Loadstep 29, LoadFactor 1.0000
Reinforcement Coeuchy Total Stresses: Sxx, layer 1
min: -0.00N/mm² max: 253.69N/mm²

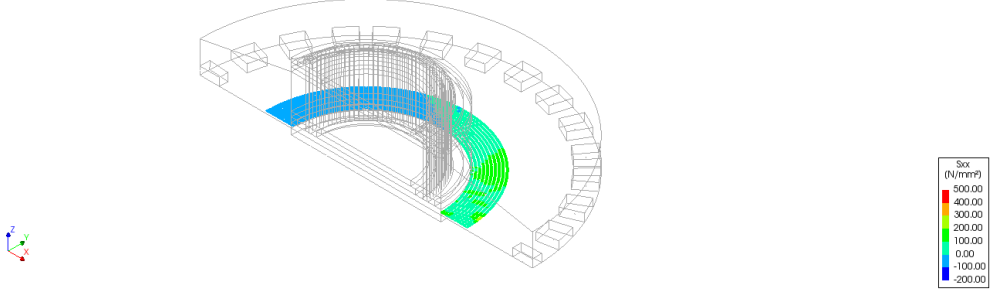


Figure 5.21: Rebars in the bottom tangential position

Analysis1
Phase 1 1 - wind_ref, Loadstep 29, LoadFactor 1.0000
Reinforcement Coeuchy Total Stresses: Sxx, layer 1
min: -19.01N/mm² max: 449.99N/mm²

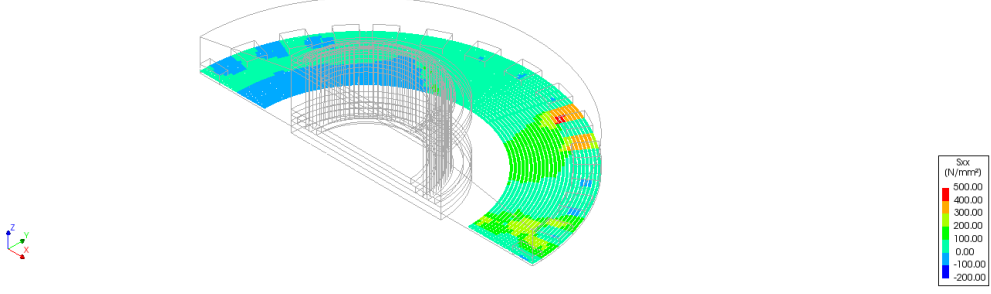


Figure 5.22: Rebars in the bottom tangential position near the piles

Analysis1
Phase 1 1 - wind_ref, Loadstep 29, LoadFactor 1.0000
Reinforcement Cauchy Total Stresses: Sxx, layer 1
min: -59.88N/mm² max: 252.15N/mm²

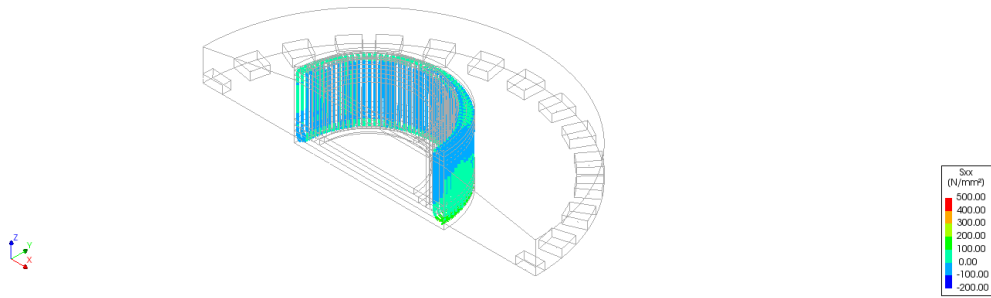


Figure 5.23: Stirrup

Analysis1
Phase 1 1 - wind_ref, Loadstep 29, LoadFactor 1.0000
Reinforcement Cauchy Total Stresses: Sxx, layer 1
min: -108.02N/mm² max: 308.37N/mm²

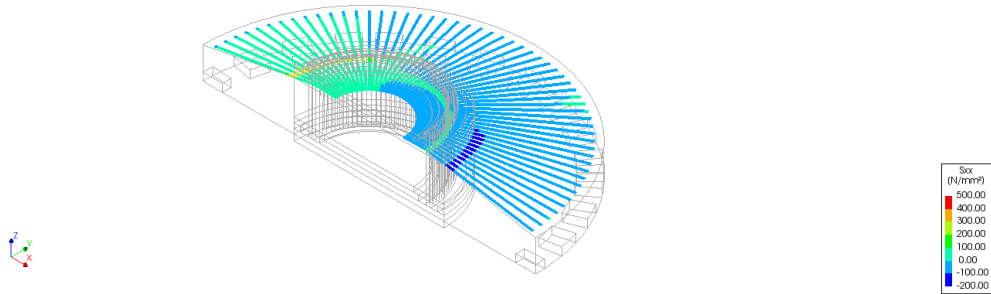


Figure 5.24: Rebars in the top radial position

Analysis1
Phase 1 1 - wind_ref, Loadstep 29, LoadFactor 1.0000
Reinforcement Cauchy Total Stresses: Sxx, layer 1
min: -51.83N/mm² max: 475.49N/mm²

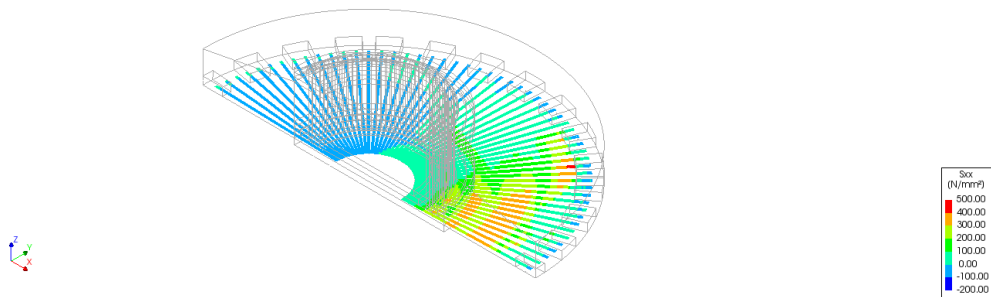


Figure 5.25: Rebars in the bottom radial position

Below Table 5.7 describes the maximum tensile and compressive stresses in the reinforcement groups at each location according to the current DIANA calculations. This data has been extracted from the last load step of the calculation. The maximum steel stresses in the below table represent the stresses only in the locations of the sensors and not the whole rebar group. The measuring direction D is not present since the 3D model in the DIANA is symmetrical. A closer look at the pictorial representations of the steel stresses is presented in section B.1.

Table 5.7: Steel stresses as a result of structural analysis

Measuring Locations	Directions	Tensile stress (MPa)	Compressive stress (MPa)
L02	A	256.3	-
	B	-	-19.56
	C	-	-84.7
L03	A	8.56	-
	B	-	-3.24
	C	-	-9.96
L04	A	52.88	-
	B	-	-9.6
	C	-	-7.22
L05	A	-	-17.43
	B	118.02	-
	C	290.67	-
L06	A	-	-3.35
	B	61.04	-
	C	68.5	-
L07	A	5	-
	B	-	-20.71
	C	-	-38.22
L08	A	1.55	-
	B	6.16	-
	C	184.8	-

The below Table 5.8 depicts the comparison between the field measurement and the structural analysis in FE software. Since the model does not include the shaft, there are no readings at that position in the numerical analysis. Also, it is to be noted that the DIANA model is a symmetrical model which is why there are no resultant stress outcomes in the 'D' direction. Nevertheless, the FE calculations showed tensile and compressive stresses at a particular direction based on the applied bending moment. The values absent in the table mean there are no stress results to mention.

Table 5.8: Comparison between the Field measurement and DIANA structural analysis

Measuring Locations	Directions	Field Measurement 2017		DIANA Structural Analysis	
		Tensile stress (MPa)	Compressive stress (MPa)	Tensile stress (MPa)	Compressive stress (MPa)
L01	A	182.21	-118.53	-	-
	B	10.66	-20.16	-	-
	C	117.07	-160.99	-	-
	D	-	-	-	-
L02	A	21.97	-12.47	256.3	-
	B	5.1	-3.4	-	-19.56
	C	15.4	-19.94	-	-84.7
	D	3.06	-4.68	-	-
L03	A	3.13	-1.87	8.56	-
	B	1.08	-0.76	-	-3.24
	C	3.13	-4.13	-	-9.96
	D	0.7	-1.15	-	-
L04	A	4.64	-2.94	52.88	-
	B	1.32	-0.92	-	-9.6
	C	3.7	-5.1	-	-7.22
	D	0.96	-1.42	-	-
L05	A	5.04	-7.5	-	-17.43
	B	1.67	-2.33	118.02	-
	C	8.96	-6.04	290.67	-
	D	2.23	-1.55	-	-
L06	A	2.12	-2.9	-	-3.35
	B	0.85	-1.19	61.04	-
	C	3.13	-1.99	68.5	-
	D	0.94	-0.68	-	-
L07	A	2.49	-1.13	13.41	-
	B	0.5	-0.38	-	-20.71
	C	0.82	-0.73	-	-38.22
	D	0.25	-0.33	-	-
L08	A	1.46	-2.17	1.55	-
	B	0.61	-0.81	6.16	-
	C	2.09	-1.39	184.8	-
	D	0.76	-0.5	-	-

Conclusion: From [3], it can be deduced that the radial steel bars are in tension or compression depending on the position of the rebars. It can be seen that there is a large amount of difference in the reinforcement stresses when compared with the experimental results. In certain areas, such as the top radial in the North and the bottom radial in the South, the steel experiences high levels of stress, with a factor of 10 and 30, respectively as presented in Table 5.8. To mimic the structural behavior of the real concrete foundation, the heat of hydration effect will be introduced in the model. Further analysis will be based on the hydration heat calculations and their effect on the steel stresses. After analyzing the hydration heat calculations, other factors such as bedding, dynamic maturity effect, and changing the hydration heat coefficients will be explored.

Thermo-mechanical Non-linear Finite element analysis

6.1. Heat Flow effects

A 3D model considering the hydration heat effect is used for heat flow analysis purposes. The finite element method is a useful technique to model the behavior of the heat transfer, hence it is used to conduct thermal analysis of the mass concrete [27]. In order to do so, various parameters have been estimated based on the conditions of the wind turbine foundation. To stimulate the hydration heat, a convection heat transfer mechanism is used. This heat transfer happens when a fluid is in motion. It is driven by the temperature differences across that fluid. For the thermal computation, the heat of hydration is applied using the adiabatic curves for a duration of 7 days according to the cement mixture used while the external temperature is assumed to be constant for the simplification purpose. The initial temperature of the concrete and the external temperature of surrounding were obtained from KNMI, as a mean temperature for the particular days of concrete foundation casting. The convection coefficient along with the external temperature is assigned to the surfaces of the model as thermal boundaries. 3-D transient thermal analysis is used to monitor the temperature development inside the concrete as a function of time. The necessary parameters required to execute hydration heat analysis are provided below:

6.1.1. Material Properties

The material properties which are considered for this project are presented below:

Table 6.1: Material Properties

Concrete grade base top	C 50/60
Concrete grade base bottom	C 30/37
Concrete grade base	C 30/37
Cement type	CEM III/A 42.5 N LH
Reinforcement	B 500B
Soil density (bearing capacity)	18 kN/m^3
Soil density (backfilling-dry)	17 kN/m^3
Soil density (backfilling-saturated)	19 kN/m^3
Soil type	Very dense sand

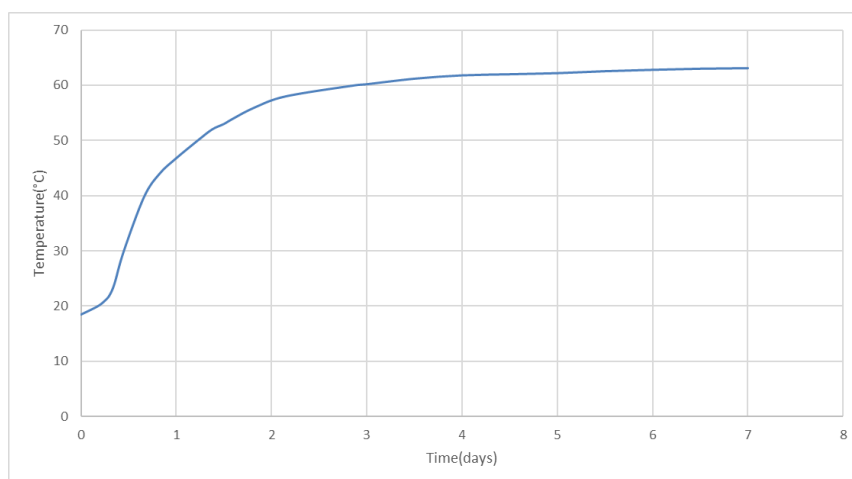
6.1.2. Adiabatic heat curve

The adiabatic curve is estimated based on the type of cement mixture for a duration of 7 days. The Adiabatic heat curve for the used cement mixture CEM III/A 42.5 N LH is presented below in Table 6.2:

Table 6.2: Temperature variation wrt the number of days

Time(Days)	Temperature (Celsius)
0	18.5
0.175	20
0.25	21
0.3	22
0.35	24
0.45	30
0.6625	39.8
0.825	44
1	46.8
1.225	50
1.375	52
1.5	53
1.6	54
1.825	56
2.15	58
2.875	60
3	60.2
3.5	61.2
4	61.8
4.5	62
5	62.2
5.5	62.55
6	62.8
6.5	63
7	63.1

The graph for the adiabatic heat curve for the cement mixture is shown below Figure 6.1:

**Figure 6.1:** Adiabatic curve for CEM III/A 42.5 N LH [31]

6.1.3. Initial temperature during casting

The initial temperature is calculated by adding 5°C to the mean temperature. The mean temperature is estimated for the fresh concrete mixture. Since most of the mass comes from the aggregate that was stored outside, the outside average temperature of the concrete pouring day including 2 days prior to it, has been considered. In accordance with the KNMI, the mean temperature = 15.6°C . Therefore, the initial temperature during casting = $15.6^{\circ}\text{C} + 5^{\circ}\text{C} = 20.6^{\circ}\text{C}$.

6.1.4. External temperature

The external temperature is estimated as the mean temperature of 4 days from the date of pouring of concrete to the backfilling of soil.

6.1.5. Time dependent Heat transfer coefficient

One of the most important parameters in the analysis of the hydration heat effect is the heat transfer coefficient. The related theory is described in subsection 2.6.3. For the FEM analysis, two variables are decided. A comparative study will be performed in DIANA to indicate the relation between HTC and heat development inside the foundation. With the help of obtained data from the company responsible for concrete pouring in the foundation, the HTC will be calculated over a period of 3 days. The interaction goes as follows:

Day 1, Concrete to steel formwork:

To calculate the HTC between concrete and steel, Equation 2.6 is used. The formwork thickness is 7mm. The heat conduction coefficient for the formwork is assumed to be 50 W/mK and from [38] the heat transfer coefficient for the steel formwork is $9.9 \text{ W/m}^2\cdot^{\circ}\text{C}$.

$\alpha_{res} = 9.88 \text{ W/m}^2\cdot^{\circ}\text{C}$. Another variant has been considered which equals $12 \text{ W/m}^2\cdot^{\circ}\text{C}$.

Day 2, Concrete to air:

The interaction of concrete to air will only be at the top surface after the removal of the formwork. Hence, the HTC for both the top and bottom will be different. The heat conduction coefficient for concrete is 2.6 W/mK . According to the data obtained from KNMI, wind speed on that day was 3.8 m/s . Therefore, from [31], the value of the heat transfer coefficient can be assumed to be 16 and $20 \text{ W/m}^2\cdot^{\circ}\text{C}$ for two variants. For the bottom surface, since there will be no contact with wind, the $\alpha_c = 5.6$ and $8 \text{ W/m}^2\cdot^{\circ}\text{C}$ respectively.

Day 3, Concrete to soil:

The type of soil at Riemst is very dense sandy soil. This value is assumed to be equal to $5.6 \text{ W/m}^2\cdot^{\circ}\text{C}$ and $8 \text{ W/m}^2\cdot^{\circ}\text{C}$. The below tables summarize the HTC values for different interactions for 3 days.

Table 6.3: Summarized values for the Heat transfer coefficient

Days	Interactions (For side)	HTC 1 [$W/m^2 \cdot ^\circ C$]	HTC 2 [$W/m^2 \cdot ^\circ C$]
1	Concrete to steel formwork	9.8	12
2	Concrete to air	16	20
3	Concrete to soil	5.6	8

Days	Interactions (For bottom)	HTC 1 [$W/m^2 \cdot ^\circ C$]	HTC 2 [$W/m^2 \cdot ^\circ C$]
1	Concrete to soil	5.6	8
2	Concrete to soil	5.6	8
3	Concrete to soil	5.6	8

Days	Interactions (For top)	HTC 1 [$W/m^2 \cdot ^\circ C$]	HTC 2 [$W/m^2 \cdot ^\circ C$]
1	Concrete to air	16	20
2	Concrete to air	16	20
3	Concrete to soil	5.6	8

Days	Interactions (For top pedestal)	HTC 1 [$W/m^2 \cdot ^\circ C$]	HTC 2 [$W/m^2 \cdot ^\circ C$]
1	Concrete to air	16	20
2	Concrete to air	16	20
3	Concrete to air	16	20

6.1.6. Summary

A summary of the values which are obtained on the basis of the material properties and with the help of the literature presented in section 2.5 and section 2.6 are depicted in the tabular form for hydration heat calculation:

Table 6.4: Summary of the values

Initial temperature during casting	20.6°C
External temperature	17.525°C
Thermal expansion coefficient	$1 \times 10^{-05} m/m \cdot ^\circ C$
Heat flow conductivity	2.6W/mK
Reference temperature	20°C
Heat diffusion coefficient	$0.9 \times 10^{-06} m^2/s$
Specific heat	1kJ/kgK
Heat capacity	2549.3kJ/m ³ ·°C

6.2. Summary of the analysis performed

Table 6.5: Summary of the variants

Variant	Analysis type	Maturity	HTC	Bedding	Piles type
0	Structural	Constant after 28 days	-	-	Straight
1	Structural & Heat	Constant after 28 days	1	-	Straight
2	Structural & Heat	Varying after 28 days	1	-	Straight
3	Structural & Heat	Varying after 28 days	2	-	Straight
4	Structural & Heat	Varying after 28 days	2	Bedding provided below with a stiffness= 3600 kN/m ³	Straight
5	Structural & Heat	Varying after 28 days	2	Bedding provided below with a stiffness= 6950 kN/m ³	Straight
6	Structural & Heat	Varying after 28 days	2	Bedding provided on all sides with a stiffness=3600 kN/m ³	Straight
7	Structural & Heat	Varying after 28 days	2	-	Inclined with horizontal stiffness= 60 MN/m
8	Structural & Heat	Varying after 28 days	2	Bedding provided on all sides with a stiffness= 3600 kN/m ³	Inclined with horizontal stiffness= 60 MN/m
9	Structural & Heat	Varying after 28 days	2	Bedding provided on all sides with a stiffness= 20000 kN/m ³	Inclined with horizontal stiffness= 300 MN/m

6.3. Effect of constant maturity

The first section of the hydration heat analysis deals with the effect of both transient heat and structural analysis along with the maturity effects in the concrete material properties. The maturity effect is added to the material properties such as Young's modulus, Tensile strength, and fracture energy. It increases dynamically with time up to 28 days, after which it remains constant for the rest of the period. The plots for the same are shown in section 5.3.

6.3.1. Results of Variant 1

This variant deals with the effects of hydration heat in the concrete foundation. In order to generate the results of the hydration heat, transient heat transfer analysis is performed. The methodology to conduct the transient heat transfer is mentioned in section 6.1. At first, the hydration heat analysis is performed in the model to demonstrate the heat flow in the mass structure, followed by the nonlinear structural analysis. The results calculated are due to the application of heat generated inside the foundation. The wind directions mentioned in this section are depicted in the Figure 6.2.

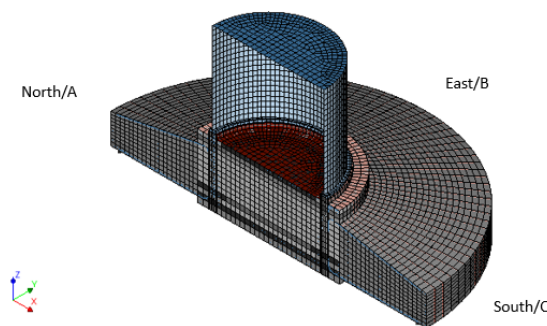


Figure 6.2: Wind turbine foundation-Wind directions

Temperature evolution in the concrete foundation

From the theory, it is clear that the mass structures release heat due to the hydration effect, hence it is necessary to include those effects in the numerical calculations in order to mimic the real structural behavior. To obtain the temperature development inside the foundation, transient heat transfer analysis is performed in DIANA. When this analysis is conducted, it is noticed that the concrete foundation starts to heat up after pouring the concrete and reaches the equilibrium point with the environment after 60 days. Also, the inner part of the foundation heats up the most and it cools down slowly after 3 days. The maximum temperature in the foundation is nearly 61.21 °C, which is a bit less than the maximum adiabatic temperature obtained for the CEM III/A 42.5 N LH which is 63 °C. The boundary conditions for the heat flow are applied based on the different surface conditions such as the top, pedestal, bottom, and side of the foundation, and the values for the heat transfer coefficient are obtained from the Table 6.3 which is based on many simplifying assumptions and estimates. The following calculation has been performed with the estimates of HTC 1. Also, it is to be noted that the heat generation inside the foundation is assumed to be uniform since the impact of heat generation in a nonuniform manner is averaged out by the large thermal inertia of the foundation as provided in subsection 2.1.2. The different boundary conditions have different effects on the structure which is shown in Figure 6.5. It is observed that the heat loss is predominated over the top surface since it is exposed to the air, whereas, the bottom portion is insulated by the soil. The high thermal inertia of the foundation allows it to retain temperatures as high as 30 °C for at least 28 days. The numerical analysis is performed for the whole 60 days and the results are shown below:

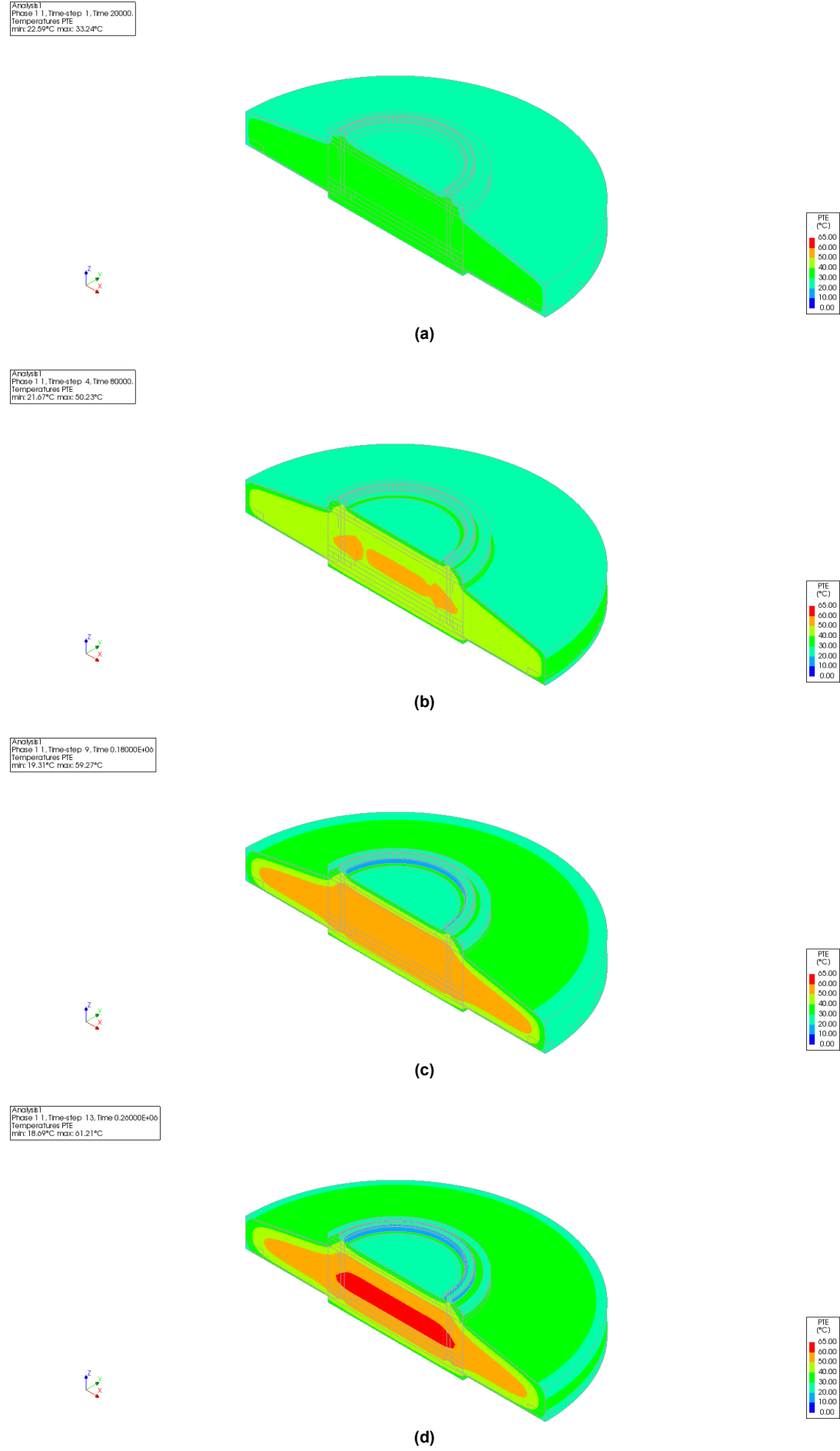
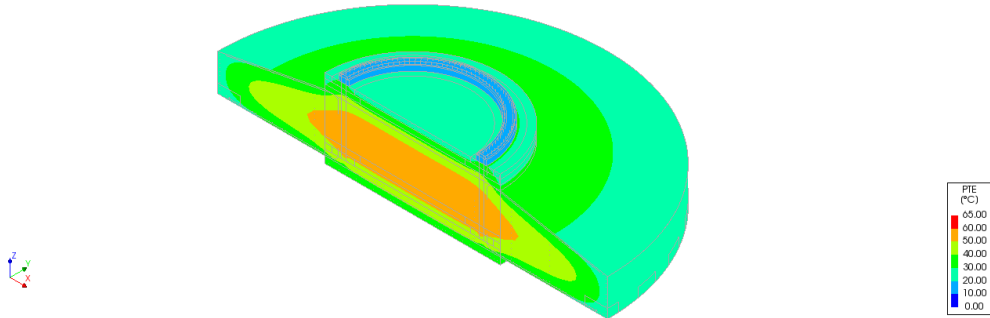


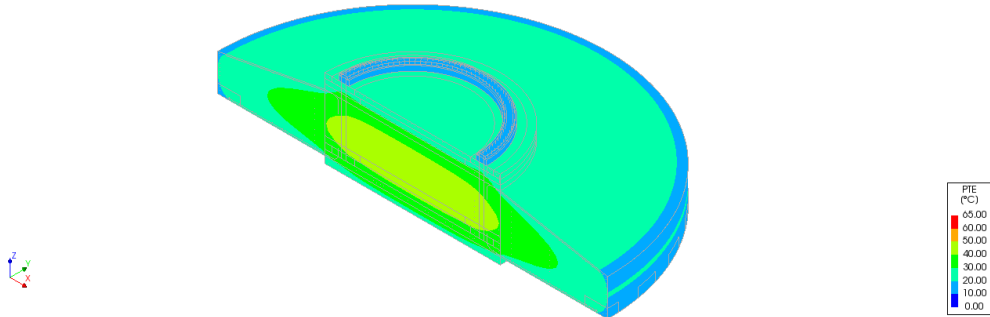
Figure 6.3: Temperature Evolution in concrete foundation a) Day 0, b) Day 1, c) Day 2, d) Day 3

Analysis 1
Phase 1 1, Time-step 30, Time 0.0000E+00
Temperatures PTE
min: 17.77°C max: 58.27°C



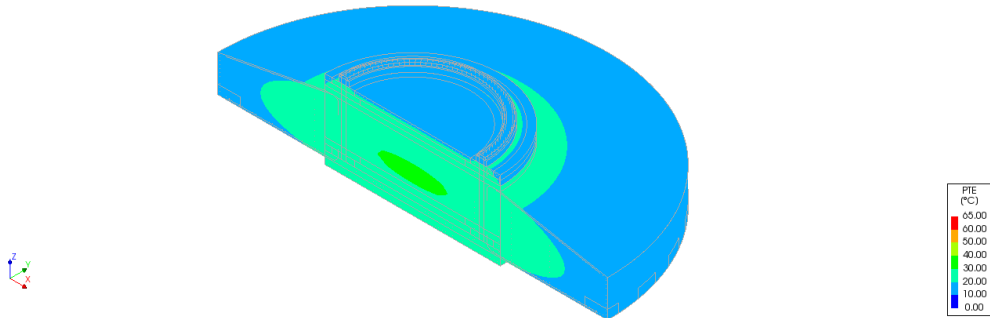
(e)

Analysis 1
Phase 1 1, Time-step 61, Time 0.12200E+07
Temperatures PTE
min: 17.55°C max: 46.24°C



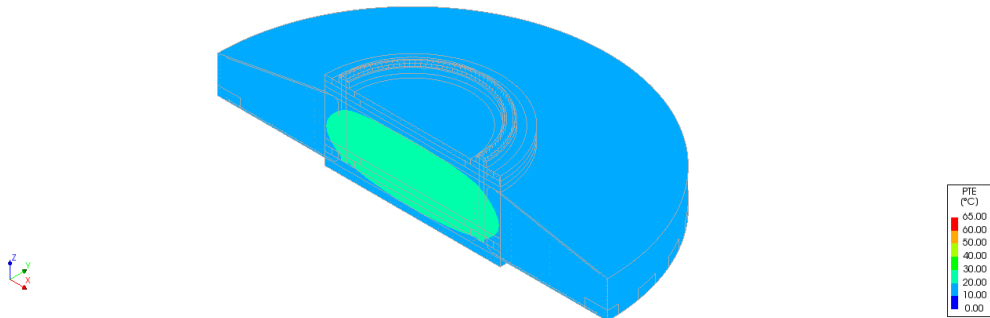
(f)

Analysis 1
Phase 1 1, Time-step 117, Time 0.24200E+07
Temperatures PTE
min: 17.48°C max: 30.59°C



(g)

Analysis 1
Phase 1 1, Time-step 176, Time 0.39000E+07
Temperatures PTE
min: 17.45°C max: 22.09°C



(h)

Figure 6.3: Temperature Evolution in concrete foundation e) Day 7, f) Day 14, g) Day 28, h) Day 45

[AF0]SE1
Phase 1 1, Time-step 222, Time 0.51000E+07
Temperatures PTE
Min: 17.45°C max: 19.28°C

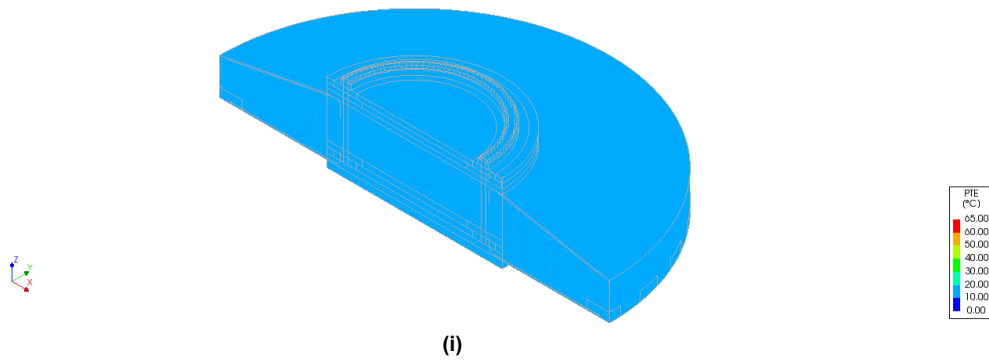


Figure 6.3: Temperature Evolution in concrete foundation i) Day 60

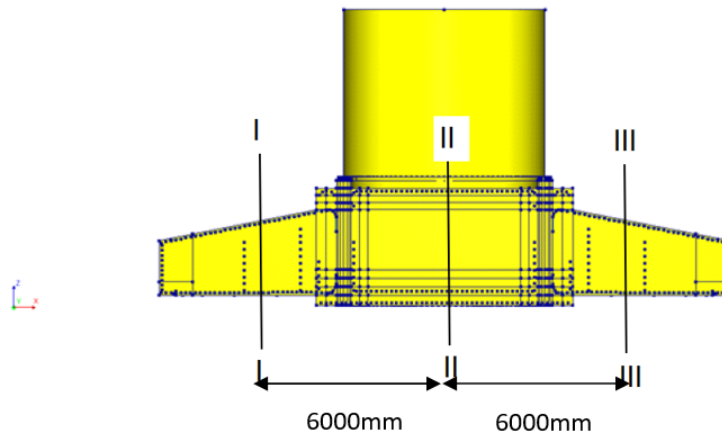
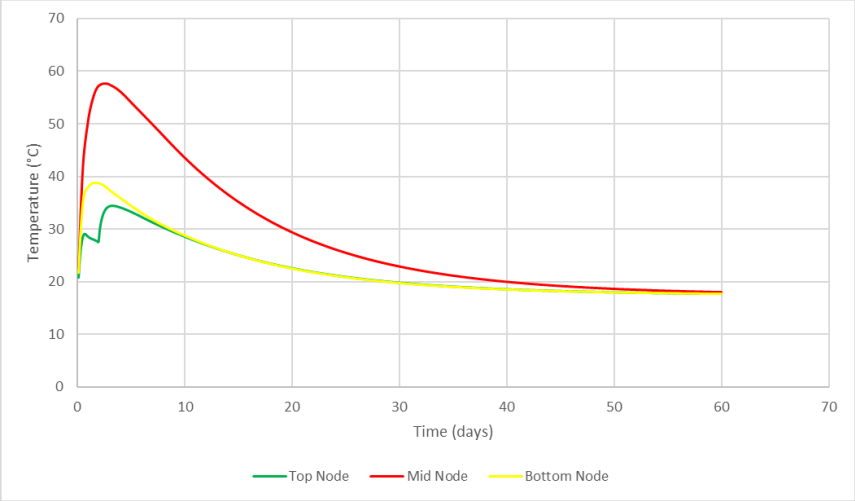
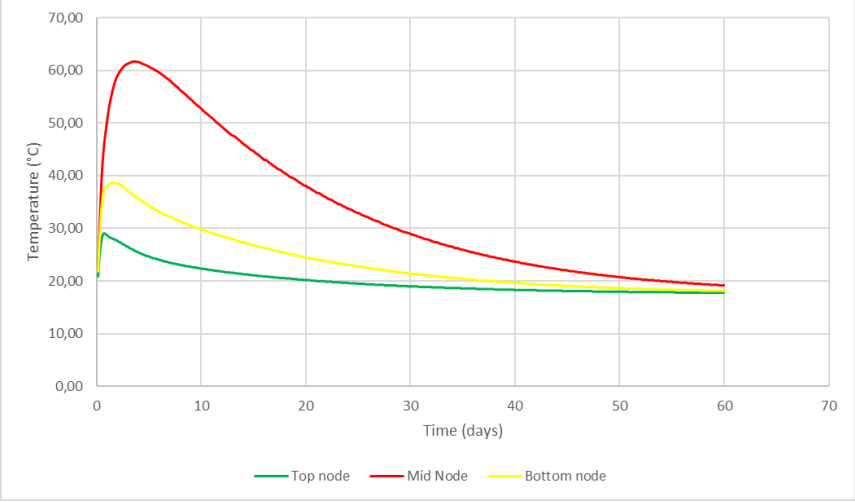


Figure 6.4: Wind turbine foundation-section layout

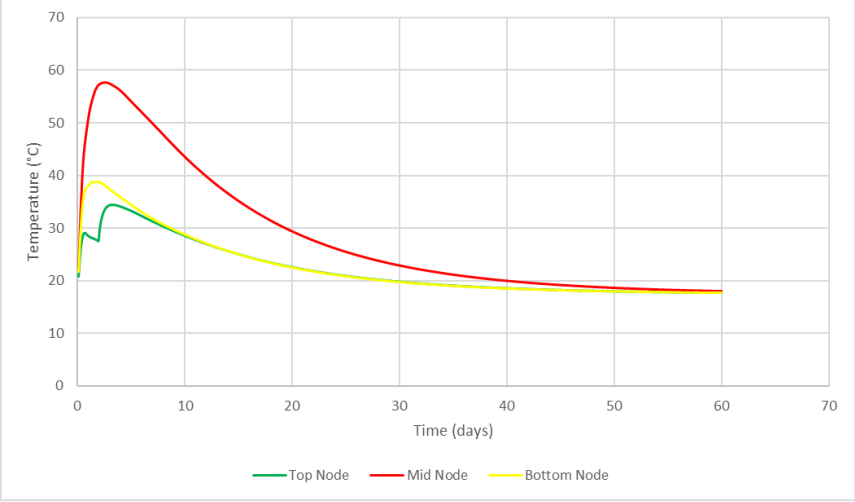
The below Figure 6.5, depicts the plot for temperature with respect to the time in each section of the foundation. Both left (section I-I) and right (section III-III) are equidistant from the middle section (section II-II) of the foundation. The graphs are plotted for nodes at different positions in each section. From all the graphs, it is evident that the innermost middle section reaches the highest temperature and the top part has the lowest temperature as compared to the other nodes. From Figure 2.7, it is also evident that the node close to the foundation core experiences higher temperature as compared to the nodes away from the foundation core. A sudden drop in the temperature is experienced in the topmost node of sections I-I and III-III, which again increases on day 3 when the soil backfilling occurs. This is due to the fact that after the backfilling of the soil, the insulation capacity of the foundation increases and it results in less heat loss. Whereas, in section II-II that is not the case due to the presence of the pedestal at the top surface of the foundation. The lowest temperature of the top surface occurs due to the interaction of the concrete surface with the air.



(a)

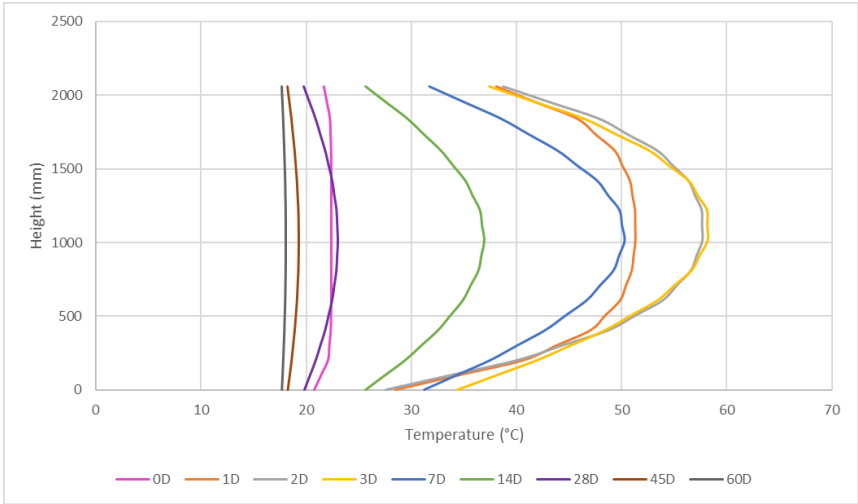


(b)

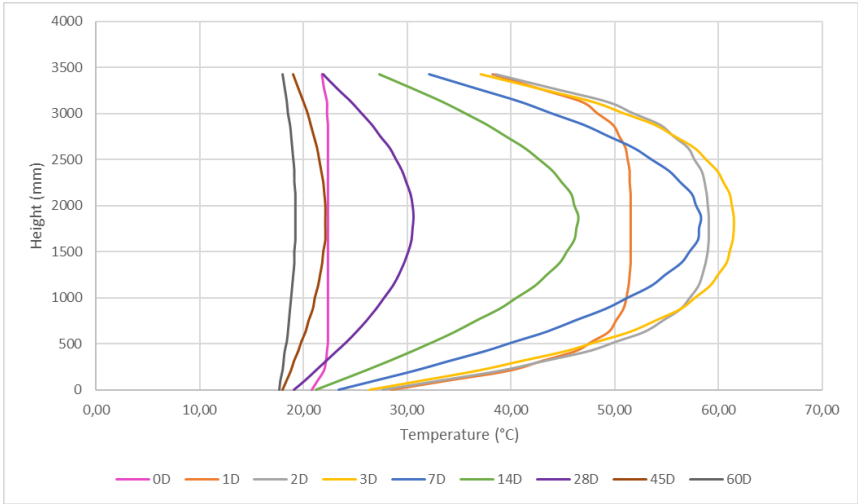


(c)

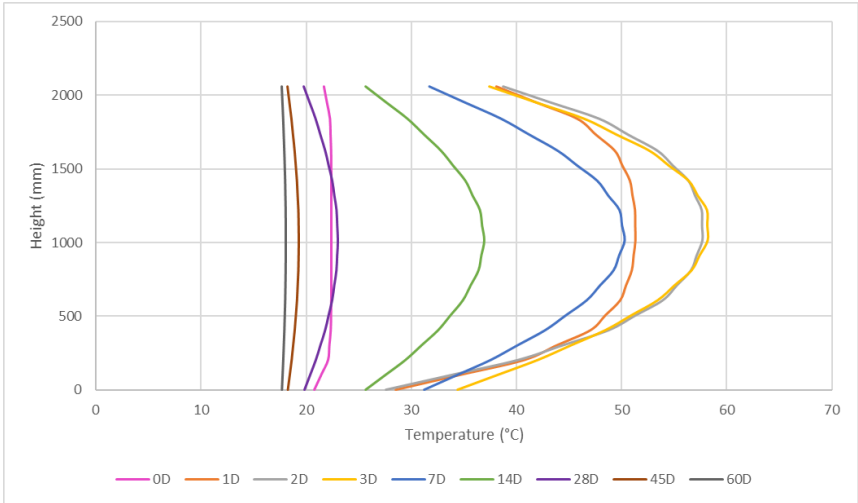
Figure 6.5: Temperature vs Time plots for different sections of the concrete foundation a) Left section-I-I, b) Middle section-II-II, c) Right section-III-III



(a)



(b)



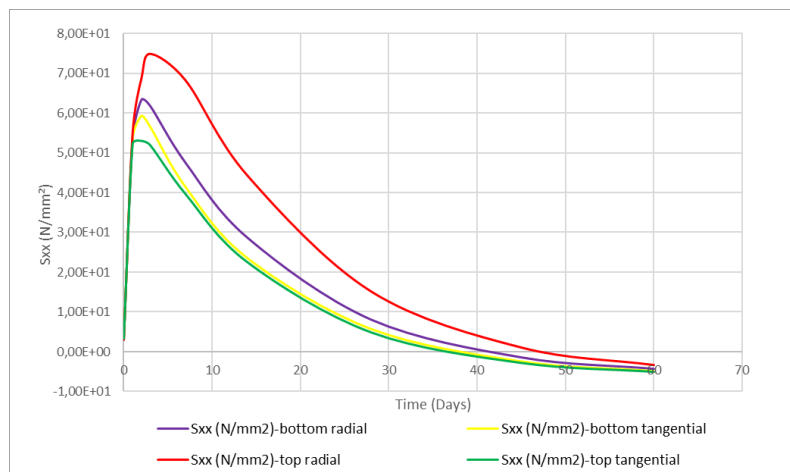
(c)

Figure 6.6: Height vs Temperature plots for different sections of the concrete foundation a) Left section-I-I, b) Middle section-II-II, c) Right section-III-III

The next graphs depicted in Figure 6.6, show the variation of the temperature along the height of the foundation for various days. It is observed from the graphs for three sections, that the maximum temperature is attained on Day 3 at the middle height of the foundation after which it gradually decreases and the final equilibrium is reached at the end of 60 days. Another purpose of the vertical temperature gradient is to find the thermal cracking in the mass structure. From the Figure 6.6, it is observed that the maximum gradient is obtained at an age of 7 days where the maximum temperature difference between the core and the topmost surface is 35°C . This is also with the reference with Figure 2.9 where the maximum temperature gradient is obtained at an age of 9 days. From [8], the concrete is most likely susceptible to cracking if the temperature gradient is higher than 25°C . Since the temperature difference is much more than the limits, the foundation is prone to show visible thermal cracks.

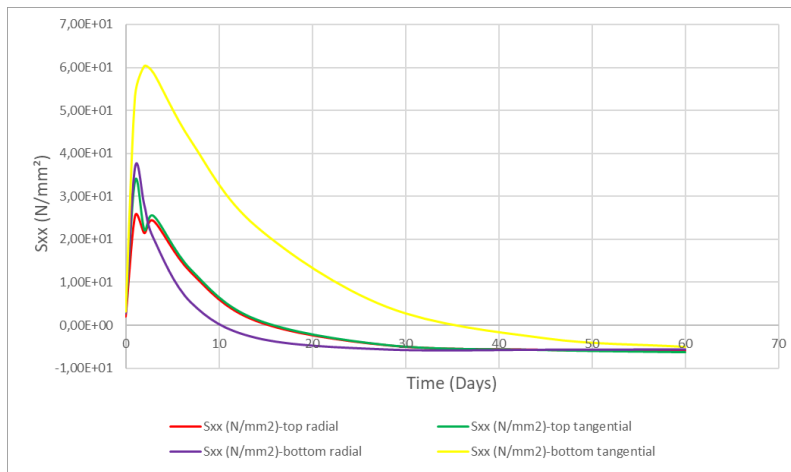
Steel stresses due to the Hydration heat

In subsection 6.3.1, the evolution of the temperature is discussed along with the time. To determine the stresses in the reinforcement bars, a structural non-linear analysis is performed to check the developed steel stresses due to the effect of hydration heat. In the analysis mentioned in section 5.4, the model did not include the effects of the hydration heat of the concrete which resulted in the steel stresses only due to the structural calculations. Whereas, now with the inclusion of the heat of hydration in the wind turbine foundation model, the concrete is allowed to mimic the real structural behavior, and hence the generated steel stresses due to this phenomenon can be observed. When the stress in the reinforcement bars is compared at different locations in the foundation a peculiar behavior is observed between the innermost and outermost nodes as depicted in Figure 6.7. The nodes closer to the pedestal in the radial direction appear to undergo more considerable stresses due to the bending of the rebar at that point. Otherwise, at the outer node, the top radial bar experiences a change in peaks due to the applied boundary conditions. This is also similar to the graph obtained in Figure 6.5. In the case of the tangential bars, the position of the nodes does not matter since in both the nodes the bottom bars have higher stresses than the top tangential bars. This is also evident from the Figure 6.8 where bottom bars at both radial and tangential positions experience more significant stress, especially on the second and third day after concrete pouring because, unlike the top steel bars, the bottom ones are only exposed to the surrounding soil which has higher insulation capacity as compared to the other boundary conditions such as air or steel cage.



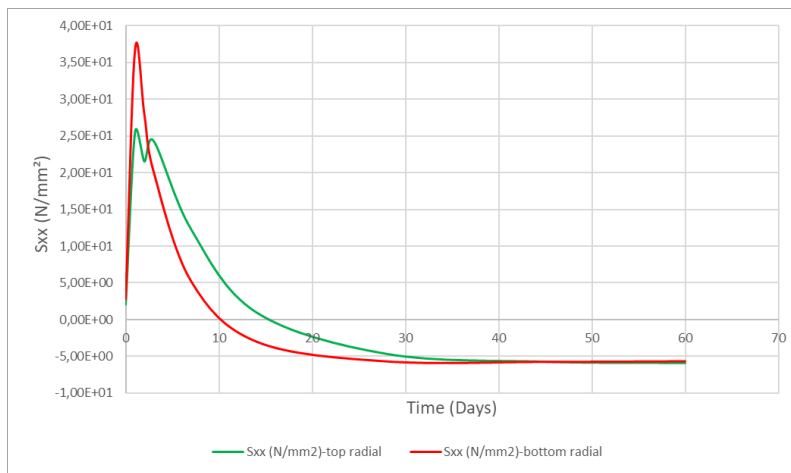
(a)

Figure 6.7: Steel stress wrt time at different locations in the rebar a) Inner node

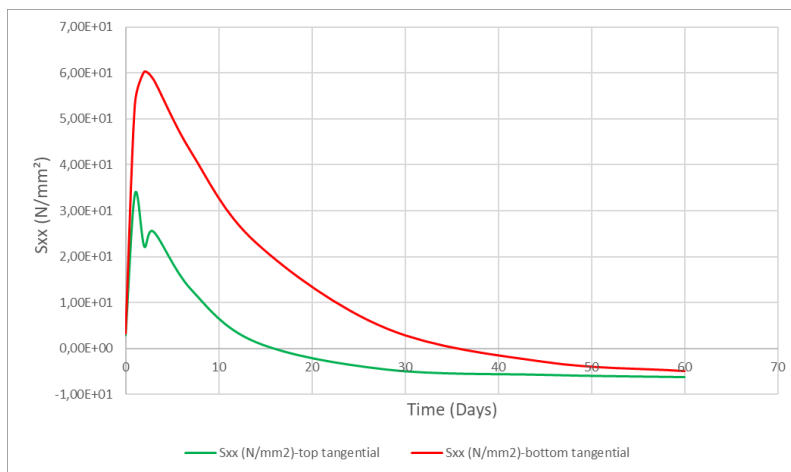


(b)

Figure 6.7: Steel stress wrt time at different locations in the rebar b) Outer node



(a)

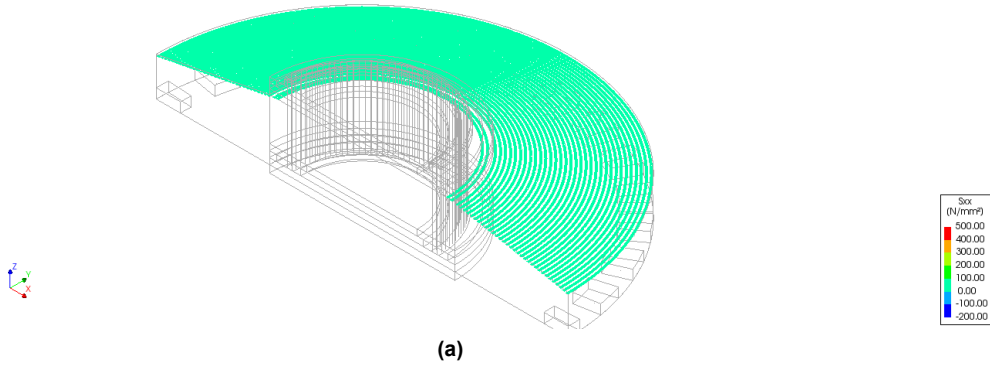


(b)

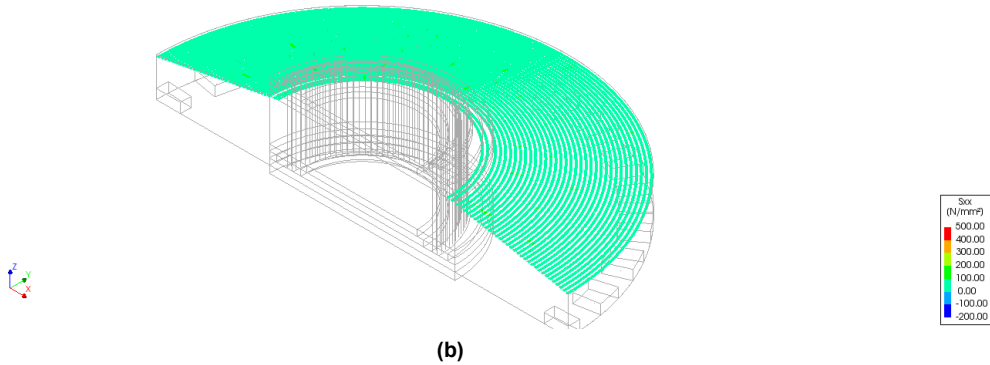
Figure 6.8: Steel stress wrt time for different positions in the foundation a) Radial, b) Tangential

The stress generated in the rebars due to the influence of hydration heat over the period is shown in the figures below:

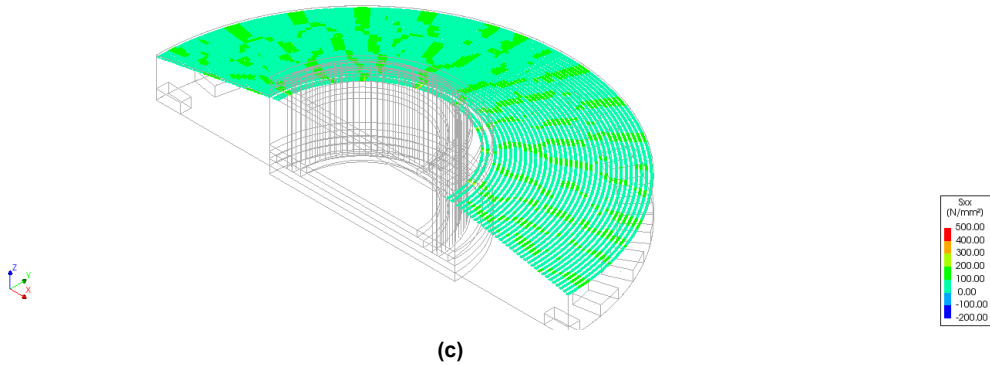
Analysis 1
Phase 1, Time-step 1, Time 20000.
Reinforcement Couch; Total Stresses Six layer 1
min: 21.63N/mm² max: 23.70N/mm²



Analysis 1
Phase 1, Time-step 4, Time 80000.
Reinforcement Couch; Total Stresses Six layer 1
min: 24.46N/mm² max: 131.64N/mm²



Analysis 1
Phase 1, Time-step 9, Time 0.18000E+06
Reinforcement Couch; Total Stresses Six layer 1
min: 17.52N/mm² max: 294.72N/mm²



Analysis 1
Phase 1, Time-step 13, Time 0.26000E+06
Reinforcement Couch; Total Stresses Six layer 1
min: 22.33N/mm² max: 345.85N/mm²

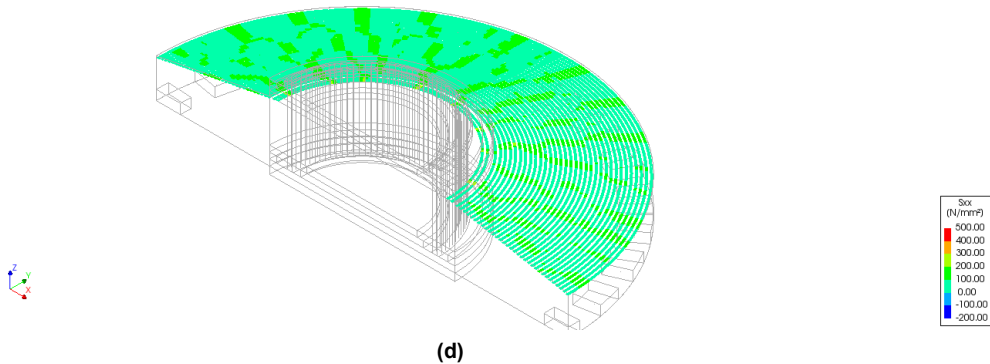
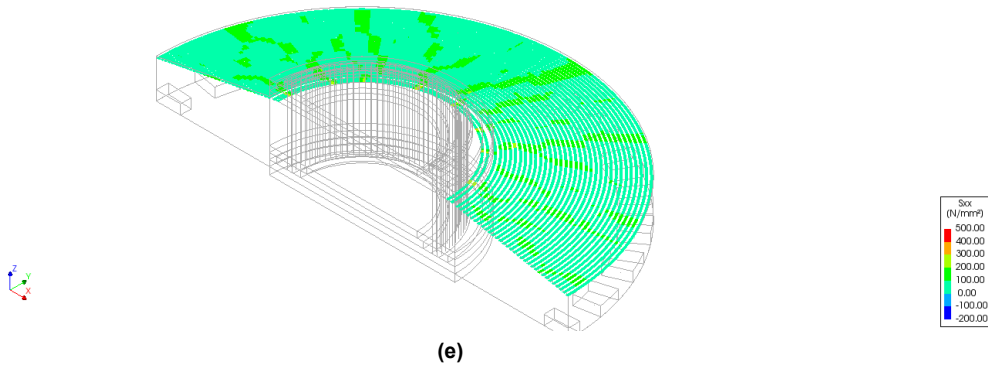
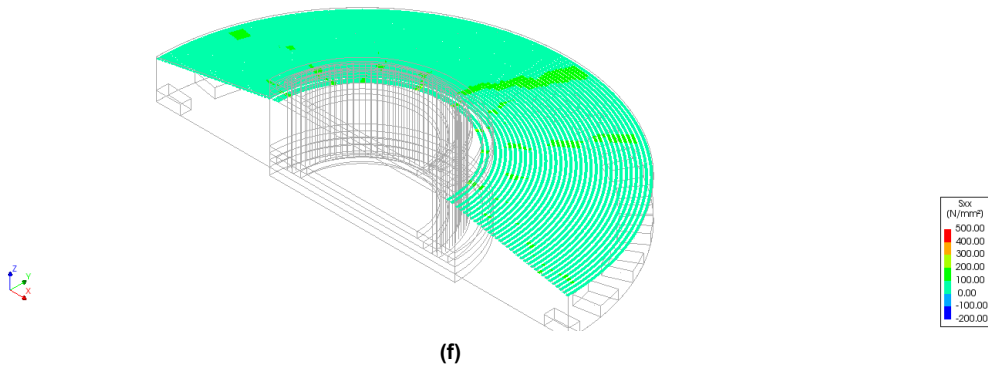


Figure 6.9: Steel stress in the Top tangential rebars a) Day 0, b) Day 1, c) Day 2, d) Day 3

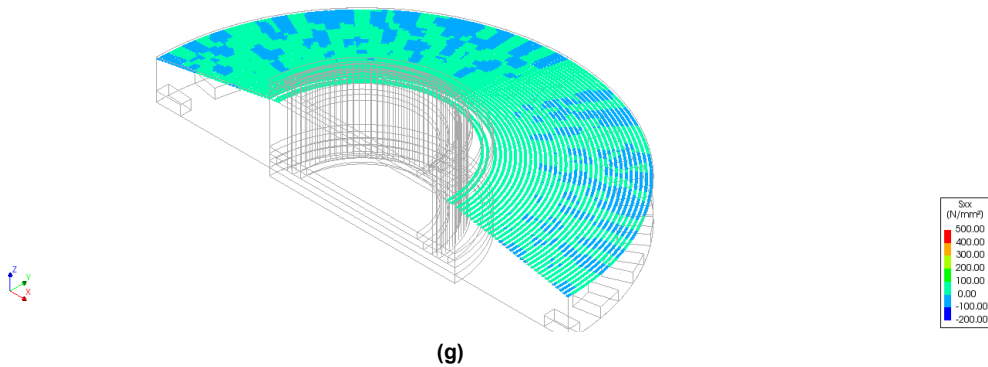
Analysis 1
Phase 1, Time-step 30, Time 0.60000E+06
Reinforcement Cauchy Total Stresses Six layer 1
min: 12.14N/mm² max: 381.16N/mm²



Analysis 1
Phase 1, Time-step 61, Time 0.12200E+07
Reinforcement Cauchy Total Stresses Six layer 1
min: 0.57N/mm² max: 283.66N/mm²



Analysis 1
Phase 1, Time-step 117, Time 0.24200E+07
Reinforcement Cauchy Total Stresses Six layer 1
min: -5.06N/mm² max: 127.58N/mm²



Analysis 1
Phase 1, Time-step 176, Time 0.39000E+07
Reinforcement Cauchy Total Stresses Six layer 1
min: -0.46N/mm² max: 41.00N/mm²

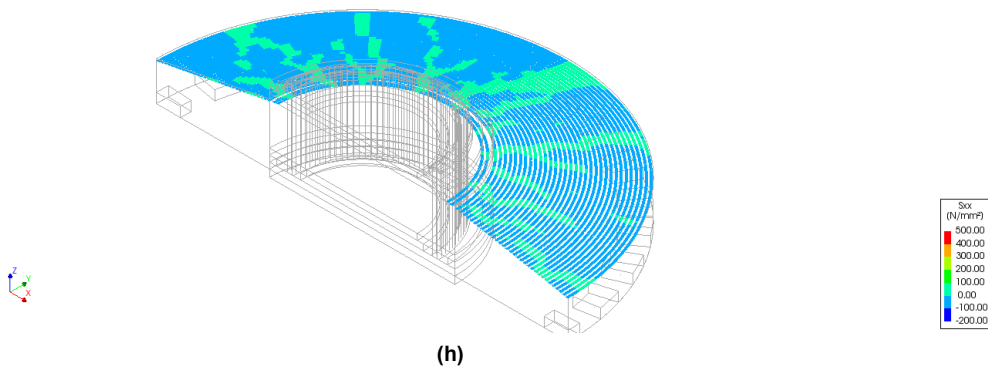
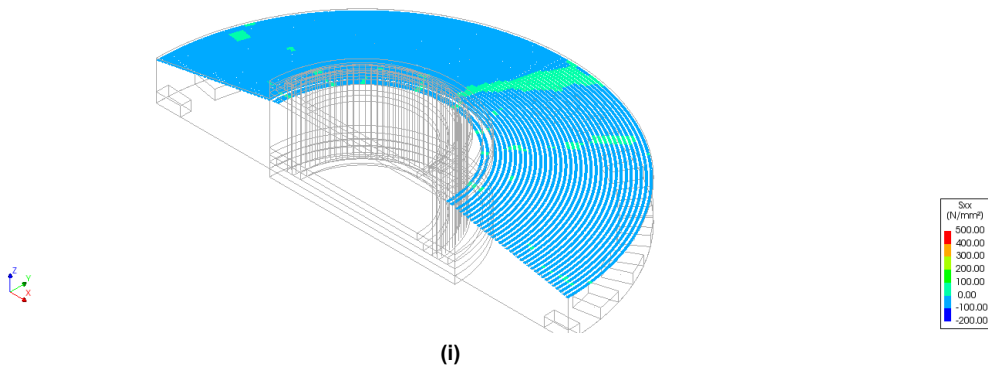


Figure 6.9: Steel stress in the Top tangential rebars e) Day 7, f) Day 14, g) Day 28, h) Day 45

Analysis 1
Phase 1, Time-step 222, Time 0.51e00E+07
Reinforcement Couchy Total Stresses Six layer 1
min: -0.54N/mm² max: 12.61N/mm²

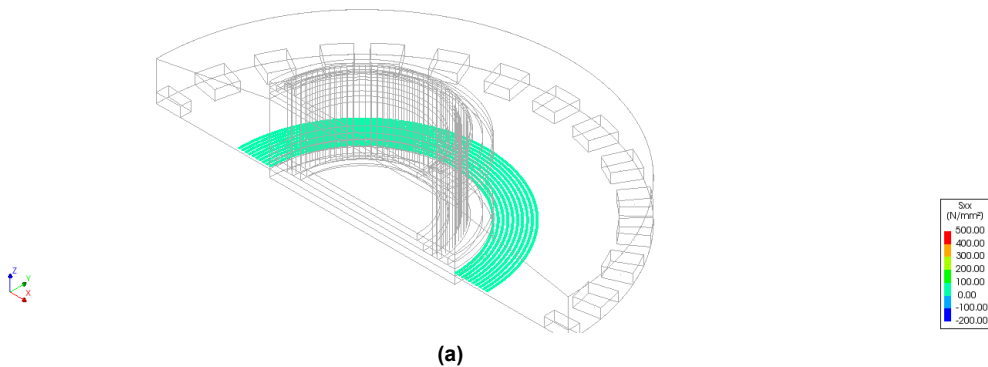


(i)

Figure 6.9: Steel stress in the Top tangential rebars i) Day 60

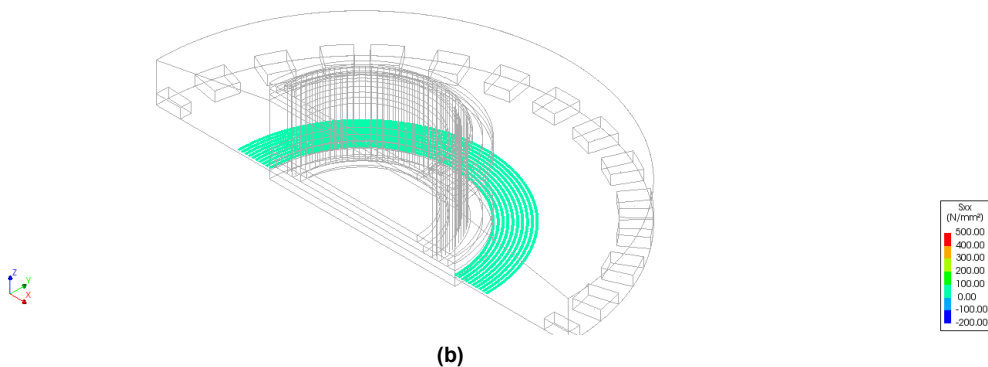
Observation Figure 6.9: When the foundation starts to heat up due to the hydration effect, the results are reflected in the stresses in the rebars. In the case of the tangential bars at the top position, an asymmetrical pattern can be observed in the radial direction which is maximum on days 2 and 3, and slowly after day 7, it starts to localize to certain areas. The tensile steel stresses reach their peak value on day 7 after which it gradually begins to decrease and the compressive stresses start to occur after 28 days.

Analysis 1
Phase 1, Time-step 1, Time 20000
Reinforcement Couchy Total Stresses Six layer 1
min: 22.54N/mm² max: 22.92N/mm²



(a)

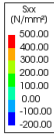
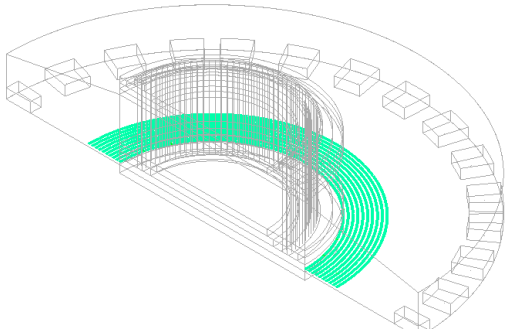
Analysis 1
Phase 1, Time-step 4, Time 80000
Reinforcement Couchy Total Stresses Six layer 1
min: 47.81N/mm² max: 59.05N/mm²



(b)

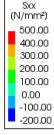
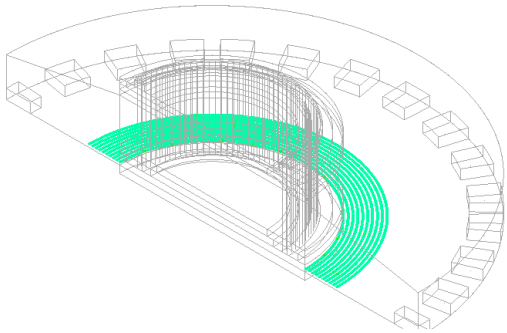
Figure 6.10: Steel stress in the Bottom tangential rebars a) Day 0, b) Day 1

Analysis 1
Phase 1, Time-step 9, Time 0.18000E+00
Reinforcement Cauchy Total Stresses Six layer 1
min: 44.24N/mm² max: 106.53N/mm²



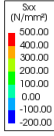
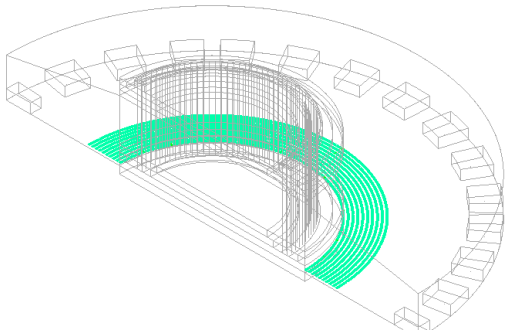
(c)

Analysis 1
Phase 1, Time-step 13, Time 0.26000E+00
Reinforcement Cauchy Total Stresses Six layer 1
min: 41.93N/mm² max: 124.27N/mm²



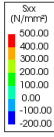
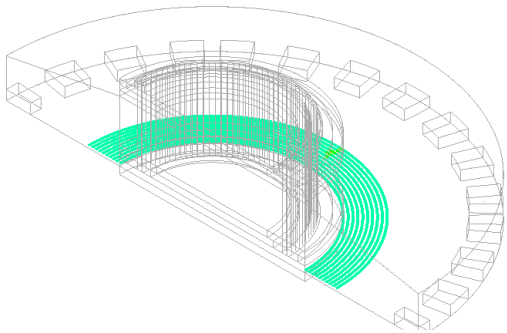
(d)

Analysis 1
Phase 1, Time-step 30, Time 0.60000E+00
Reinforcement Cauchy Total Stresses Six layer 1
min: 29.52N/mm² max: 114.94N/mm²



(e)

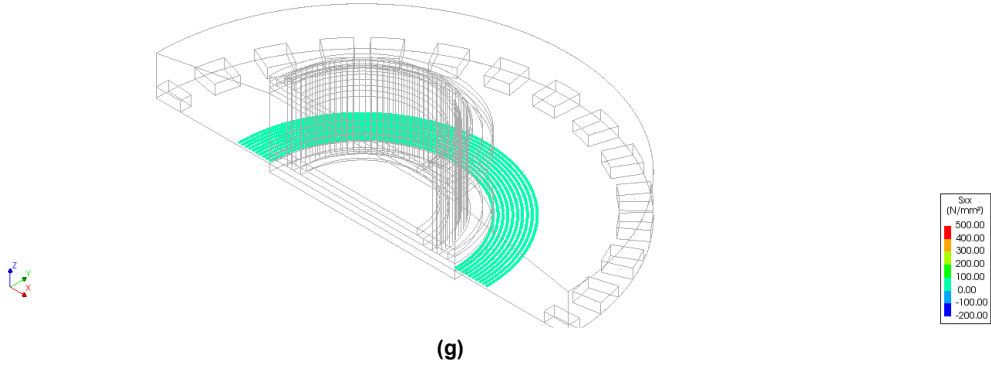
Analysis 1
Phase 1, Time-step 61, Time 0.12200E+07
Reinforcement Cauchy Total Stresses Six layer 1
min: 14.19N/mm² max: 134.89N/mm²



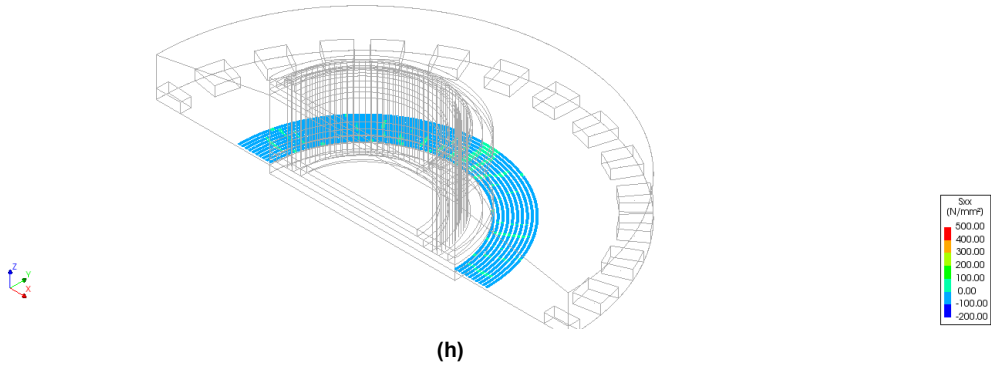
(f)

Figure 6.10: Steel stress in the Bottom tangential rebars c) Day 2, d) Day 3, e) Day 7, f) Day 14

Analysis 1
Phase 1, Time-step 117, Time 0.24250E+07
Reinforcement Cauchy Total Stresses Sxx layer 1
min: 0.63N/mm² max: 74.59N/mm²



Analysis 1
Phase 1, Time-step 176, Time 0.39000E+07
Reinforcement Cauchy Total Stresses Sxx layer 1
min: -4.35N/mm² max: 25.78N/mm²



Analysis 1
Phase 1, Time-step 222, Time 0.51600E+07
Reinforcement Cauchy Total Stresses Sxx layer 1
min: -5.62N/mm² max: 8.60N/mm²

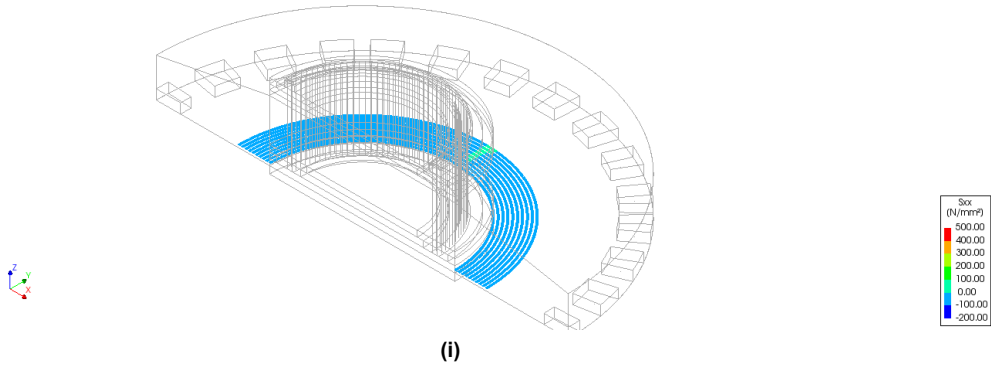
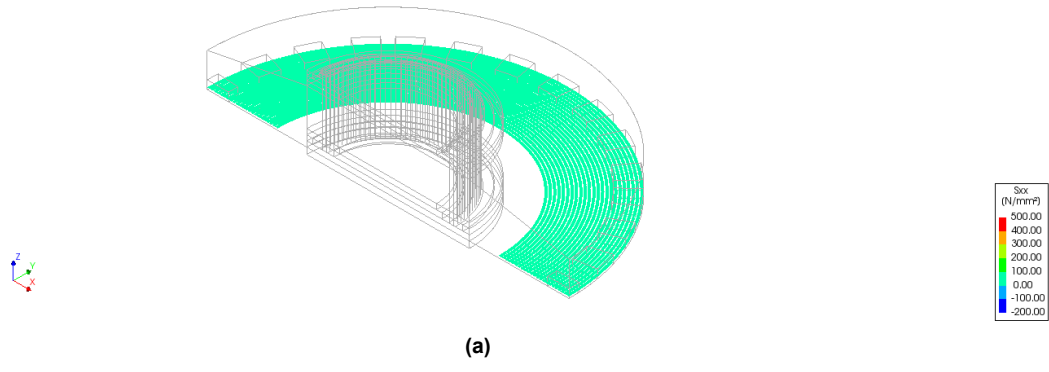


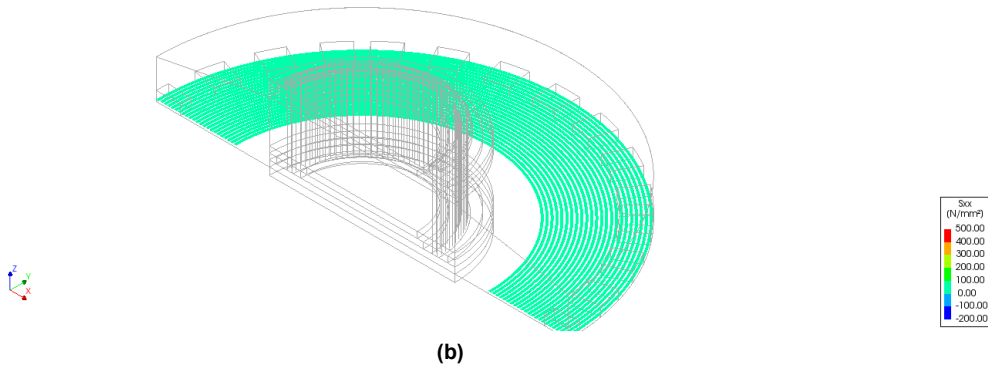
Figure 6.10: Steel stress in the Bottom tangential rebars g) Day 28, h) Day 45, i) Day 60

Observation Figure 6.10: In the case of the bottom tangential rebars near the pedestal, the maximum tensile stress occurs on day 3. Whereas, the compressive stress starts to occur after 30 days, increasing until the foundation cools down completely.

[Analysis]
Phase 1, Time-step 1, Time 20000.
Reinforcement Cauchy Total Stresses Six layer 1
min: 20.05N/mm² max: 24.42N/mm²



[Analysis]
Phase 1, Time-step 4, Time 80000.
Reinforcement Cauchy Total Stresses Six layer 1
min: 37.77N/mm² max: 80.92N/mm²



[Analysis]
Phase 1, Time-step 9, Time 0.18000E+06
Reinforcement Cauchy Total Stresses Six layer 1
min: 25.91N/mm² max: 142.08N/mm²

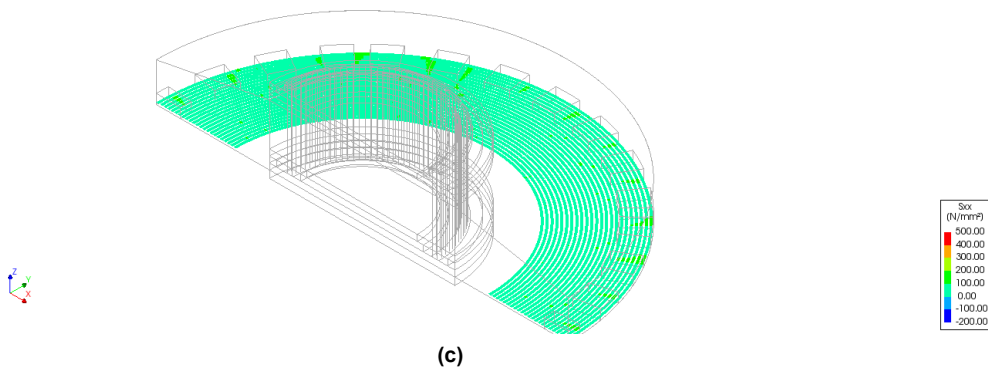
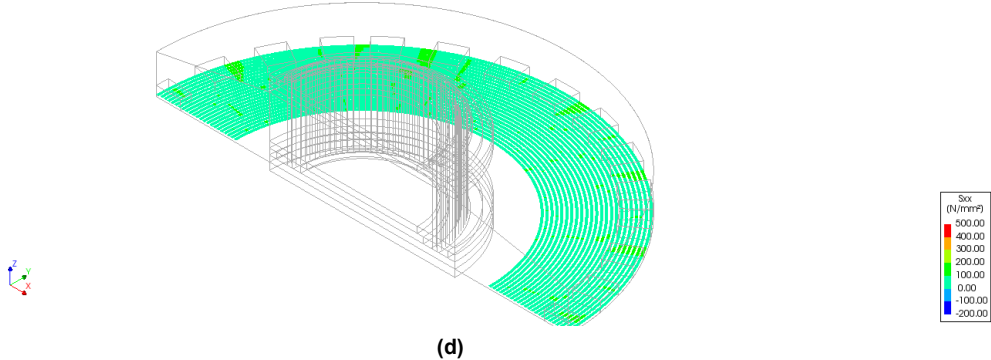
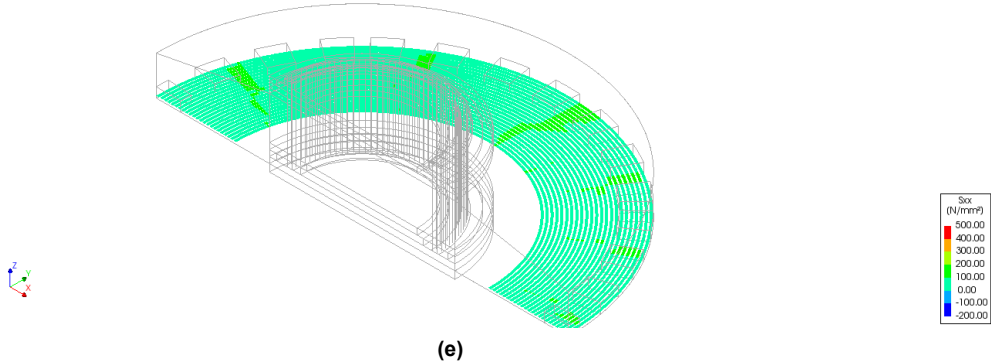


Figure 6.11: Steel stress in the Bottom tangential rebars near the piles a) Day 0, b) Day 1, c) Day 2

Analysis 1
Phase 1, Time-step 13, Time 0.20000E+00
Reinforcement Cauchy Total Stresses Six layer 1
min: 20.12N/mm² max: 151.10N/mm²



Analysis 1
Phase 1, Time-step 30, Time 0.60000E+00
Reinforcement Cauchy Total Stresses Six layer 1
min: 11.13N/mm² max: 174.33N/mm²



Analysis 1
Phase 1, Time-step 61, Time 0.12200E+07
Reinforcement Cauchy Total Stresses Six layer 1
min: -0.27N/mm² max: 174.96N/mm²

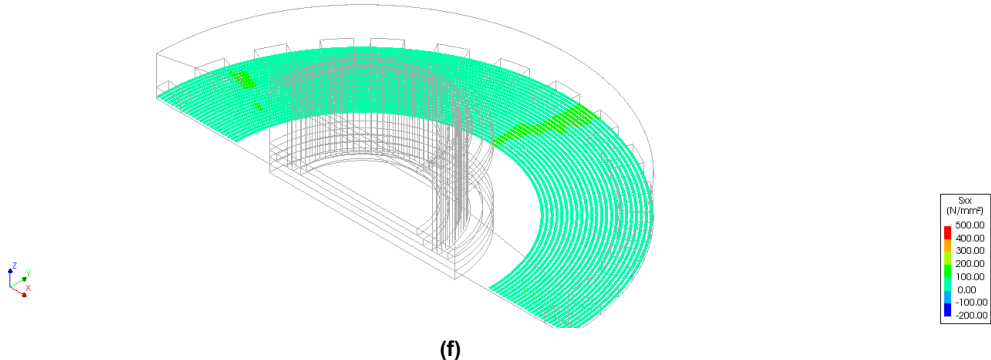
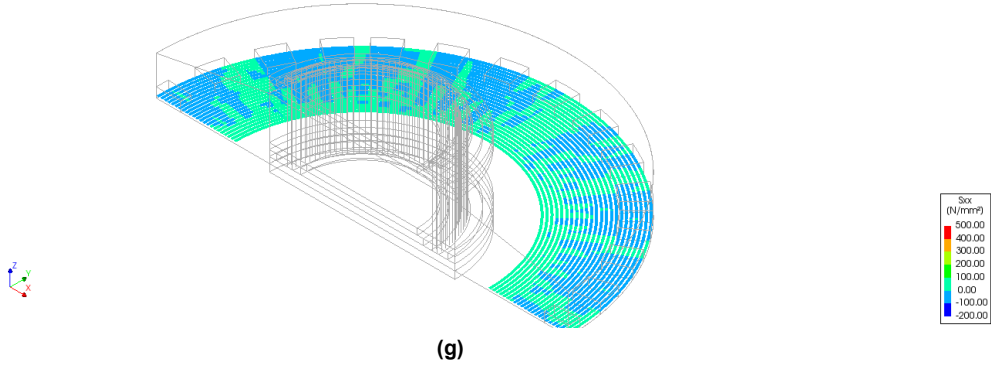
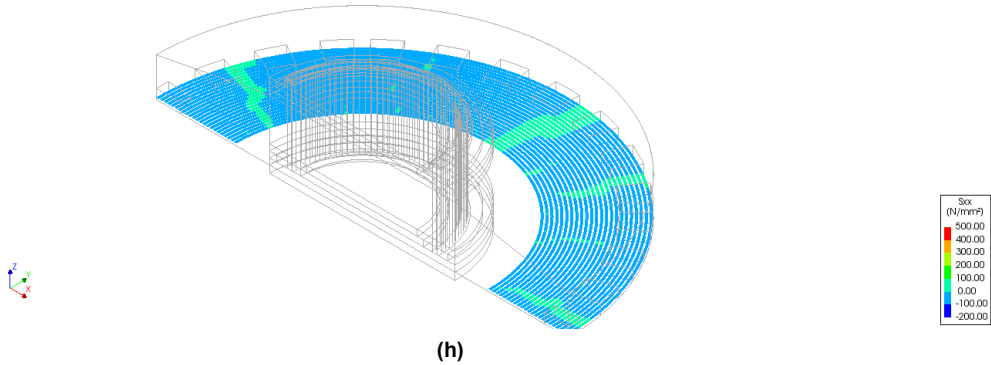


Figure 6.11: Steel stress in the Bottom tangential rebars near the piles d) Day 3, e) Day 7, f) Day 14

Analysis 1
Phase 1, Time-step 117, Time 0.24250E+07
Reinforcement Cauchy Total Stresses Sxx layer 1
min: -5.41N/mm² max: 95.50N/mm²



Analysis 1
Phase 1, Time-step 176, Time 0.39000E+07
Reinforcement Cauchy Total Stresses Sxx layer 1
min: -0.52N/mm² max: 33.16N/mm²



Analysis 1
Phase 1, Time-step 222, Time 0.51000E+07
Reinforcement Cauchy Total Stresses Sxx layer 1
min: -0.64N/mm² max: 11.61N/mm²

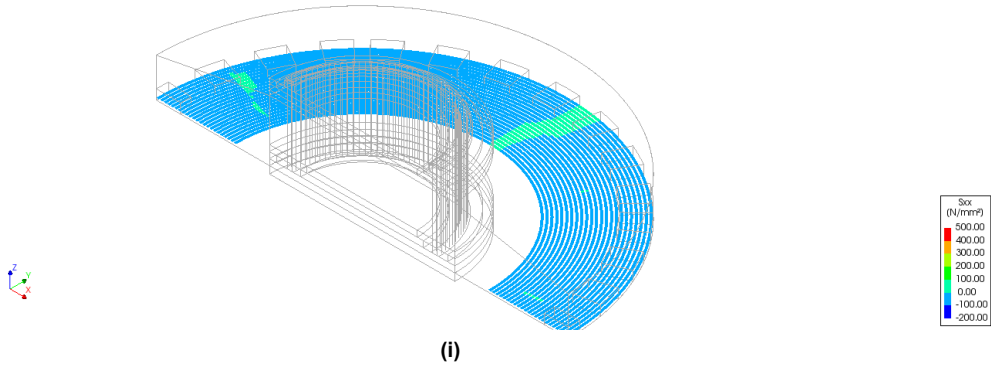


Figure 6.11: Steel stress in the Bottom tangential rebars near the piles g) Day 28, h) Day 45, i) Day 60

Observation Figure 6.11: The tangential reinforcements near the piles experience a similar effect as the top tangential as it experiences the highest tensile stress on the 7th day, after which this decreases gradually and leads to the rise of the compressive stress after 14 days.

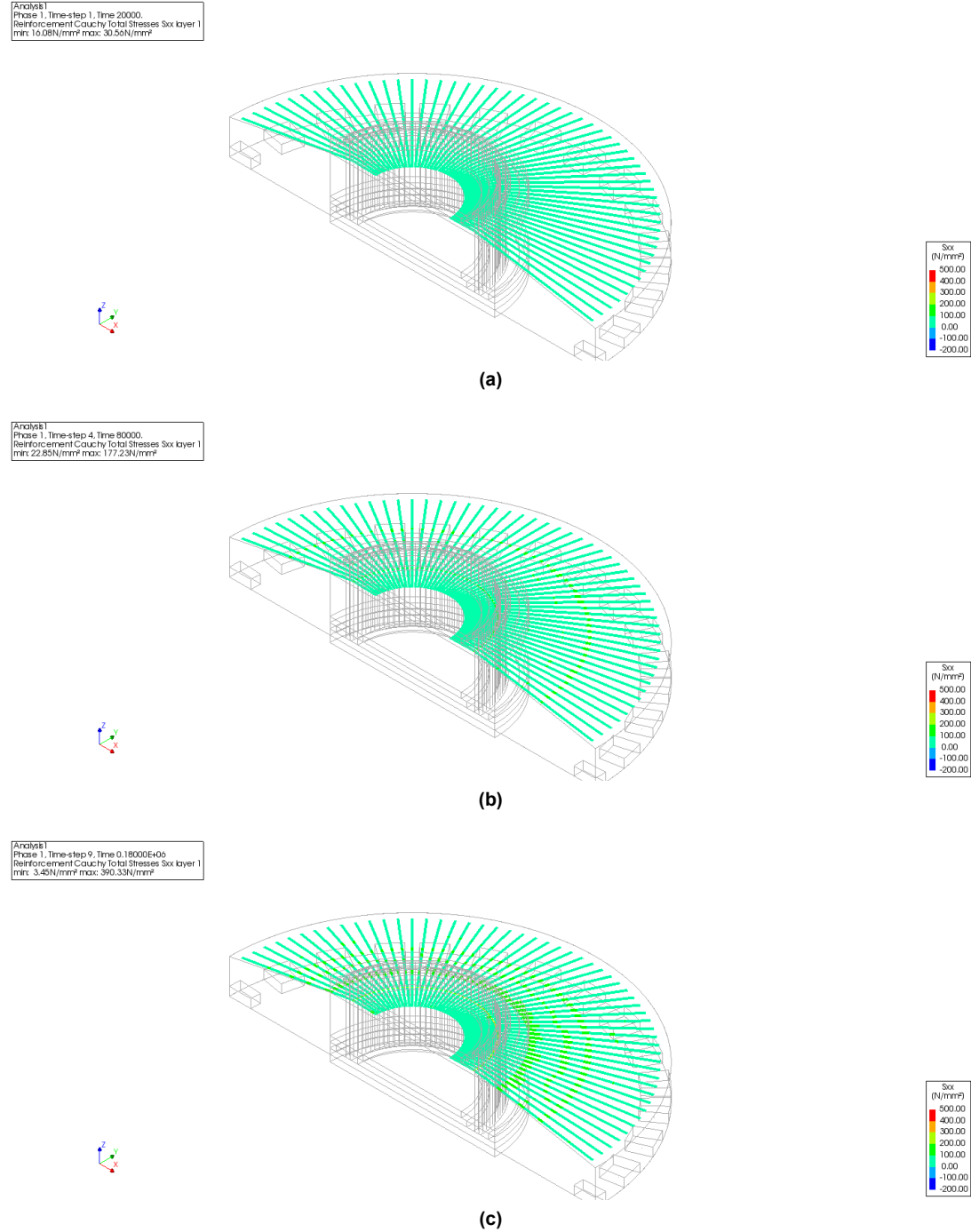
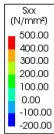
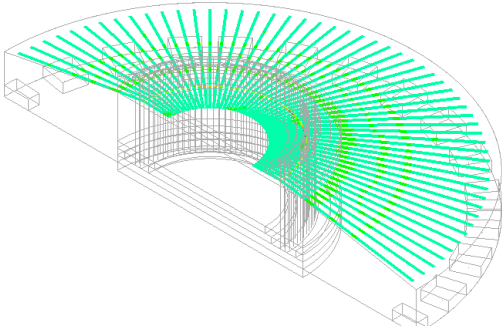


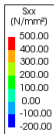
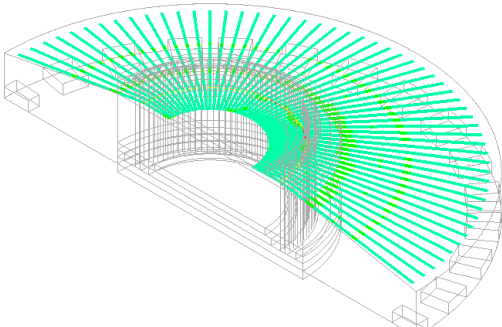
Figure 6.12: Steel stress in the Top radial rebars a) Day 0, b) Day 1, c) Day 2

Analysis 1
Phase 1, Time-step 13, Time 0.20000E+00
Reinforcement Cauchy Total Stresses Six layer 1
min: -15.02N/mm² max: 482.75N/mm²



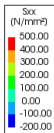
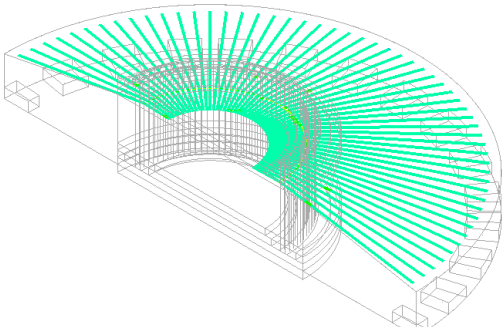
(d)

Analysis 1
Phase 1, Time-step 30, Time 0.60000E+00
Reinforcement Cauchy Total Stresses Six layer 1
min: -09.02N/mm² max: 300.96N/mm²



(e)

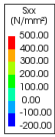
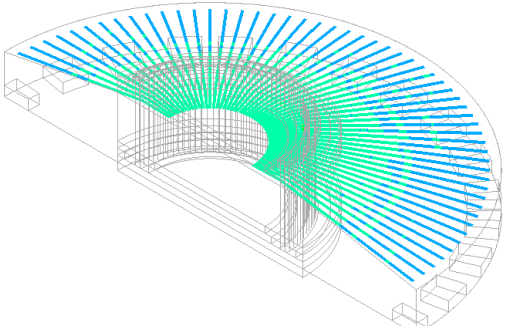
Analysis 1
Phase 1, Time-step 61, Time 0.12200E+07
Reinforcement Cauchy Total Stresses Six layer 1
min: -02.05N/mm² max: 343.67N/mm²



(f)

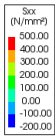
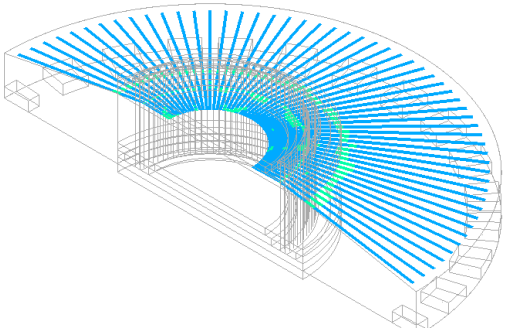
Figure 6.12: Steel stress in the Top radial rebar d) Day 3, e) Day 7, f) Day 14

Analysis 1
Phase 1, Time-step 117, Time 0.24290E+07
Reinforcement Cauchy Total Stresses Six layer 1
min: -39.20N/mm² max: 135.17N/mm²



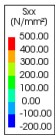
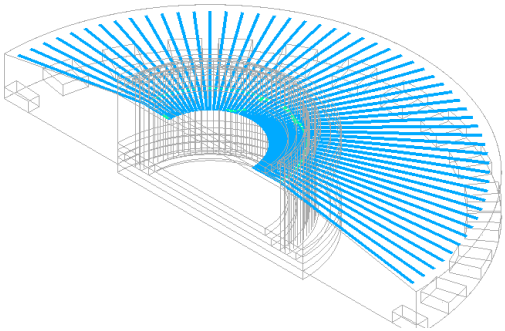
(g)

Analysis 1
Phase 1, Time-step 176, Time 0.39000E+07
Reinforcement Cauchy Total Stresses Six layer 1
min: -85.95N/mm² max: 57.15N/mm²



(h)

Analysis 1
Phase 1, Time-step 222, Time 0.51400E+07
Reinforcement Cauchy Total Stresses Six layer 1
min: -129.76N/mm² max: 32.11N/mm²

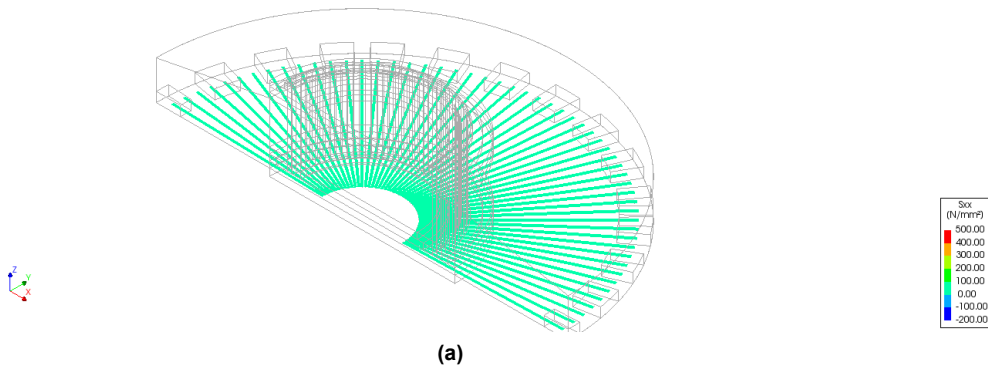


(i)

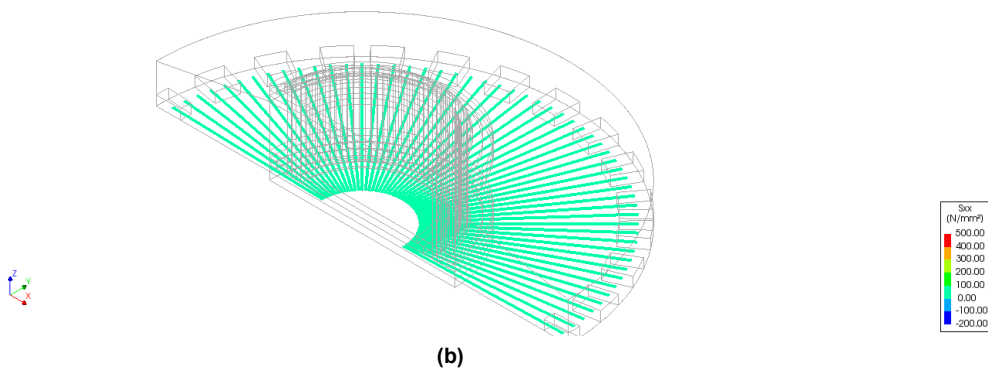
Figure 6.12: Steel stress in the Top radial rebars g) Day 28, h) Day 45, i) Day 60

Observation Figure 6.12: The top radial bars attain the maximum tensile stress on day 7, which is also accompanied by compressive stresses. These higher stresses are near the areas of the bends in the rebar. The position of the bend is shown in Figure 5.19. A ring-shaped crack pattern can be observed in the radial group in the temperature-rising phase which disappears slowly during the temperature-drop phase and the compressive stresses develops in the steel bars. The ring pattern formed in the radial bars due to the stress concentration during the heating phase of the foundation and when it cooled down the compressive stresses got distributed uniformly in the whole rebar set.

[Analysis]
Phase 1, Time-step 1, Time 20000.
Reinforcement Cauchy Total Stresses Six layer 1
min: 19.37N/mm² max: 24.72N/mm²



[Analysis]
Phase 1, Time-step 4, Time 80000.
Reinforcement Cauchy Total Stresses Six layer 1
min: 35.03N/mm² max: 89.73N/mm²



[Analysis]
Phase 1, Time-step 9, Time 0.18000E+06
Reinforcement Cauchy Total Stresses Six layer 1
min: 29.24N/mm² max: 136.15N/mm²

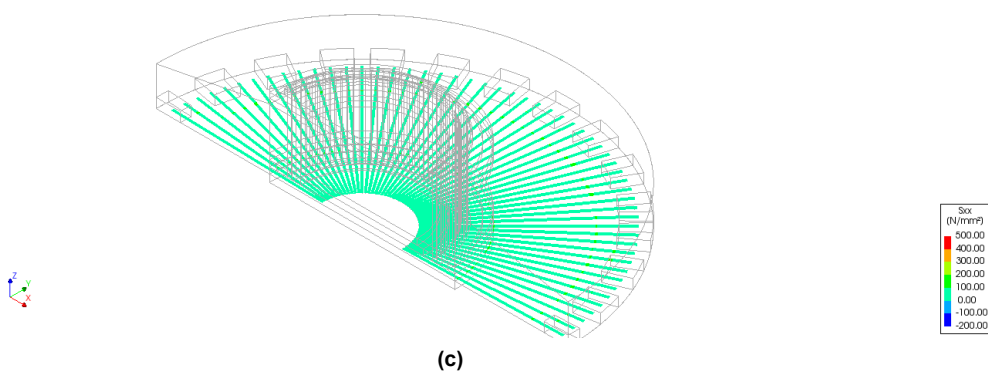
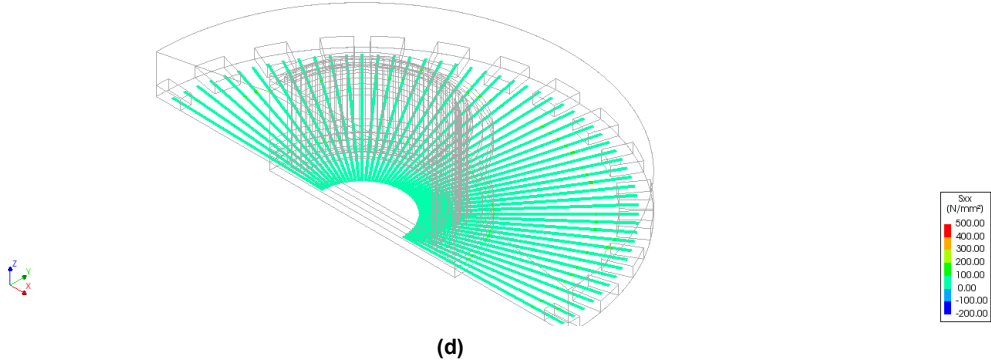
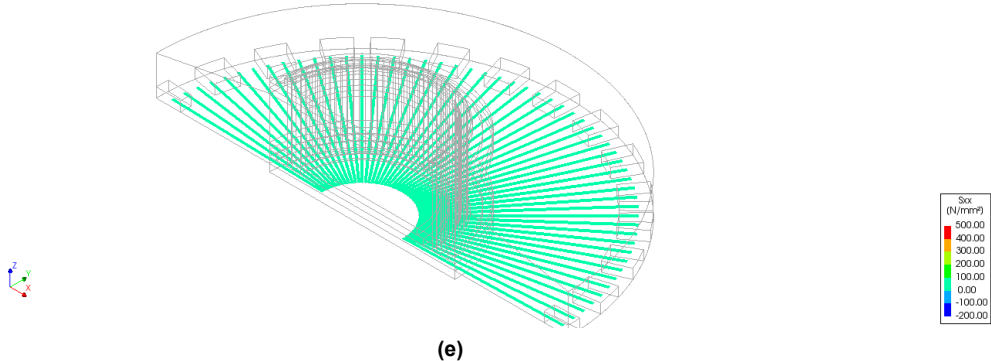


Figure 6.13: Steel stress in the Bottom radial rebars a) Day 0, b) Day 1, c) Day 2

Analysis 1
Phase 1, Time-step 13, Time 0.20000E+00
Reinforcement Cauchy Total Stresses Six layer 1
min: 24.05N/mm² max: 134.85N/mm²



Analysis 1
Phase 1, Time-step 30, Time 0.60000E+00
Reinforcement Cauchy Total Stresses Six layer 1
min: 9.32N/mm² max: 56.88N/mm²



Analysis 1
Phase 1, Time-step 61, Time 0.12200E+07
Reinforcement Cauchy Total Stresses Six layer 1
min: -1.44N/mm² max: 60.02N/mm²

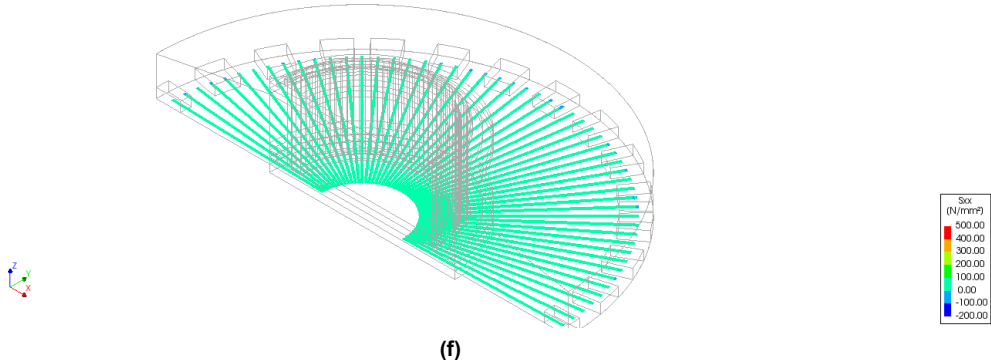
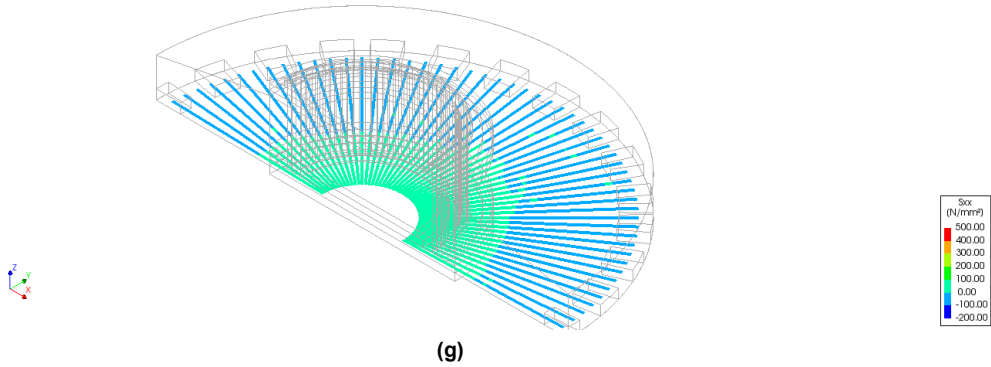
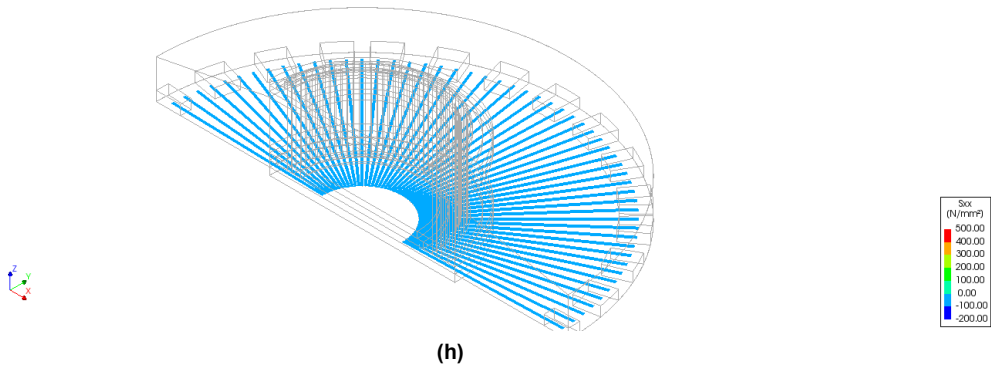


Figure 6.13: Steel stress in the Bottom radial rebars d) Day 3, e) Day 7, f) Day 14

Analysis 1
Phase 1, Time-step 117, Time 0.24250E+07
Reinforcement Cauchy Total Stresses Six layer 1
min: -7.02N/mm² max: 19.47N/mm²



Analysis 1
Phase 1, Time-step 176, Time 0.39000E+07
Reinforcement Cauchy Total Stresses Six layer 1
min: -0.97N/mm² max: 2.22N/mm²



Analysis 1
Phase 1, Time-step 222, Time 0.51000E+07
Reinforcement Cauchy Total Stresses Six layer 1
min: -0.57N/mm² max: 2.21N/mm²

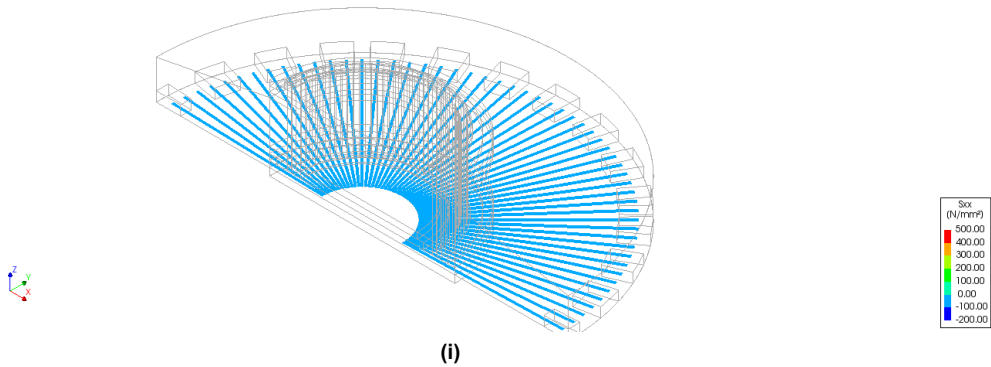
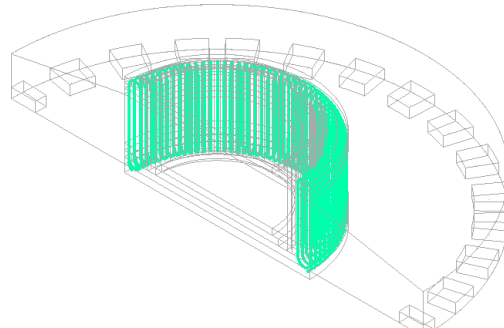


Figure 6.13: Steel stress in the Bottom radial rebars g) Day 28, h) Day 45, i) Day 60

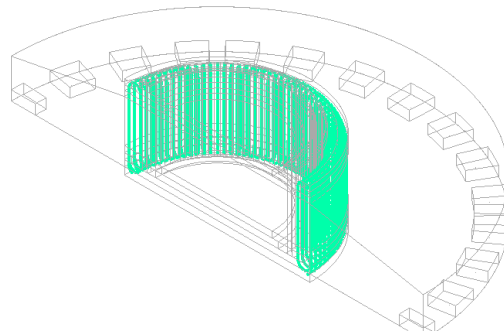
Observation Figure 6.13: The maximum tensile stress in the bottom radial reinforcement is comparatively less than the top since it is not bent near the pedestal. It reaches the maximum tensile stress on Day 2 and experiences a slight amount of compressive stress only after 14 days due to the presence of insulation from the soil it cools down slowly.

Analysis 1
Phase 1, Time-step 1, Time 20000.
Reinforcement Cauchy Total Stresses Six layer 1
min: 11.34N/mm² max: 25.15N/mm²



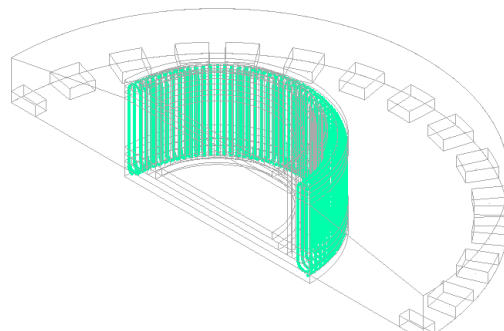
(a)

Analysis 1
Phase 1, Time-step 4, Time 80000.
Reinforcement Cauchy Total Stresses Six layer 1
min: 14.87N/mm² max: 01.02N/mm²



(b)

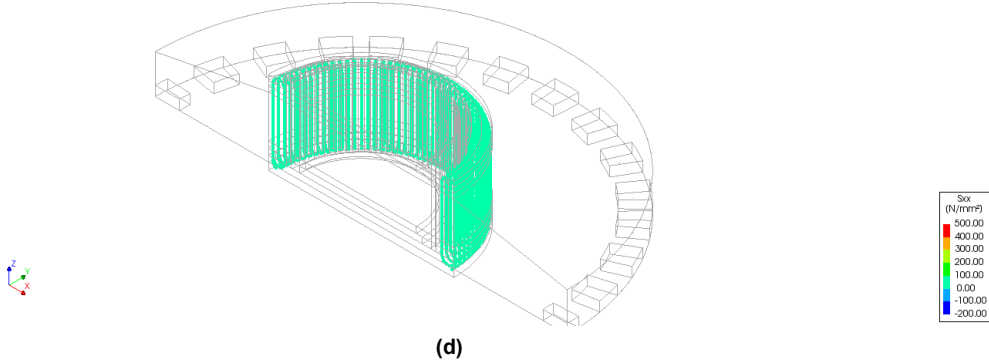
Analysis 1
Phase 1, Time-step 9, Time 0.18000E+06
Reinforcement Cauchy Total Stresses Six layer 1
min: 13.21N/mm² max: 85.71N/mm²



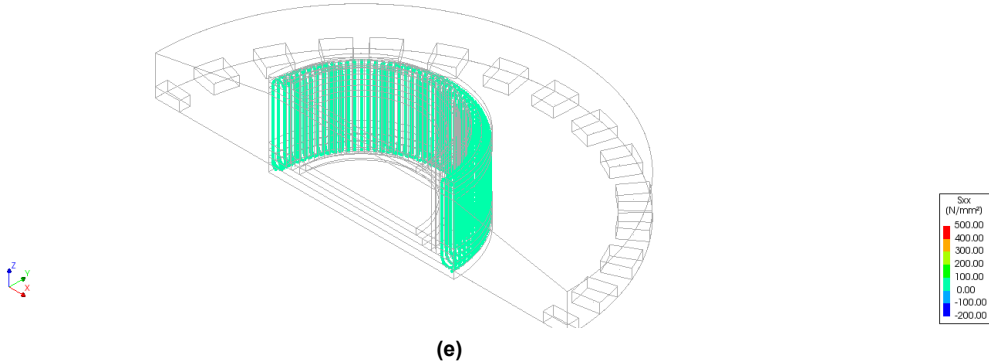
(c)

Figure 6.14: Steel stress in the side stirrups a) Day 0, b) Day 1, c) Day 2

Analysis 1
Phase 1, Time-step 13, Time 0.20000E+06
Reinforcement Cauchy Total Stresses Six layer 1
min: 17.32N/mm² max: 87.21N/mm²



Analysis 1
Phase 1, Time-step 30, Time 0.60000E+06
Reinforcement Cauchy Total Stresses Six layer 1
min: 10.80N/mm² max: 92.41N/mm²



Analysis 1
Phase 1, Time-step 61, Time 0.12200E+07
Reinforcement Cauchy Total Stresses Six layer 1
min: 3.41N/mm² max: 58.28N/mm²

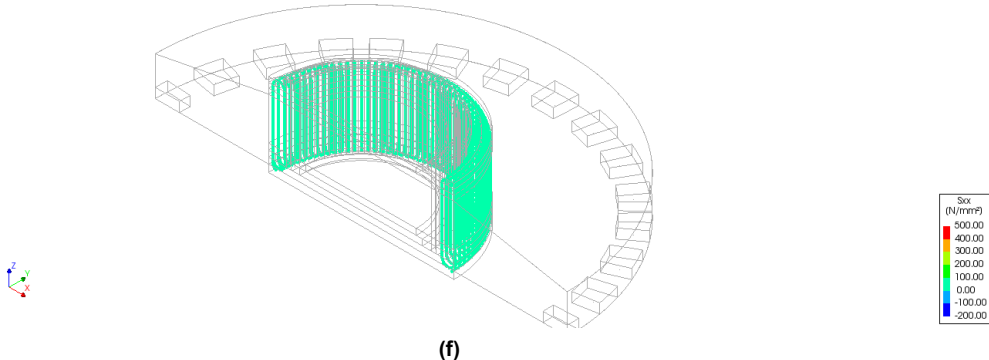
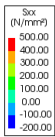
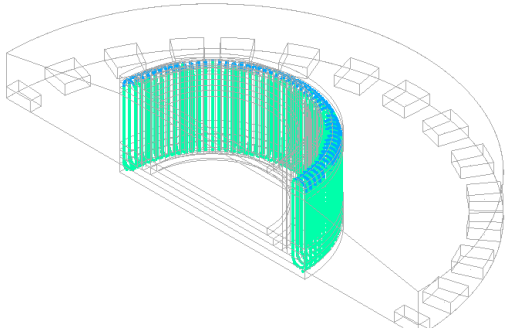


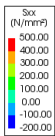
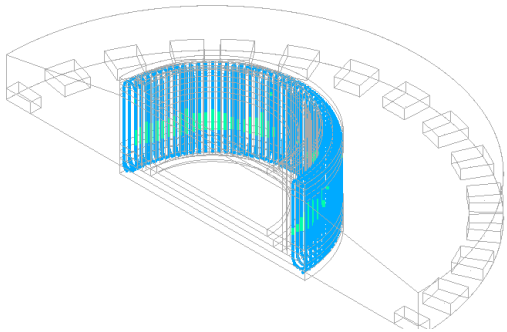
Figure 6.14: Steel stress in the side stirrups d) Day 3, e) Day 7, f) Day 14

Analysis 1
Phase 1, Time-step 117, Time 0.24250E+07
Reinforcement Cauchy Total Stresses Sxx layer 1
min: -2.63N/mm² max: 18.16N/mm²



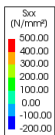
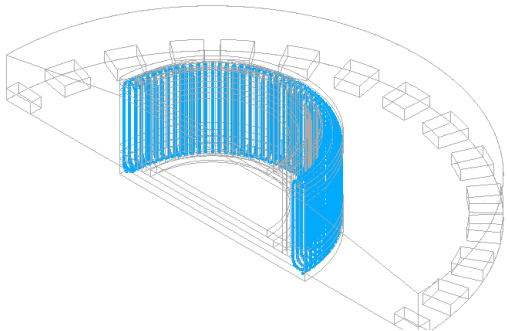
(g)

Analysis 1
Phase 1, Time-step 176, Time 0.39000E+07
Reinforcement Cauchy Total Stresses Sxx layer 1
min: -5.10N/mm² max: 1.40N/mm²



(h)

Analysis 1
Phase 1, Time-step 222, Time 0.51600E+07
Reinforcement Cauchy Total Stresses Sxx layer 1
min: -5.83N/mm² max: -3.17N/mm²



(i)

Figure 6.14: Steel stress in the side stirrups g) Day 28, h) Day 45, i) Day 60

Observation Figure 6.14: The whole stirrup group is in tension due to the hydration heat on day 7 where it also attains maximum tensile stress. A slight amount of compressive stress in the upper corners begins only after 28 days when the foundation is sufficiently cooled down.

Conclusion:

In the current analysis, the rebars containing the FBG sensors are present in the top and bottom positions of the foundation. The top part is considered the low-temperature zone dominated by tensile stresses during the temperature rise phase. As discussed earlier, the temperature gradient between the core and the surface is 35°C , which means that the core has a higher degree of temperature decay than the surface, which has weaker temperature decay as presented in Figure 6.6. Thus, tensile stress is generated because the core region is constrained during contraction by the top and bottom surfaces. In the temperature decay phase, the tensile stresses decrease gradually and compressive stresses begin to occur as described in Figure 6.9-Figure 6.14. The rebars positioned at the bottom side experience lesser heat loss as compared to the top side. This results in delaying the occurrence of compressive stress in the bottom bars. A higher temperature gradient leads to more significant tensile stress inside the foundation, making it more likely to reach the ultimate tensile stress of the concrete and result in cracks. The asymmetrical pattern cracks occur in the structure due to numerical errors since it is not possible to detect the regions with lower tensile strength in FE modeling.

Effects of Combined analysis

This section includes the combined heat and nonlinear structural analysis. In this analysis, the structural calculations are performed at three stages- prestress, vertical load, and wind load after obtaining the results from hydration heat. The below figures depict the results after each load step:

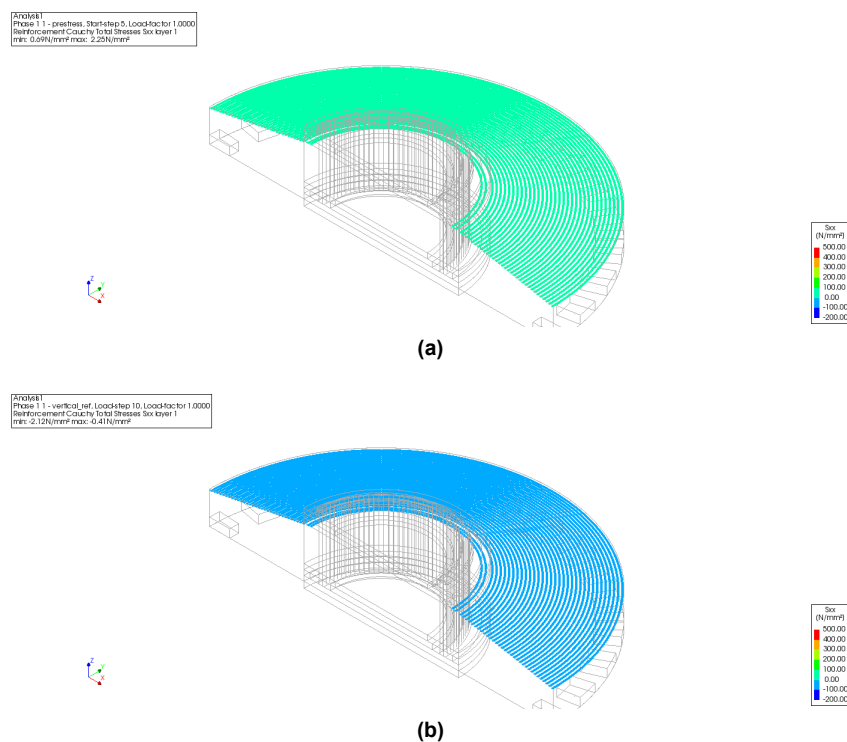


Figure 6.15: Steel stress in the Top tangential rebars a) After prestress, b) After vertical load

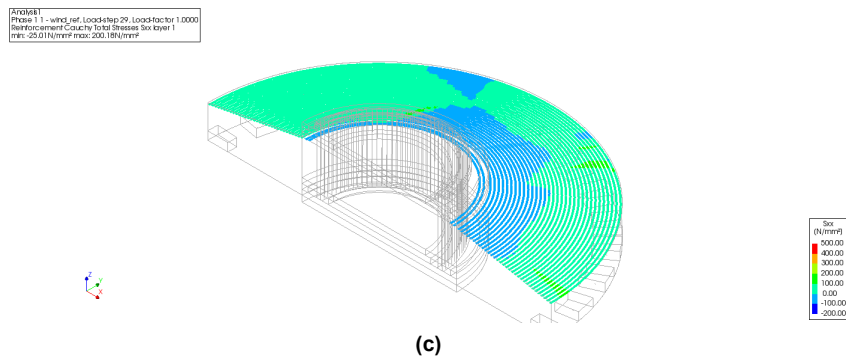


Figure 6.15: Steel stress in the Top tangential rebars c) After wind load

Observation Figure 6.15: When the prestress force is applied to the foundation, it is subjected to the tensile forces only. But after the complete application of the vertical loads, compressive stresses of less magnitude start to develop resulting in both tensile and compressive stress at the end of the wind load. The bars near the pedestal are compressed due to the anchor pretensioning bolts. From the wind directions represented in Figure 6.2, it is observed that the North direction experiences tensile stress, and the south undergoes compressive stresses since the bending moment is applied from North to the south as shown in Figure 3.6.

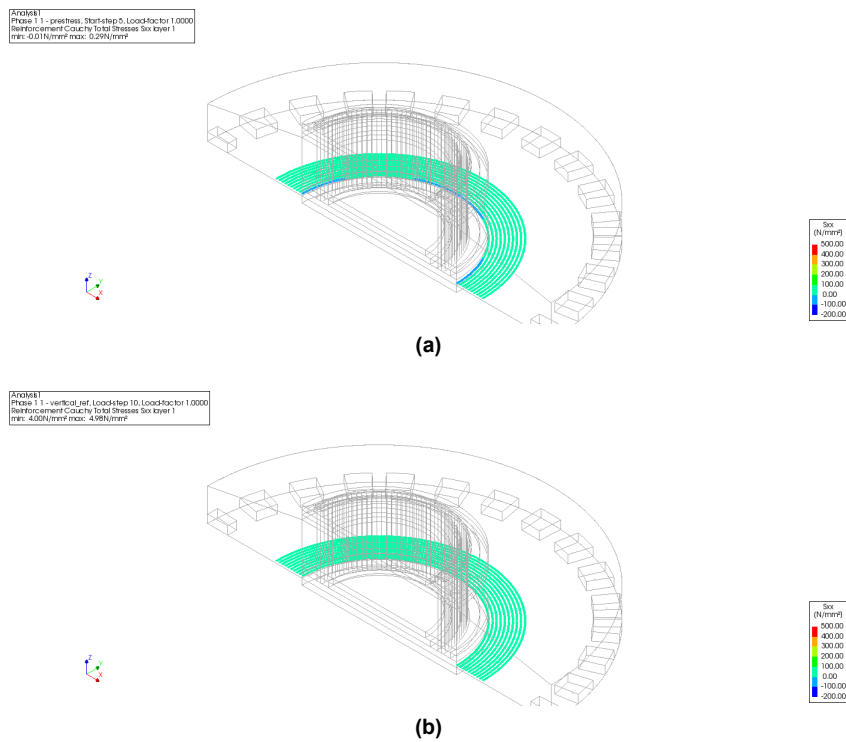


Figure 6.16: Steel stress in the Bottom tangential rebars a) After prestress, b) After vertical load

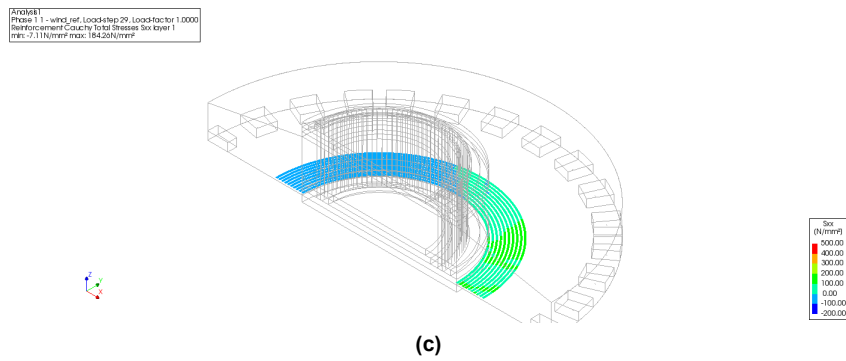


Figure 6.16: Steel stress in the Bottom tangential rebars c) After wind load

Observation Figure 6.16: The bottom tangential rebars near the pedestal experience tension on the south side (prevailing wind direction) and the north side experiences compression after the wind load step. This is logical since the bottom portion will experience stress opposite to the top side. It experiences less stress than the ones near the piles.

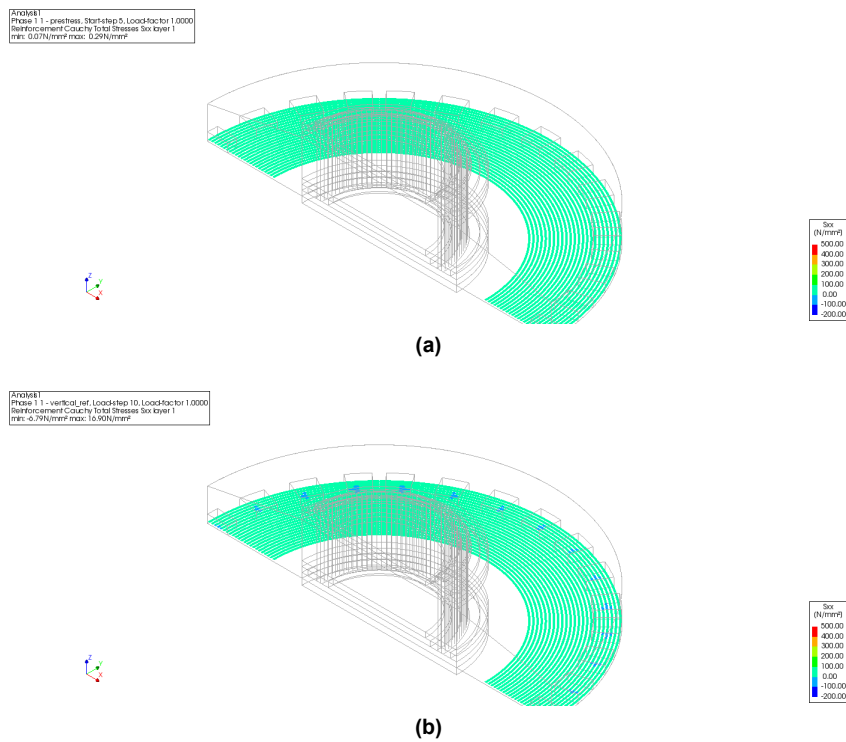


Figure 6.17: Steel stress in the Bottom tangential rebars near piles a) After prestress, b) After vertical load

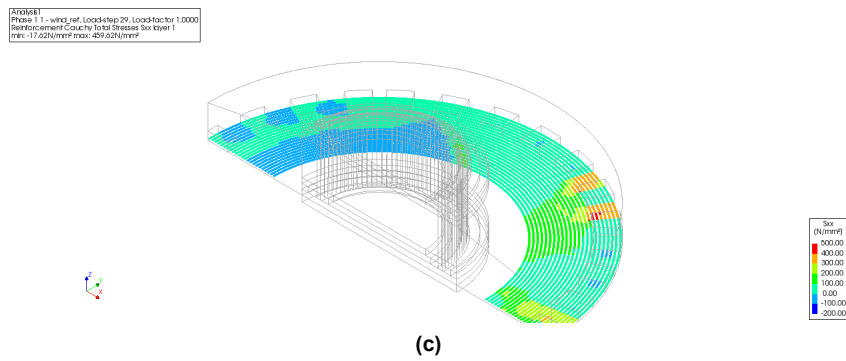


Figure 6.17: Steel stress in the Bottom tangential rebars near piles c) After wind load

Observation Figure 6.17: Tangential bars near the piles experience comparatively more stress in the reinforcements as compared to the inner steel group. It starts to experience compression in the areas where there are piles due to the applied reaction force from the piles resulting from the applied vertical load. After the applied wind load bending moment, it undergoes tension in the south region (location C) and it is observed that in some areas the stress is more. Since the pile introducers are modeled as linear elastic to avoid local failure, the bottom bars experience more stress due to this.

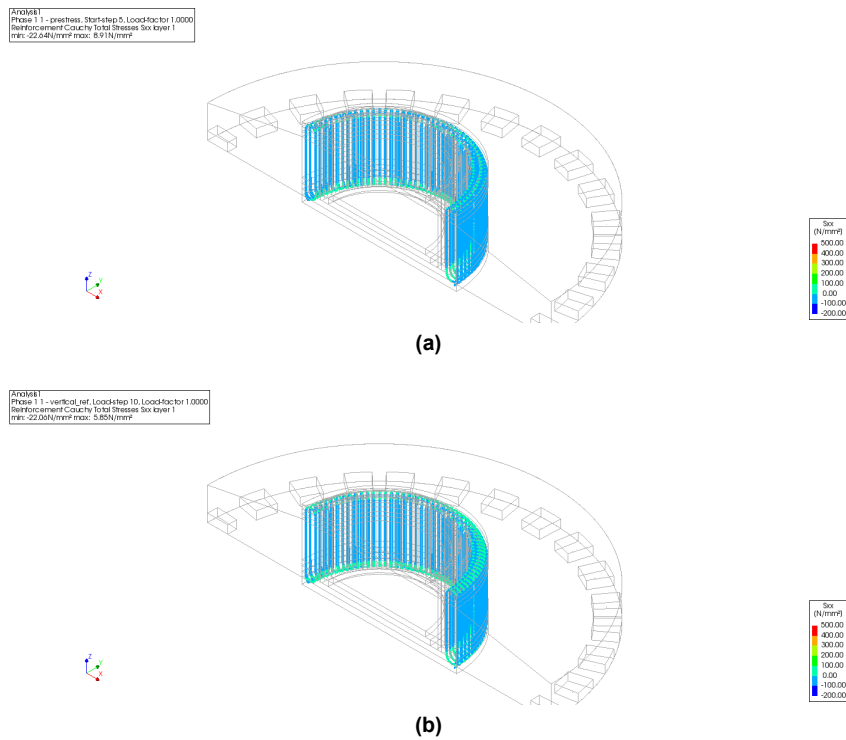


Figure 6.18: Steel stress in the stirrups a) After prestress, b) After vertical load

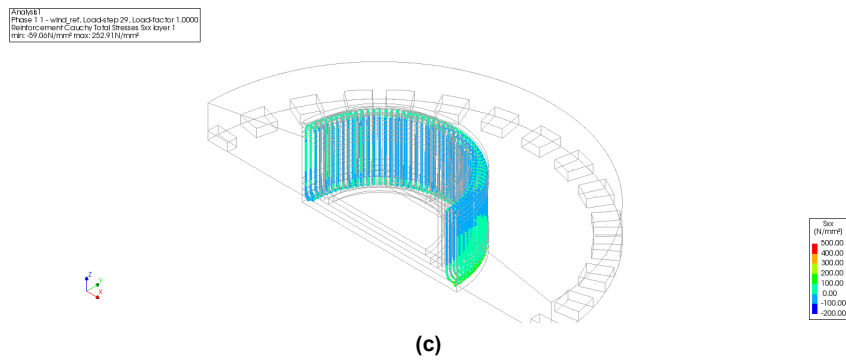


Figure 6.18: Steel stress in the stirrups c) After wind load

Observation Figure 6.18: The vertical stirrups are present near the anchor cage, which experiences compressive stresses due to the applied anchor pretension forces. When the wind load is applied, the vertical bars experience both compressive and tensile stresses depending on the position of the stirrups. Due to the applied direction of the wind load and the bending moment, the bars located in the north direction experience tensile stresses on the top location and the bars near the south undergoes tension in the bottom part.

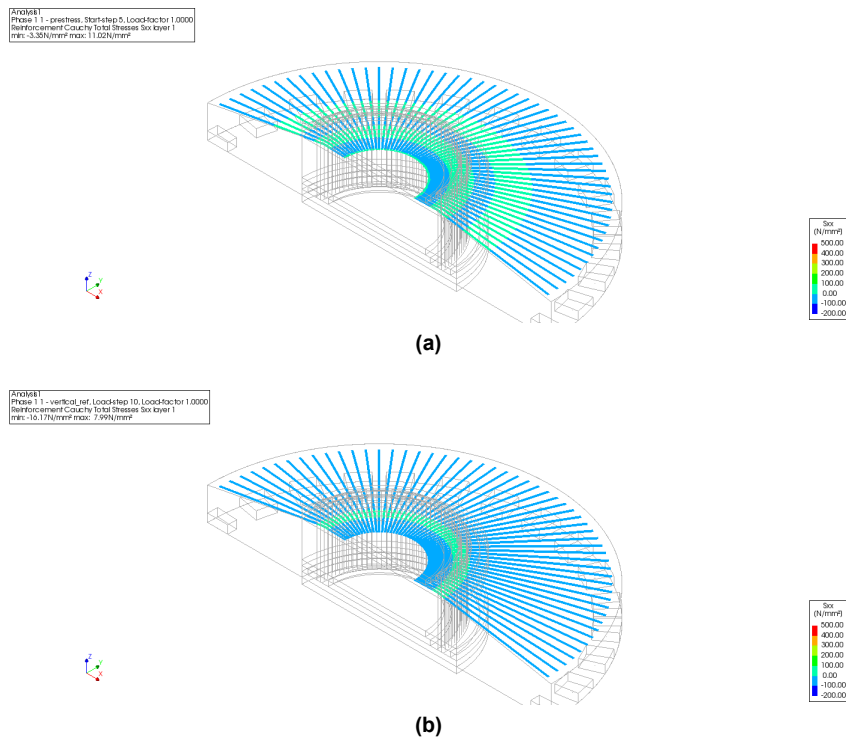


Figure 6.19: Steel stress in the Top radial rebars a) After prestress, b) After vertical load

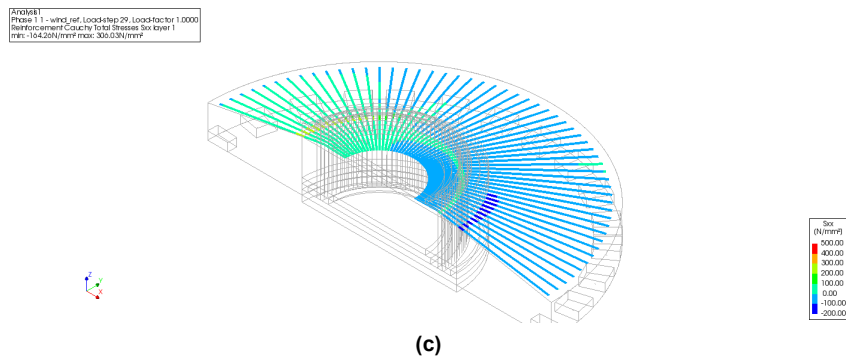


Figure 6.19: Steel stress in the Top radial rebars c) After wind load

Observation Figure 6.19: The top radial bars experience tensile stress at the position of bends near the pedestal in the bars. The bend in the bar is illustrated in Figure 5.19. After the application of the wind load, the reinforcements in the primary wind direction (south) experience compressive stress while the steel rebars in the opposite direction (north) undergo tensile stress since the overturning bending moment is acting from the North to the South. The behavior of the occurring stresses is logical. Due to the asymmetrical stress distribution pattern in the model, there are higher concentrated stresses in the radial bars.

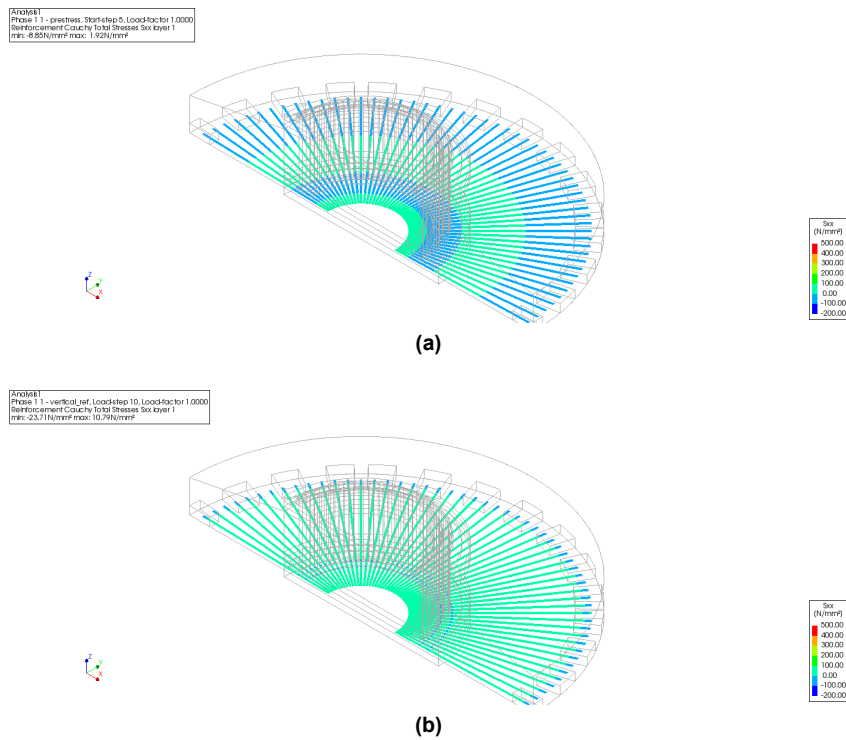


Figure 6.20: Steel stress in the Bottom radial rebars a) After prestress, b) After vertical load

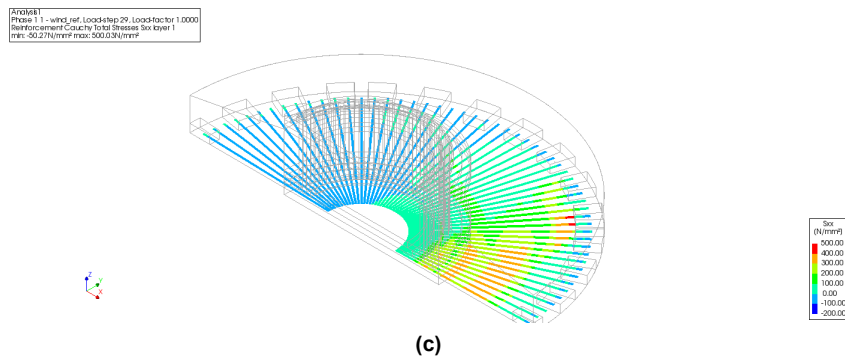


Figure 6.20: Steel stress in the Bottom radial rebars c) After wind load

Observation Figure 6.20: In the case of the bottom radial bars, after applying the vertical loads, the reinforcements near the piles experience compressive stress while the other portions have tensile stresses. After applying the wind load, the North side experience compressive stresses while the south side undergoes tensile stress. This is logical as the direction of the occurring stress is opposite to that of the top. Some areas have more stress concentrated in those regions due to the additional stress coming from the piles.

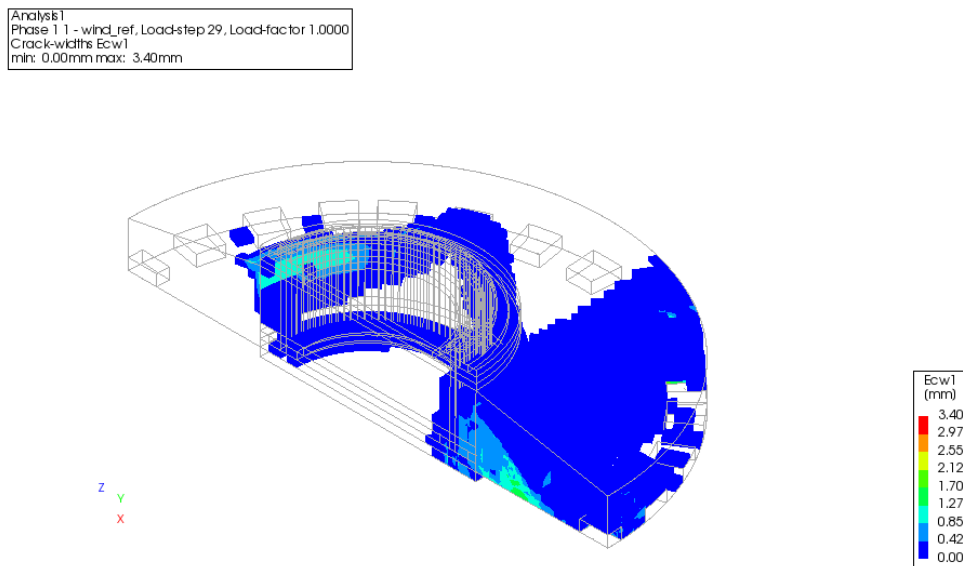


Figure 6.21: Crack patterns

Table 6.6: Comparison between the Field measurement and DIANA Model 1

Measuring Locations	Directions	Field Measurement 2017		Model 1	
		Tensile stress (MPa)	Compressive stress (MPa)	Tensile stress (MPa)	Compressive stress (MPa)
L01	A	182.21	-118.53	-	-
	B	10.66	-20.16	-	-
	C	117.07	-160.99	-	-
	D	-	-	-	-
L02	A	21.97	-12.47	247.42	-
	B	5.1	-3.4	-	-17.85
	C	15.4	-19.94	-	-73.67
	D	3.06	-4.68	-	-
L03	A	3.13	-1.87	8.49	-
	B	1.08	-0.76	-	-3.91
	C	3.13	-4.13	-	-18.4
	D	0.7	-1.15	-	-
L04	A	4.64	-2.94	19.67	-
	B	1.32	-0.92	-	-9.62
	C	3.7	-5.1	-	-15.056
	D	0.96	-1.42	-	-
L05	A	5.04	-7.5	-	-16.79
	B	1.67	-2.33	58.67	-
	C	8.96	-6.04	271.67	-
	D	2.23	-1.55	-	-
L06	A	2.12	-2.9	-	-3.26
	B	0.85	-1.19	68.13	-
	C	3.13	-1.99	99.74	-
	D	0.94	-0.68	-	-
L07	A	2.49	-1.13	4.99	-
	B	0.5	-0.38	-	-8.44
	C	0.82	-0.73	-	-15.64
	D	0.25	-0.33	-	-
L08	A	1.46	-2.17	1.47	-
	B	0.61	-0.81	6.03	-
	C	2.09	-1.39	120.76	-
	D	0.76	-0.5	-	-

Conclusion: From the Figure 6.15-Figure 6.20, it is evident that the behavior of the stresses in the reinforcements depends on the direction of the applied bending moment. The stress concentration at the bottom bars in some locations is more due to the extra stresses from the piles that are introduced in the foundation as concrete linear elastic. From Table 6.6, it can be deciphered that the steel stresses even after applying the hydration heat in the concrete foundation, are higher than the measurements by a factor of up to 56. Between the results of Table 6.6 and Table 5.8, the difference between Model 0 and Model 1 is about 3-35%. In accordance with [3], the tangential bars experience less stress than the radial ones. Also, Figure 6.21 shows the crack width in the foundation which is high and needs some minimization to match the conditions of the real structure as described in section 3.5. In order to study the outcome of other effects in the wind turbine foundation, a series of modifications are performed in the DIANA model in

the coming sections.

6.4. Effect of varying Maturity

This section describes the effects of varying maturity effect after 28 days of concrete hardening. Since after applying the hydration heat effect in subsection 6.3.1, the stresses in the reinforcements are much higher than what is detected, additional changes have been made in the maturity index. Now, instead of keeping the maturity values constant after 28 days, it is now varying with time even after 28 days. This change is done to increase the strength of the foundation even if it's more or less 5%. The graphs for the updated maturity effects are presented in the figures below:

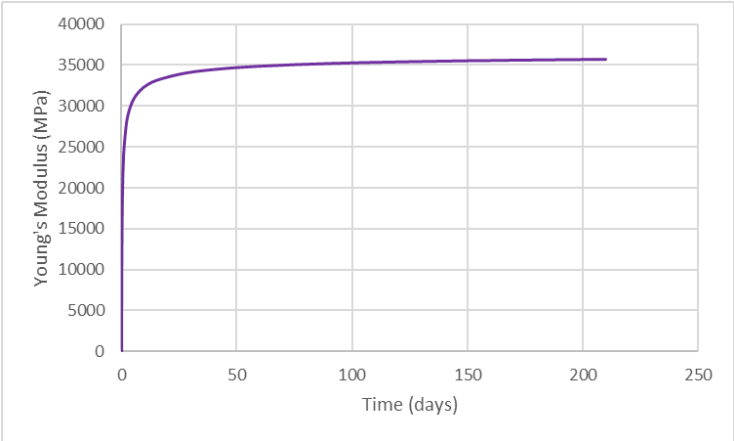


Figure 6.22: Maturity-Young's modulus graph for C35/45

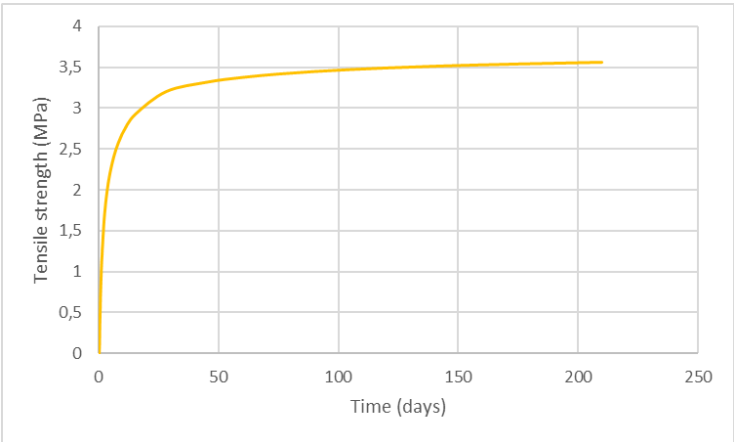


Figure 6.23: Maturity-Tensile strength graph for C35/45

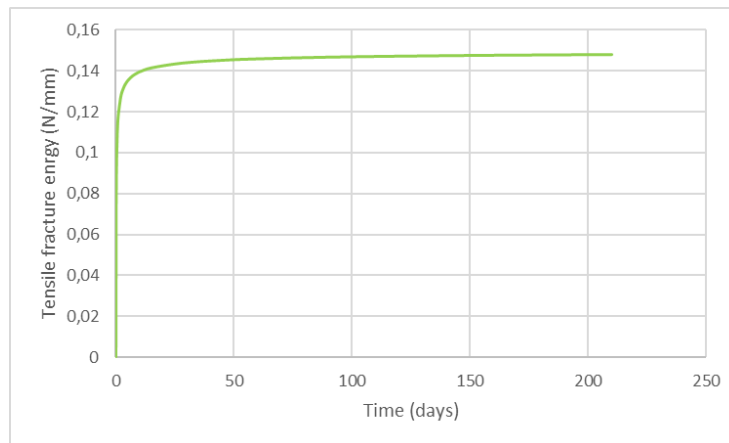


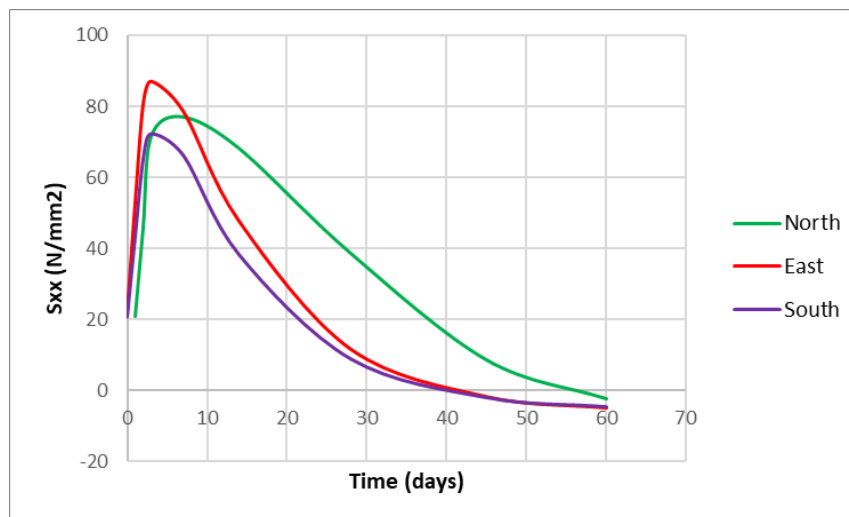
Figure 6.24: Maturity-Tensile fracture energy graph for C35/45

6.4.1. Results of Variant 2

Variant 2 contains the same hydration heat constants as Variant 1 and only the material properties have changed. Since the heat transfer coefficient remains unchanged in the model, the temperature evolution inside the foundation is the same as in Variant 1.

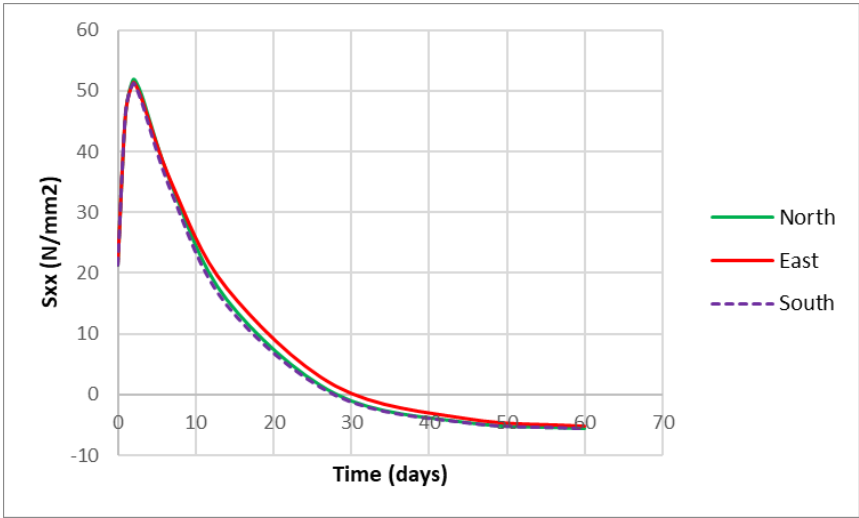
Steel stresses due to the Hydration heat

The stresses generated in the reinforcement groups due to the effect of hydration heat vary for different rebar positions in the foundation. Since the heat transfer coefficient for both Models 1 and 2 are the same, the stress generated is the same in both cases. In subsection 6.3.1, a comparison is depicted about the innermost and outermost nodes in the rebars where it is shown that the nodes closer to the pedestal in the radial bars undergo larger stress and the nodes in the outer region experience change in peaks in consideration with the change in boundary conditions. Similarly, another comparison is made between top and bottom reinforcement groups in Figure 6.8 where it is noticed that both bottom radial and tangential bars experience more stress than the steel bars in the top part because bottom reinforcements experience higher stress due to the complete load of the structure. In the current section, an overview of the steel stress over the period of time at each wind direction is presented.

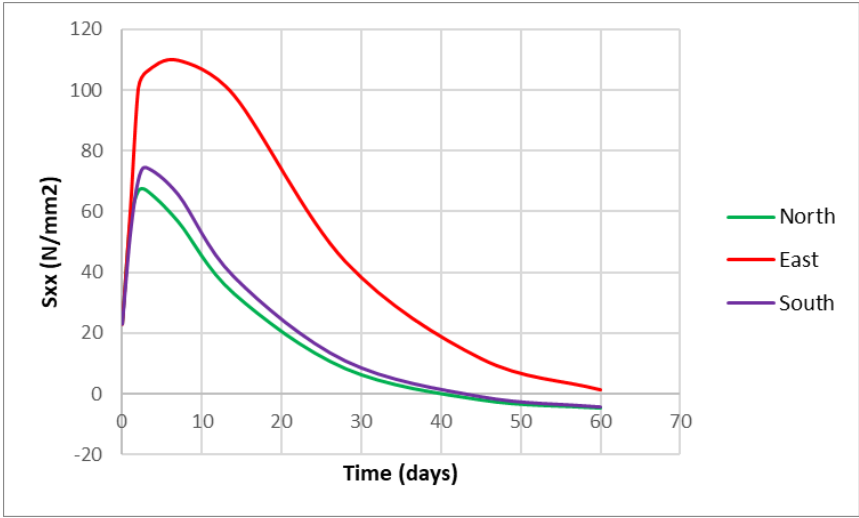


(a)

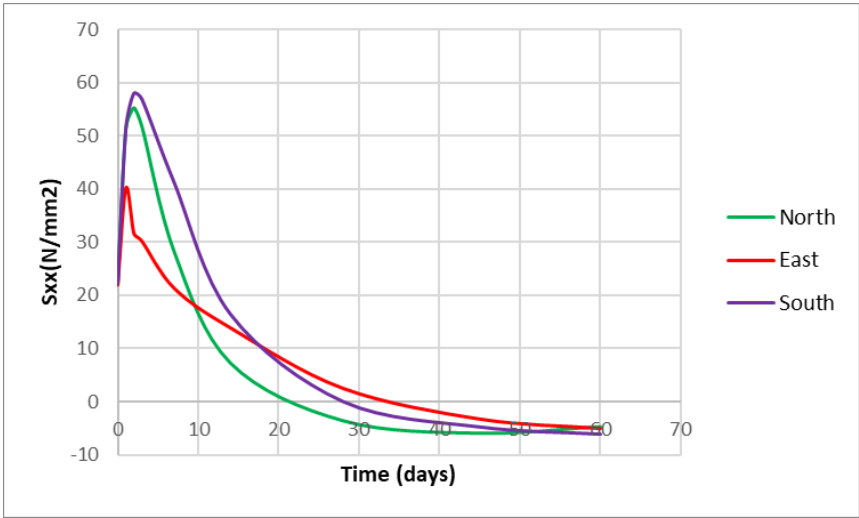
Figure 6.25: Steel stress wrt time at each wind directions a) Top radial



(b)



(c)



(d)

Figure 6.25: Steel stress wrt time at each wind directions b) Bottom radial, c) Top tangential, d) Bottom tangential

In the above figure, the top radial and tangential steel bars experience higher stress in the East direction (at location B). For the bottom radial bars, the stress generated at every location is the same while when it comes to the bottom tangential both North and South (locations A and C) experience more stress as compared to the direction East. The wind directions are shown in Figure 6.2. This uneven distribution of steel stresses is observed in each wind direction due to the numerical errors in the FE software. These numerical errors have also caused asymmetric patterns in the reinforcement groups as shown in Figure 6.9 - Figure 6.14.

Effects of Combined analysis

This section includes the combined heat and nonlinear structural analysis of Model 2. In this analysis, the structural calculations are performed at three stages- prestress, vertical load, and wind load after obtaining the results from hydration heat. Since the maturity effect now varies with time after 28 days of hardening, the steel stresses at the end of wind loading are different. The below figures depict the results of the difference between steel stress in Model 1 and Model 2:

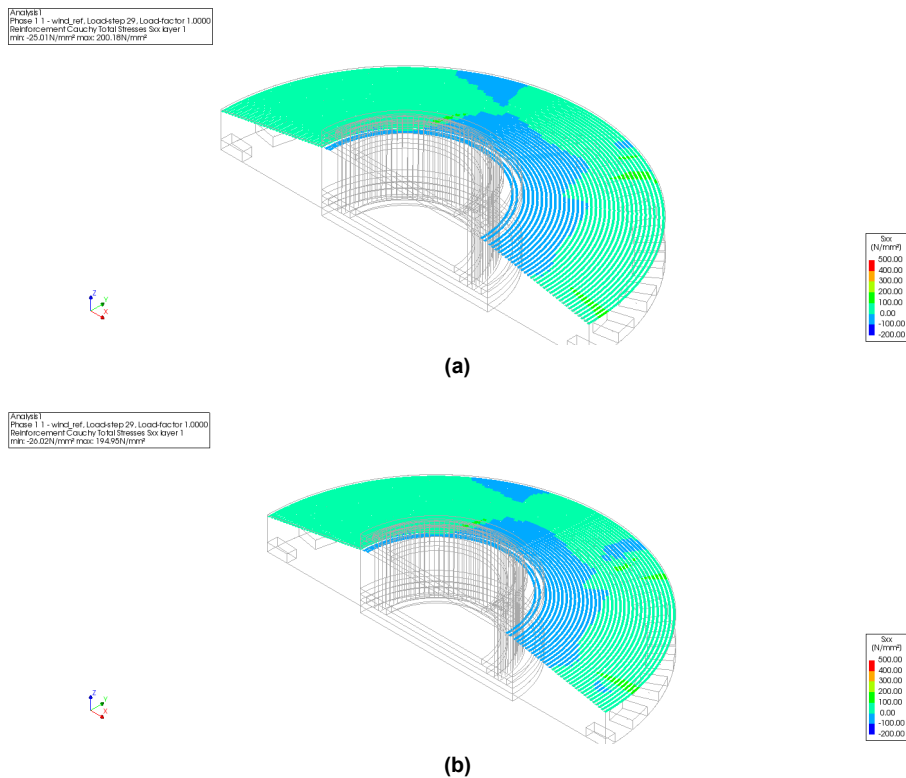


Figure 6.26: Steel stress in the Top tangential rebars a) Model 1, b) Model 2

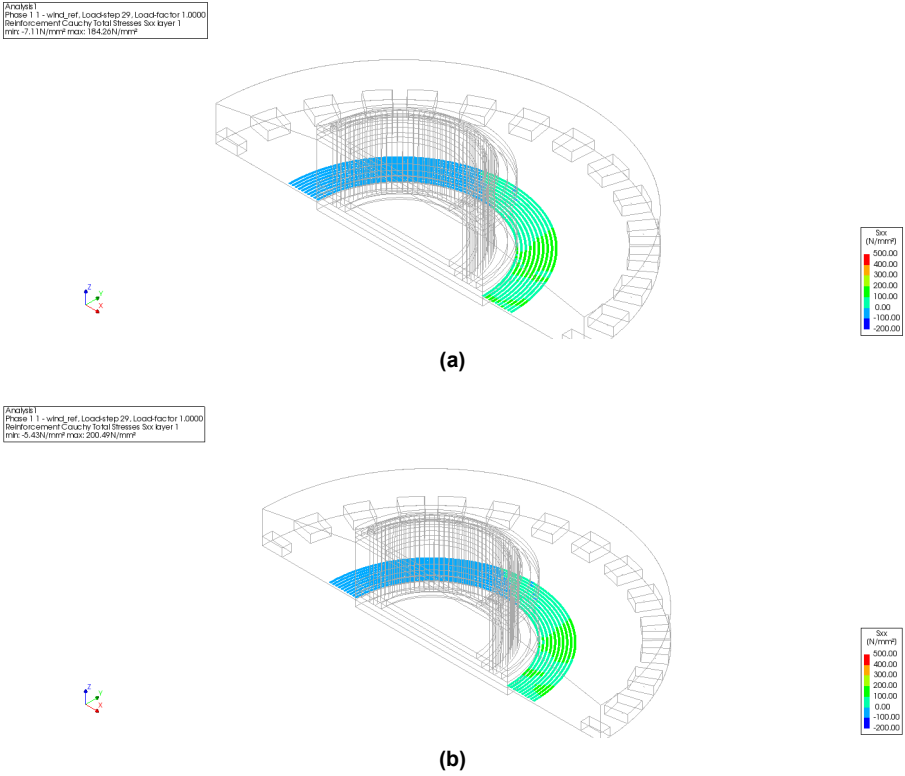


Figure 6.27: Steel stress in the Bottom tangential rebars a) Model 1, b) Model 2

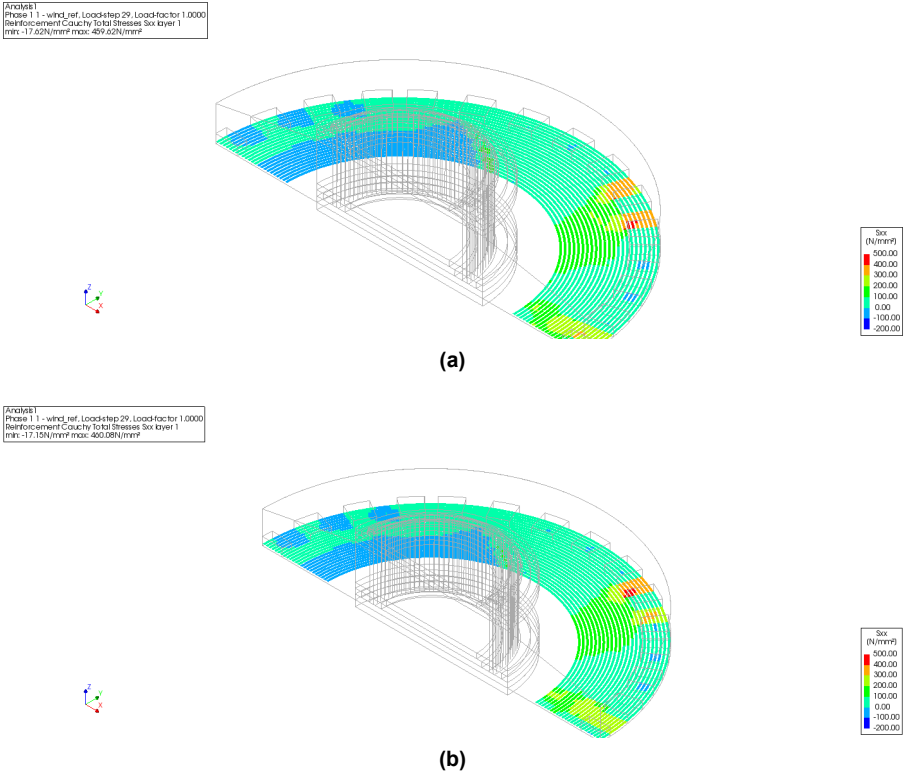


Figure 6.28: Steel stress in the Bottom tangential rebars near piles a) Model 1, b) Model 2

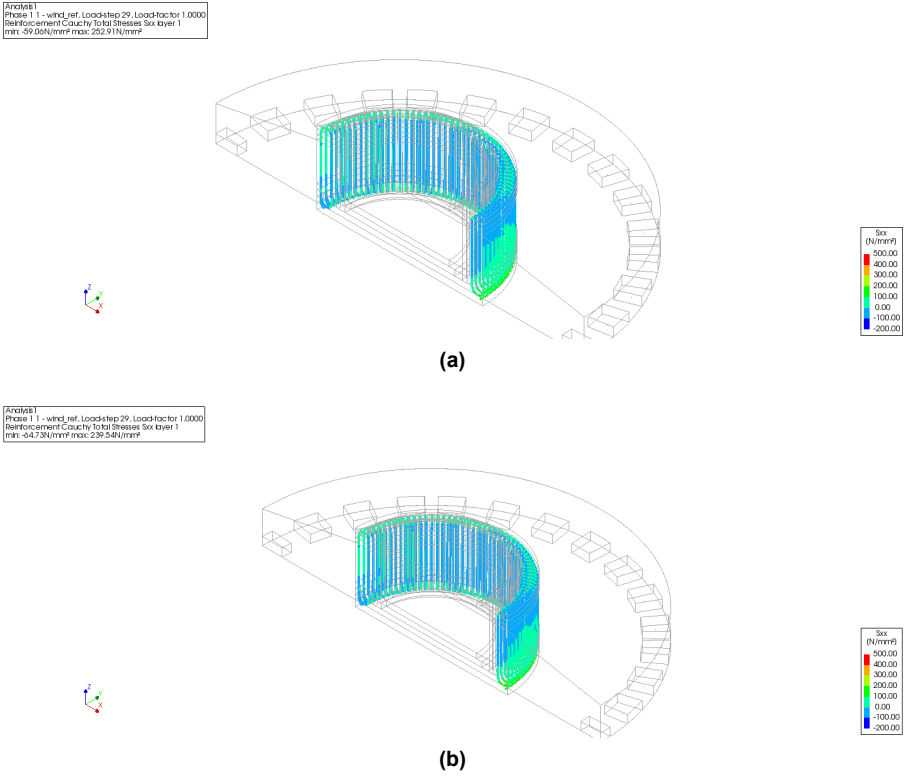


Figure 6.29: Steel stress in the stirrups a) Model 1, b) Model 2

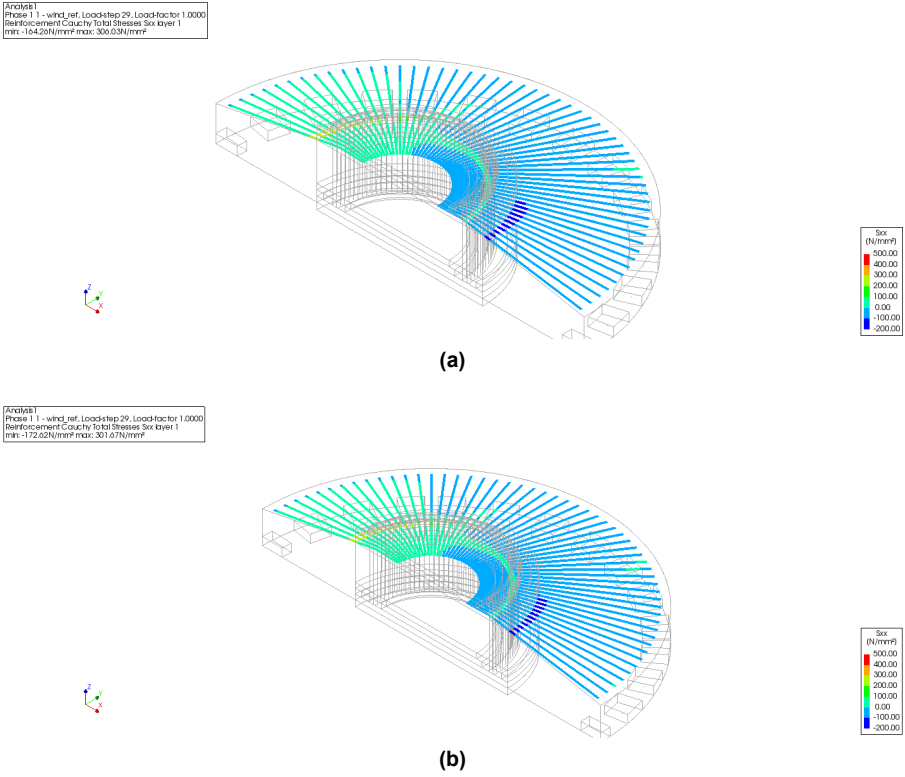


Figure 6.30: Steel stress in the Top radial rebars a) Model 1, b) Model 2

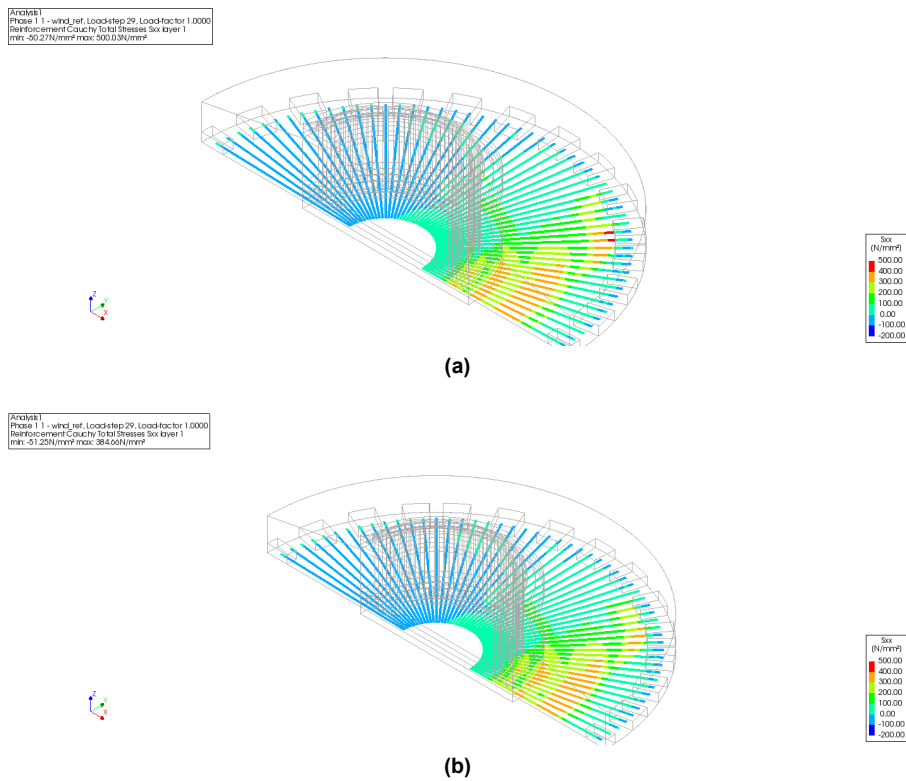


Figure 6.31: Steel stress in the Bottom radial rebars a) Model 1, b) Model 2

Conclusion: With the increase in the maturity effect over time, the steel stress at different locations reduces comparatively. This reduction for all the locations is around 4-42% when compared with Model 1. Rebars at the top location experience a reduction of up to 32% whereas, at the bottom location the decrease is up to 42%. The stresses in the reinforcements form an asymmetrical pattern in both Models 1 and 2 due to the asymmetrical load distribution. In the case of the top radial bars, higher stresses have occurred near the region of the bends. The bottom bars experience higher stresses due to the effect of extra stresses coming from the piles which are modeled as linear elastic to avoid local failure. From Table 6.7, the steel stresses at certain locations, specifically the top tangential (L03) and bottom tangential (L06 and L08), were found to be up to three times higher than the field measurements for most wind directions, North and East. On the other hand, locations like the top radial (L02) and bottom radial (L05) showed steel stresses that were up to 10-30 times higher than the experimental results. Hence the model needs more modifications.

Table 6.7: Comparison between the Field measurement and DIANA Model 2

Measuring Locations	Directions	Field Measurement 2017		Model 2	
		Tensile stress (MPa)	Compressive stress (MPa)	Tensile stress (MPa)	Compressive stress (MPa)
L01	A	182.21	-118.53	-	-
	B	10.66	-20.16	-	-
	C	117.07	-160.99	-	-
	D	-	-	-	-
L02	A	21.97	-12.47	245.023	-
	B	5.1	-3.4	-	-17.745
	C	15.4	-19.94	-	-76.571
	D	3.06	-4.68	-	-
L03	A	3.13	-1.87	8.18	-
	B	1.08	-0.76	-	-2.67
	C	3.13	-4.13	-	-14.79
	D	0.7	-1.15	-	-
L04	A	4.64	-2.94	19.262	-
	B	1.32	-0.92	-	-9.157
	C	3.7	-5.1	-	-14.443
	D	0.96	-1.42	-	-
L05	A	5.04	-7.5	-	-16.27
	B	1.67	-2.33	58.16	-
	C	8.96	-6.04	281.67	-
	D	2.23	-1.55	-	-
L06	A	2.12	-2.9	-	-3.18
	B	0.85	-1.19	59.92	-
	C	3.13	-1.99	57.66	-
	D	0.94	-0.68	-	-
L07	A	2.49	-1.13	4.95	-
	B	0.5	-0.38	-	-12.68
	C	0.82	-0.73	-	-15.507
	D	0.25	-0.33	-	-
L08	A	1.46	-2.17	1.468	-
	B	0.61	-0.81	6.14	-
	C	2.09	-1.39	121.506	-
	D	0.76	-0.5	-	-

6.5. Effect of reducing thermal gradient

In the previous sections, it has been noticed that the stresses in the reinforcements group reduce as the strength of the foundation increases. In order to increase the strength of the structure, this section will enumerate the effects of reducing the temperature gap between the core and the topmost surface that will lead to lesser thermal cracks and hence stiffer structure. Since variant 2 reduces the steel stress up to 42%, variant 3 will also include varying maturity along with modified HTC's.

6.5.1. Results of Variant 3

This model describes the combined nonlinear structural analysis and the hydration heat effect for the third variant. This includes the varying maturity values after 28 days of concrete hardening and the updated heat transfer coefficients. In the last model subsection 6.4.1, it is observed that by increasing the maturity values for Young's modulus, tensile strength, and fracture energy there has been a slight change in the steel stresses after the applied wind load. Hence, now the heat transfer coefficients are adjusted such that it reduces the temperature gap between the core and the outermost surface. In this model, the values used for the heat transfer coefficient are provided in Table 6.3 as HTC 2. The procedure for performing transient heat and structural analysis is the same as mentioned in subsection 6.3.1.

Temperature evolution in the concrete foundation

From the transient heat analysis in DIANA, it is observed that adjusting the heat transfer coefficient to an extent where the temperature gap reduces, also changes the behavior of the heat exchange of the foundation with the environment. Similar to subsection 6.3.1, the foundation core attains a maximum temperature on day 3, but this time the core reaches a slightly lower temperature of 61.03 °C, and after that, it slowly cools down. In this case, the main difference lies in the amount of surface which cools down over a certain time period. A comparison is shown in Figure 6.33 and Figure 6.34. In Figure 6.34, the dashed line represents nodes at different positions of the foundation in Variant 1 while the solid line depicts Variant 3 of section II-II (middle section) from Figure 6.4. As it is clear from the graph, that variant 3 reaches a lower maximum temperature as compared to variant 1, and the high thermal inertia of the foundation retains temperatures as high as 29 °C for at least 28 days. The results of the numerical analysis are described in Figure 6.32.

Analysis1
Phase 1.1, Time-step 1, Time 20000.
Temperatures PTE
min: 21.73°C max: 33.24°C

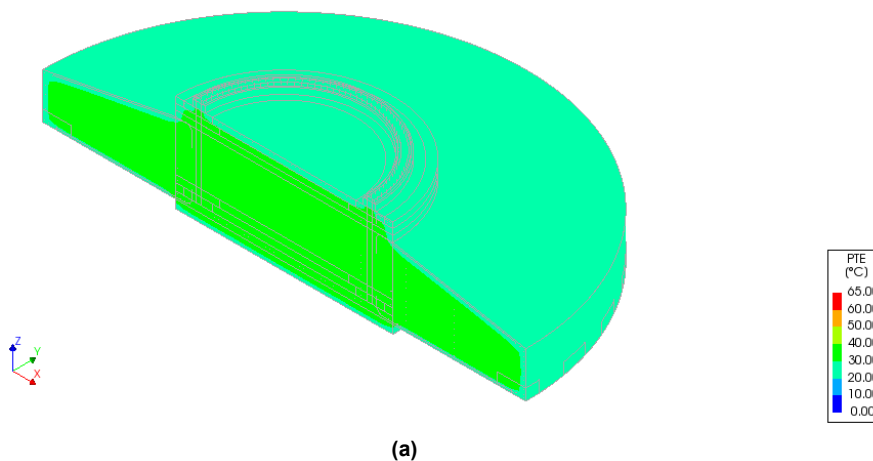
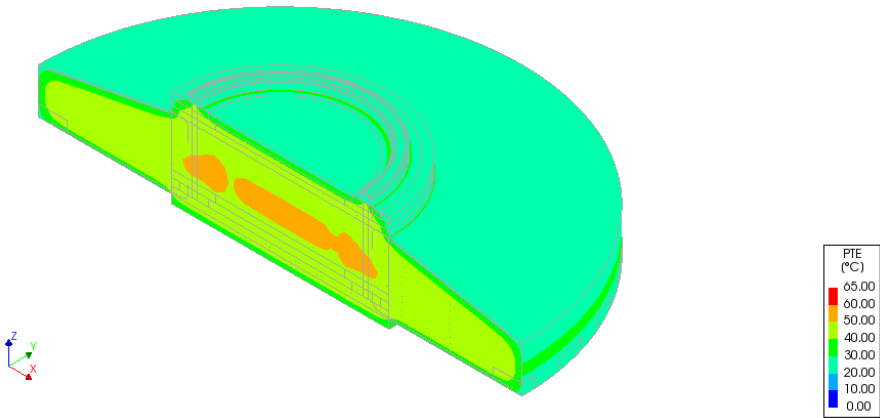


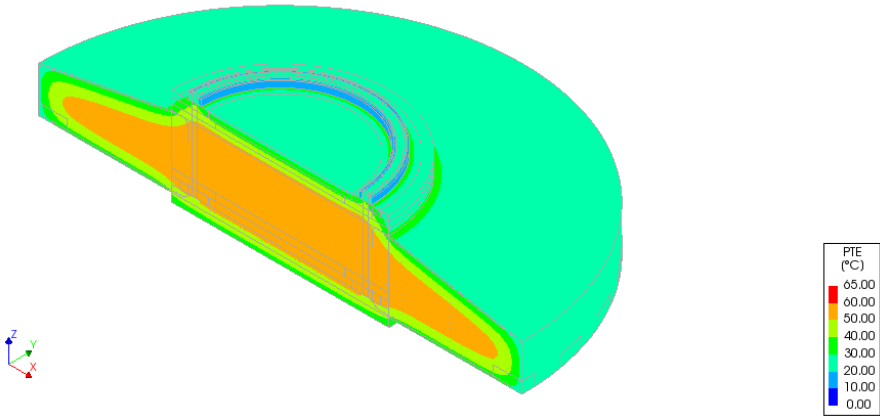
Figure 6.32: Temperature Evolution in concrete foundation a) Day 0

Analysis1
Phase 1.1, Time-step 4, Time 80000.
Temperatures PTE
min: 20.00°C max: 50.22°C



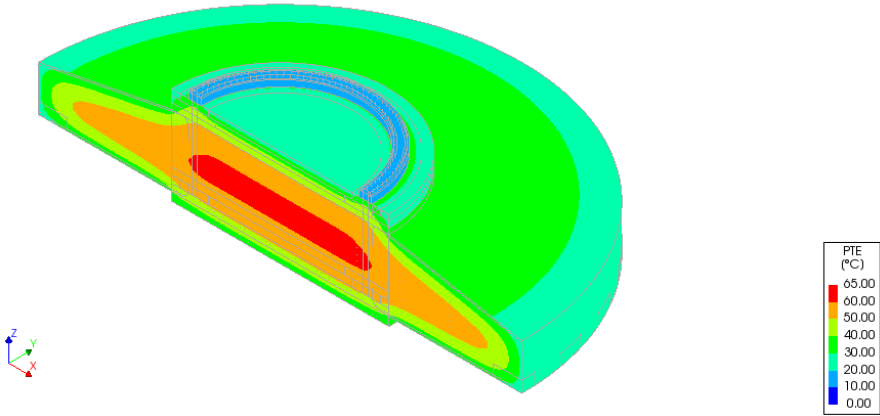
(b)

Analysis1
Phase 1.1, Time-step 9, Time 0.18000E+06
Temperatures PTE
min: 18.78°C max: 59.20°C



(c)

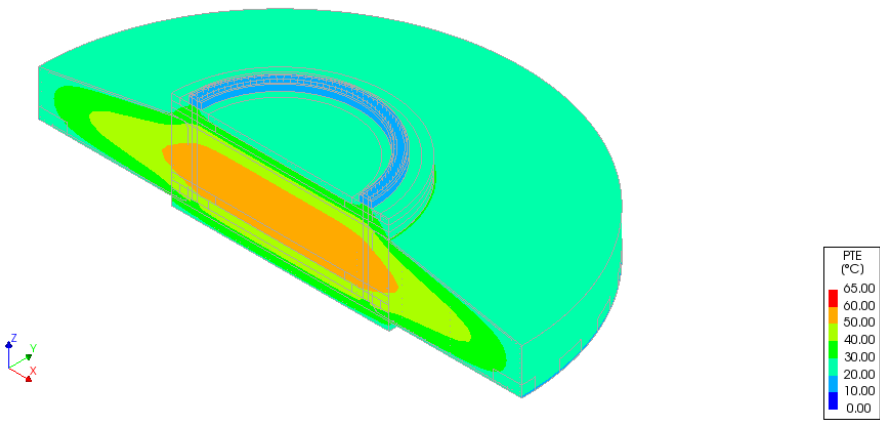
Analysis1
Phase 1.1, Time-step 13, Time 0.20000E+06
Temperatures PTE
min: 18.33°C max: 61.03°C



(d)

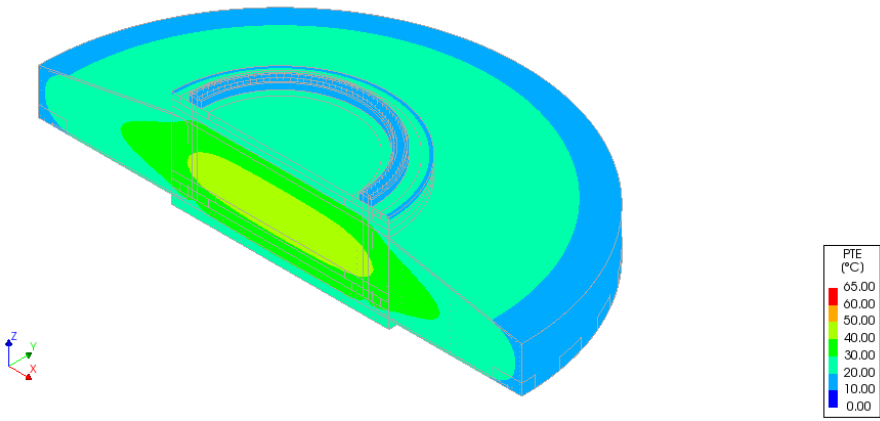
Figure 6.32: Temperature Evolution in concrete foundation b) Day 1, c) Day 2, d) Day 3

Analysis1
Phase 1.1, Time-step 30, Time 0.60000E+06
Temperatures PTE
min: 17.68°C max: 57.50°C



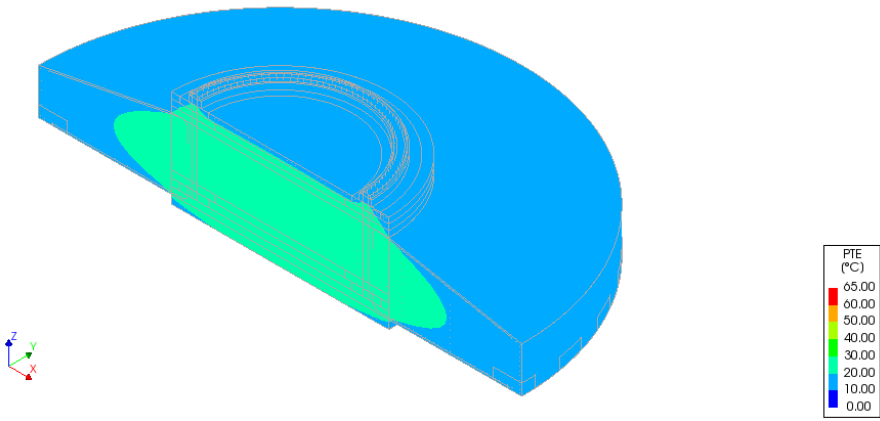
(e)

Analysis1
Phase 1.1, Time-step 61, Time 0.12200E+07
Temperatures PTE
min: 17.52°C max: 44.78°C



(f)

Analysis1
Phase 1.1, Time-step 117, Time 0.24250E+07
Temperatures PTE
min: 17.47°C max: 29.01°C



(g)

Figure 6.32: Temperature Evolution in concrete foundation e) Day 7, f) Day 14, g) Day 28

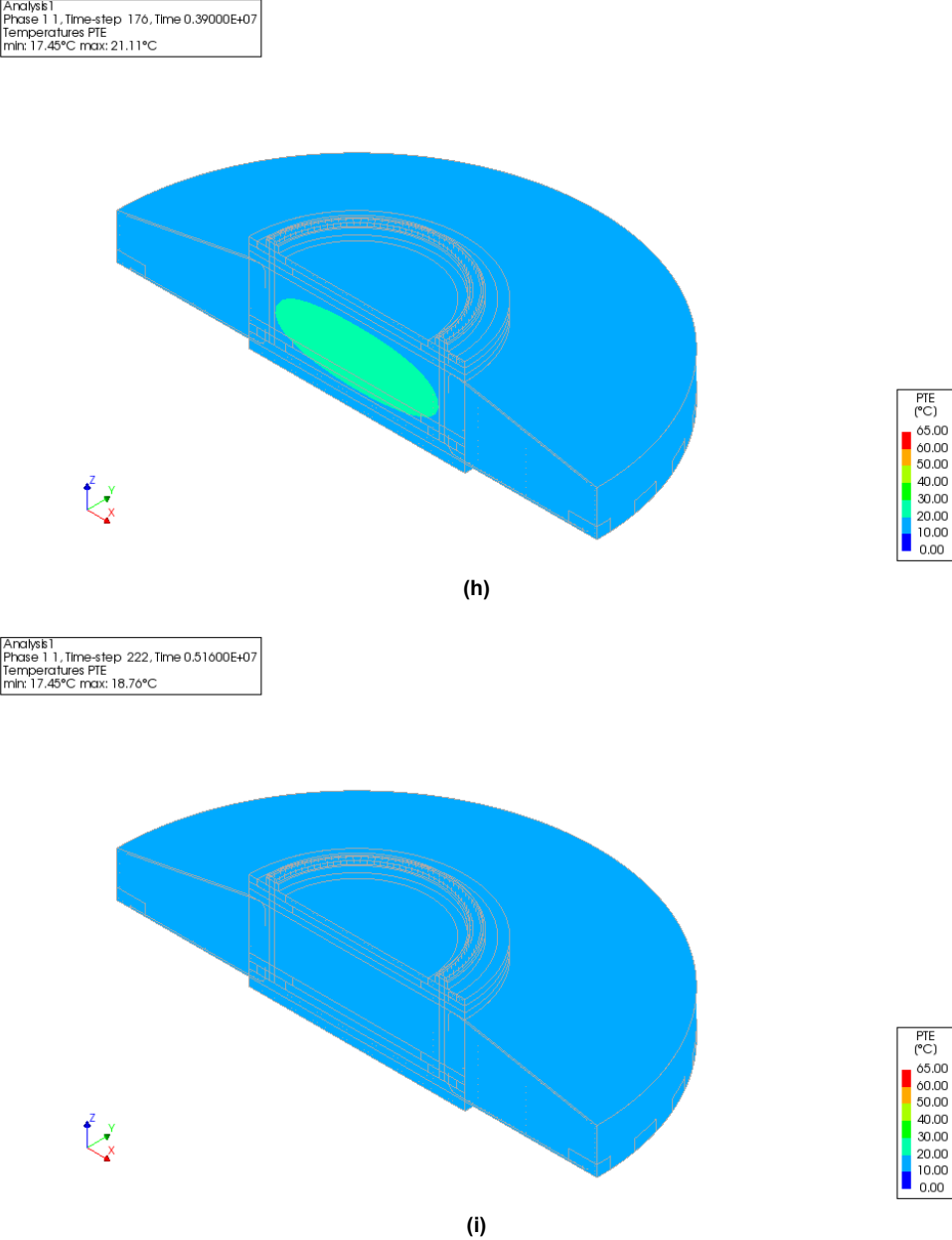


Figure 6.32: Temperature Evolution in concrete foundation h) Day 45, i) Day 60

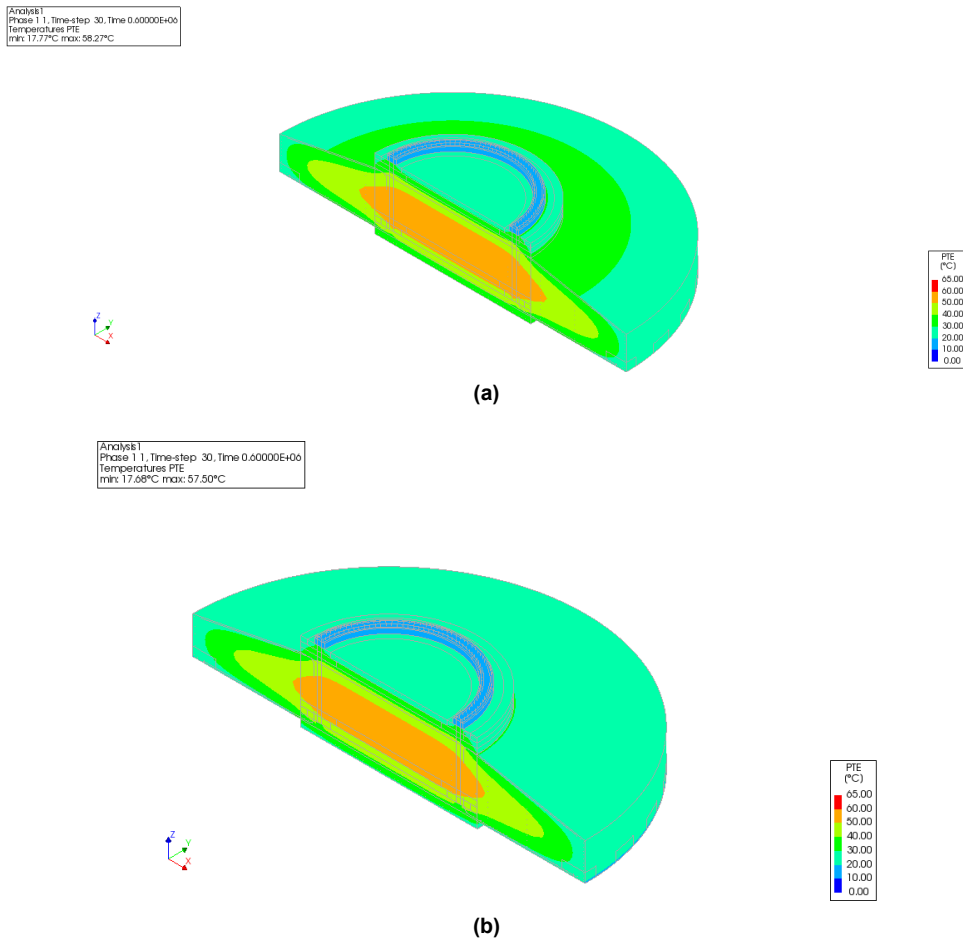


Figure 6.33: Comparison of Temperature evolution a) Variant 1 at day 7, b) Variant 3 at day 7

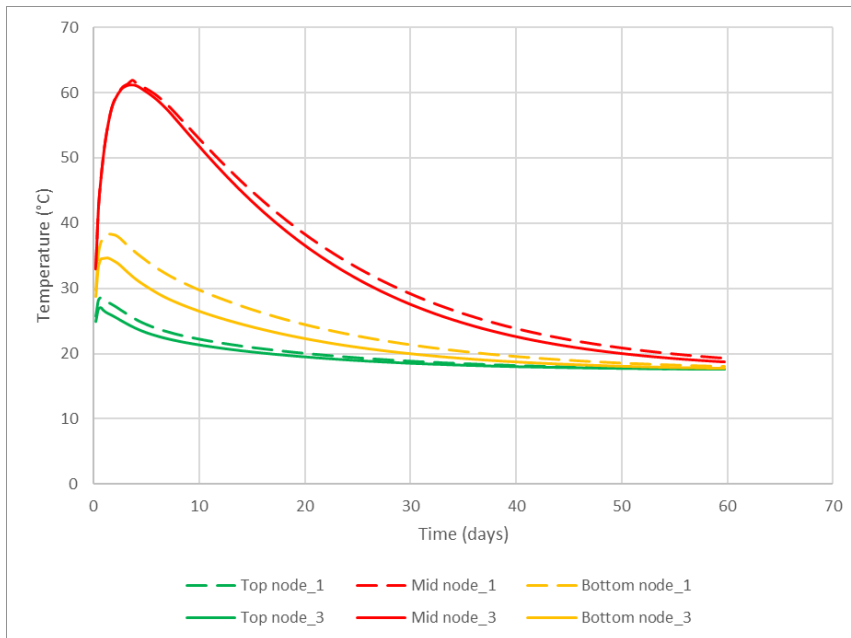
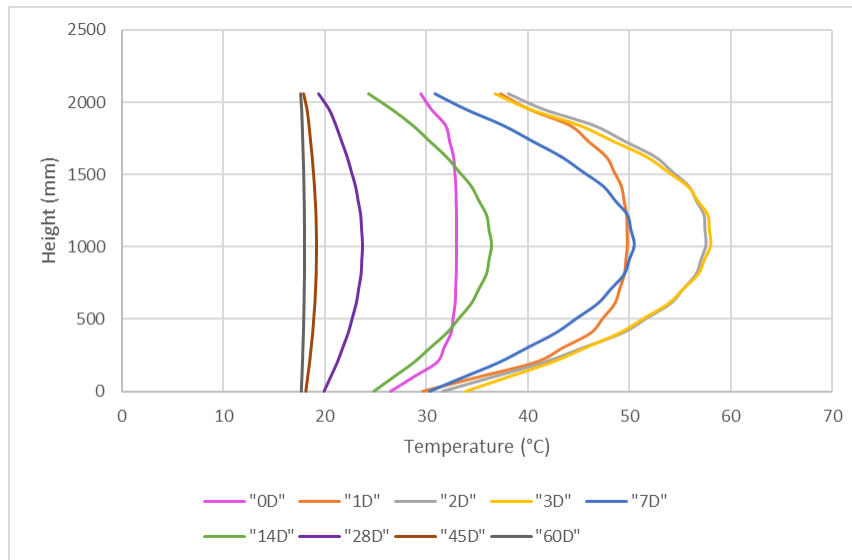
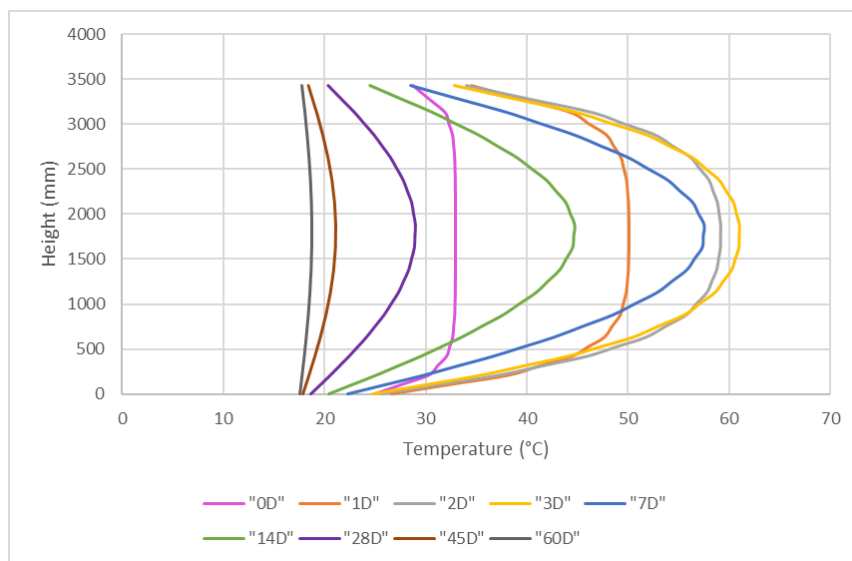


Figure 6.34: Temperature-Time comparison between Model 1 and 3

In order to determine the thermal cracking, the temperature gradient is calculated. Figure 6.35 represents the temperature gradient for different sections. It is observed that the thermal gradient for both the left and the right section is the same due to the uniform heat development while it differs in the case of the middle section. The maximum gradient is obtained for the middle section at around 7 days where the maximum temperature difference between the core and the topmost surface is 32 °C. Whereas, in the case of Model 2, the thermal gradient is 35 °C. From [8], the mass structure is susceptible to cracking if the temperature difference is more than 25 °C. Hence, a reduction of 8.6% cannot stop the occurrence of thermal cracks in the foundation.



(a)



(b)

Figure 6.35: Height vs Temperature plots for different sections of the concrete foundation a) Left section-I-I, b) Middle section-II-II

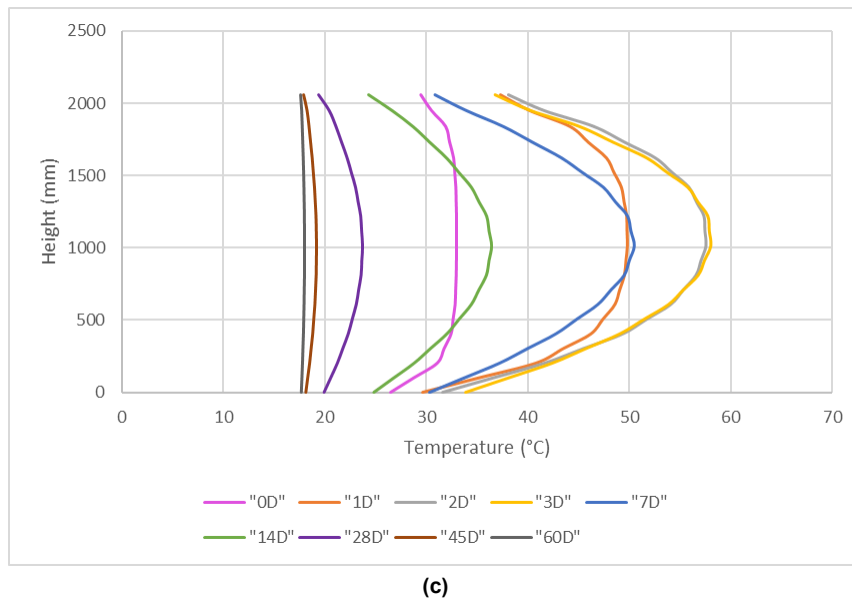


Figure 6.35: Height vs Temperature plots for different sections of the concrete foundation c) Right section-III-III

Steel stresses due to the Hydration heat

The amount of stress in the reinforcement in Variant 3 due to temperature evolution in the concrete foundation differs from both Variant 1 and Variant 2 in the amount of steel stress generated in the steel bars because of different amount of heat evolution in the foundation. The stresses in the reinforcements are shown in Figure B.23-Figure B.28.

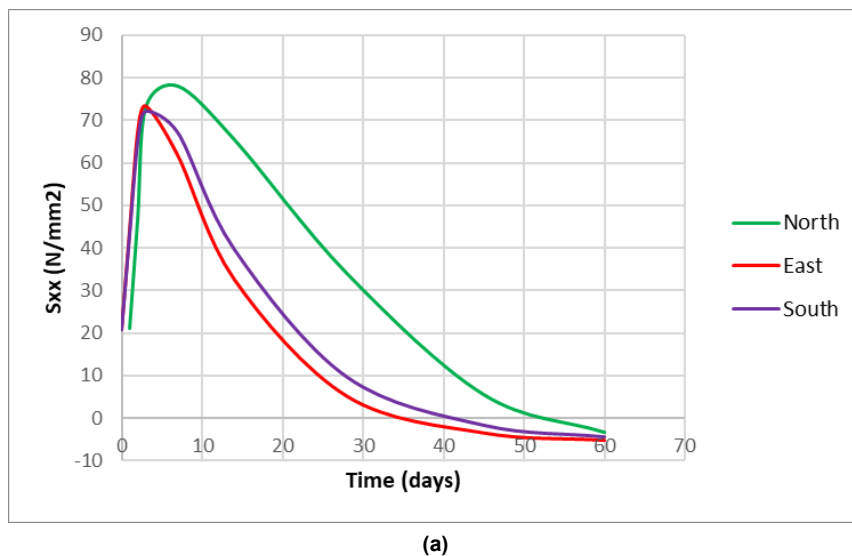
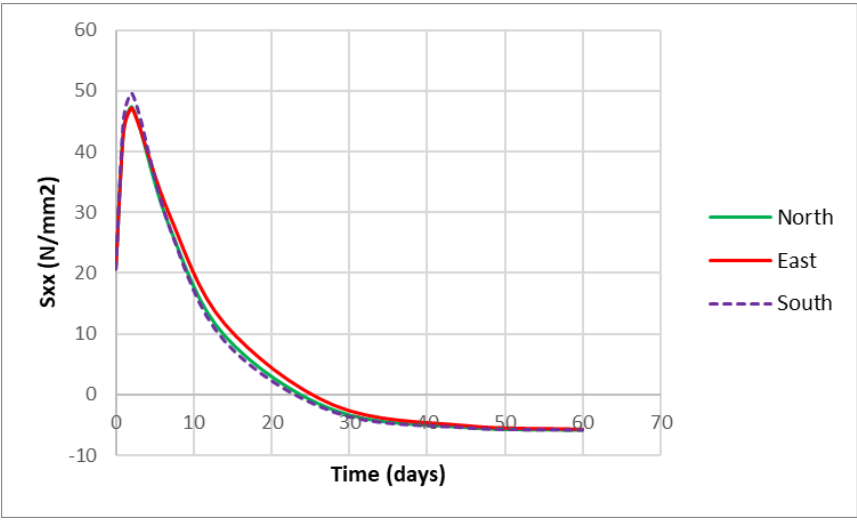
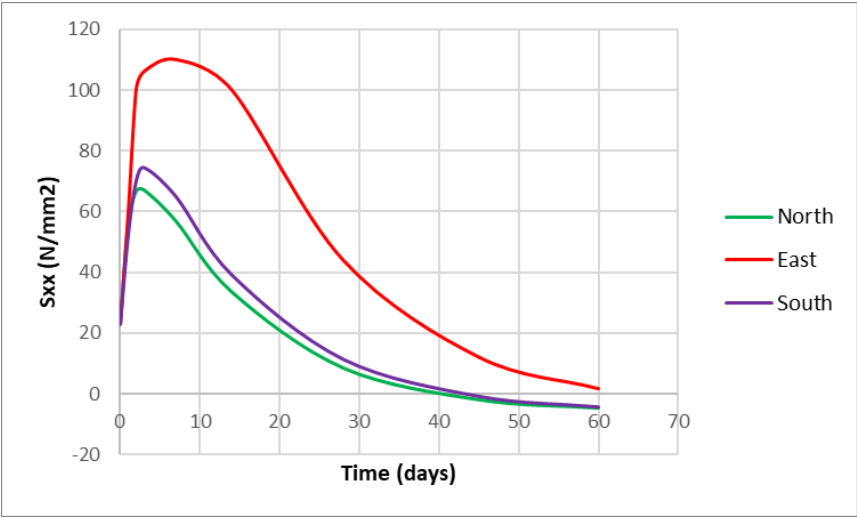


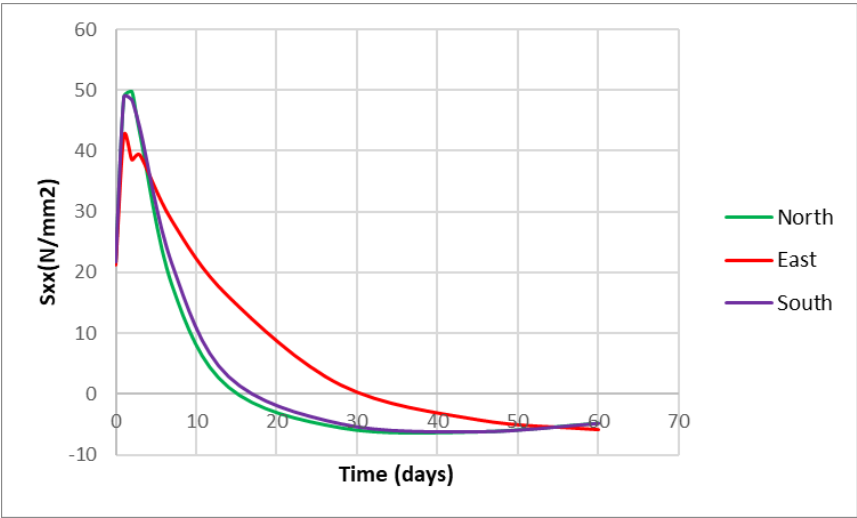
Figure 6.36: Steel stress wrt time at each wind directions a) Top radial



(b)



(c)



(d)

Figure 6.36: Steel stress wrt time at each wind directions b) Bottom radial, c) Top tangential, d) Bottom tangential

From the above graphs, the stresses in the reinforcements due to the hydration heat are plotted against the number of days of the heat analysis. It can be seen that they differ in each direction due to the asymmetrical pattern of cracks appearing in the model. The lines representing each direction should overlap with each other since an ideal situation has been assumed with uniform heat development inside the foundation but due to the numerical errors they are different in each direction for most of the rebar groups. For the bottom tangential reinforcements, a change in peak is observed in the East direction which might be an indication of possible crack in that region.

Effects of Combined analysis

This section includes the combined heat and nonlinear structural analysis. In this analysis, the structural calculations are performed at three stages- prestress, vertical load, and wind load after obtaining the results from hydration heat in subsection 6.5.1. The below figures depict the results after each load step:

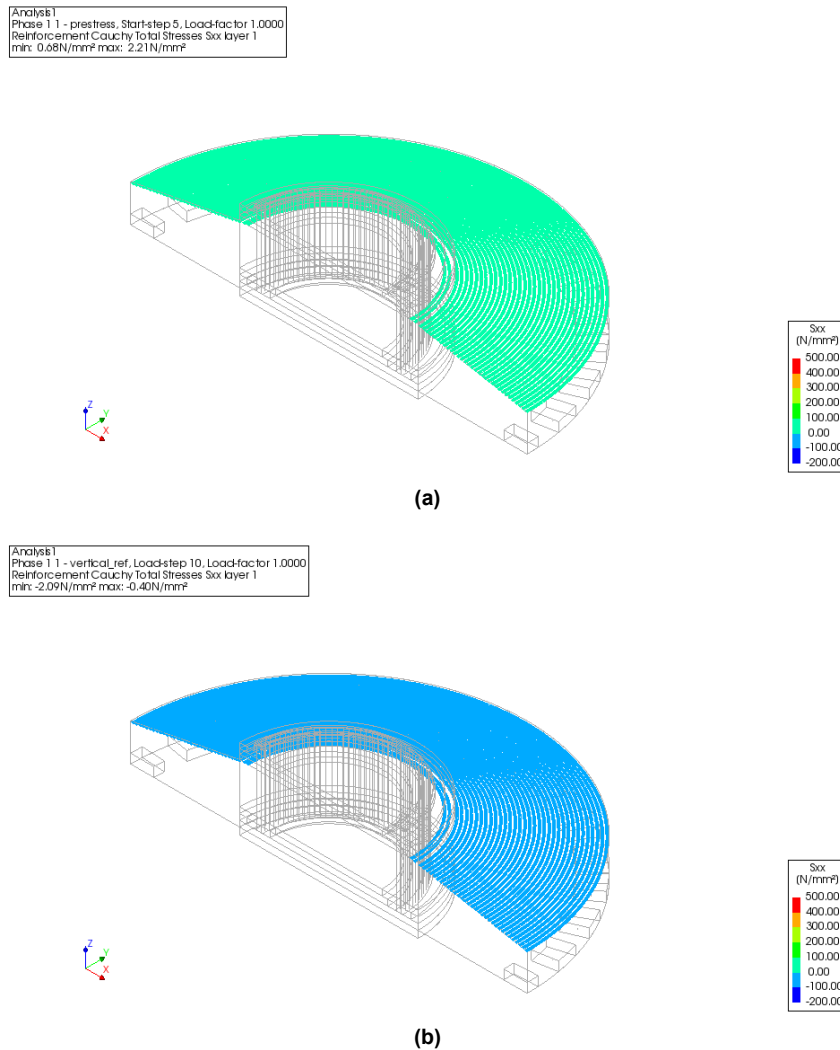


Figure 6.37: Steel stress in the Top tangential rebars a) After prestress, b) After vertical load

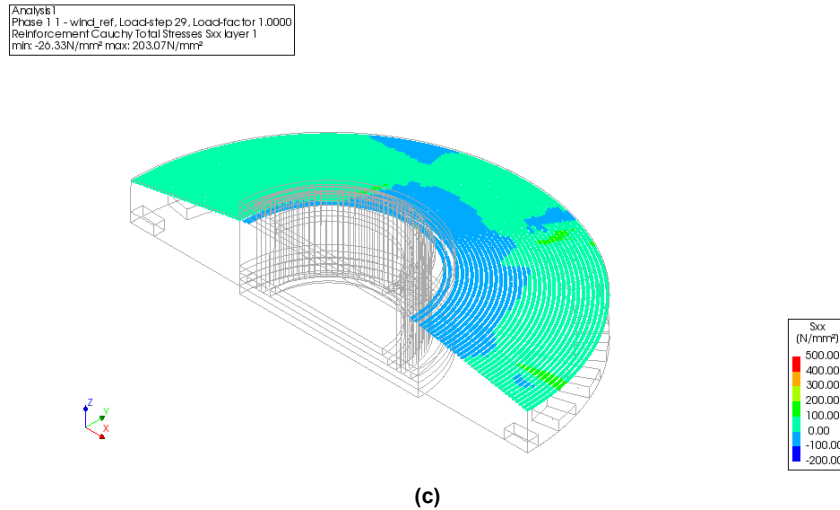


Figure 6.37: Steel stress in the Top tangential rebars c) After wind load

Observation Figure 6.37: When the prestress force is applied to the foundation, it is subjected to the tensile forces only. But after the complete application of the vertical loads, compressive stresses of less magnitude start to develop, resulting in both tensile and compressive stress at the end of the wind load. Tensile stress mainly occurs in the opposite direction of the wind while the compressive can be observed in rebars along the wind direction. The bars near the pedestal are in compression due to the anchor pretensioning bolts. Some asymmetrical crack patterns can be observed due to numerical errors.

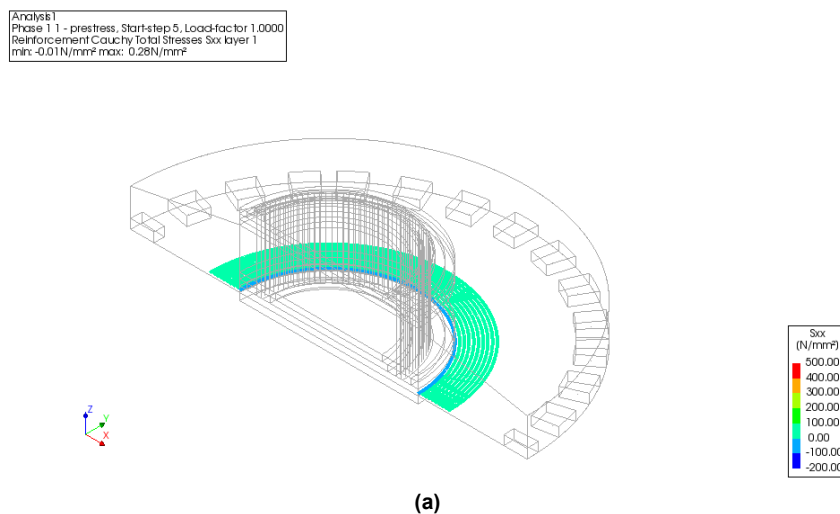


Figure 6.38: Steel stress in the Bottom tangential rebars a) After prestress

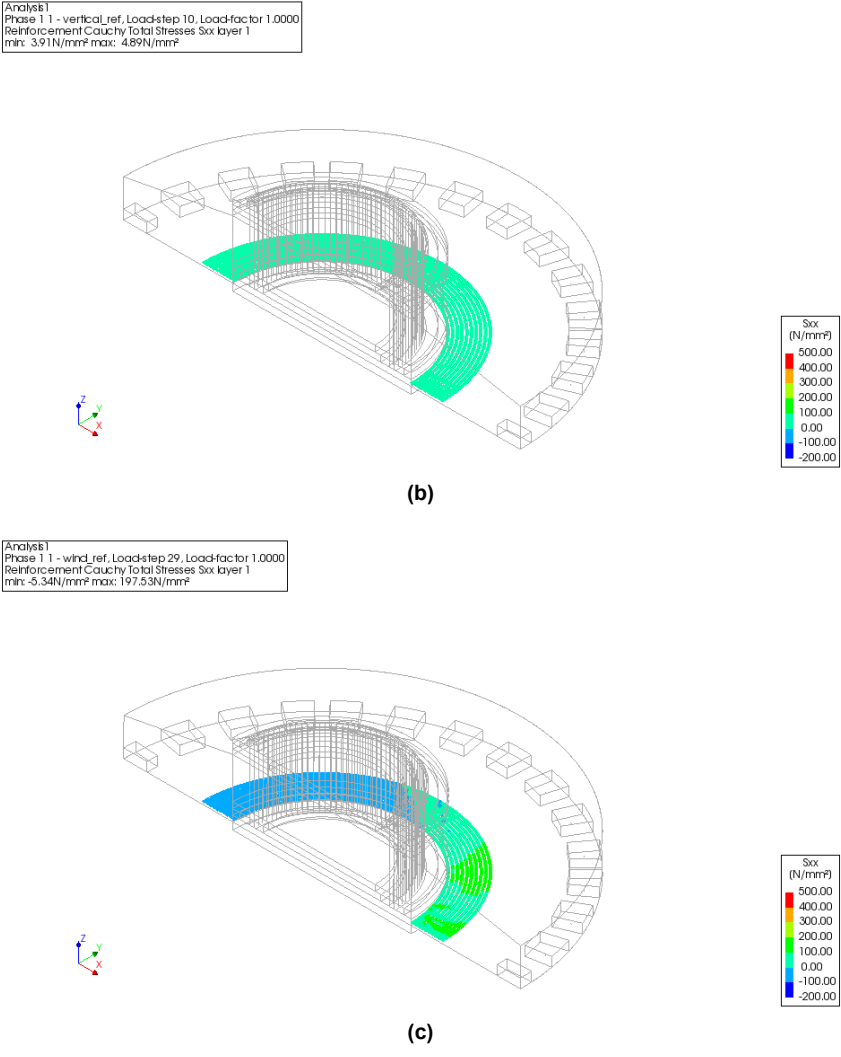


Figure 6.38: Steel stress in the Bottom tangential rebars b) After vertical load, c) After wind load

Observation Figure 6.38: The bottom tangential rebars near the pedestal experience tension on the south side (prevailing wind direction) and the north side experiences compression after the wind load step. The mentioned wind directions are depicted in Figure 6.2. The compressive stress only occurs after the application of the wind load.

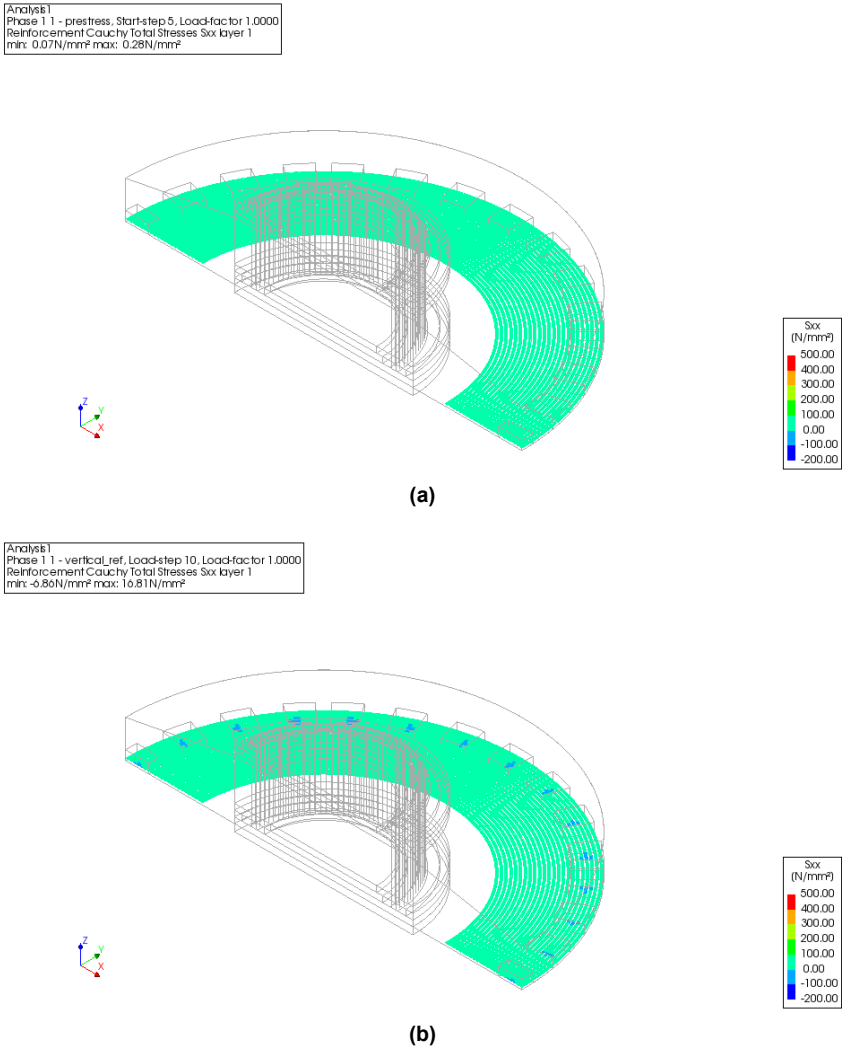


Figure 6.39: Steel stress in the Bottom tangential rebars near piles a) After prestress, b) After vertical load

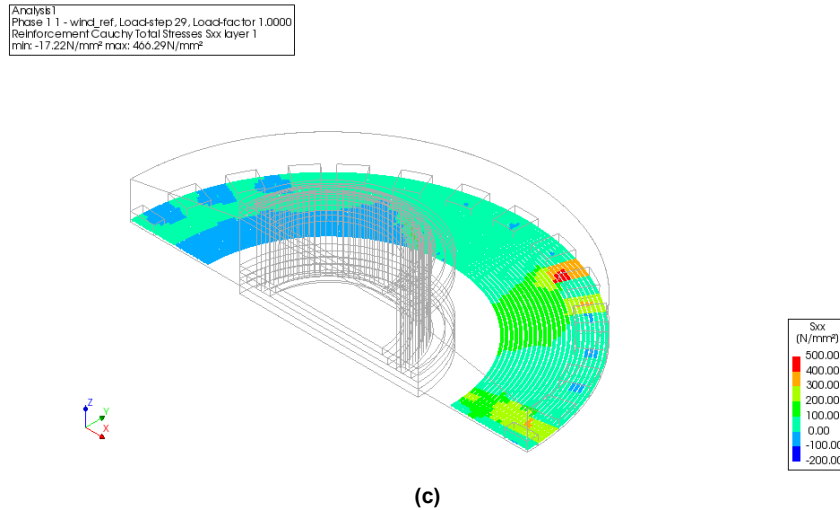


Figure 6.39: Steel stress in the Bottom tangential rebars near piles c) After wind load

Observation Figure 6.39: These groups experience comparatively more stress in the reinforcements as compared to the inner steel group. It starts to experience compression in the areas where there are piles due to the applied reaction force from the piles resulting from the applied vertical load. After the wind load, some more areas develop compressive stresses in the reinforcements towards the North direction. Whereas, there are some areas in the south direction of the foundation that experience comparatively higher tensile stresses. This happens due to the modeling of linear elastic piles in the foundation. Since the piles do not crack, the stresses get transferred to the bottom reinforcements in both tangential and radial directions which leads to higher stresses as compared to the tangential group present near the pedestal.

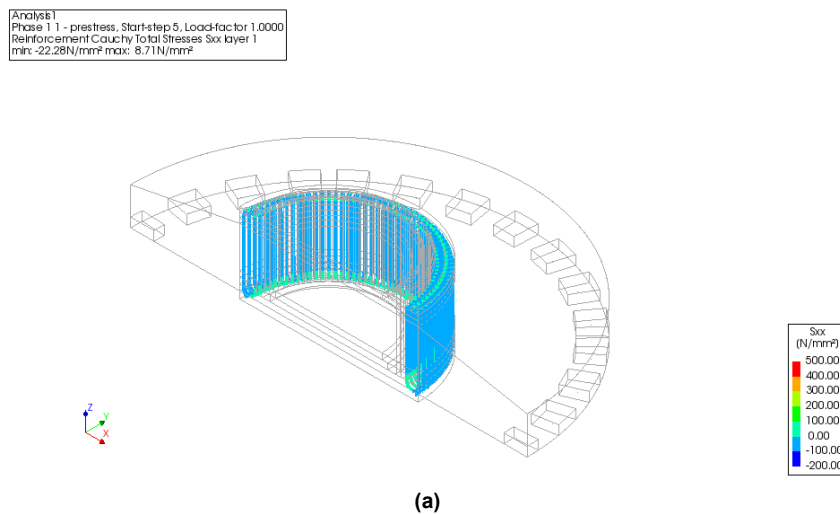
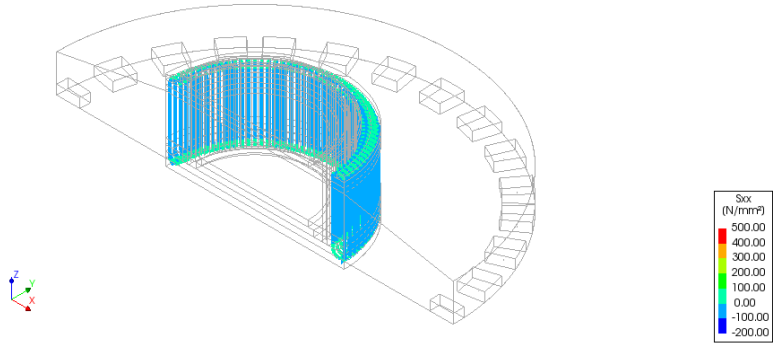


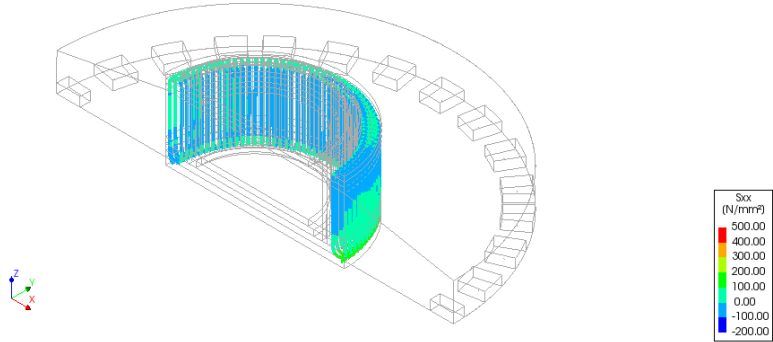
Figure 6.40: Steel stress in the stirrups a) After prestress

Analysis 1
Phase 1 1 - vertical_ref, Loadstep 10, Loadfactor 1.0000
Reinforcement Cauchy Total Stresses Sxx layer 1
min: -21.73N/mm² max: 5.88N/mm²



(b)

Analysis 1
Phase 1 1 - wind_ref, Loadstep 29, Loadfactor 1.0000
Reinforcement Cauchy Total Stresses Sxx layer 1
min: -59.25N/mm² max: 233.44N/mm²

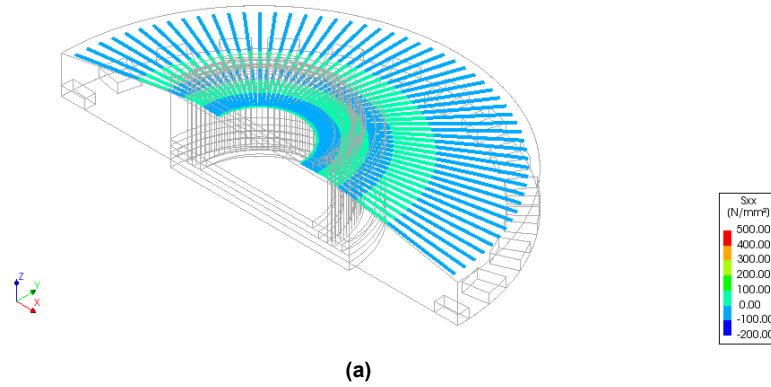


(c)

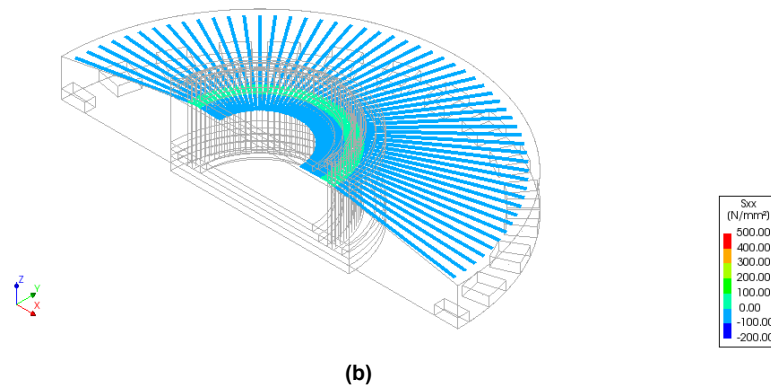
Figure 6.40: Steel stress in the stirrups b) After vertical load, c) After wind load

Observation Figure 6.40: With the application of pretension forces from the anchor bolts, the vertical stirrups experience compressive stresses. When the wind load is applied, the vertical bars are in both compression and tension depending on the position of the bars and the applied bending moment.

Analysis1
Phase 1.1 - prestress, Start-step 5, Load-factor 1.0000
Reinforcement Cauchy Total Stresses Six layer 1
min: -3.30N/mm² max: 10.79N/mm²



Analysis1
Phase 1.1 - vertical_ref, Load-step 10, Load-factor 1.0000
Reinforcement Cauchy Total Stresses Six layer 1
min: -15.89N/mm² max: 7.83N/mm²



Analysis1
Phase 1.1 - wind_ref, Load-step 29, Load-factor 1.0000
Reinforcement Cauchy Total Stresses Six layer 1
min: -165.83N/mm² max: 302.26N/mm²

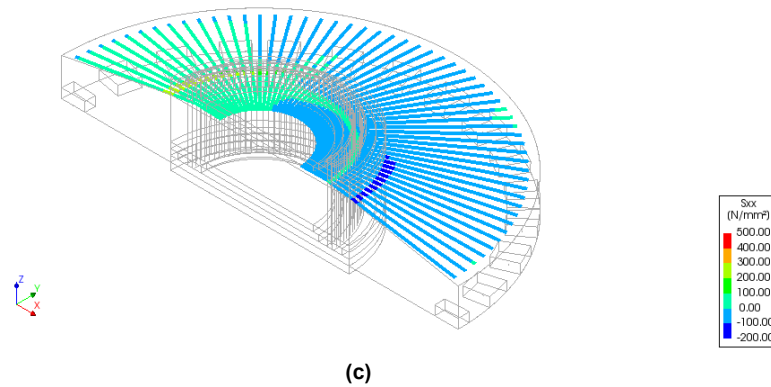


Figure 6.41: Steel stress in the Top radial rebars a) After prestress, b) After vertical load, c) After wind load

Observation Figure 6.41: The top radial bars experience higher tensile stress at the position of bends in the bars. After the application of the wind load, compressive stress occurs in most of the areas of the reinforcements in the primary wind direction (south) while the steel rebars in the opposite direction (north) undergo tensile stress since the overturning bending moment is acting from the North to the South.

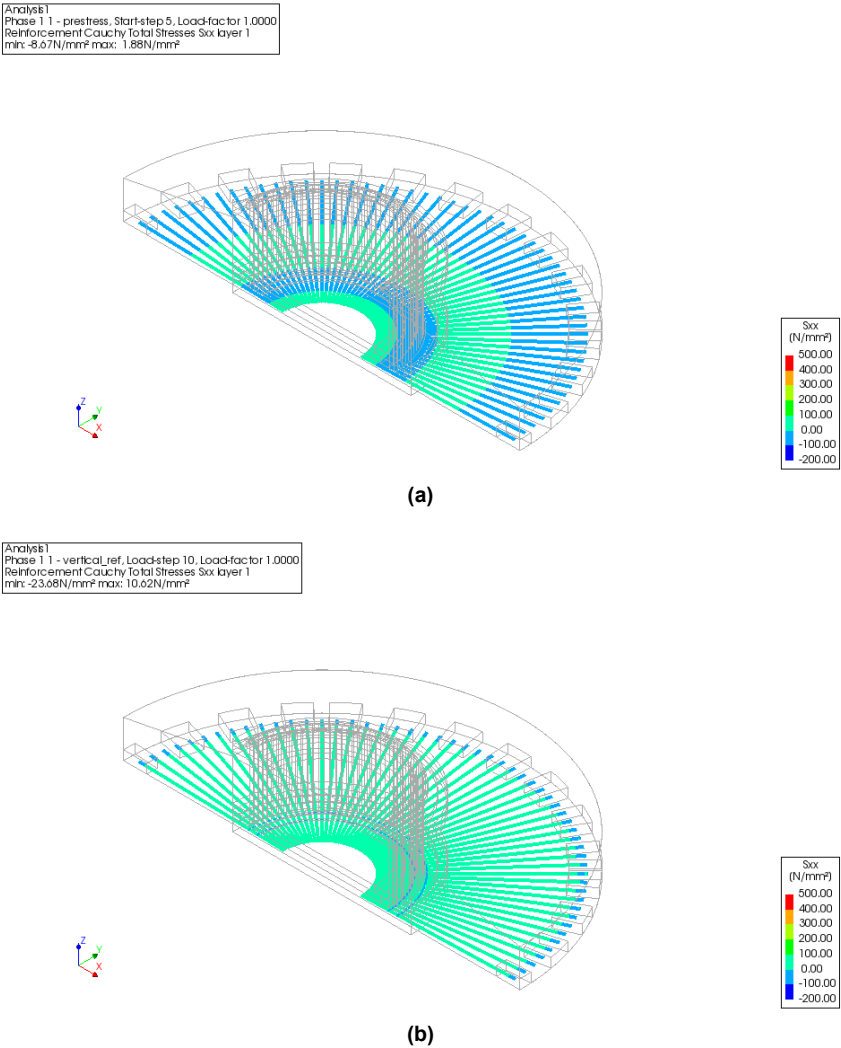


Figure 6.42: Steel stress in the Bottom radial rebars a) After prestress, b) After vertical load

Analysis1
Phase 1 1 - wind_ref, Load-step 29, Load-factor 1.0000
Reinforcement Cauchy Total Stresses Six layer 1
min: -51.78N/mm² max: 378.70N/mm²

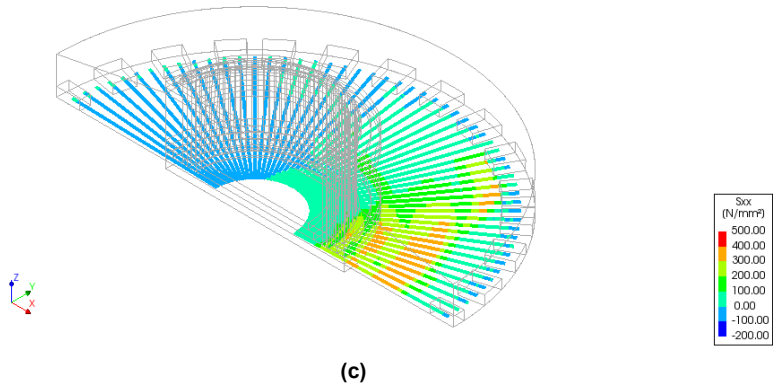


Figure 6.42: Steel stress in the Bottom radial rebars c) After wind load

Observation Figure 6.42: In the case of the bottom radial bars, after the application of the vertical loads, the reinforcements near the piles experience compressive stress while the other portions have tensile stresses. The behavior changes after the wind load application where it is observed that the tensile stress only remains in the prevailing wind direction and the rest of the rebars are under compression.

Analysis1
Phase 1 1 - wind_ref, Load-step 29, Load-factor 1.0000
Crack-widths Ecw1
min: 0.00mm max: 3.20mm

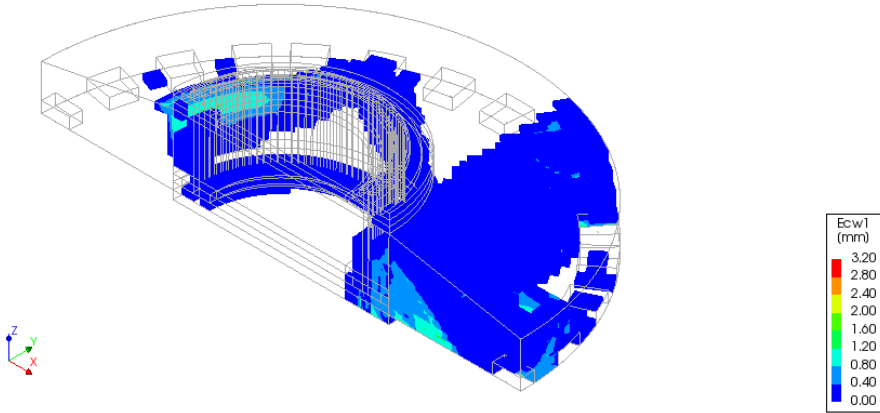


Figure 6.43: Crack patterns

Table 6.8: Comparison between the Field measurement and DIANA Model 3

Measuring Locations	Directions	Field Measurement 2017		Model 3	
		Tensile stress (MPa)	Compressive stress (MPa)	Tensile stress (MPa)	Compressive stress (MPa)
L01	A	182.21	-118.53	-	-
	B	10.66	-20.16	-	-
	C	117.07	-160.99	-	-
	D	-	-	-	-
L02	A	21.97	-12.47	244.532	-
	B	5.1	-3.4	-	-16.666
	C	15.4	-19.94	-	-60.323
	D	3.06	-4.68	-	-
L03	A	3.13	-1.87	8.216	-
	B	1.08	-0.76	-	-2.662
	C	3.13	-4.13	-	-14.685
	D	0.7	-1.15	-	-
L04	A	4.64	-2.94	19.225	-
	B	1.32	-0.92	-	-9.157
	C	3.7	-5.1	-	-13.174
	D	0.96	-1.42	-	-
L05	A	5.04	-7.5	-	-12.887
	B	1.67	-2.33	58.225	-
	C	8.96	-6.04	271.107	-
	D	2.23	-1.55	-	-
L06	A	2.12	-2.9	-	-3.18
	B	0.85	-1.19	60.309	-
	C	3.13	-1.99	73.742	-
	D	0.94	-0.68	-	-
L07	A	2.49	-1.13	4.94	-
	B	0.5	-0.38	-	-8.524
	C	0.82	-0.73	-	-15.542
	D	0.25	-0.33	-	-
L08	A	1.46	-2.17	1.49	-
	B	0.61	-0.81	6.291	-
	C	2.09	-1.39	121.552	-
	D	0.76	-0.5	-	-

Conclusion: The behavior of the stress patterns is the same in all the 3 models described above. The only difference between them is the magnitude of the occurring stresses in the rebars. Now that the foundation core reaches a lower temperature as compared to Models 1 and 2, the temperature gap between the top and core is less which results in lesser thermal cracks in the foundation. After reducing the temperature gradient between the top surface and the core, cracks due to wind load have decreased as well. Even though there is no direct correlation between thermal cracks and mechanical cracks or more thermal cracks might result in narrower cracks during the service life but it is possible that the presence of thermal cracks can alter the distribution of stresses, leading to different crack patterns due to wind load. The steel stresses have now shown a reduction of about 6-33% more as compared to Model 2. Among this, the top bars have shown a considerable decrease in the stresses due to the adjustments made in the HTC's. Since certain locations such as the top radial bar in the North direction and the bottom radial bar

in the south direction show a larger amount of tensile steel stress, they need further reduction in order to prevent cracking. The possible explanation for higher tensile stress in the bottom bars can be due to the effect of extra stress coming from the piles which are modeled as linear elastic. It is deduced from Table 6.8, that the steel stresses in Model 3 are still higher up to a factor of 30 in radial (L05 and L02) positions. While other locations such as tangential showed a variation of up to a factor of 9 for North and East wind directions. On the contrary, stress specifically in the south direction for tangential bars showed higher stresses. In order to reduce the range of variation, one possible way is to limit the cracks as much as possible by increasing the stiffness of the foundation as it might have a positive impact on the steel stresses. This leaves room for discussion about the other effects since there is still a difference between the measured and numerical analysis values.

6.6. Effect of Bedding

In the previous models, it is observed that the hydration heat lowers the stress in the reinforcements groups to a certain extent but in order to limit the occurring cracks in the foundation and to reduce the steel stress even more, the bedding has been added in the foundation along with the piles. Usually, the bedding is modeled in a shallow foundation as surface support in the DIANA but in this case, with a piled foundation, the bedding is modeled as a boundary interface with a certain stiffness. The purpose of including the bedding in a piled foundation is to demonstrate the effect of soil stiffness during the foundation construction where the surrounding soil attains a certain amount of prestress which may reduce the steel stress inside the foundation after the applied wind load. In this section, all the models presented will be combined effectively with the heat of hydration. Among HTC 1 and HTC 2, HTC 2 has a lower temperature gradient, hence all the further models will include HTC 2 as the heat transfer coefficients.

6.6.1. Results of Variant 4

Variant 4 represents the model with the inclusion of bedding underneath the foundation. The calculated bedding stiffness is 3600 kN/m^3 according to the soil conditions at the site. The bedding applied is shown in the following figure:

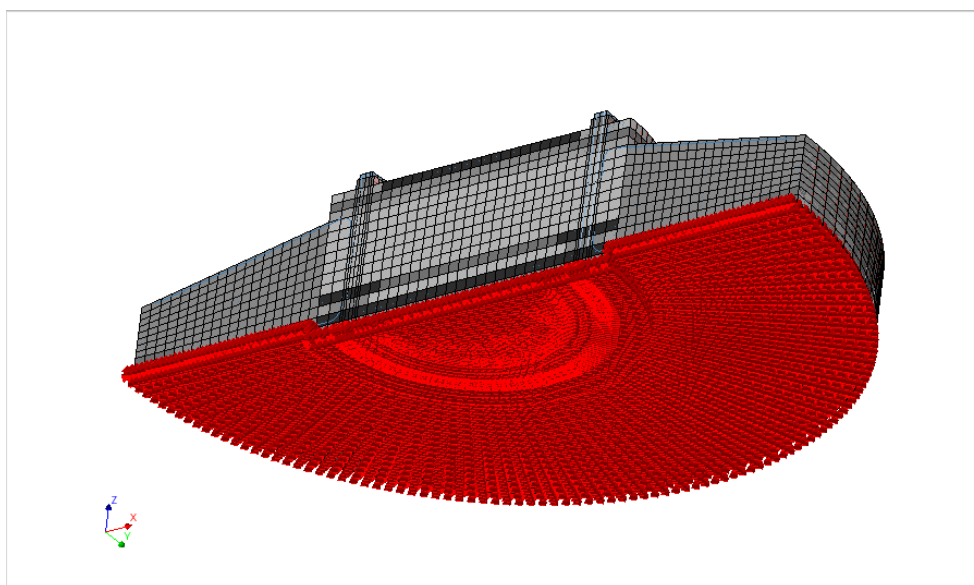
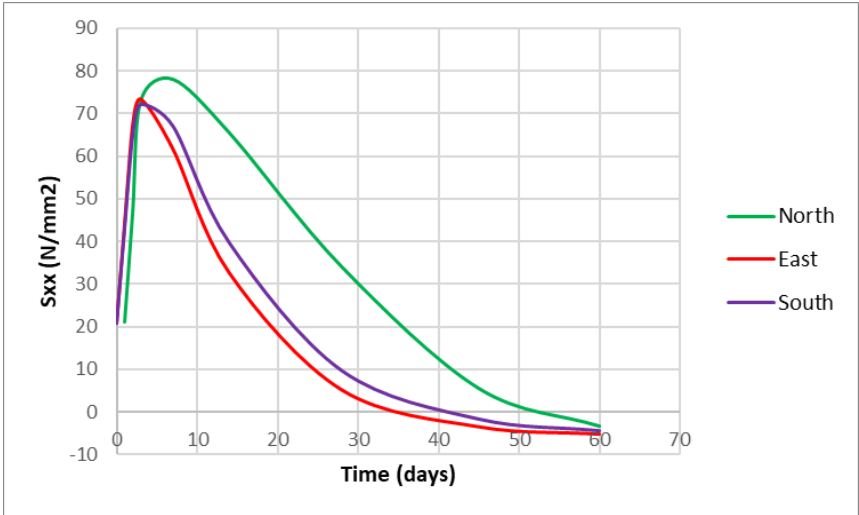


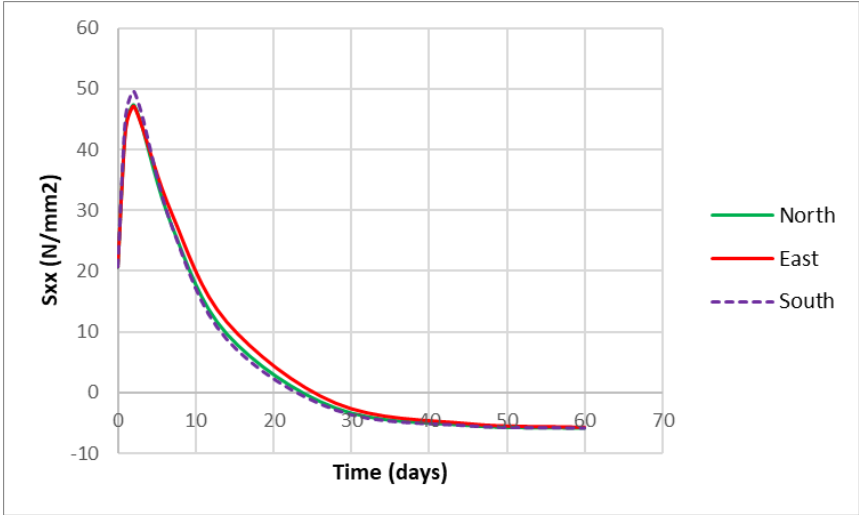
Figure 6.44: Bedding underneath the foundation

Since the HTC's for the boundary conditions are the same as Variant 3, the temperature evolution inside the foundation will be the same. Figure 6.32 represents the heat development in the foundation for 60 days.

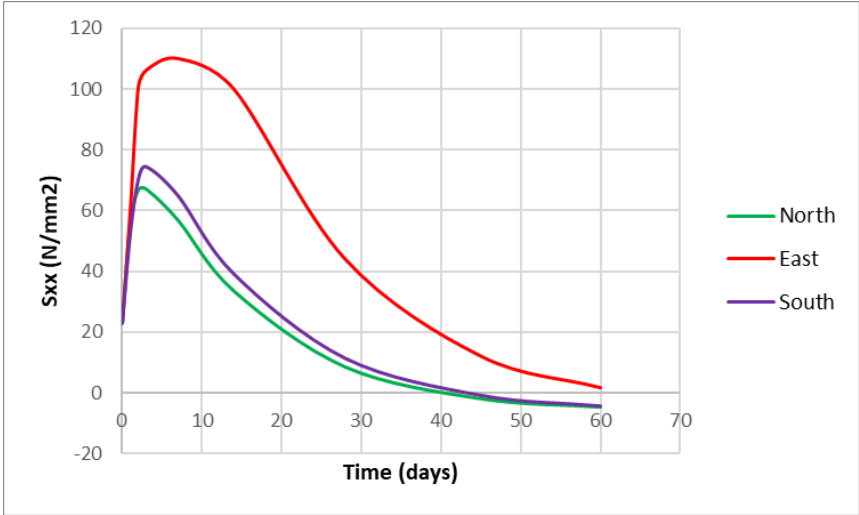
Steel stresses due to the Hydration heat



(a)

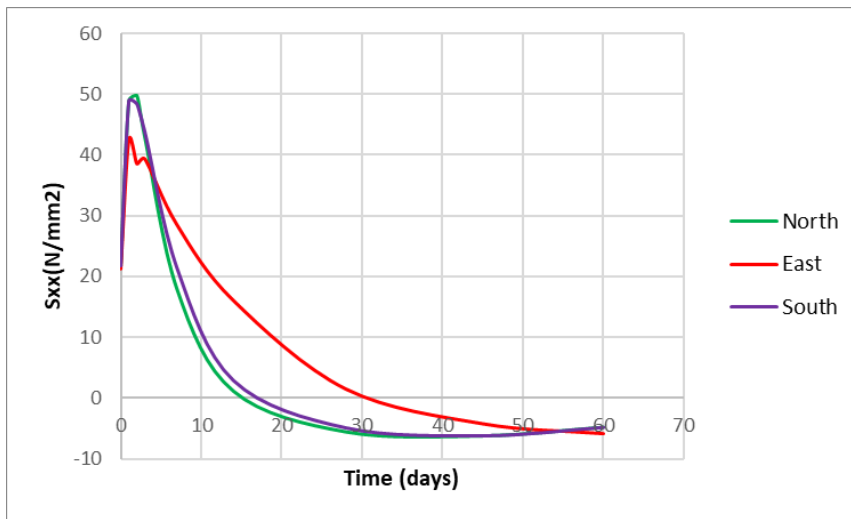


(b)



(c)

Figure 6.45: Steel stress wrt time at each wind directions a) Top radial, b) Bottom radial, c) Top tangential



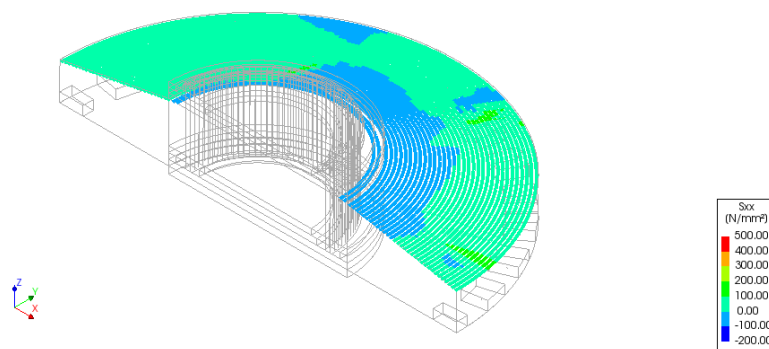
(d)

Figure 6.45: Steel stress wrt time at each wind directions d) Bottom tangential

The stresses due to the heat of hydration are the same for both models 3 and 4 due to the presence of the same hydration heat parameters. From Figure 6.36 and Figure 6.45, it is clear that the presence of bedding in the Variant 4 does not affect the stress development inside the foundation due to the heat because during the hydration heat analysis, the heat evolution of the soil has been considered already and the bedding stiffness has nothing to do with the exothermic reaction of the concrete. Now, the effect of bedding will be analyzed after combining both heat and structural analysis in order to determine the final stress generated inside the foundation.

Effects of Combined analysis

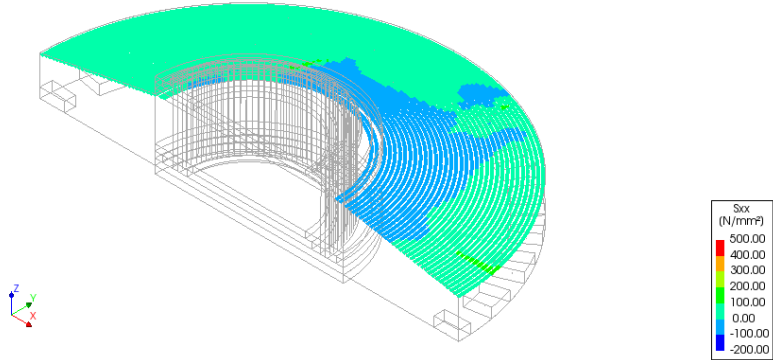
Analysis 1
 Phase 1.1 - wind_ref. Loadstep 29. Loadfactor 1.0000
 Reinforcement Cauchy Total Stresses Sxx layer 1
 min: -20.33N/mm² max: 203.07N/mm²



(a)

Figure 6.46: Steel stress in the Top tangential rebars a) Model 3

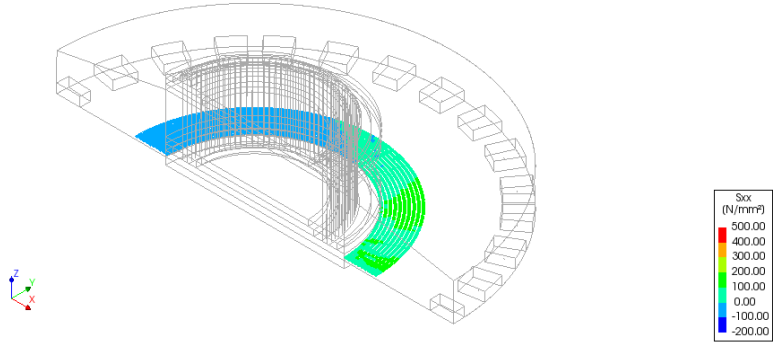
Analysis 1
Phase 1 1 - wind_ref, Load-step 29, Load-factor 1.0000
Reinforcement Cauchy Total Stresses Sxx layer 1
min: -19.85N/mm² max: 190.19N/mm²



(b)

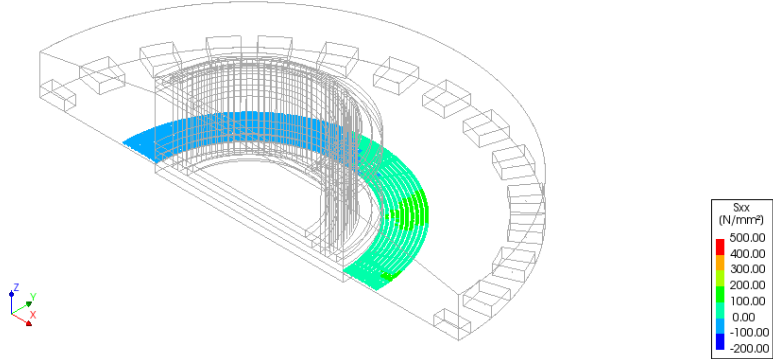
Figure 6.46: Steel stress in the Top tangential rebars b) Model 4

Analysis 1
Phase 1 1 - wind_ref, Load-step 29, Load-factor 1.0000
Reinforcement Cauchy Total Stresses Sxx layer 1
min: -5.34N/mm² max: 197.53N/mm²



(a)

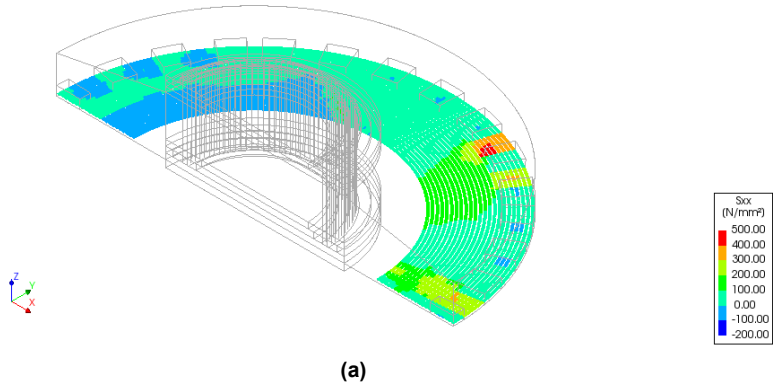
Analysis 1
Phase 1 1 - wind_ref, Load-step 29, Load-factor 1.0000
Reinforcement Cauchy Total Stresses Sxx layer 1
min: -7.02N/mm² max: 159.35N/mm²



(b)

Figure 6.47: Steel stress in the Bottom tangential rebars a) Model 3, b) Model 4

Analysis1
Phase 1.1 - wind_ref, Load-step 29, Load-factor 1.0000
Reinforcement Cauchy Total Stresses Sxx layer 1
min: -17.22N/mm² max: 466.29N/mm²



Analysis1
Phase 1.1 - wind_ref, Load-step 29, Load-factor 1.0000
Reinforcement Cauchy Total Stresses Sxx layer 1
min: -17.54N/mm² max: 447.07N/mm²

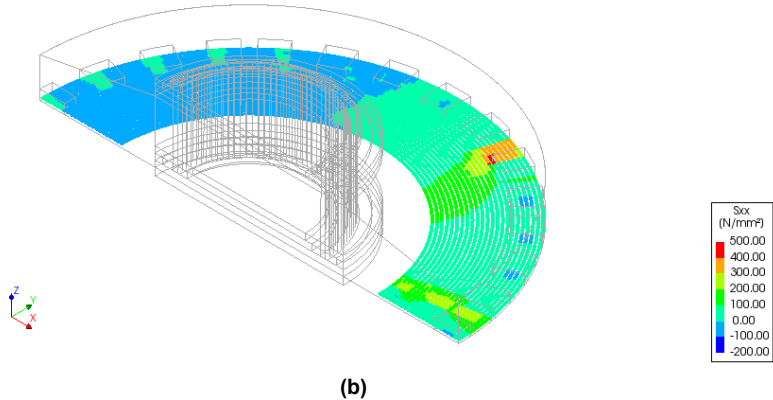


Figure 6.48: Steel stress in the Bottom tangential rebars near piles a) Model 3, b) Model 4

Analysis1
Phase 1.1 - wind_ref, Load-step 29, Load-factor 1.0000
Reinforcement Cauchy Total Stresses Sxx layer 1
min: -59.25N/mm² max: 233.44N/mm²

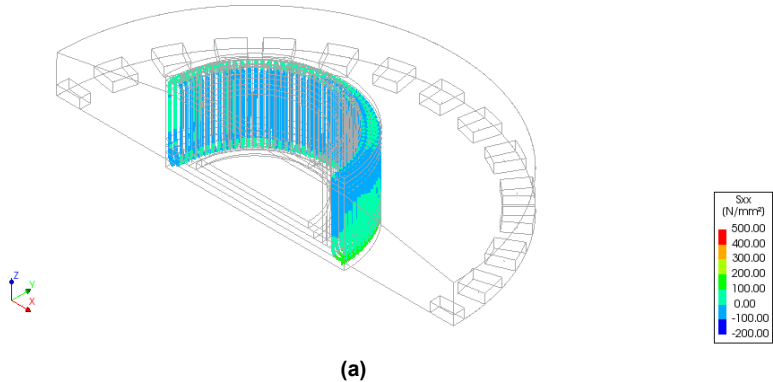
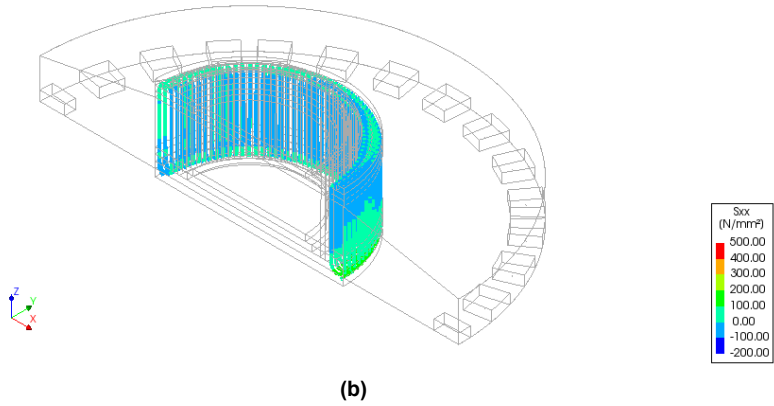


Figure 6.49: Steel stress in the stirrups a) Model 3

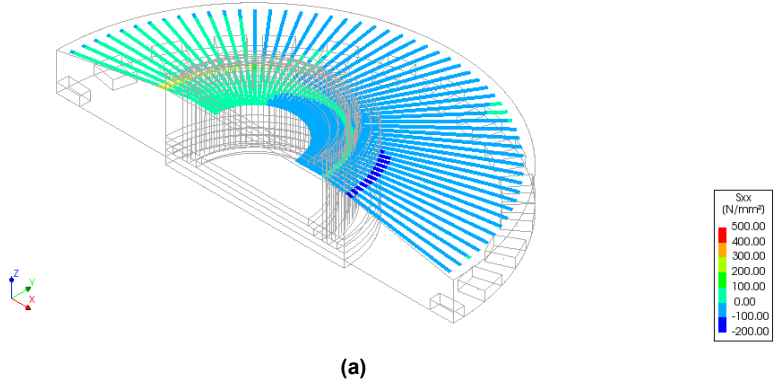
Analysis1
Phase 1 1 - wind_ref, Load-step 29, Load-factor 1.0000
Reinforcement Cauchy Total Stresses Sxx layer 1
min: -57.12N/mm² max: 201.50N/mm²



(b)

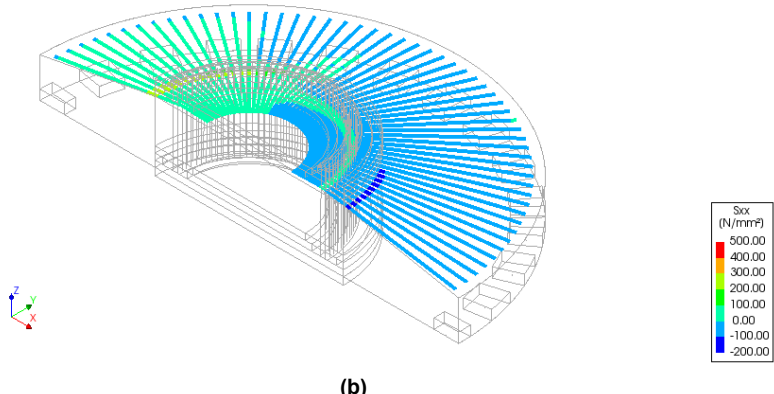
Figure 6.49: Steel stress in the stirrups b) Model 4

Analysis1
Phase 1 1 - wind_ref, Load-step 29, Load-factor 1.0000
Reinforcement Cauchy Total Stresses Sxx layer 1
min: -105.83N/mm² max: 302.20N/mm²



(a)

Analysis1
Phase 1 1 - wind_ref, Load-step 29, Load-factor 1.0000
Reinforcement Cauchy Total Stresses Sxx layer 1
min: -132.98N/mm² max: 302.69N/mm²



(b)

Figure 6.50: Steel stress in the Top radial rebars a) Model 3, b) Model 4

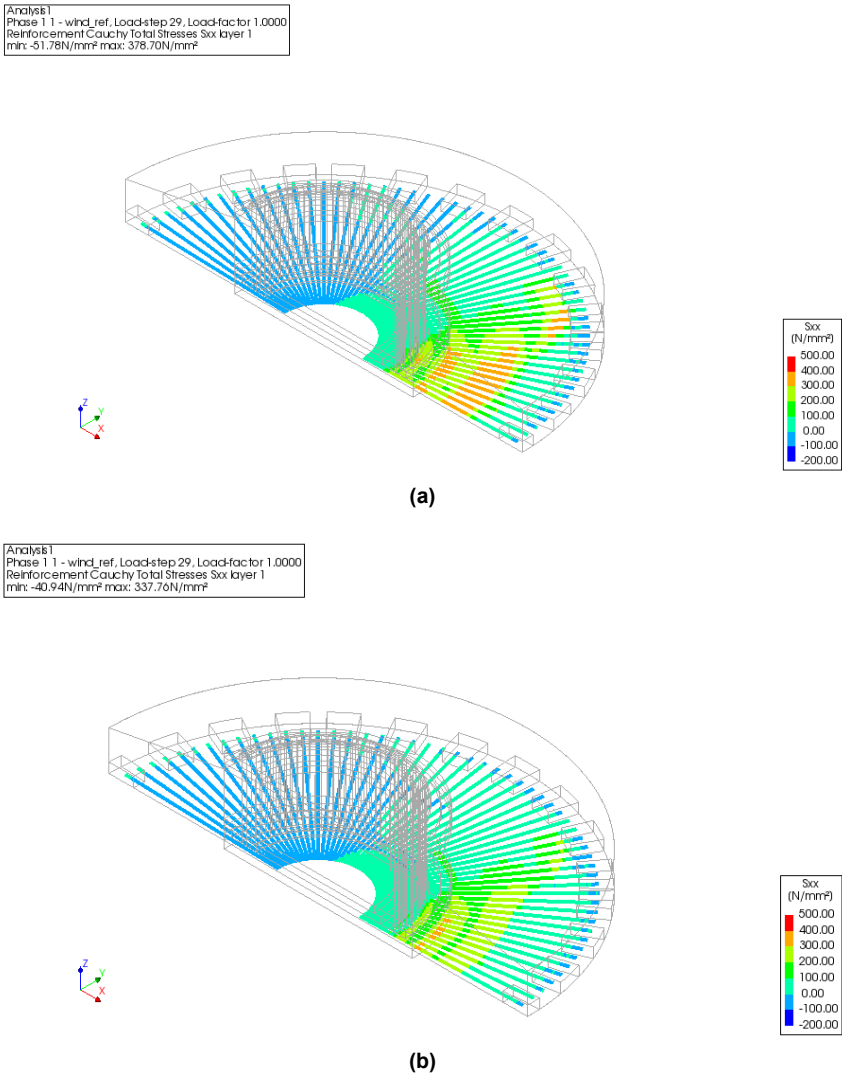


Figure 6.51: Steel stress in the Bottom radial rebar a) Model 3, b) Model 4

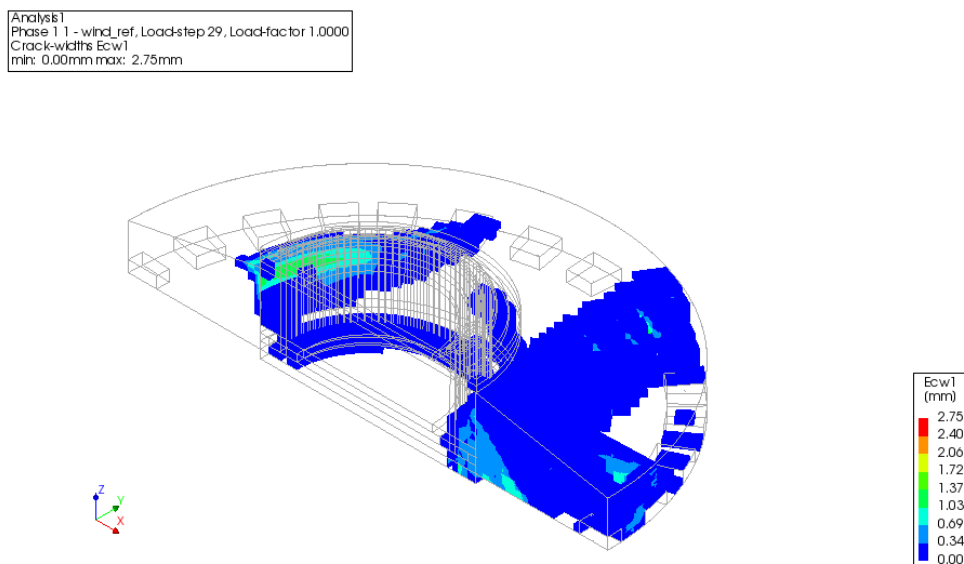


Figure 6.52: Crack patterns

Conclusion: The soil bedding is added to the foundation in order to strengthen the structure and provide some extra compression to the bottom reinforcements. The effect of adding bedding beneath the foundation has some effect on the steel stresses especially in the East and South wind directions as it reduced the steel stresses up to 77% as shown in Table 6.9. Whereas, in the case of the North direction that is not the case. Theoretically, if bedding is provided below the foundation then it is expected to reduce the stresses in all directions. But in the case of FEM analyses, it is difficult to find the stress distribution in the model, hence there remains a possibility that after providing the bedding, the stress is more concentrated in the North direction as compared to the other locations in the numerical model. Nevertheless, from the last model, there has been a reduction of up to 77% in the stresses on the bottom surface due to the additional stiffness obtained from the soil bedding. Hence, the purpose of including bedding is satisfied. Although if a comparison has to be drawn from Table 6.10, it is observed that there is still a marginal difference between the measurements and the DIANA model especially in the radial bars positioned in the North direction (L02) and in the south direction (L05). The range of variations lies between a factor of 10-26. Even though the stresses have reduced in Model 4 when compared to the previous models, these reductions are not yet satisfactory to provide an appropriate match with the experimental data. From Figure 6.43 and Figure 6.52, it can be observed that the cracks have also reduced from 3.2mm to 2.75mm after applying bedding beneath the foundation. This happened because the tensile stress in the bottom region is reduced resulting in narrower cracks. In order to determine the effect of bedding in an exclusive manner for the sensitivity study, the next model will focus on an upper-limit approximation of the bedding stiffness.

Table 6.9: Comparison between the DIANA Model 3 and DIANA Model 4

Measuring Locations	Directions	Model 3		Model 4	
		Tensile stress (MPa)	Compressive stress (MPa)	Tensile stress (MPa)	Compressive stress (MPa)
L01	A	-	-	-	-
	B	-	-	-	-
	C	-	-	-	-
	D	-	-	-	-
L02	A	244.532	-	245.802	-
	B	-	-16.666	-	-9.701
	C	-	-60.323	-	-58.09
	D	-	-	-	-
L03	A	8.216	-	10.233	-
	B	-	-2.662	-	-0.602
	C	-	-14.685	-	-12.905
	D	-	-	-	-
L04	A	19.225	-	20.131	-
	B	-	-9.157	-	-8.689
	C	-	-13.174	-	-9.67
	D	-	-	-	-
L05	A	-	-12.887	-	-16.23
	B	58.225	-	14.143	-
	C	271.107	-	242.37	-
	D	-	-	-	-
L06	A	-	-3.182	-	-4.65
	B	60.309	-	-	-2.403
	C	73.742	-	38.523	-
	D	-	-	-	-
L07	A	4.94	-	5.3	-
	B	-	-8.524	-	-5.724
	C	-	-15.542	-	-12.663
	D	-	-	-	-
L08	A	1.49	-	-	-0.094
	B	6.291	-	3.854	-
	C	121.552	-	70.806	-
	D	-	-	-	-

Table 6.10: Comparison between the Field measurement and DIANA Model 4

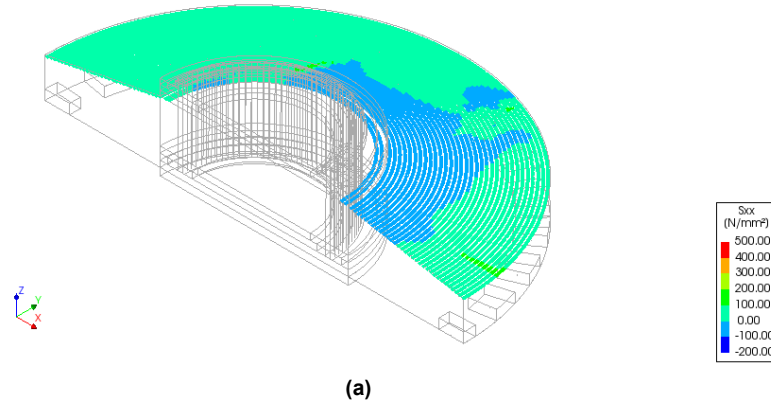
Measuring Locations	Directions	Field Measurement 2017		Model 4	
		Tensile stress (MPa)	Compressive stress (MPa)	Tensile stress (MPa)	Compressive stress (MPa)
L01	A	182.21	-118.53	-	-
	B	10.66	-20.16	-	-
	C	117.07	-160.99	-	-
	D	-	-	-	-
L02	A	21.97	-12.47	245.802	-
	B	5.1	-3.4	-	-9.701
	C	15.4	-19.94	-	-58.09
	D	3.06	-4.68	-	-
L03	A	3.13	-1.87	10.233	-
	B	1.08	-0.76	-	-0.602
	C	3.13	-4.13	-	-12.905
	D	0.7	-1.15	-	-
L04	A	4.64	-2.94	20.131	-
	B	1.32	-0.92	-	-8.689
	C	3.7	-5.1	-	-9.67
	D	0.96	-1.42	-	-
L05	A	5.04	-7.5	-	-16.23
	B	1.67	-2.33	14.143	-
	C	8.96	-6.04	242.37	-
	D	2.23	-1.55	-	-
L06	A	2.12	-2.9	-	-4.65
	B	0.85	-1.19	-	-2.403
	C	3.13	-1.99	38.523	-
	D	0.94	-0.68	-	-
L07	A	2.49	-1.13	5.3	-
	B	0.5	-0.38	-	-5.724
	C	0.82	-0.73	-	-12.663
	D	0.25	-0.33	-	-
L08	A	1.46	-2.17	-	-0.094
	B	0.61	-0.81	3.854	-
	C	2.09	-1.39	70.806	-
	D	0.76	-0.5	-	-

6.6.2. Sensitivity analysis-Variant 5

In this section, a model with higher bedding stiffness is discussed. A fictitious stiffness of 6950 kN/m^3 , is used as the soil stiffness in order to determine the effects in the wind turbine foundation. This is a fictitiously high value of the bedding stiffness in order to determine the effect of bedding in a sensitivity study. The idea behind putting such stiffness is to consider the effect of extra prestressing from the soil present all over the foundation when the concrete was poured into the structure.

Effects of Combined analysis

Analysis 1
Phase 1.1 - wind_ref, Load-step 29, Load-factor 1.0000
Reinforcement Cauchy Total Stresses Sxx layer 1
min: -19.85N/mm² max: 190.19N/mm²



Analysis 1
Phase 1.1 - wind_ref, Load-step 29, Load-factor 1.0000
Reinforcement Cauchy Total Stresses Sxx layer 1
min: -10.00N/mm² max: 170.14N/mm²

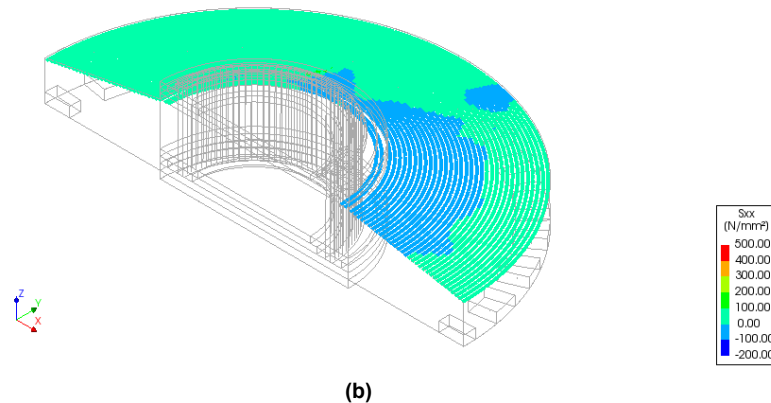
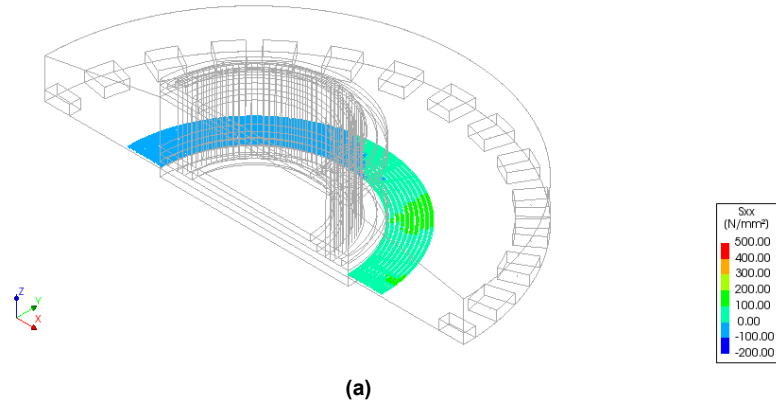


Figure 6.53: Steel stress in the Top tangential rebars a) Model 4, b) Model 5

Analysis 1
Phase 1.1 - wind_ref, Load-step 29, Load-factor 1.0000
Reinforcement Cauchy Total Stresses Sxx layer 1
min: -7.62N/mm² max: 159.35N/mm²



Analysis 1
Phase 1.1 - wind_ref, Load-step 29, Load-factor 1.0000
Reinforcement Cauchy Total Stresses Sxx layer 1
min: -5.72N/mm² max: 172.44N/mm²

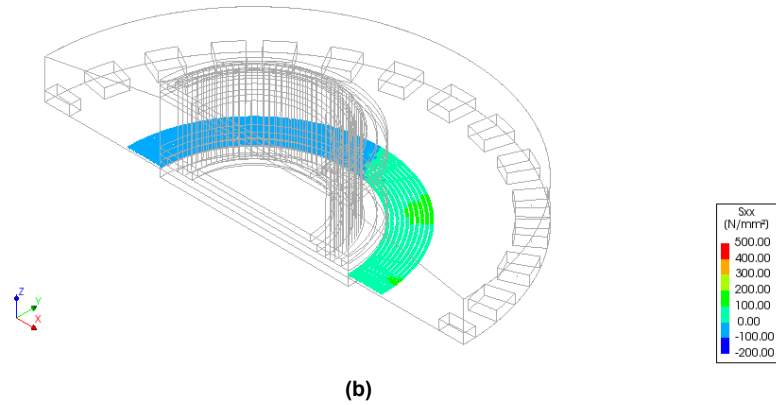


Figure 6.54: Steel stress in the Bottom tangential rebars a) Model 4, b) Model 5

Analysis 1
Phase 1.1 - wind_ref, Load-step 29, Load-factor 1.0000
Reinforcement Cauchy Total Stresses Sxx layer 1
min: -17.54N/mm² max: 447.07N/mm²

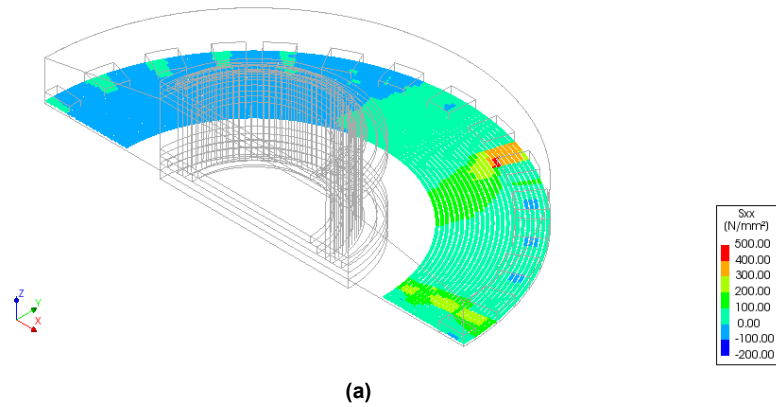
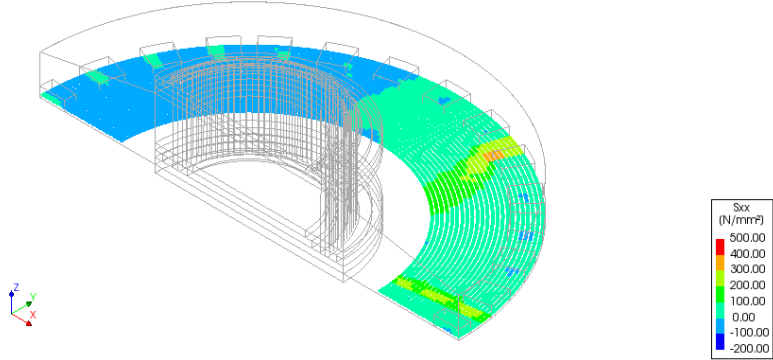


Figure 6.55: Steel stress in the Bottom tangential rebars near piles a) Model 4

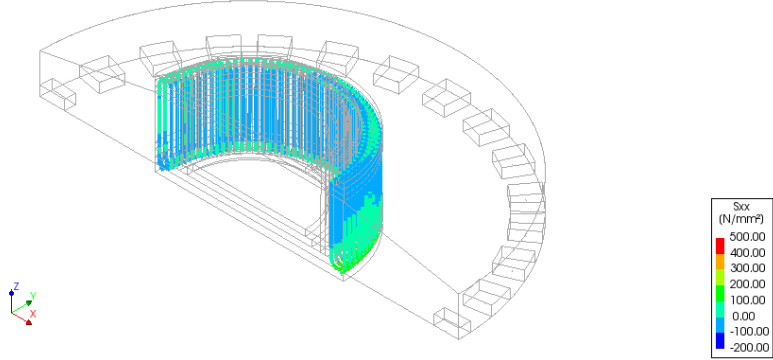
Analysis 1
Phase 1.1 - wind_ref, Load-step 29, Load-factor 1.0000
Reinforcement Cauchy Total Stresses Sxx layer 1
min: -14.78N/mm² max: 308.87N/mm²



(b)

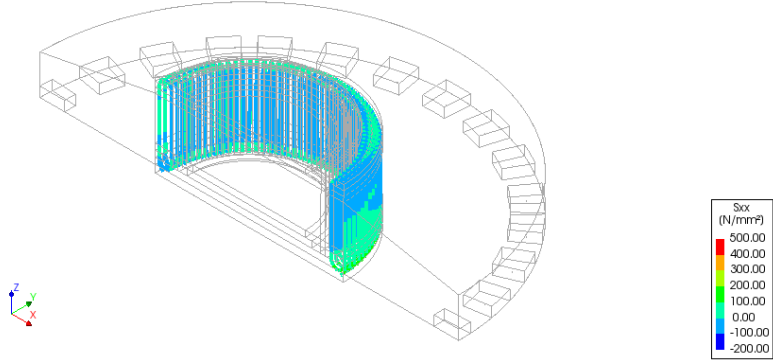
Figure 6.55: Steel stress in the Bottom tangential rebars near piles b) Model 5

Analysis 1
Phase 1.1 - wind_ref, Load-step 29, Load-factor 1.0000
Reinforcement Cauchy Total Stresses Sxx layer 1
min: -57.12N/mm² max: 201.50N/mm²



(a)

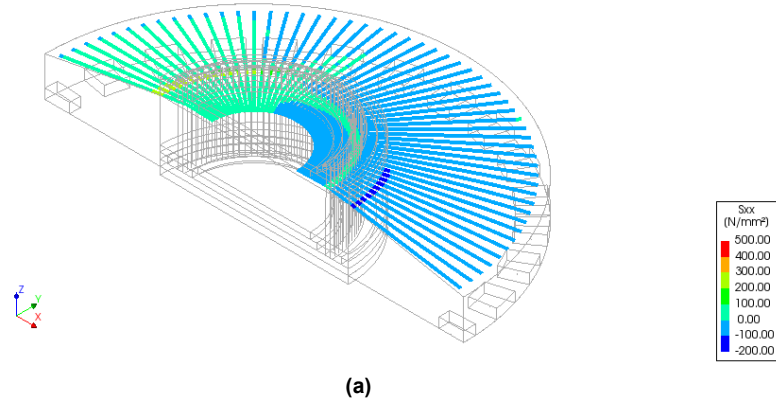
Analysis 1
Phase 1.1 - wind_ref, Load-step 29, Load-factor 1.0000
Reinforcement Cauchy Total Stresses Sxx layer 1
min: -44.01N/mm² max: 180.47N/mm²



(b)

Figure 6.56: Steel stress in the stirrups a) Model 4, b) Model 5

Analysis 1
Phase 1.1 - wind_ref, Load-step 29, Load-factor 1.0000
Reinforcement Cauchy Total Stresses Sxx layer 1
min: -132.98N/mm² max: 302.69N/mm²



Analysis 1
Phase 1.1 - wind_ref, Load-step 29, Load-factor 1.0000
Reinforcement Cauchy Total Stresses Sxx layer 1
min: -112.13N/mm² max: 303.66N/mm²

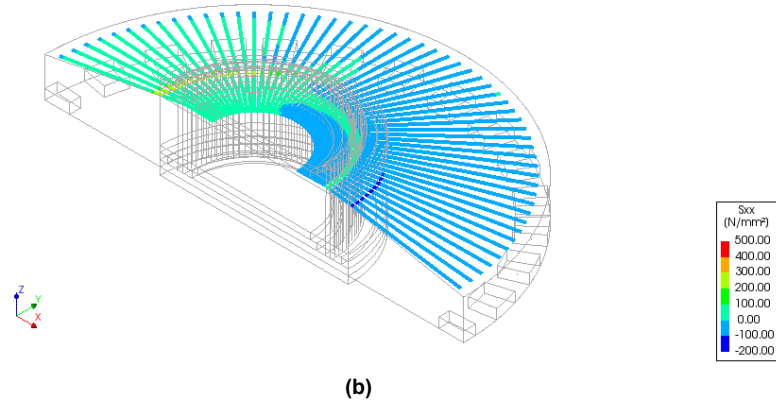


Figure 6.57: Steel stress in the Top radial rebar a) Model 4, b) Model 5

Analysis 1
Phase 1.1 - wind_ref, Load-step 29, Load-factor 1.0000
Reinforcement Cauchy Total Stresses Sxx layer 1
min: -40.94N/mm² max: 337.76N/mm²

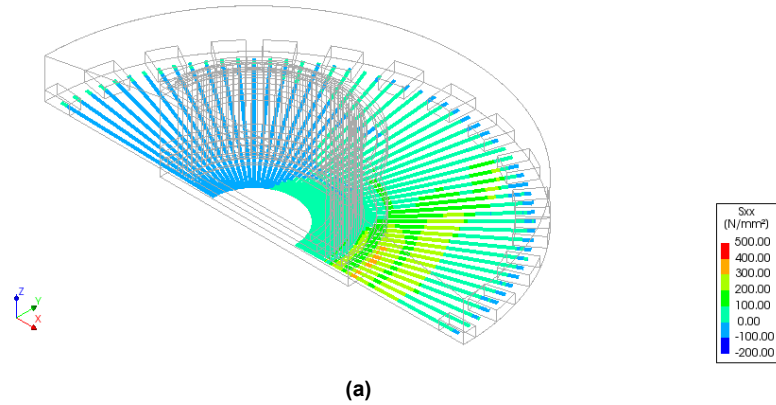


Figure 6.58: Steel stress in the Bottom radial rebar a) Model 4

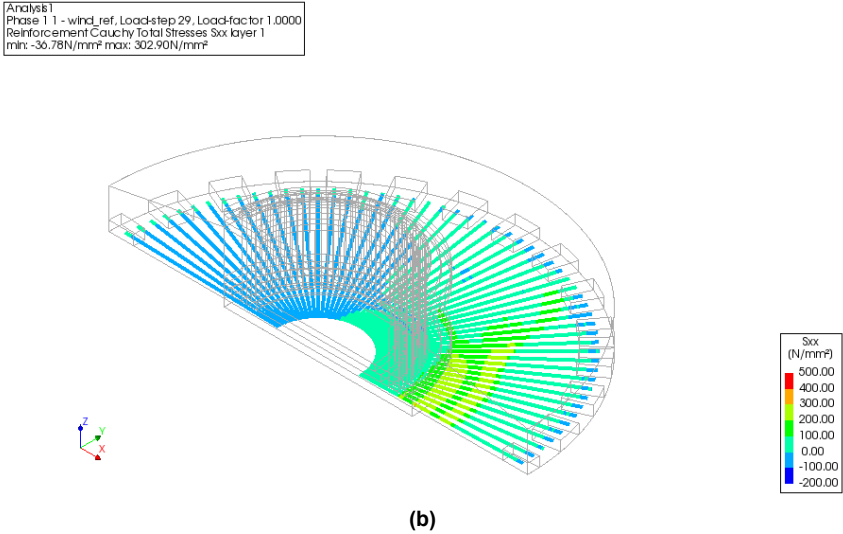


Figure 6.58: Steel stress in the Bottom radial rebar b) Model 5

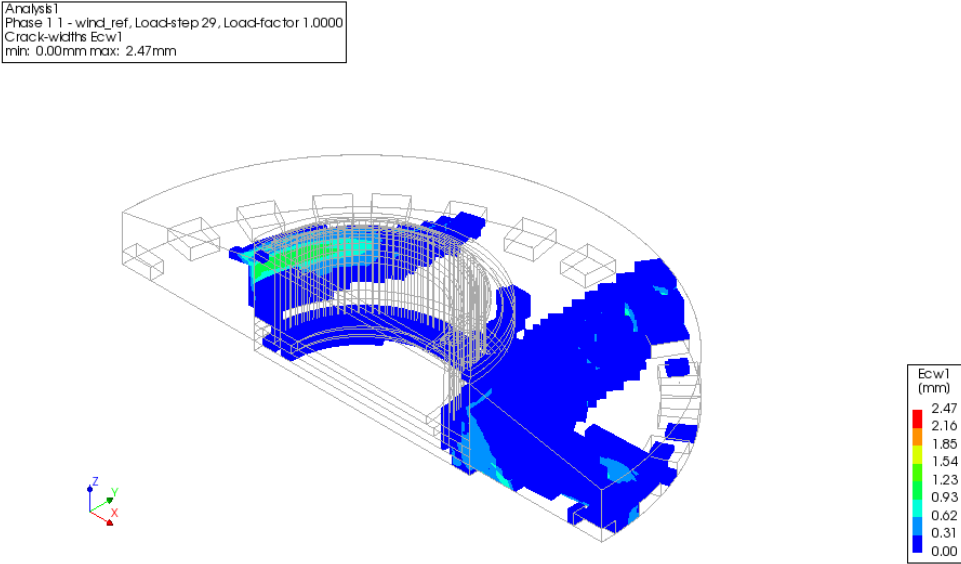


Table 6.11: Comparison between the DIANA Model 4 and DIANA Model 5

Measuring Locations	Directions	Model 4		Model 5	
		Tensile stress (MPa)	Compressive stress (MPa)	Tensile stress (MPa)	Compressive stress (MPa)
L01	A	-	-	-	-
	B	-	-	-	-
	C	-	-	-	-
	D	-	-	-	-
L02	A	245.802	-	238.57	-
	B	-	-9.701	-	-7.5
	C	-	-58.09	-	-52.03
	D	-	-	-	-
L03	A	10.233	-	10.93	-
	B	-	-0.602	0.38	-
	C	-	-12.905	-	-13.16
	D	-	-	-	-
L04	A	20.131	-	17.3	-
	B	-	-8.689	-	-8.83
	C	-	-9.67	-	-0.85
	D	-	-	-	-
L05	A	-	-16.23	-	-15.85
	B	14.143	-	6.3	-
	C	242.37	-	217.1743	-
	D	-	-	-	-
L06	A	-	-4.65	-	-5.35
	B	-	-2.403	-	-1.24
	C	38.523	-	22.37	-
	D	-	-	-	-
L07	A	5.3	-	5.43	-
	B	-	-5.724	-	-4.34
	C	-	-12.663	-	-11.884
	D	-	-	-	-
L08	A	-	-0.094	-	-0.771
	B	3.854	-	2.802	-
	C	70.806	-	11.04	-
	D	-	-	-	-

Table 6.12: Comparison between the Field measurement and DIANA Model 5

Measuring Locations	Directions	Field Measurement 2017		Model 5	
		Tensile stress (MPa)	Compressive stress (MPa)	Tensile stress (MPa)	Compressive stress (MPa)
L01	A	182.21	-118.53	-	-
	B	10.66	-20.16	-	-
	C	117.07	-160.99	-	-
	D	-	-	-	-
L02	A	21.97	-12.47	238.57	-
	B	5.1	-3.4	-	-7.5
	C	15.4	-19.94	-	-52.03
	D	3.06	-4.68	-	-
L03	A	3.13	-1.87	10.93	-
	B	1.08	-0.76	0.38	-
	C	3.13	-4.13	-	-13.16
	D	0.7	-1.15	-	-
L04	A	4.64	-2.94	17.3	-
	B	1.32	-0.92	-	-8.83
	C	3.7	-5.1	-	-0.85
	D	0.96	-1.42	-	-
L05	A	5.04	-7.5	-	-15.85
	B	1.67	-2.33	6.3	-
	C	8.96	-6.04	217.174	-
	D	2.23	-1.55	-	-
L06	A	2.12	-2.9	-	-5.35
	B	0.85	-1.19	-	-1.24
	C	3.13	-1.99	22.37	-
	D	0.94	-0.68	-	-
L07	A	2.49	-1.13	5.43	-
	B	0.5	-0.38	-	-4.34
	C	0.82	-0.73	-	-11.884
	D	0.25	-0.33	-	-
L08	A	1.46	-2.17	-	-0.771
	B	0.61	-0.81	2.802	-
	C	2.09	-1.39	11.04	-
	D	0.76	-0.5	-	-

Conclusion: Both models 4 and 5 contain soil bedding under the foundation but in comparison to Model 4, the current model has a high bedding stiffness. When a comparison is drawn between the two models in Table 6.11, it is noticed that the high bedding stiffness does have a significant effect on the steel stress and the crack width. The stresses in the bottom reinforcements have reduced significantly as compared to the top reinforcements as also shown in the Figure 6.53-Figure 6.58. The stress in the bottom reinforcements has decreased up to 84% more than the Model 4 and the stress in the other locations has been lowered until 92%. The presence of bedding resulted in compressive stresses in the bottom which in turn limited the crack widths as depicted in Figure 6.59. Now the cracks have reduced comparatively on the bottom side to 2.47mm. This proves that providing high stiffness to the model in DIANA can mimic the behavior of the real structure. Although the stress in the top and bottom radial are 9 and 23 times higher respectively as represented in Table 6.12 than what is measured, the next sections will focus more on reducing the stresses in those locations. Since adding bedding underneath worked well for the bottom reinforcements the same thing will be repeated for all other sides.

6.6.3. Results of Variant 6

In the previous sections, the bedding stiffness along with the piles helped in lowering the steel stresses and limited the crack width to a certain extent for the bottom reinforcements. Since the concrete foundation is fully covered in the soil, and the ground level is much higher in this foundation as shown in Figure 5.1, Model 6 will represent the exact situation where the bedding stiffness is provided in all the surfaces i.e. top, bottom, and side. A bedding stiffness of 3600 kN/m^3 along with the HTC 2 is provided in the model. Figure 6.60 shows the foundation model along with the bedding.

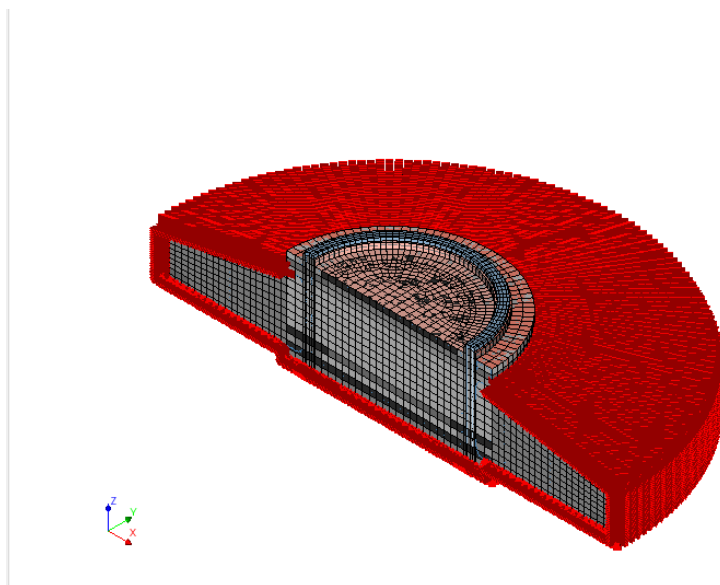


Figure 6.60: Bedding on all sides of the foundation

Effects of Combined analysis

Since the hydration heat analysis remains the same as the previous models, and it is already been noted in subsection 6.6.1, that the bedding does not have any effect on the hydration process due to the modeling simplification in the DIANA, the final results after applying the wind load are discussed in this section.

Analysis1
Phase 1.1 - wind_ref, Load-step 29, Load-factor 1.0000
Reinforcement Cauchy Total Stresses Sxx layer 1
min: -17.71N/mm² max: 162.94N/mm²

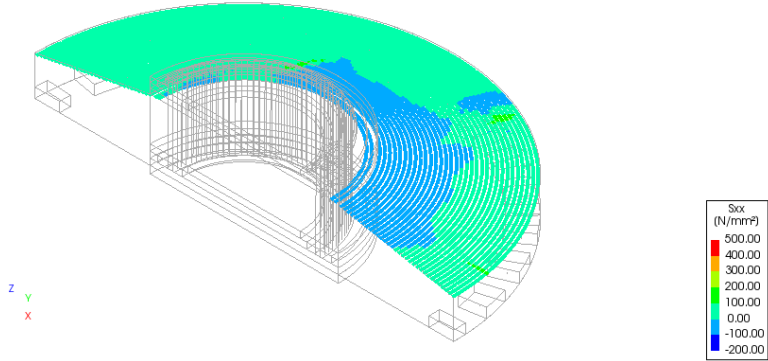


Figure 6.61: Top tangential rebar

Analysis1
Phase 1.1 - wind_ref, Load-step 29, Load-factor 1.0000
Reinforcement Cauchy Total Stresses Sxx layer 1
min: -5.00N/mm² max: 163.11N/mm²

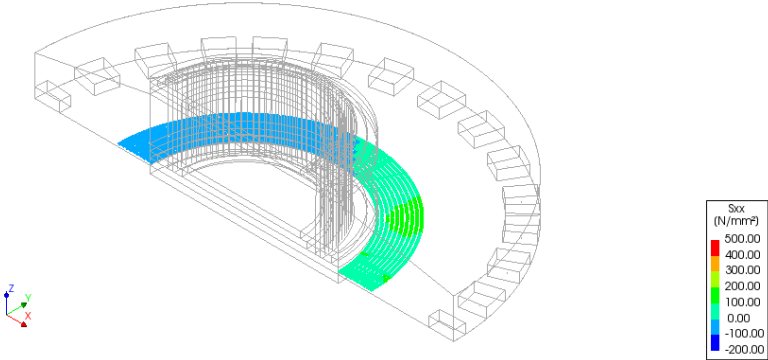


Figure 6.62: Bottom tangential rebar

Analysis1
Phase 1.1 - wind_ref, Load-step 29, Load-factor 1.0000
Reinforcement Cauchy Total Stresses Sxx layer 1
min: -10.98N/mm² max: 303.58N/mm²

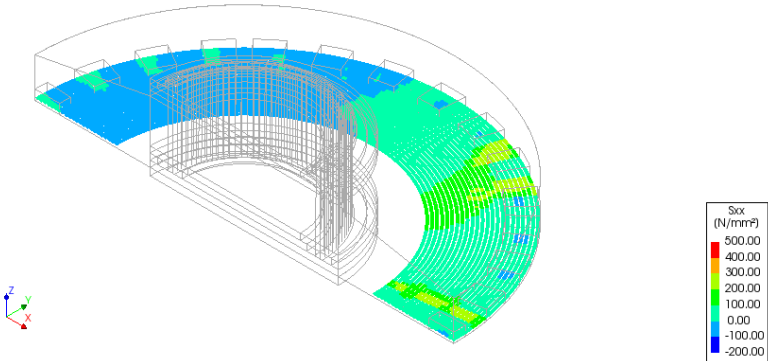


Figure 6.63: Bottom tangential rebar near the piles

Analysis1
Phase 1.1 - wind_ref, Load-step 29, Load-factor 1.0000
Reinforcement Cauchy Total Stresses Sxx layer 1
min: -64.87N/mm² max: 208.80N/mm²

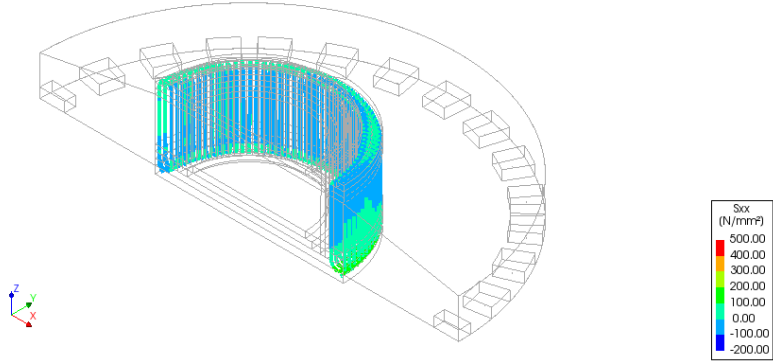


Figure 6.64: Side stirrup

Analysis1
Phase 1.1 - wind_ref, Load-step 29, Load-factor 1.0000
Reinforcement Cauchy Total Stresses Sxx layer 1
min: -136.37N/mm² max: 307.45N/mm²

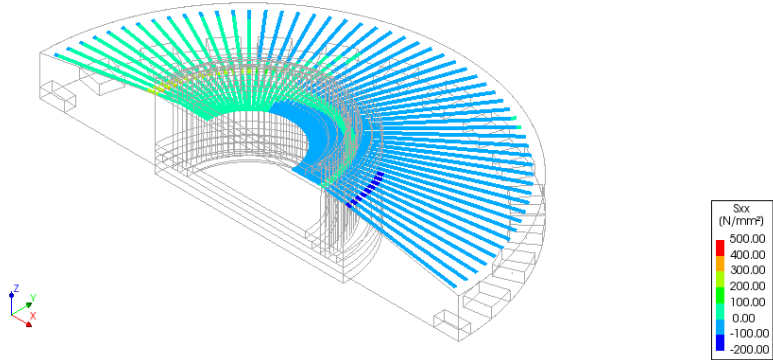


Figure 6.65: Top radial rebar

Analysis1
Phase 1.1 - wind_ref, Load-step 29, Load-factor 1.0000
Reinforcement Cauchy Total Stresses Sxx layer 1
min: -41.97N/mm² max: 342.97N/mm²

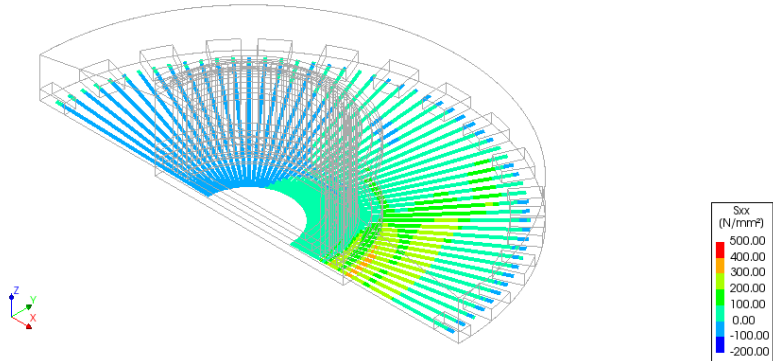


Figure 6.66: Bottom radial rebar

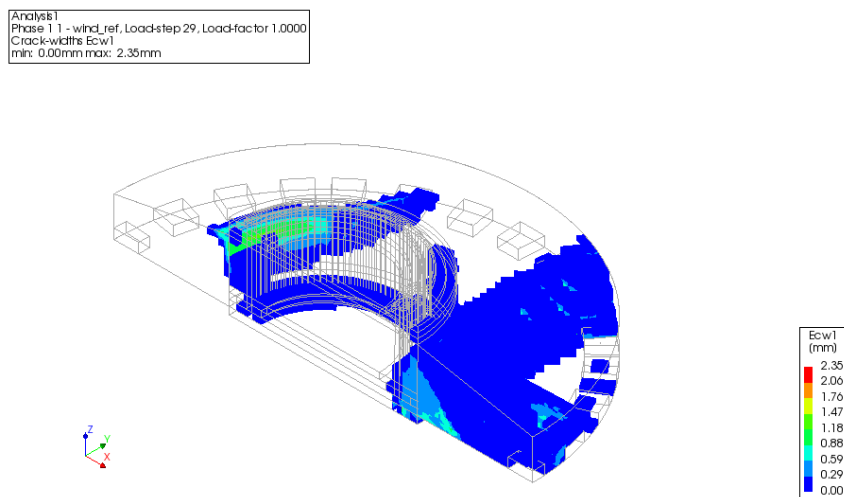


Figure 6.67: Crack patterns

Conclusion: The stress behavior is logical as described in Figure 6.61 to Figure 6.66. The top bars contain tensile stress in the North direction and compressive stress in the south direction. While the exact opposite behavior is observed in the case of the bottom bars. From the Table 6.8 and Table 6.13, this is observed that steel stresses in different locations lowered quite a lot as compared to Model 3, especially in the top radial rebars (L02) where a reduction of 57% is observed in the North position and a reduction of up to 92% is observed in the case of the bottom rebars. Hence the purpose of adding soil bedding on all sides is satisfied since it resulted in more compression in the foundation structure leading to less tensile stresses in the foundation and resulting in narrower crack patterns as presented in Figure 6.67. Even though the soil bedding is modeled as a simplified boundary interface in the model, this variant has shown positive results. Also, it is to be noted that there are no tensile stresses present in the interface between the bedding and the concrete foundation. Unlike Model 4 and Model 5, in this case, the reduction is noticed in both top and bottom locations. Even though the bottom radial bars (L05) are still experiencing higher stresses in regions such as L05 C which is still 26 times higher than the field measurements as presented in Table 6.13. This may also happen due to the uneven distribution of stresses in the model due to the modeling of linear elastic piles. In the case of the other locations, such as the top, the stresses in the rebars deviate up to only 4 times which showed a deviation of a factor of 10 in previous models. Taking this into consideration, another effect will be added to the model after which the DIANA model will exactly replicate the structure present on-site.

Table 6.13: Comparison between the Field measurement and DIANA Model 6

Measuring Locations	Directions	Field Measurement 2017		Model 6	
		Tensile stress (MPa)	Compressive stress (MPa)	Tensile stress (MPa)	Compressive stress (MPa)
L01	A	182.21	-118.53	-	-
	B	10.66	-20.16	-	-
	C	117.07	-160.99	-	-
	D	-	-	-	-
L02	A	21.97	-12.47	105.9	-
	B	5.1	-3.4	-	-10
	C	15.4	-19.94	-	-58.8
	D	3.06	-4.68	-	-
L03	A	3.13	-1.87	10.09	-
	B	1.08	-0.76	-	-0.61
	C	3.13	-4.13	-	-13.94
	D	0.7	-1.15	-	-
L04	A	4.64	-2.94	6.5	-
	B	1.32	-0.92	-	-8.5
	C	3.7	-5.1	-	-1.031
	D	0.96	-1.42	-	-
L05	A	5.04	-7.5	-	-16.344
	B	1.67	-2.33	7.68	-
	C	8.96	-6.04	242.87	-
	D	2.23	-1.55	-	-
L06	A	2.12	-2.9	-	-4.55
	B	0.85	-1.19	-	-0.6
	C	3.13	-1.99	27.58	-
	D	0.94	-0.68	-	-
L07	A	2.49	-1.13	4.71	-
	B	0.5	-0.38	-	-5.8
	C	0.82	-0.73	-	-13.44
	D	0.25	-0.33	-	-
L08	A	1.46	-2.17	0.117	-
	B	0.61	-0.81	2.446	-
	C	2.09	-1.39	25.272	-
	D	0.76	-0.5	-	-

6.7. Effect of Inclined Piles

In the Riemst wind turbine foundation, there are 28 piles placed equidistantly in an inclined direction as shown in Figure 6.68. In the DIANA models, the piles are modeled as a dummy bond-slip reinforcement where at the bottom of the foundation, a point interface element depicted as a linear elastic spring is attached to the dummy bond-slip reinforcement, and the other end is supported in x, y, and z directions. When a foundation is supported on inclined piles, the foundation is restrained in the horizontal direction as well. This restraint provides a horizontal stiffness to the foundation, which again may help to reduce the steel stresses in the bottom reinforcements and limit the crack width. This chapter will be dedicated to the models with such effects along with the thermo-mechanical analysis and inclusion of the bedding in the wind turbine foundation.

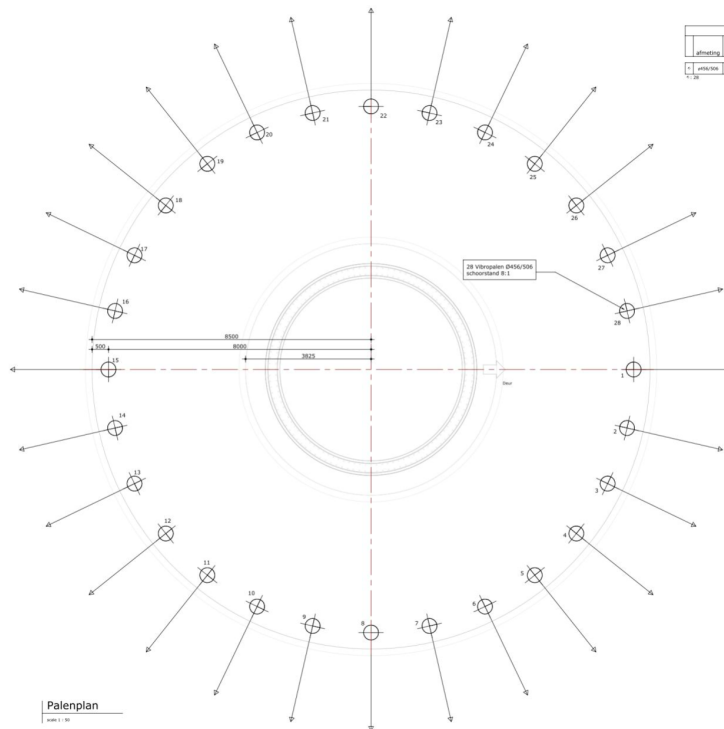


Figure 6.68: Depiction of Piles in the Riemst wind turbine foundation

6.7.1. Results of Variant 7

The wind turbine foundation in Riemst contains 28 inclined piles which in the previous models were just modeled as straight pile springs. Even after so many modifications in the earlier models, the steel stress in the top radial and bottom radial in the North and South positions respectively are very high. The wind directions are mentioned in Figure 6.2. Hence, in the current model, the inclusion of inclined piles is taken into account along with the thermo-mechanical analysis. In this, the piles are assumed to be inclined at a ratio of 1:8. Piles are inclined and modeled as support springs in the following way:

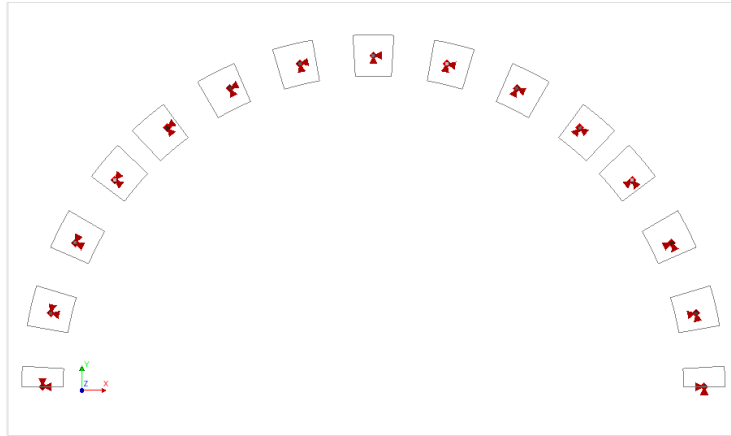


Figure 6.69: Inclined pile supports in the model

The pile stiffness values are calculated as follows-

$$k_{\text{axial}} = 270 \frac{MN}{m} \quad (6.1)$$

$$k_{\text{lateral}} = 27 \frac{MN}{m}$$

$$\tan \alpha = \frac{1}{8} \rightarrow \alpha = 7.125^\circ \quad (6.2)$$

$$k_{\text{vertical}} \approx k_{\text{axial}} = 270 \frac{MN}{m}$$

$$k_{y'} = k_{\text{lateral}} = 27 \frac{MN}{m} \quad (6.3)$$

$$k_{x'} = k_{\text{lateral}} + k_{\text{axial}} \cdot \sin \alpha = 27 + 33 = 60 \frac{MN}{m}$$

The inclined piles provide horizontal stiffness to the foundation, which results in additional horizontal reaction forces in the foundation. Often this may lead to an arching effect in the bottom part of the concrete structure leading to compressive stresses on the bottom side. This is illustrated in Figure 6.70, where the red arc is the effect of the arching due to the additional horizontal forces.

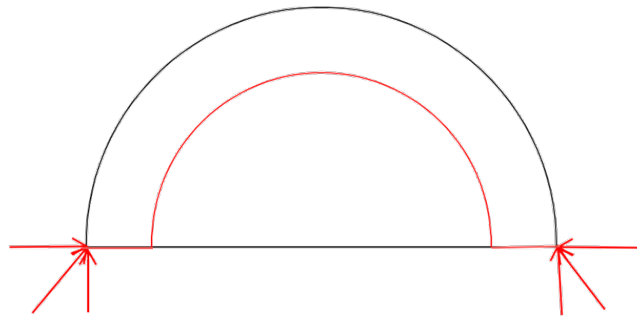
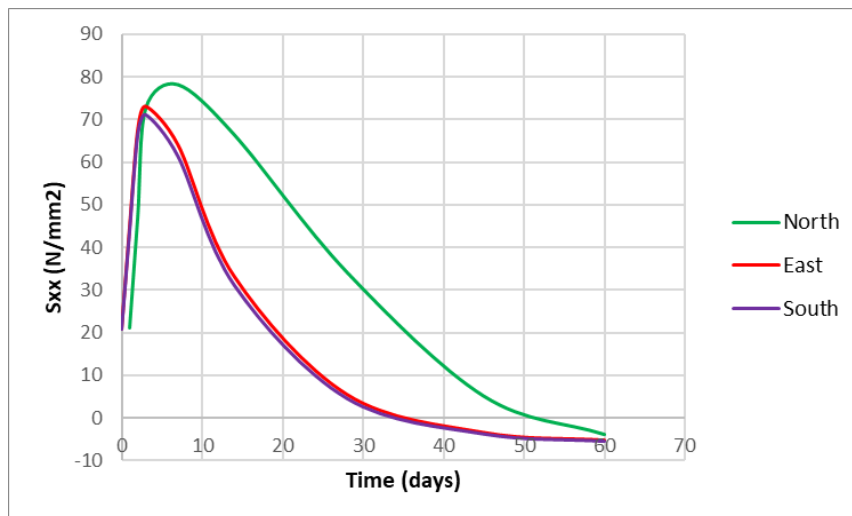


Figure 6.70: Illustration of the arching effect

The heat development inside the mass structure due to the hydration effect remains the same as in Models 3 to 5 since the heat boundary conditions are the same. The inner core reaches the maximum temperature of 61 °C on day 3, after which it gradually begins to cool down. The thermal evolution is presented in the Figure 6.32.

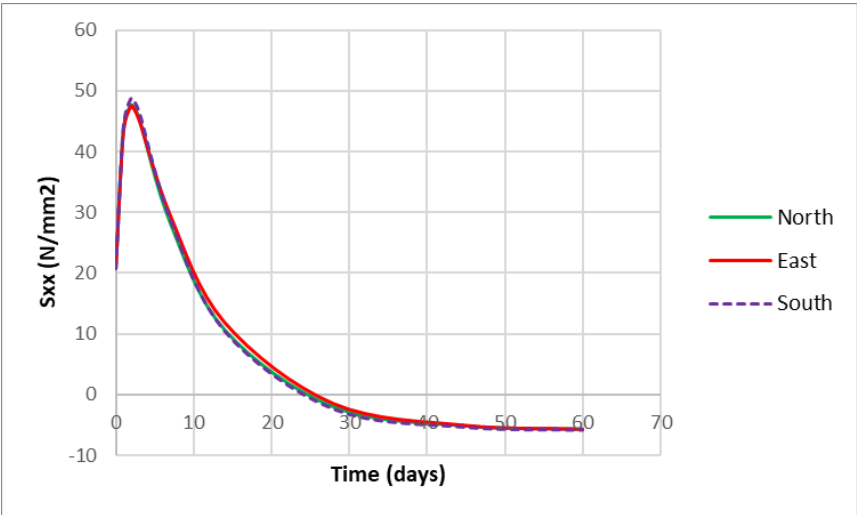
Steel stresses due to the Hydration heat

Due to the same hydration heat parameters, the generated stress in the reinforcements is identical to that in Model 3. The horizontal stiffness from the inclined piles will not have any effect on the heat of hydration calculations.

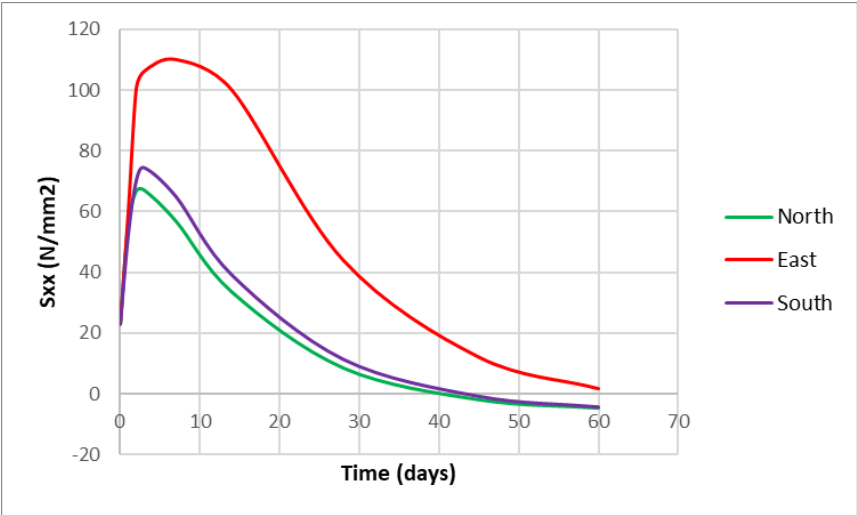


(a)

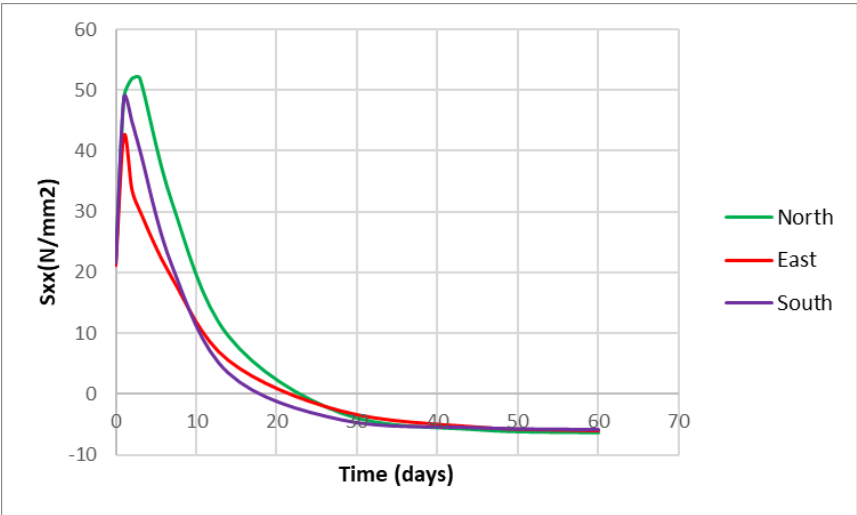
Figure 6.71: Steel stress wrt time at each wind directions a) Top radial



(b)



(c)



(d)

Figure 6.71: Steel stress wrt time at each wind directions b) Bottom radial, c) Top tangential, d) Bottom tangential

Effects of Combined analysis

This section deals with the combined analysis after including the inclined piles in the model. The loads applied will be the same in this case as well and the final result after applying the measured bending moment is presented below:

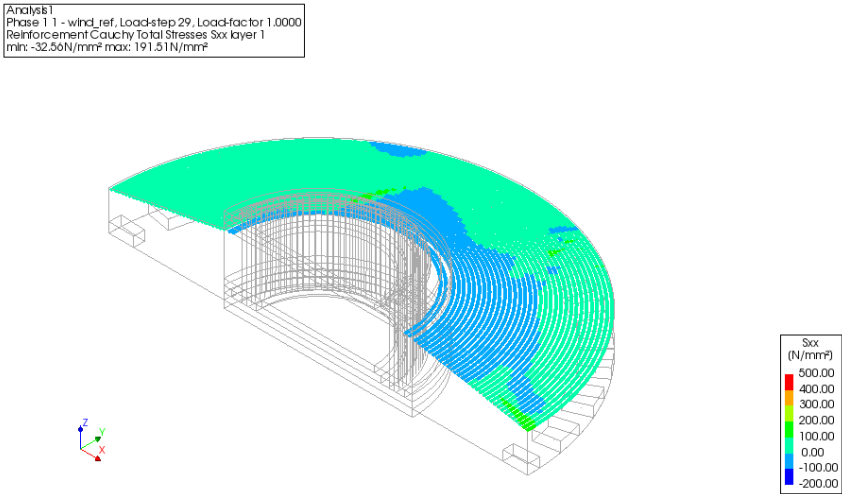


Figure 6.72: Top tangential rebar

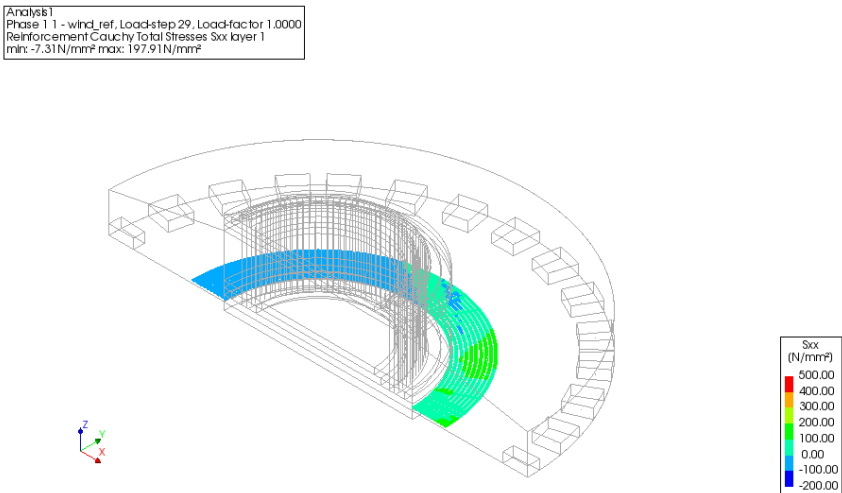


Figure 6.73: Bottom tangential rebar

Analysis1
Phase 1.1 - wind_ref, Load-step 29, Load-factor 1.0000
Reinforcement Cauchy Total Stresses Sxx layer 1
min: -16.36N/mm² max: 391.32N/mm²

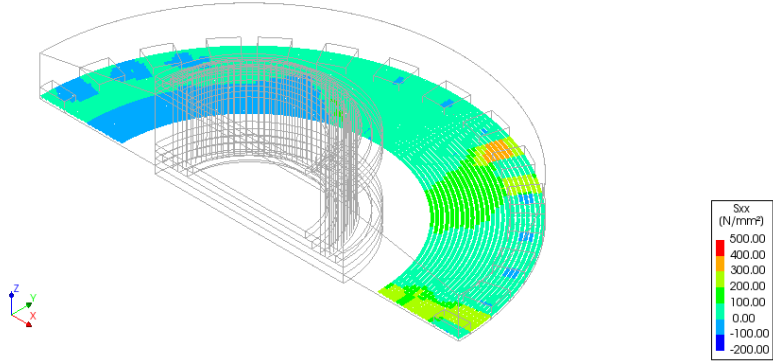


Figure 6.74: Bottom tangential rebar near the piles

Analysis1
Phase 1.1 - wind_ref, Load-step 29, Load-factor 1.0000
Reinforcement Cauchy Total Stresses Sxx layer 1
min: -62.49N/mm² max: 184.76N/mm²

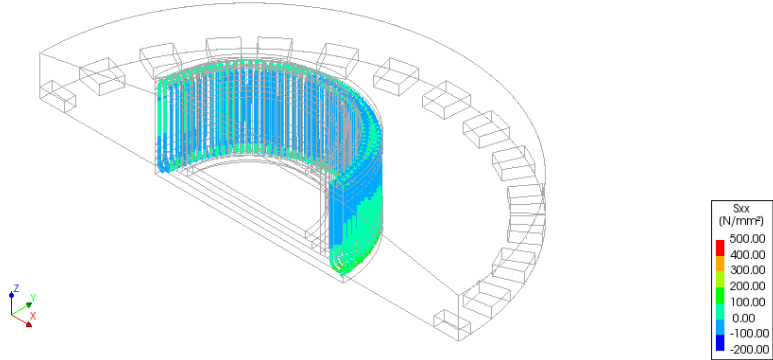


Figure 6.75: Side stirrup

Analysis1
Phase 1.1 - wind_ref, Load-step 29, Load-factor 1.0000
Reinforcement Cauchy Total Stresses Sxx layer 1
min: -159.70N/mm² max: 306.91N/mm²

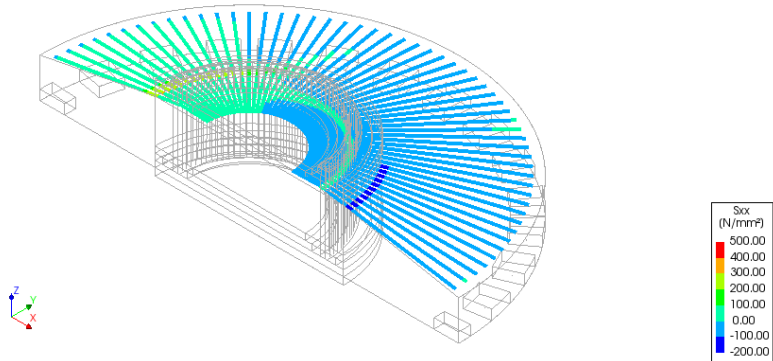


Figure 6.76: Top radial rebar

Analysis1
Phase 1.1 - wind_ref, Load-step 29, Load-factor 1.0000
Reinforcement Cauchy Total Stresses Sxx layer 1
min: -72.58N/mm² max: 339.76N/mm²

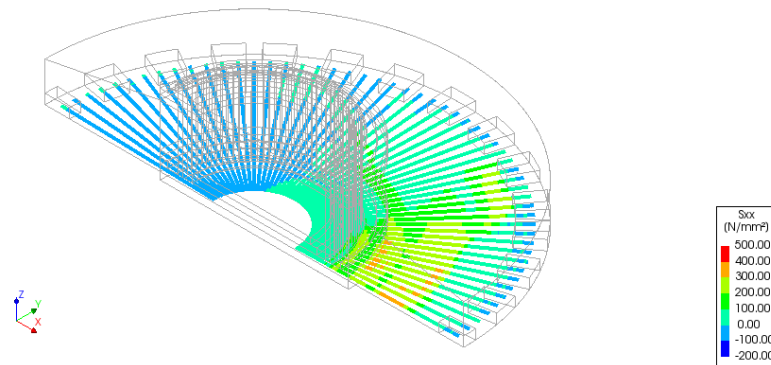


Figure 6.77: Bottom radial rebar

Analysis1
Phase 1.1 - wind_ref, Load-step 29, Load-factor 1.0000
Crack-widths Ecw1
min: 0.00mm max: 2.93mm

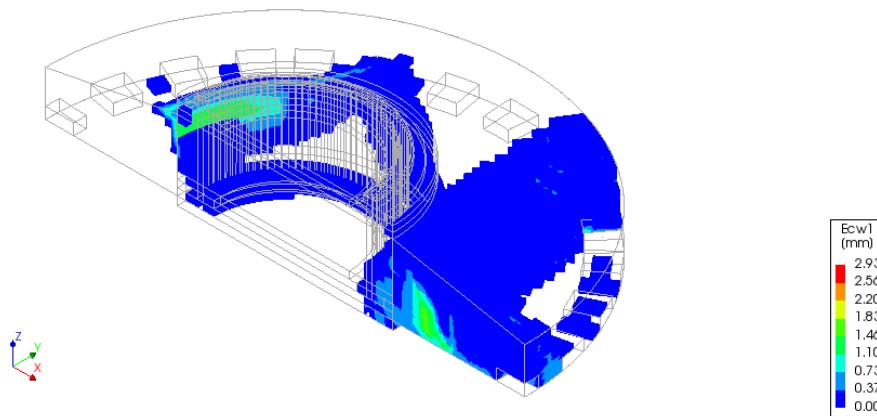


Figure 6.78: Crack patterns

Conclusion: The combined analysis of Model 7 leads to a reduction within a range of 5-30% in the steel stresses when compared with Model 3. Comparing both Figure 6.43 and Figure 6.78, the crack widths have reduced from 3.2mm to 2.93mm due to the lesser tensile stresses at the bottom location. The occurrence of less tensile stress is due to the extra compressive stress from the horizontal stiffness of the piles. When compared to Model 6, Model 7 did not have a positive impact on the steel stresses of top bars, as there was an observed increase of up to four times.

It can be observed from Table 6.8 and Table 6.14 that the effect of inclined piles is restricted to the bottom reinforcements. A reduction of 30% is observed between the bottom steel bars of Model 3 and Model 7. Due to the restraints provided in the horizontal direction, the stresses form an arch at the bottom rebars. Such an arching effect leads to an increase in compressive stresses at the bottom location that lowers the tensile stresses. Based on the data presented in Table 6.14, it is clear that the stress levels predicted by the model only led to a decrease in the factor of the bottom bars. Specifically, the difference was reduced from 26 times the expected results to 24 times. Another attempt will be made to combine the properties of Model 6 and Model 7 in order to observe the changes in the steel stresses due to the combination of soil bedding and the inclined piles.

Table 6.14: Comparison between the Field measurement and DIANA Model 7

Measuring Locations	Directions	Field Measurement 2017		Model 7	
		Tensile stress (MPa)	Compressive stress (MPa)	Tensile stress (MPa)	Compressive stress (MPa)
L01	A	182.21	-118.53	-	-
	B	10.66	-20.16	-	-
	C	117.07	-160.99	-	-
	D	-	-	-	-
L02	A	21.97	-12.47	174.12	-
	B	5.1	-3.4	-	-19.06
	C	15.4	-19.94	-	-50.73
	D	3.06	-4.68	-	-
L03	A	3.13	-1.87	8.64	-
	B	1.08	-0.76	-	-3.23
	C	3.13	-4.13	-	-26.535
	D	0.7	-1.15	-	-
L04	A	4.64	-2.94	20.4	-
	B	1.32	-0.92	-	-9.204
	C	3.7	-5.1	-	-10.625
	D	0.96	-1.42	-	-
L05	A	5.04	-7.5	-	-14.211
	B	1.67	-2.33	68.7	-
	C	8.96	-6.04	229.51	-
	D	2.23	-1.55	-	-
L06	A	2.12	-2.9	-	-3.4
	B	0.85	-1.19	66.018	-
	C	3.13	-1.99	61.96	-
	D	0.94	-0.68	-	-
L07	A	2.49	-1.13	4.28	-
	B	0.5	-0.38	-	-9.5
	C	0.82	-0.73	-	-20.15
	D	0.25	-0.33	-	-
L08	A	1.46	-2.17	1.56	-
	B	0.61	-0.81	4.413	-
	C	2.09	-1.39	105.26	-
	D	0.76	-0.5	-	-

6.7.2. Results of Variant 8

In Model 6, it is observed that providing bedding on all sides of the foundation helped in lowering the steel stresses to a large extent. Also, in Model 7 it is noticed that the horizontal stiffness does provide a certain amount of restraint in the bottom portion of the concrete foundation which lowers the steel stresses present at the bottom location. Now, in this model, both the effects of bedding on all sides with a bedding stiffness = 3600 kN/m^3 and inclined piles are combined. The horizontal pile stiffness is provided in subsection 6.7.1.

Effects of Combined analysis

Analysis1
Phase 1.1 - wind_ref. Load-step 29. Load-factor 1.0000
Reinforcement Cauchy Total Stresses Sxx layer 1
min: -26.46N/mm² max: 193.58N/mm²

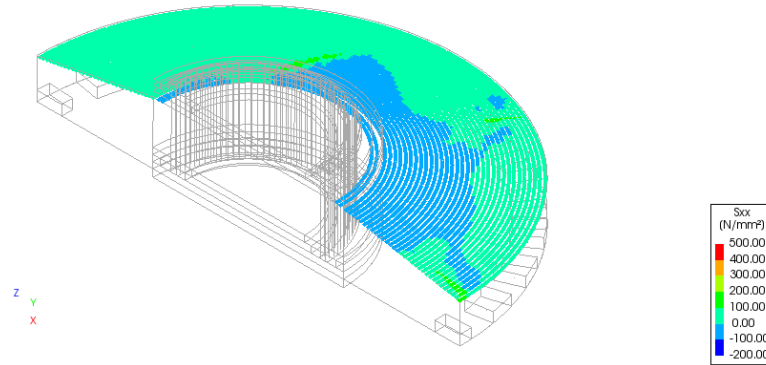


Figure 6.79: Top tangential rebar

Analysis1
Phase 1.1 - wind_ref. Load-step 29. Load-factor 1.0000
Reinforcement Cauchy Total Stresses Sxx layer 1
min: -6.51N/mm² max: 197.09N/mm²

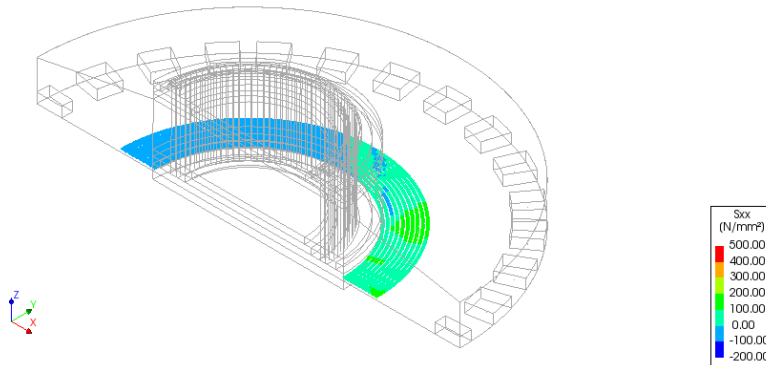


Figure 6.80: Bottom tangential rebar

Analysis 1
Phase 1.1 - wind_ref, Load-step 29, Load-factor 1.0000
Reinforcement Cauchy Total Stresses Six layer 1
min: -17.46N/mm² max: 341.23N/mm²

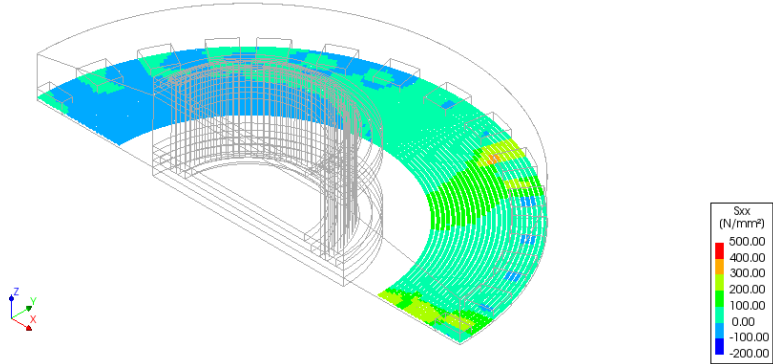


Figure 6.81: Bottom tangential rebar near the piles

Analysis 1
Phase 1.1 - wind_ref, Load-step 29, Load-factor 1.0000
Reinforcement Cauchy Total Stresses Six layer 1
min: -47.10N/mm² max: 181.49N/mm²

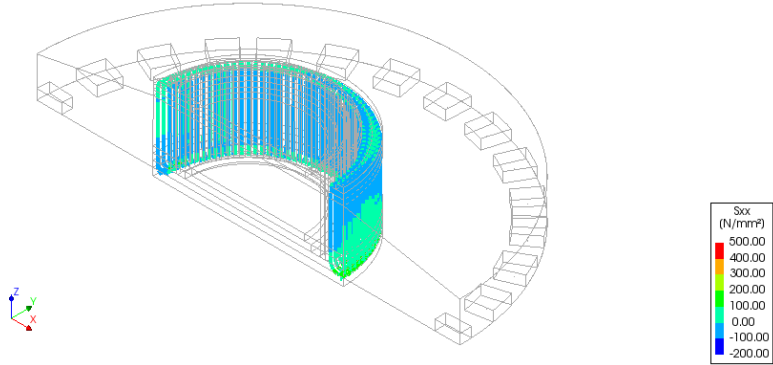


Figure 6.82: Side stirrup

Analysis 1
Phase 1.1 - wind_ref, Load-step 29, Load-factor 1.0000
Reinforcement Cauchy Total Stresses Six layer 1
min: -131.99N/mm² max: 316.02N/mm²

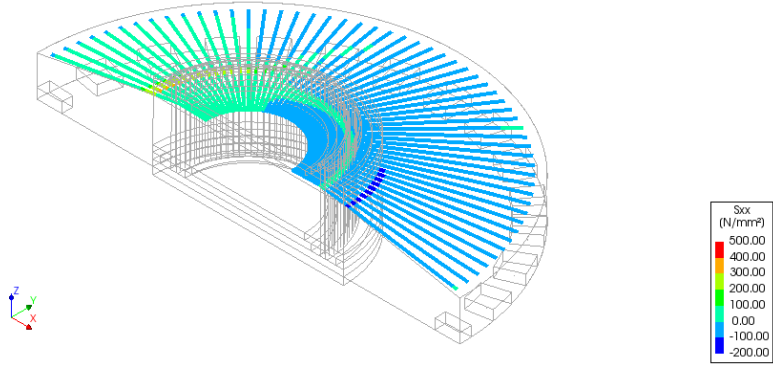


Figure 6.83: Top radial rebar

Analysis1
Phase 1 1 - wind_ref, Load-step 29, Load-factor 1.0000
Reinforcement Cauchy Total Stresses Six layer 1
min: -62.68N/mm² max: 318.89N/mm²

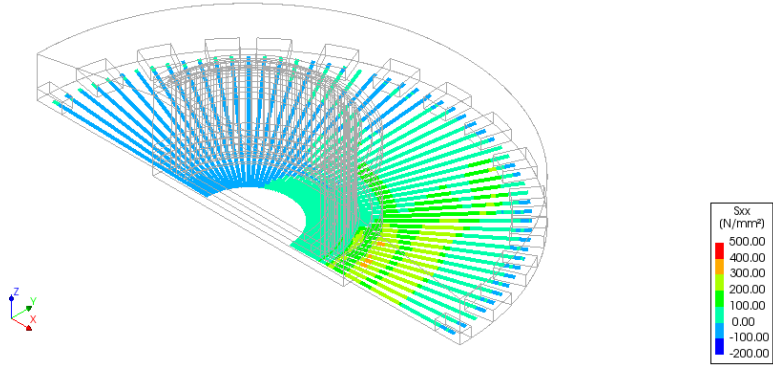


Figure 6.84: Bottom radial rebar

Analysis1
Phase 1 1 - wind_ref, Load-step 29, Load-factor 1.0000
Crack-widths Ecw1
min: 0.00mm max: 2.34mm

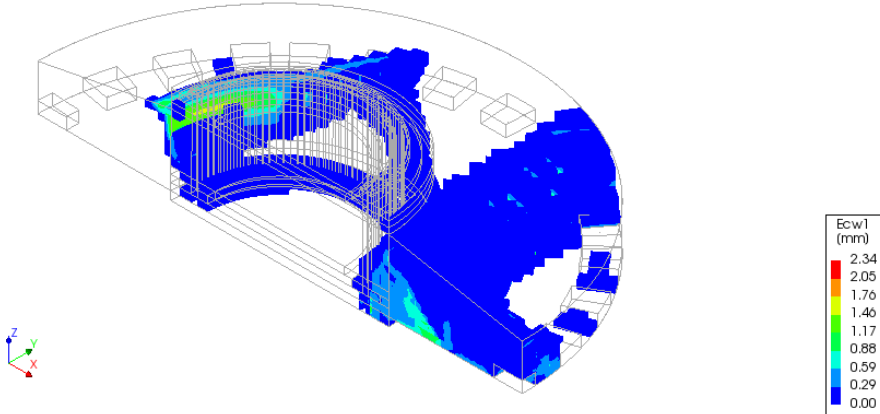


Figure 6.85: Crack patterns

Table 6.15: Comparison between the Field measurement and the DIANA Model 8

Measuring Locations	Directions	Field Measurement 2017		Model 8	
		Tensile stress (MPa)	Compressive stress (MPa)	Tensile stress (MPa)	Compressive stress (MPa)
L01	A	182.21	-118.53	-	-
	B	10.66	-20.16	-	-
	C	117.07	-160.99	-	-
	D	-	-	-	-
L02	A	21.97	-12.47	135.67	-
	B	5.1	-3.4	-	-14.58
	C	15.4	-19.94	-	-56.48
	D	3.06	-4.68	-	-
L03	A	3.13	-1.87	9.75	-
	B	1.08	-0.76	-	-2.42
	C	3.13	-4.13	-	-23
	D	0.7	-1.15	-	-
L04	A	4.64	-2.94	9.8	-
	B	1.32	-0.92	-	-8.46
	C	3.7	-5.1	-	-2.5
	D	0.96	-1.42	-	-
L05	A	5.04	-7.5	-	-18.134
	B	1.67	-2.33	45.61	-
	C	8.96	-6.04	207.405	-
	D	2.23	-1.55	-	-
L06	A	2.12	-2.9	-	-4.033
	B	0.85	-1.19	56.68	-
	C	3.13	-1.99	58.64	-
	D	0.94	-0.68	-	-
L07	A	2.49	-1.13	4.43	-
	B	0.5	-0.38	-	-8.3
	C	0.82	-0.73	-	-17.95
	D	0.25	-0.33	-	-
L08	A	1.46	-2.17	0.55	-
	B	0.61	-0.81	3.305	-
	C	2.09	-1.39	63.143	-
	D	0.76	-0.5	-	-

Conclusion: The combined effect of both inclined piles and the bedding has successfully reduced the percentage difference of steel stresses between Model 7 and Model 8 up to 77%. This shows that the provided bedding on all sides relatively reduces the generated stress in the reinforcements at all locations. Whereas, when the comparison is drawn between Models 6 and 8, a significant reduction has been noticed only in the bottom bars. This decrease is up to 20%. Not only this but due to the additional horizontal restraints in the bottom portion of the foundation, there are locations that have concentrated higher compressive stresses. These additional compressive stresses at the bottom location reduced the bottom tensile stresses, especially at the location of L05 C. The steel stress in Model 6 was 242 MPa while in the current model, it is 207 MPa. Based on the information presented in Table 6.13 and Table 6.15, it can be concluded that the steel stresses vary significantly compared to the field measurement. Specifically, the stresses differ by 26 times and 22 times in Model 6 and Model 8, respectively. While the percentage

gap has increased in Model 8 to Model 6 in the case of the top rebars by 45%. From Figure 6.85, the cracks are narrower in comparison to Figure 6.67. This implies that the addition of both inclined piles and bedding has a positive influence in reducing the cracks in the foundation.

6.7.3. Sensitivity Analysis-Variant 9

This section will include a model with a fictitiously high bedding stiffness of $20E+06 \text{ kN}/m^3$ and a very high horizontal pile stiffness of $300 \text{ MN}/m$.

Effect of Combined analysis

Analysis1
Phase 1 1 - wind_ref, Load-step 29, Load-factor 1.0000
Reinforcement Cauchy Total Stresses Sxx layer 1
min: -11.65N/mm² max: 171.10N/mm²

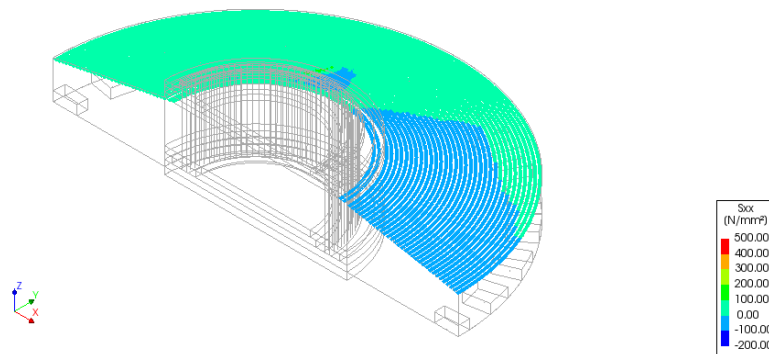


Figure 6.86: Top tangential rebar

Analysis1
Phase 1 1 - wind_ref, Load-step 29, Load-factor 1.0000
Reinforcement Cauchy Total Stresses Sxx layer 1
min: -5.98N/mm² max: 147.67N/mm²

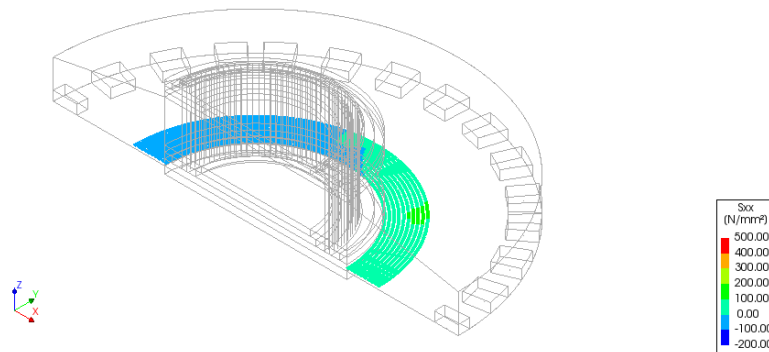


Figure 6.87: Bottom tangential rebar

Analysis1
Phase 1.1 - wind_ref, Load-step 29, Load-factor 1.0000
Reinforcement Cauchy Total Stresses Sxx layer 1
min: -9.45N/mm² max: 228.18N/mm²

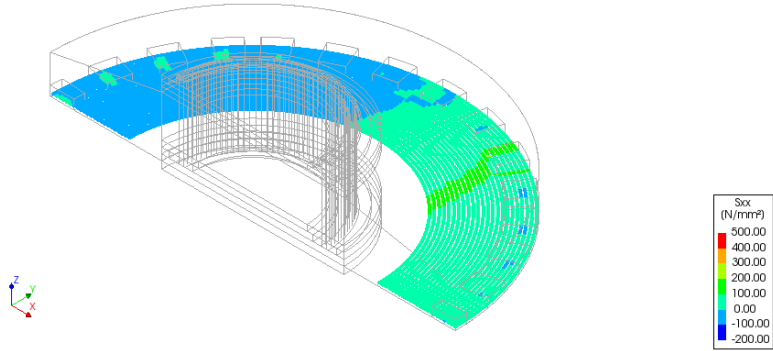


Figure 6.88: Bottom tangential rebar near the piles

Analysis1
Phase 1.1 - wind_ref, Load-step 29, Load-factor 1.0000
Reinforcement Cauchy Total Stresses Sxx layer 1
min: -39.77N/mm² max: 96.99N/mm²

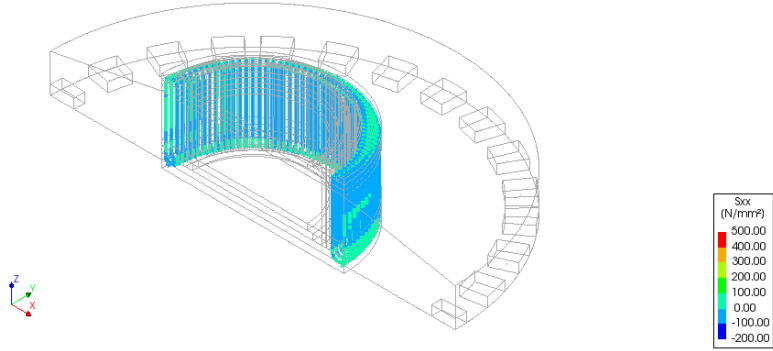


Figure 6.89: Side stirrup

Analysis1
Phase 1.1 - wind_ref, Load-step 29, Load-factor 1.0000
Reinforcement Cauchy Total Stresses Sxx layer 1
min: -69.17N/mm² max: 312.96N/mm²

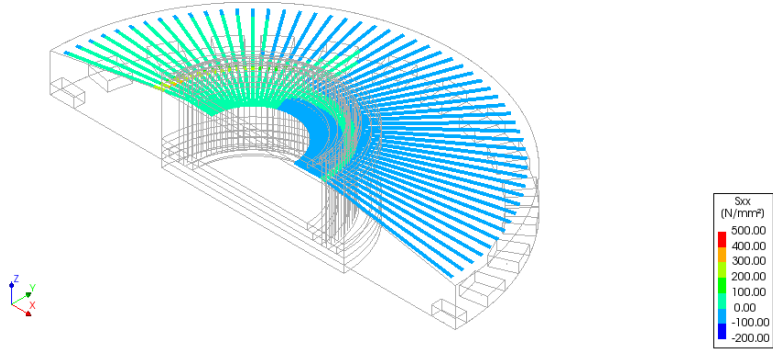


Figure 6.90: Top radial rebar

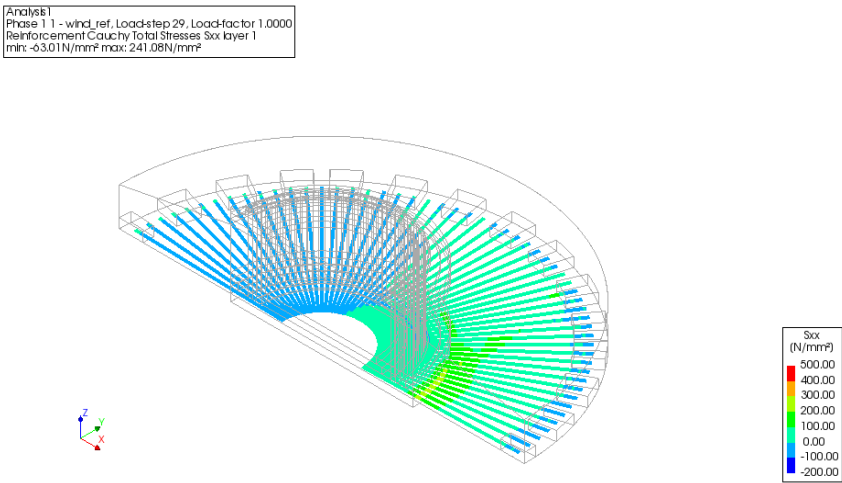


Figure 6.91: Bottom radial rebar

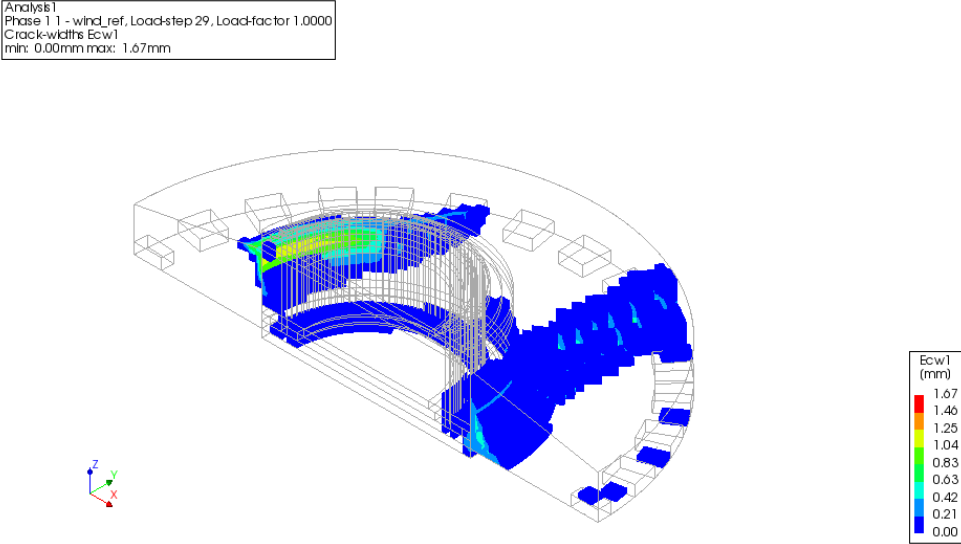


Figure 6.92: Crack patterns

Table 6.16: Comparison between the Field measurement and the DIANA Model 9

Measuring Locations	Directions	Field Measurement 2017		Model 9	
		Tensile stress (MPa)	Compressive stress (MPa)	Tensile stress (MPa)	Compressive stress (MPa)
L01	A	182.21	-118.53	-	-
	B	10.66	-20.16	-	-
	C	117.07	-160.99	-	-
	D	-	-	-	-
L02	A	21.97	-12.47	99.38	-
	B	5.1	-3.4	-	-6.56
	C	15.4	-19.94	-	-42.86
	D	3.06	-4.68	-	-
L03	A	3.13	-1.87	11.54	-
	B	1.08	-0.76	1.08	-
	C	3.13	-4.13	-	-10.25
	D	0.7	-1.15	-	-
L04	A	4.64	-2.94	6.13	-
	B	1.32	-0.92	-	-8.45
	C	3.7	-5.1	-	-1.755
	D	0.96	-1.42	-	-
L05	A	5.04	-7.5	-	-16.33
	B	1.67	-2.33	7.6	-
	C	8.96	-6.04	164.97	-
	D	2.23	-1.55	-	-
L06	A	2.12	-2.9	-	-5.51
	B	0.85	-1.19	11.58	-
	C	3.13	-1.99	12.37	-
	D	0.94	-0.68	-	-
L07	A	2.49	-1.13	3.26	-
	B	0.5	-0.38	-	-4.4
	C	0.82	-0.73	-	-14.62
	D	0.25	-0.33	-	-
L08	A	1.46	-2.17	-	-0.79
	B	0.61	-0.81	0.711	-
	C	2.09	-1.39	11.10	-
	D	0.76	-0.5	-	-

Conclusion: Figure 6.86-Figure 6.91 shows the stress distribution for Model 9. It is noticed that the stress concentrations are lesser as compared to the previous models, especially at the bottom reinforcements due to the extra stiffness. Providing a higher bedding stiffness and horizontal pile stiffness not only helped in achieving better results for the steel stresses but also reduced the cracks in the foundation when compared to Model 8. The maximum crack widths have decreased from 2.34mm to 1.67mm. Due to the extra prestressing force coming from the soil, the cracks in the foundation after applying the measured bending moment have decreased. From the observed results in Figure 6.92, the cracks are fewer, and the generated steel stresses due to the applied bending moment are low as well as described in Table 6.16. Between Model 8 and Model 9, the reduction in the current model is in the range of 20-244%. The values used for the sensitivity study are fictional but this model did give better results since it successfully not only lowered the steel stress but also reduced the cracks in the foundation. When compared with the field measurement in Table 6.16, the steel stresses are still higher but now the difference of the variation has been reduced to 3-17 times which was earlier varying within a range 10-30 times higher the measured values. Hence, it can be deduced from all the models analyzed that the wind turbine foundation is getting additional stiffness from the surrounding which is helping it to remain uncracked due to the cyclic loading. Also, the stress distribution in the bars plays a significant role to achieve similar conditions in the FEM model.

Results and Discussion

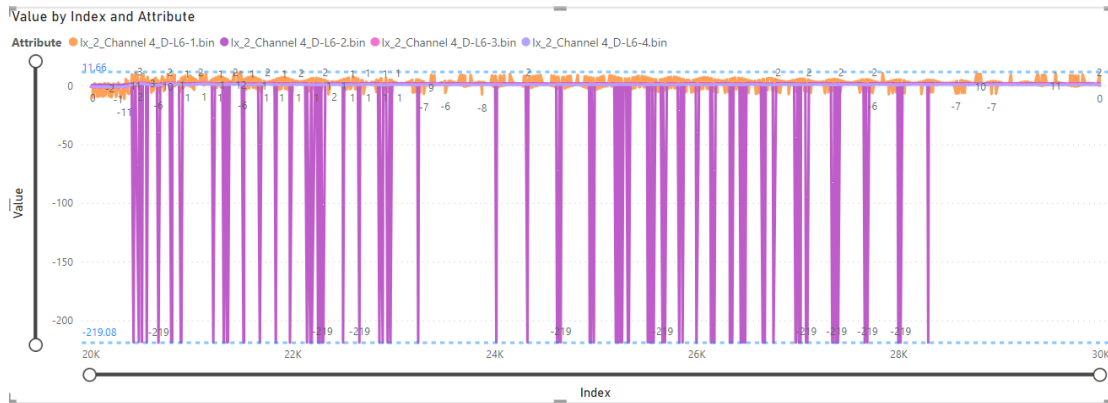
This chapter includes the results of all the analyses conducted for the current research project and is explained consecutively. The section also consists of a detailed report of the field measurement and the structural SCIA calculation to verify the FEM model.

7.1. Field Monitoring of strain measurements

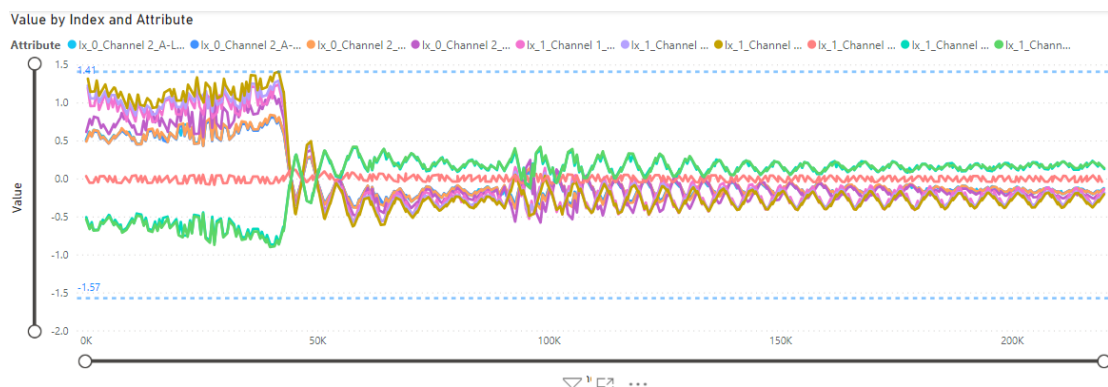
The third chapter of the project includes the structural monitoring of the concrete foundation present at Riemst, Belgium. The fiber optic sensors are installed in the onshore wind turbine foundation during its construction at various locations to monitor the wind turbine foundation during its service life. The measurements from the FBG sensors are differential. Three measurements have been conducted on this concrete foundation. A brief discussion of the results obtained from these three measurements is discussed below:

- **Measurement from 2017:** During 2017, the measurement was conducted just after the construction of the wind turbine foundation. At that time, the wind speed was 6.8 m/s flowing in the direction of the south-southwest. Since the wind was flowing from South to North, the overturning bending moment was from North to South. This overturning moment is measured in the shaft sensor which determines the amount of dynamic bending moment going inside the foundation during the emergency stop. The obtained strain measurements from FO sensors are converted into stress values for each location. The maximum bending moment going inside the foundation is 151.07 MNm. It can be observed that the stresses in every location are within the linear elastic limit indicating the fact that the structure is uncracked. This can be verified with frequency analysis of consecutive years to determine the stiffness of the foundation. The frequency of the tower is calculated to be 0.157 Hz which is within the limits of the range provided by the turbine company.
- **Measurement from 2022:** This measurement was conducted to determine the structural health of the concrete foundation after a few years of turbine operation. Same as in 2017, the wind data was collected during the measurement but the strain data was missing from many sensors. There is one sensor present in the bottom tangential position which gave stress values up to 220 MPa which may seem like the foundation is cracked in the given region but when compared at the opposite wind direction, the steel stress was low while it is expected to show a similar range in stresses. One more thing which was missing from the data was the complete inputs from the shaft sensor. That leads to missing information on the bending moment going inside the foundation. While monitoring the wind data such as wind speed and wind direction, the prevailing wind direction was towards the West, which means that the shaft sensors present in the West and East direction will measure the primary bending moment but the data did not include those results. Another attempt of assumption has been made to obtain the bending moment analytically but that was also not enough since the data from other sensors can also not be trusted fully due to weird stress at the bottom tangential sensor.
- **Measurement from 2023:** To mitigate the shortcomings of the previous measurement, another measurement was conducted in 2023. The wind speed during the measurement was 10m/s which was higher than both measurements conducted earlier. The wind speed is directly related to the amount of stress in the reinforcement [3], hence it was expected to measure higher steel stresses. On the contrary, after analyzing the data, it has been observed that the stresses are less as compared to

2017, and due to the malfunctioning of the interrogators of shaft sensors, the data from two directions are missing. The conduction of this experiment also confirmed the malfunctioning of some sensors. Take the sensor at the bottom tangential reinforcement which measured stress of 220 MPa in the previous year, if that has to be true then even this year it should have measured higher stress indicating the possibility of cracks in the mass structure. But instead, it showed lower stress in the rebars whereas, the other two sensors at vertical stirrups and bottom tangential near piles measured higher stresses. Due to the above-mentioned reasons, the measurements of this year have also been discarded and the finite element analyses contain the overturning moment of 2017.



(a)



(b)

Figure 7.1: Comparison of bottom tangential piles in a) 2022, b) 2023

7.2. SCIA engineering calculations

The SCIA calculations are mainly performed with the purpose of verifying the DIANA model. A 2-D plate model representing the concrete foundation has been modeled with the same material properties and loading conditions as the real structure. In order to verify both DIANA and the SCIA calculations, the reaction forces of both models are compared which showed some variations, especially in the tensile force. The tensile force in the SCIA is up to 39% higher than the tensile force obtained from the DIANA analysis. While the variation in the compressive force only exists up to 3% in both calculations. The provided SCIA calculations also showed the stresses in the concrete structure which is within elastic limits. The SCIA analysis varies up to a factor of 0.5 when compared to the experimental results. This also verifies that considering linearity in the structure both the models in SCIA and in DIANA are working fine and there is no discrepancy in the model.

7.3. Structural analysis in DIANA

At present, while designing wind turbine foundations only structural analysis is considered in the FEM. For this research project, the structural analysis in the DIANA is performed by applying the same amount of horizontal load and bending moment measured during the field monitoring. The results obtained from the structural calculations showed cracks at the end of the applied wind load, which is not the case in real life. From the conclusions drawn in chapter 3, it is deduced that the foundation is still uncracked. Some amount of marginal difference is accepted between the two since the FEM calculations can never match the real structural behavior due to the presence of many simplifications and assumptions. But in this case, the difference is way more than what is to be expected, about 10-80 times higher than the measurements. The variation differs for different wind directions at each location. The comparisons of the steel stress at every measuring location with different wind directions are presented in Figure 7.2-Figure 7.7. The wind directions North, East, and South are represented in Red, Yellow, and Green colors respectively. It is evident from the below figures that both field measurements and the FE model provide stresses with the same signs. The main difference occurs in the magnitude of the stresses in the reinforcements where an overestimation of up to 80 times the expected value has occurred. This may also result in a more costly construction process. From the experiments conducted in [3], the measured stresses were in line with stresses calculated using FEM analysis. The FEM analysis performed by Zhou et. al was a linear analysis hence no scope for any disparities while in this research, a finite element non-linear analysis is performed. Convergence of force and energy simultaneously is difficult because of the size and nature of the non-linear analysis. It is seen that there are a few non-converged steps in the iteration and that the force norm exceeds the acceptable 10 % at the end of the analysis. However, the unbalance at the symmetry plane is small compared to the applied forces. Using engineering judgment and checking the results and the global structural behavior, it is decided to accept the results.

In order to mitigate the difference between FEM analyses and the field measurements results and to limit the cracks, the effects of the heat of hydration will be added to the model since a mass structure releases a huge amount of heat during the hardening stages and hence that heat may add extra compressive stresses to the structure which leads to fewer cracks.

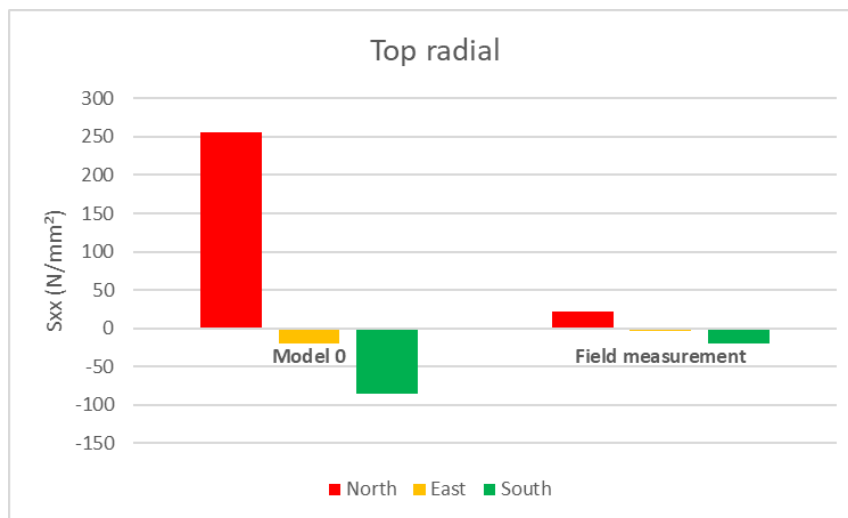


Figure 7.2: Steel stress at Top radial (L02) in North(A), East(B), South(C) directions

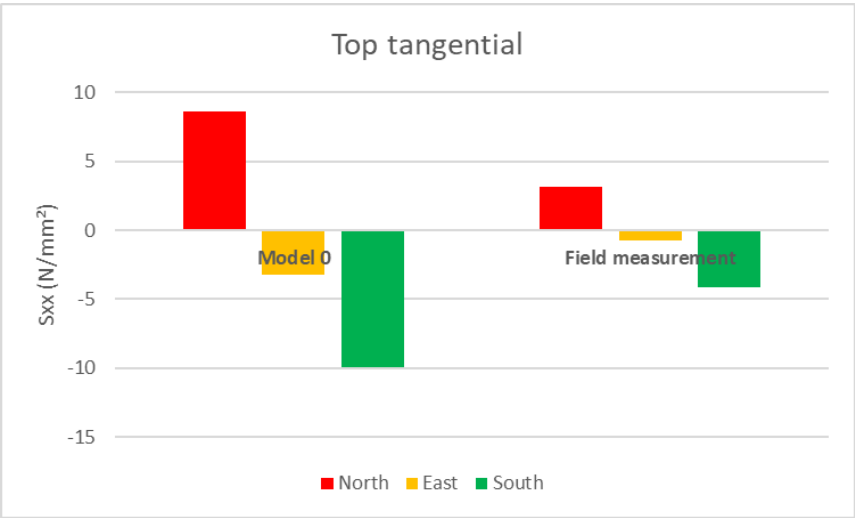


Figure 7.3: Steel stress at Top tangential (L03) in North(A), East(B), South(C) directions

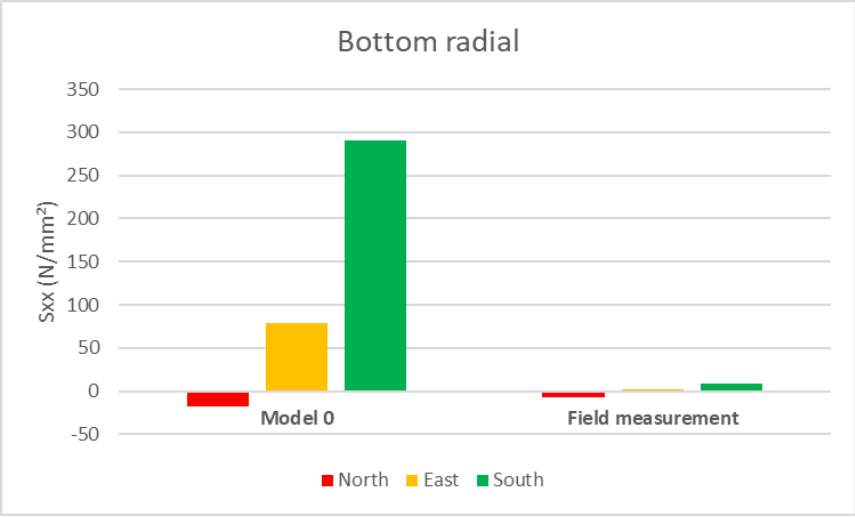


Figure 7.4: Steel stress at Bottom radial (L05) in North(A), East(B), South(C) directions

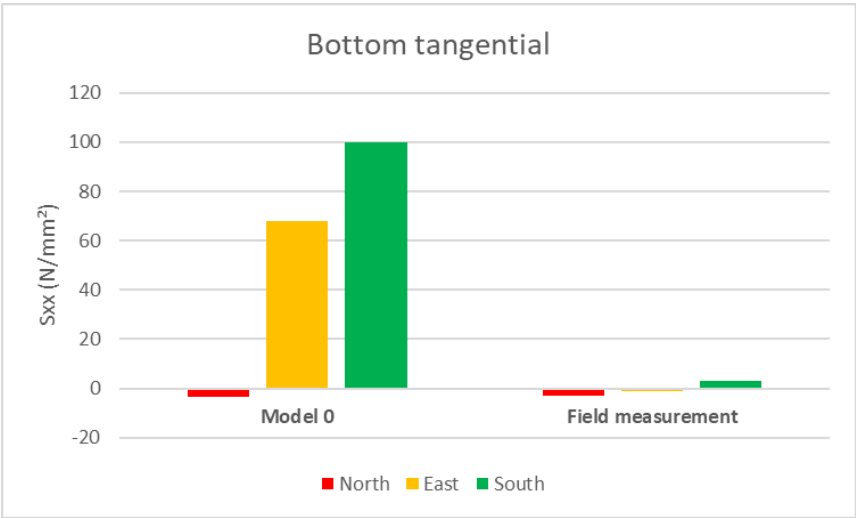


Figure 7.5: Steel stress at Bottom tangential (L06) in North(A), East(B), South(C) directions

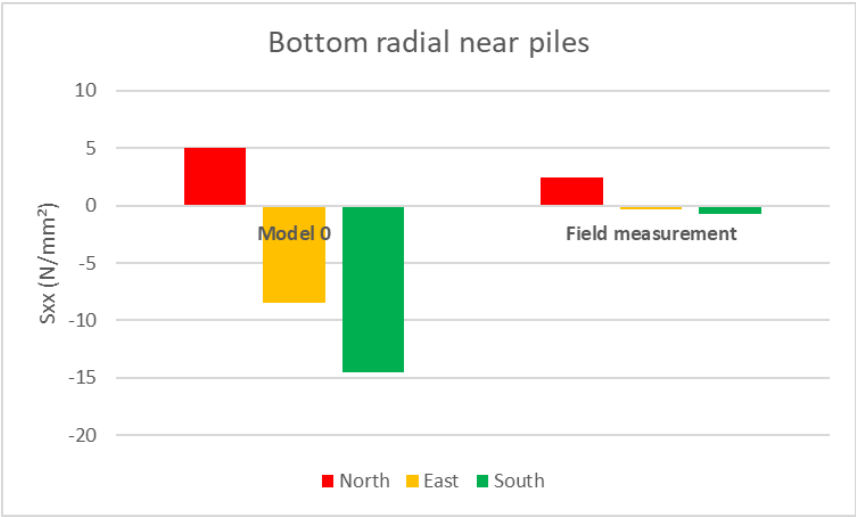


Figure 7.6: Steel stress at Bottom radial near piles (L07) in North(A), East(B), South(C) directions

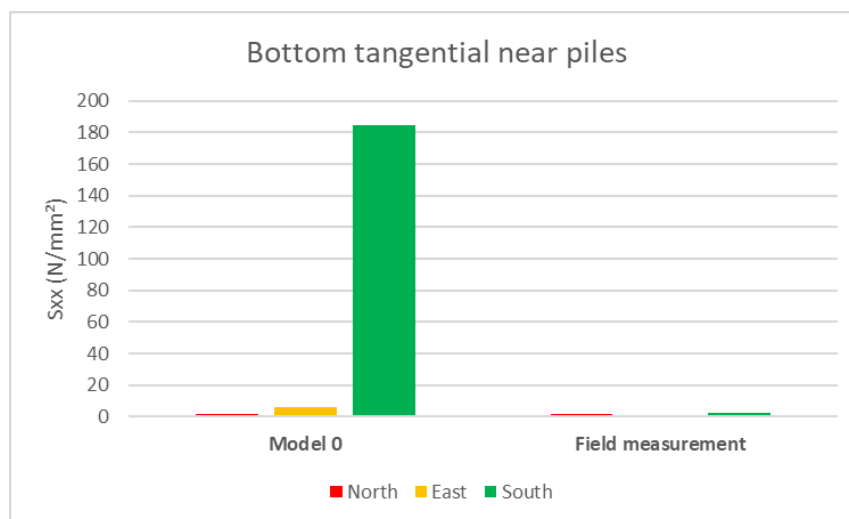


Figure 7.7: Steel stress at Bottom tangential near piles (L08) in North(A), East(B), South(C) directions

7.4. Thermo-mechanical analysis on a wind turbine foundation

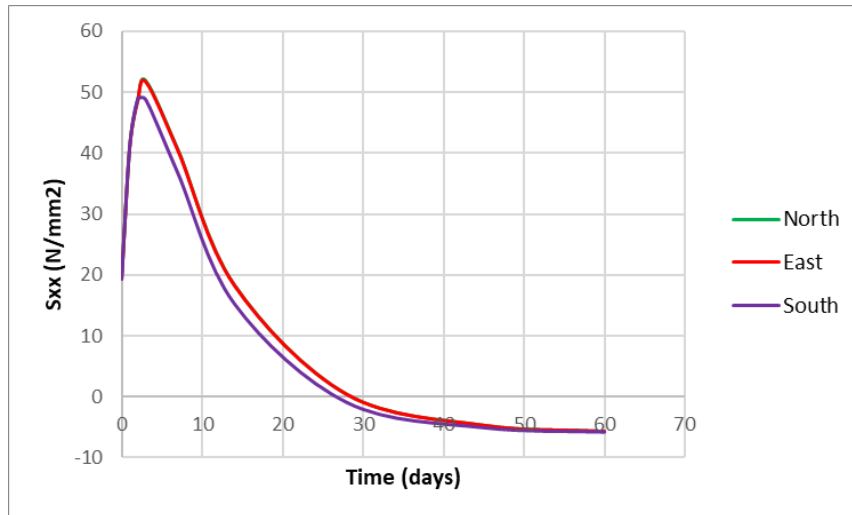
This section will deal with the outcomes of chapter 6 and include a detailed discussion of the obtained results.

7.4.1. Temperature and steel stress evolution due to the hydration heat

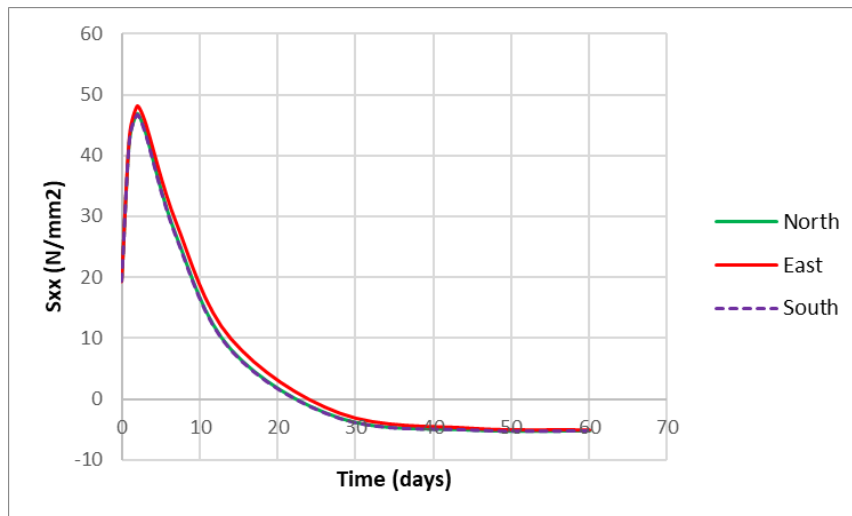
- During concrete hardening, it releases an enormous amount of heat which leads to concrete expansion and once it cools, the structure shrinks down. This expansion and shrinking of the concrete structure generates thermal cracks due to the existing temperature gradient between the top and the core of the foundation. The heat development is non-uniform in real life but for simplicity purposes, uniform heat development has been considered in DIANA. While conducting the heat of hydration analysis, it has been observed that the foundation starts to heat up on Day 1. The core reaches its maximum temperature on the third day. Afterward, it cools down, and the entire foundation achieves equilibrium with the environment after 60 days. Similar behavior is also observed in [7], where the foundation core reaches a maximum temperature of 62.5 °C. The heat generated is so intense that it retains the temperature of around 30 °C till day 28 in the foundation core. One of the most important parameters in this analysis is the heat transfer coefficients which decide the amount of heat evolution in the structure. The values of the HTC parameters are obtained from the literature and are presented in subsection 6.1.5. There are two HTCs discussed in the project out of which HTC 2 gives better results since the temperature gradient is 32 °C whereas it is 35 °C in HTC 1. Both these values are greater than the limit of 25 °C which means that the model is more prone to thermal cracks [8]. Also, with HTC 2 the foundation core reaches a lesser temperature as compared to the temperature attained by the foundation core due to HTC 1. Although there is no direct correlation between thermal cracks and cracks occurring due to wind load, the presence of thermal cracks does influence the crack pattern distribution during its service life.
- Next, to the temperature evolution in the foundation the occurring stresses due to the heat of hydration are studied. It is observed that the steel stresses follow a similar distribution pattern as the temperature. The bottom rebars experience more stress as compared to the top bars since the complete load of the structure is acting on the bottom part of the foundation. Also, the stress development is directly related to the HTCs provided during the transient heat analysis. Since the bottom portion is well insulated with the soil layers, it generates more heat as compared to the top surface which is exposed to the air. This insulation also results in more stress in the rebars located at the bottom position. In the case of the top steel bars, the generated stress changes its peak just like in the temperature plot Figure 6.5.

Another interesting thing that has been noticed during this analysis is that the steel stresses are different in each wind direction although the heat development is considered to be uniform. In real-life this behavior would have made sense since the external environmental conditions keep on changing

from time to time. There is a possibility of one wind direction getting more solar radiations or wind which will result in more or less stress respectively at that location. Despite omitting such conditions in DIANA for simplicity purposes, it showed different stresses for different directions. This can happen due to various reasons such as problems in the model or due to any numerical errors occurring due to non-linearity in the material properties. For this, a model with all the linear material properties is made to run which showed that the stresses in the steel bars are coinciding on top of each other in all directions at every position. The results of the linear FE analysis are presented in Figure 7.8. This shows that the variations in the steel stresses at each wind location happened due to numerical errors which also lead to asymmetrical patterns of cracks in the foundation.

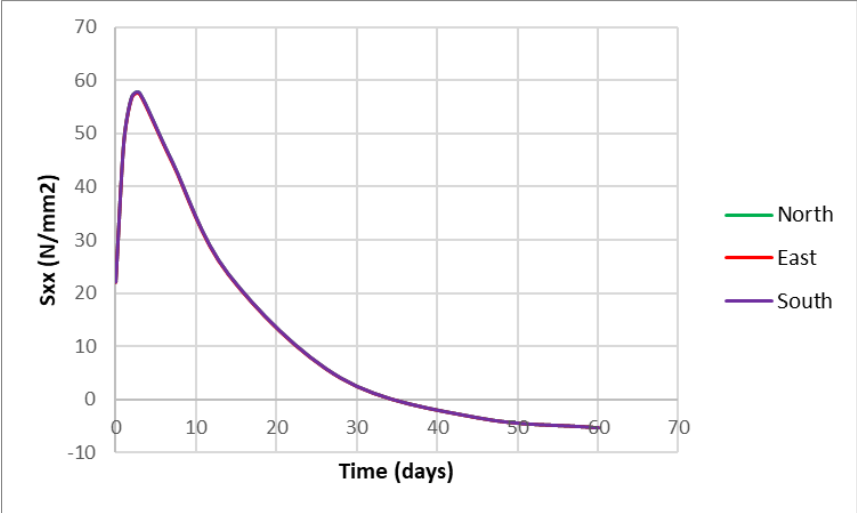


(a)

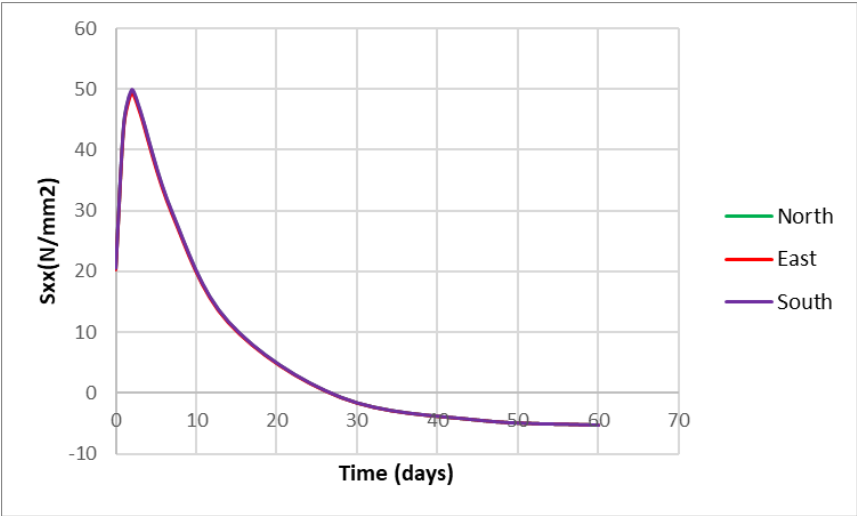


(b)

Figure 7.8: Steel stress wrt time at each wind directions a) Top radial, b) Bottom radial



(c)



(d)

Figure 7.8: Steel stress wrt time at each wind directions c) Top tangential, d) Bottom tangential

7.4.2. Effect of Combined analysis

This part will focus on the outcomes of the combined analysis of both transient heat and non-linear structural analysis of all the models discussed in the chapter 6.

- When the hydration heat analysis is performed along with the structural analysis, it is observed that the stresses in the reinforcements did reduce to up to 34% between Model 0 and Model 1. Since this reduction is not sufficient, various modifications have been performed during the course of the research. One such variation is done in Model 2 where the maturity properties were varied with time. Since this model only helped to achieve a reduction of up to 42% than Model 1, another model with different HTCs is used in order to reduce the thermal gradient. Between Model 2 and Model 3, the difference lies in the heat boundary conditions. The temperature gradient in Model 2 is 35 °C while for Model 3 it is 32 °C. A slight reduction in the temperature gap does not reduce the thermal cracks but it does affect the distribution of the stresses in the reinforcements. subsubsection 6.5.1, showed that the cracks are still occurring in the concrete foundation and the stresses in the reinforcements are much higher especially in the bottom tangential near piles position in the south location (L08) as compared to what is measured in the field. In this case, the stresses are almost 58 times higher whereas, at the same measuring location but in other wind directions, the stresses are only 9 times higher than the field results as shown in Figure 7.14. Now a comparison is drawn between the model with only non-linear FEA (Model 0) and thermo-mechanical FEA (Model 3) where a decrease of 4-33% in the steel stresses has been observed at different measuring locations. This reduction did have some effect while comparing the stress outcomes with the measurements. For instance, in the case of bottom radial bars in the South direction, the stresses were 31 times higher in Model 0 while this slightly reduces to 29 times in Model 3 when compared with the measurements as depicted in Figure 7.11. While at the above-mentioned tangential position, the stresses were 87 times over-estimated from the field data in Model 0 which is reduced to 58 times in Model 3 after applying the hydration heat. The representative graphs are presented below:

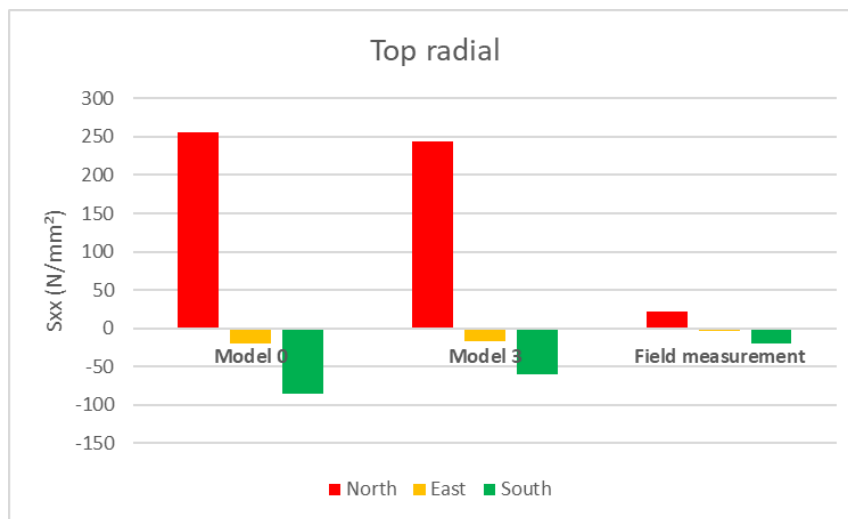


Figure 7.9: Steel stress at Top radial (L02) in North(A), East(B), South(C) directions

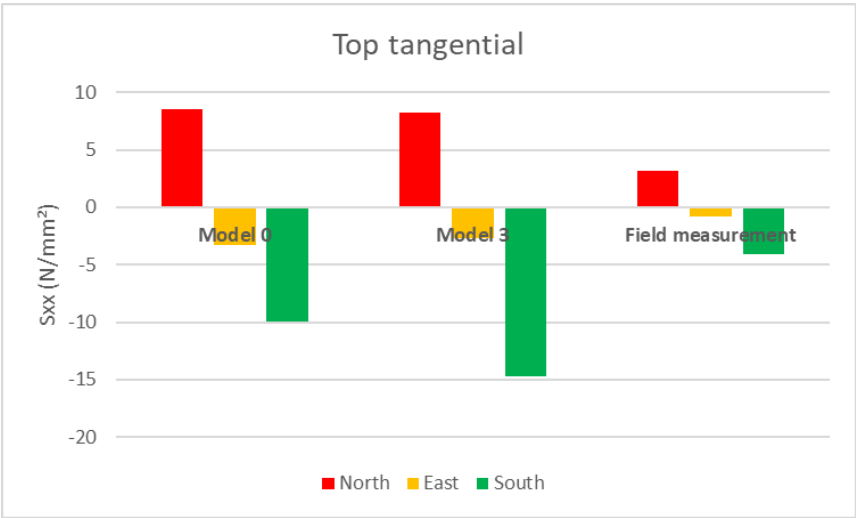


Figure 7.10: Steel stress at Top tangential (L03) in North(A), East(B), South(C) directions

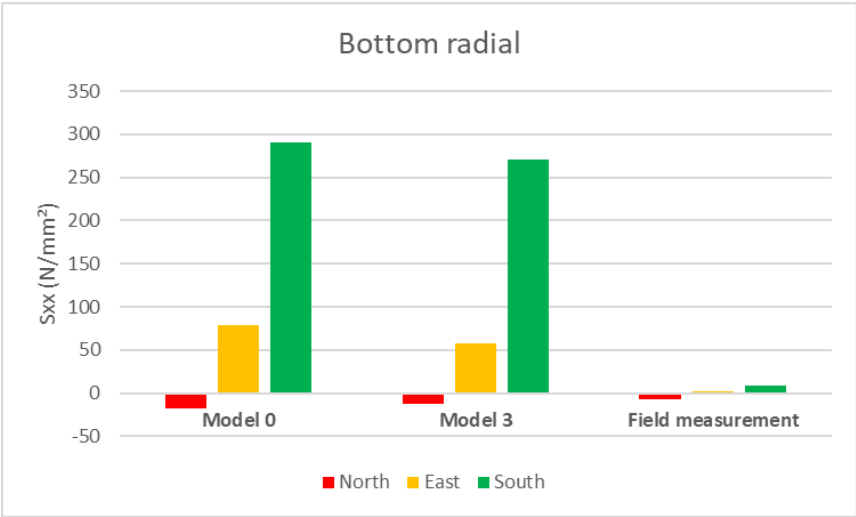


Figure 7.11: Steel stress at Bottom radial (L05) in North(A), East(B), South(C) directions

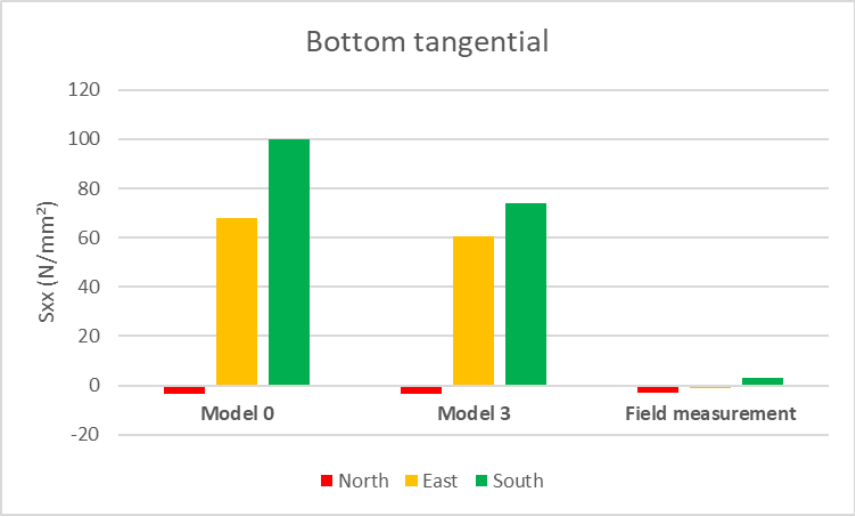


Figure 7.12: Steel stress at Bottom tangential (L06) in North(A), East(B), South(C) directions

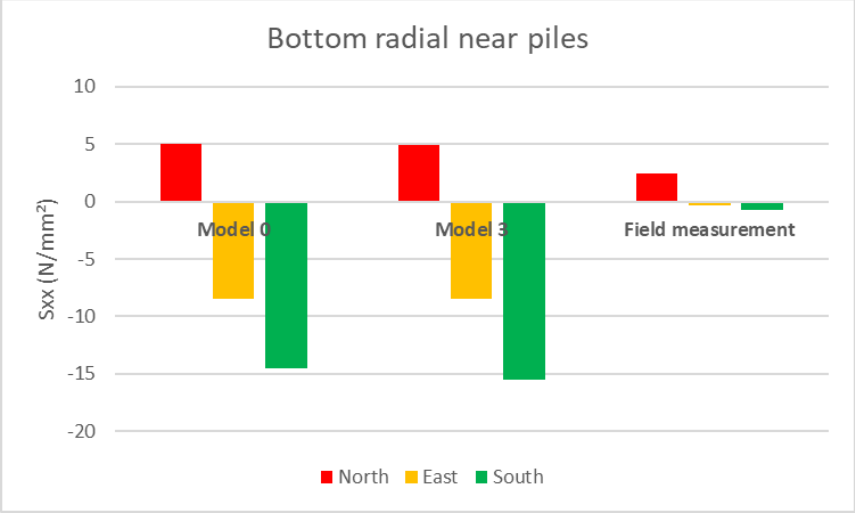


Figure 7.13: Steel stress at Bottom radial near piles (L07) in North(A), East(B), South(C) directions

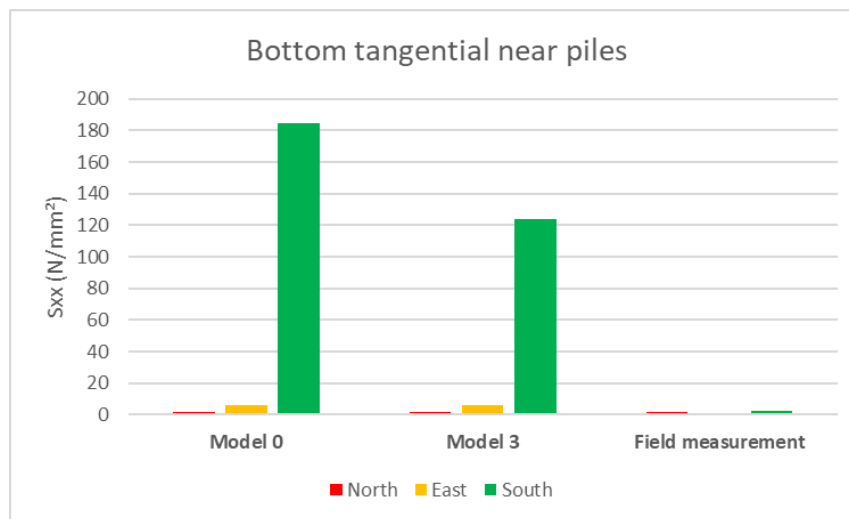


Figure 7.14: Steel stress at Bottom tangential near piles (L08) in North(A), East(B), South(C) directions

- When bedding is added beneath the foundation in Model 4 to achieve greater stability in the structure, it is noticed that the steel stresses due to the heat of hydration did not change because of the presence of bedding. Still, at the end of the wind load levels, the tensile steel stresses at the bottom location did get reduced up to 75% as compared to Model 3 due to the extra compressive forces reaching the foundation. This compressive force from the soil stiffness reduces steel stresses and narrows the gap between FEM analysis and field measurements to a maximum factor of 30, compared to 50 in Model 3. In Model 3, the crack widths are 3.2 mm whereas it is reduced to 2.75 mm in Model 4. The interface between the bedding and concrete foundation must not have tensile stress to prevent foundation overturning.
- Another variant, Model 6 with the bedding stiffness on all three sides provided much better results than the previous models. Since the soil stiffness is provided in all three surfaces, the compressive forces due to this effect, lowered the stress values and reduced the crack widths. Now the stress has reduced in both the top and bottom surfaces, 57%, and 64% respectively when compared with Model 4. The cracks are more narrower in this case with a maximum crack width of 2.35mm. From Figure 7.15-Figure 7.20, it is evident that a marginal reduction has occurred in the steel stresses at most of the measuring locations. In Model 4, the stress of the top radial bars facing North was ten times higher than the experimental results as shown in Figure 7.15. However, in Model 6, the steel stress differed only by a factor of four compared to the measurement data. Similarly, at other locations, Model 6 showed overestimation ranging from 0.5-7 in comparison to the expected outcomes. On the other hand, the bottom radial at the south has still not shown any positive result as it is still 26 times higher than the field data as presented in Figure 7.17.

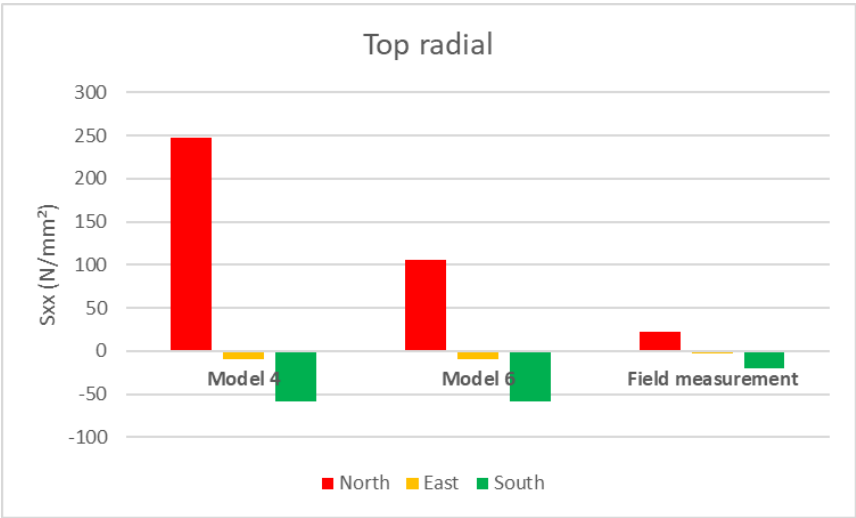


Figure 7.15: Steel stress at Top radial (L02) in North(A), East(B), South(C) directions

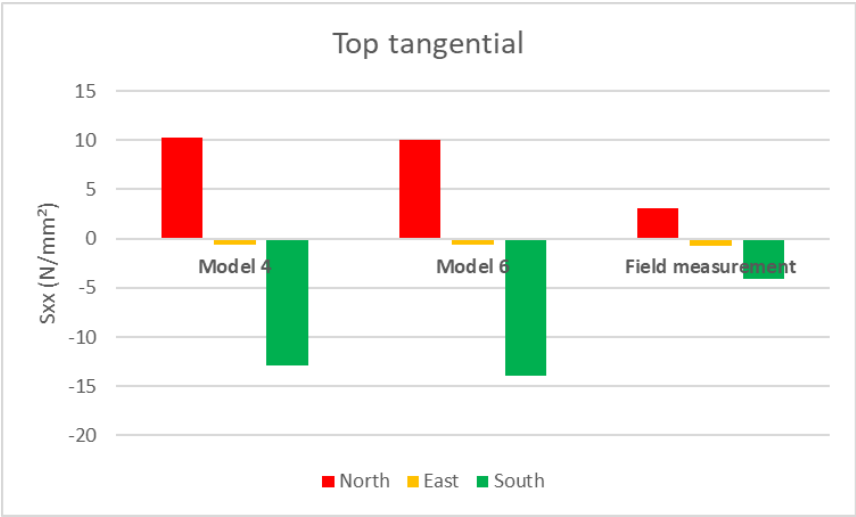


Figure 7.16: Steel stress at Top tangential (L03) in North(A), East(B), South(C) directions

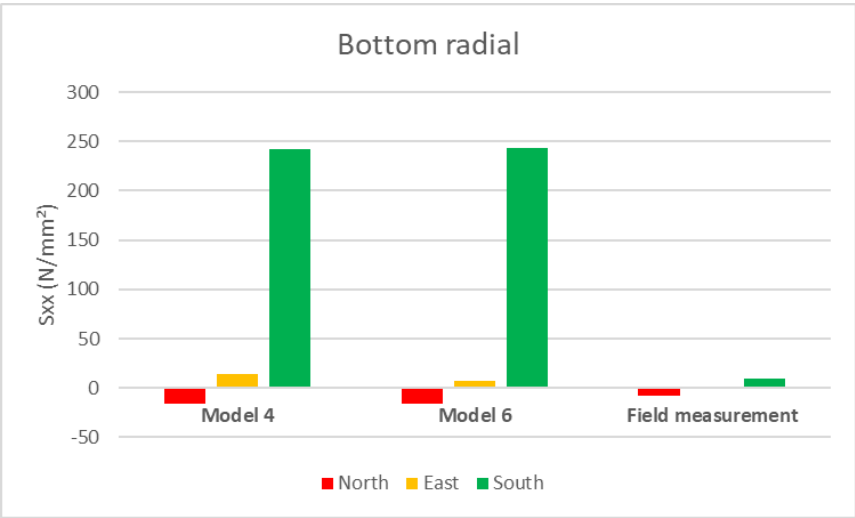


Figure 7.17: Steel stress at Bottom radial (L05) in North(A), East(B), South(C) directions

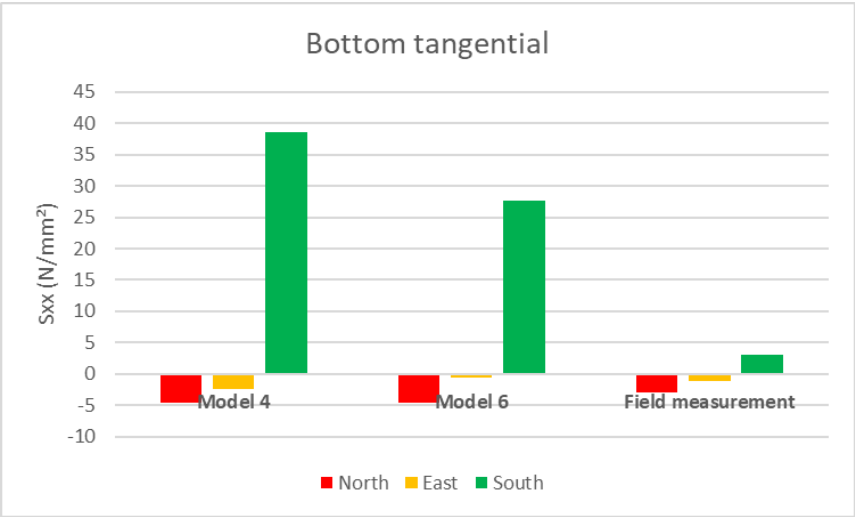


Figure 7.18: Steel stress at Bottom tangential (L06) in North(A), East(B), South(C) directions

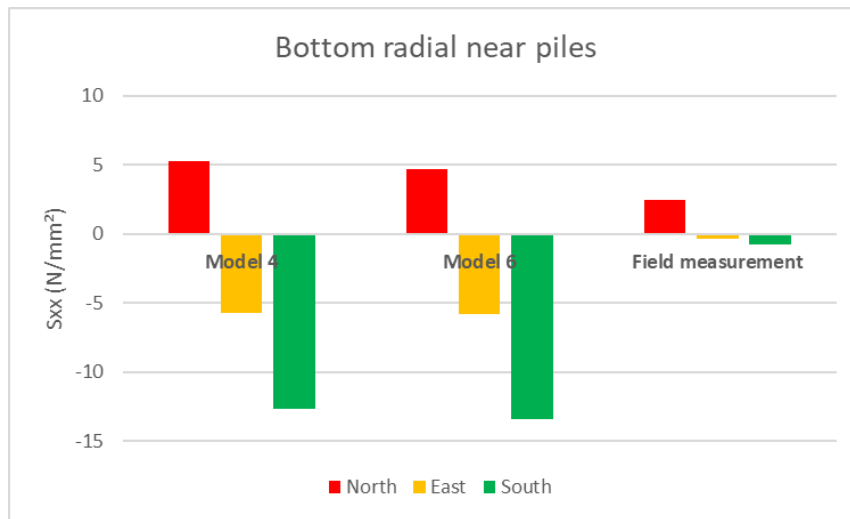


Figure 7.19: Steel stress at Bottom radial near piles (L07) in North(A), East(B), South(C) directions

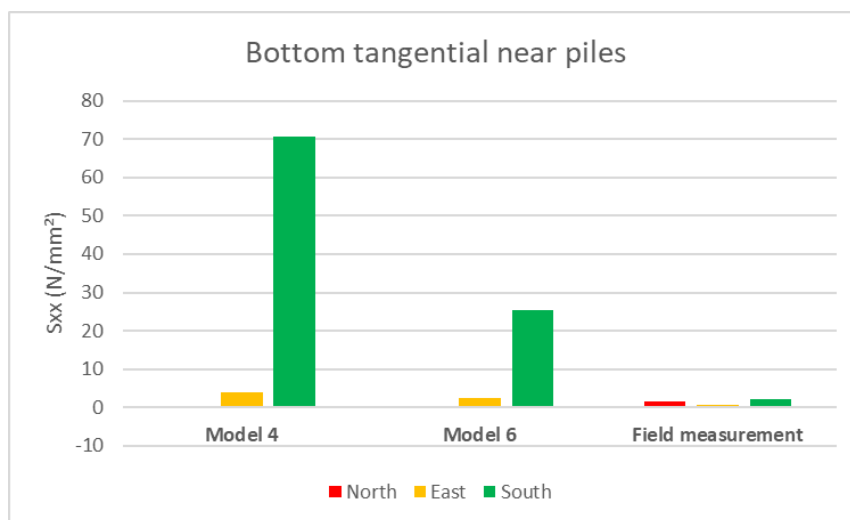


Figure 7.20: Steel stress at Bottom tangential near piles (L08) in North(A), East(B), South(C) directions

- When a foundation lays over inclined piles, it gets extra horizontal stiffness from the piles. This theory is proved in Model 7, where a decrease of 30% in the steel stress has been observed in the bottom bars as compared to Model 3. This provides a scope for generating extra compressive stresses in the bottom side of the foundation. The horizontal restraint forms an arch-like stress condition on the bottom surface. There have not been many changes observed in other locations where the stresses are more or less similar to the Model 3. Adding inclined piles only helps in lowering the bottom steel reinforcements since it lowered the bottom steel stresses to a factor of 24 instead of 26 in the previous models compare to the field results.
- Model 7 did not show any better results as compared to Model 6, which included soil bedding in all directions. But Model 8 with both inclined piles and bedding on all sides performed well not only in lowering the stresses but also narrowing the crack patterns when compared with Model 7. Whereas concerning Model 6 the steel stresses in Model 8 are higher up to 50%. When compared with the field results, Model 8 showed an overestimation of approximately 22 times in the bottom bars. While the difference in the top bars is up to 5 times that of the field results. Due to the presence of both inclined piles and soil bedding underneath, in certain areas, it did give rise to more compressive stresses which helped to decrease the cracks at the bottom. But it seems that in Model 8 the steel stresses are not properly distributed which leads to higher stress concentrations in some locations.

One thing that is vividly clear from all the analyses is that if the cracks have to be limited in the foundation model, then it needs to achieve sufficient stiffness from the surrounding which will act as an extra strengthening to the foundation.

- A sensitivity study is conducted with a higher horizontal pile stiffness and higher bedding stiffness which limited the cracks to a large extent. Maximum crack width changed from 2.34 mm to 1.67 mm from Model 8 to Model 9. This reduction in the occurrence of cracks also resulted in the lowering of stresses in the reinforcements. When the bedding stiffness is very high, it resulted in large compressive forces in the foundation which helped in getting matching results with the field measurements. Since the bedding is provided in all three directions, the steel bars located at the top position also showed positive results along with the bottom rebars. In the case of the bottom rebars, the compressive forces are resulting from both bedding stiffness and the horizontal pile stiffness of the inclined piles. Such large compressive stresses result in major changes in the bottom reinforcements. A reduction of up to 80% is observed between Model 8 and Model 9 in the case of the bottom rebars whereas a 55% decrease has been observed for the top radial bars. Not only the decrease in the steel stress has been observed between Models 8 and 9, but also the range of the overestimation has been reduced between Model 9 and the experimental results. The steel stresses of radial bars are overestimated in the range of 3-19 while the stresses in the tangential bars are 0.3-8 times higher than the field results as shown in Figure 7.21-Figure 7.26.

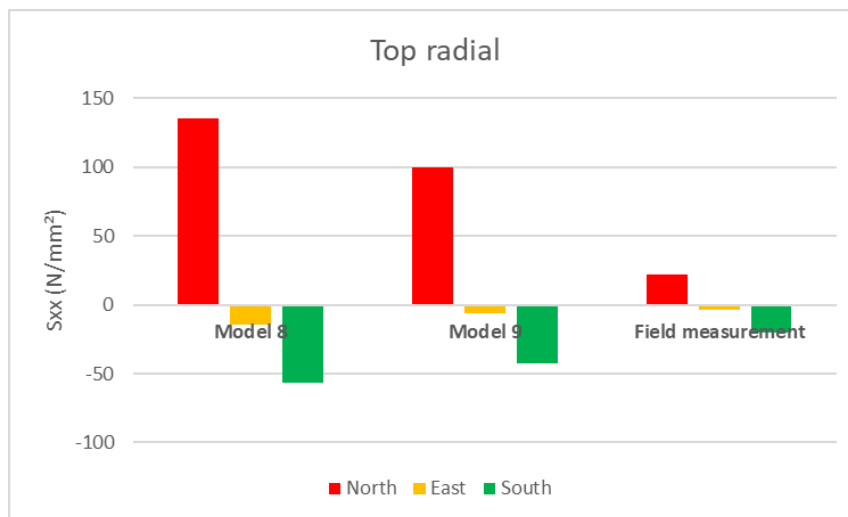


Figure 7.21: Steel stress at Top radial (L02) in North(A), East(B), South(C) directions

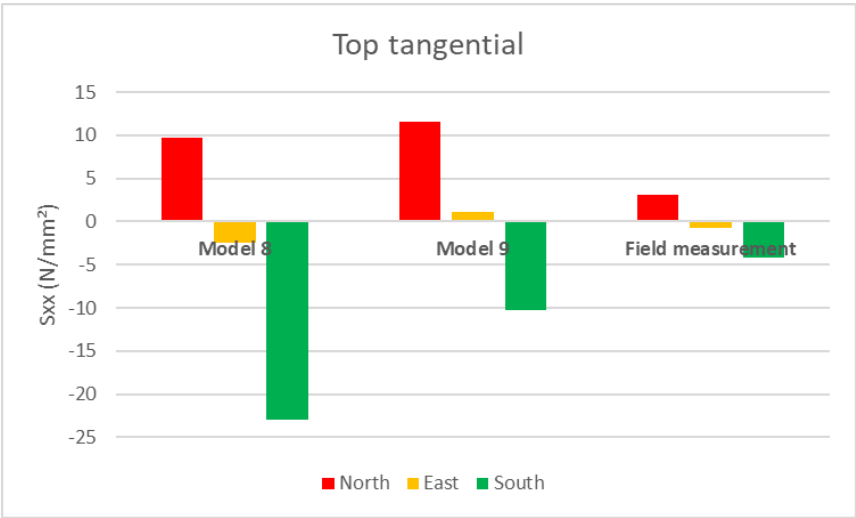


Figure 7.22: Steel stress at Top tangential (L03) in North(A), East(B), South(C) directions

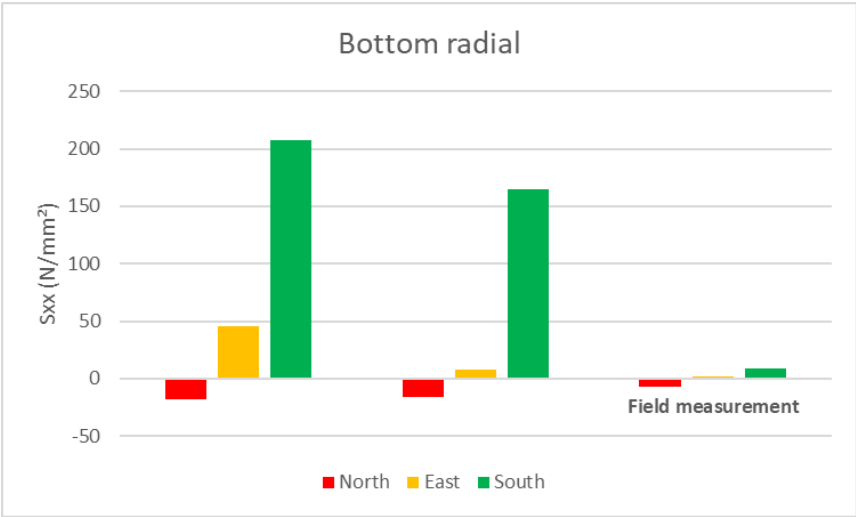


Figure 7.23: Steel stress at Bottom radial (L05) in North(A), East(B), South(C) directions

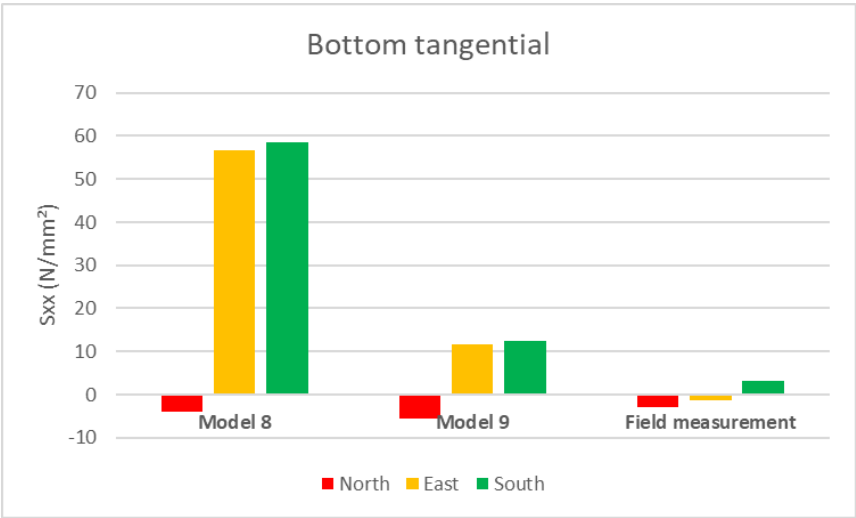


Figure 7.24: Steel stress at Bottom tangential (L06) in North(A), East(B), South(C) directions

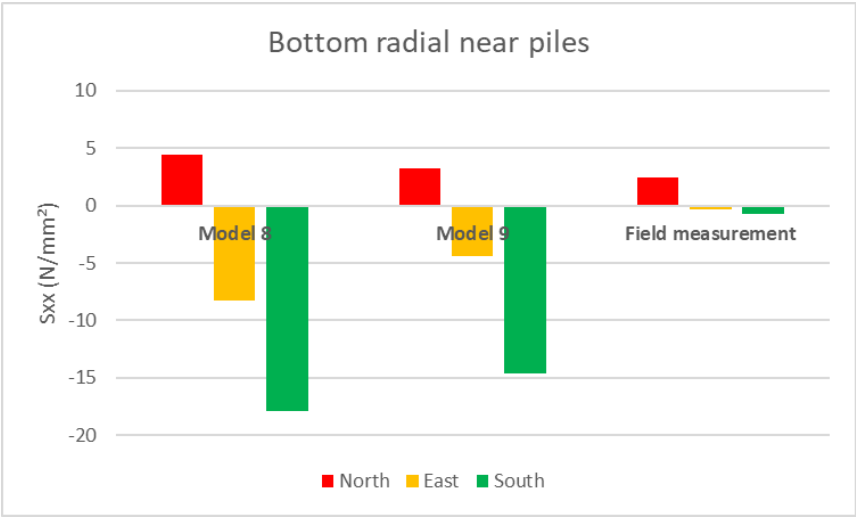


Figure 7.25: Steel stress at Bottom radial near piles (L07) in North(A), East(B), South(C) directions

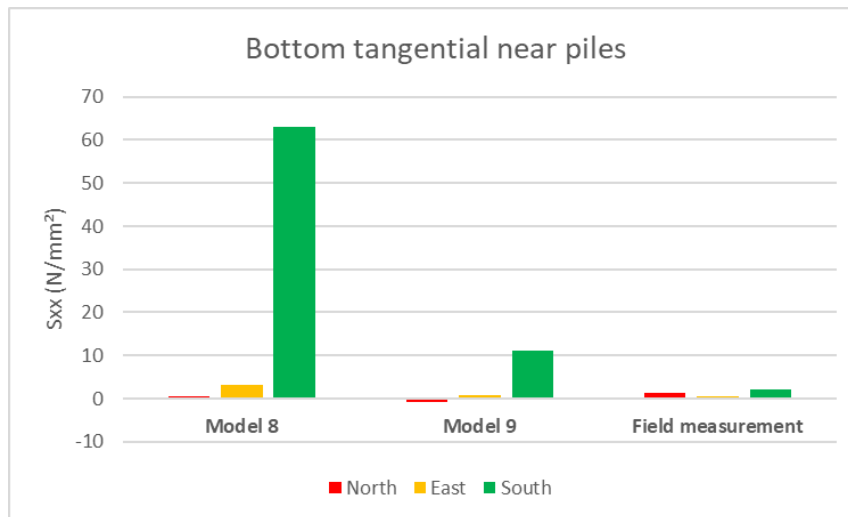


Figure 7.26: Steel stress at Bottom tangential near piles (L08) in North(A), East(B), South(C) directions

7.5. Discussion

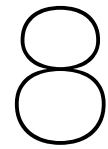
The validation of the steel stresses is a crucial aspect as it ensures the accuracy and reliability of the FE analyses. The strain monitoring in the wind turbine foundation is conducted using FBG sensors that are temperature sensitive as mentioned in section 2.2. Even though, the company that conducted the measurements stated that during short-term monitoring, FBGs do not show any kind of variations and it's very stable but the measurement data from both 2022 and 2023 did show major differences at particular locations. One such difference is presented in Figure 7.1. Hence, it is best to consider the initial measurements conducted in the concrete foundation when the sensors were just placed.

From subsection 2.1.1, it is clear that the stresses in the bars present in the foundation are within elastic range when a linear numerical analysis is performed and the stresses in the FEM calculations show an adequate match with the field measurement. This is also proved in chapter 4, where the SCIA model is prepared, and the generated stresses in the SCIA analysis are also within the elastic limit due to the linear analysis. Although, the SCIA model is used only for validating the FE model and not for the purpose of further research due to the low approximation approach. While in the case of the FEM non-linear simulations performed in this research project, it showed a major overestimation of about 87 times when a comparison is made between the obtained steel stress and the DIANA analysis. This also resulted in cracks in the foundation. But, from the section 3.5, the operational wind turbine's foundation is still uncracked. This implies that the concrete foundation is receiving horizontal prestressing along with vertical prestressing from the anchor bolts. One way the foundation is getting prestressed is in the form of hydration heat as mentioned in section 2.4. To eradicate differences between the steel stress of field measurement and the numerical simulation, hydration heat analysis is performed in the current project and its outcomes are studied. It is observed that despite including the effect of hydration heat in the DIANA model, cracks are still occurring in the numerical analysis. Also due to the horizontal prestressing from the hydration heat, 33% of extra prestressing forces are generated in the structure along with the vertical prestressing. Although the gap has been reduced to an extent of a factor of 58 and the occurring steel stresses are much lower than the results obtained in chapter 5, there is still scope for more modifications in the model. The research thesis follows an iterative approach to ensure that the FEM model is refined to achieve the closest match with the observed behavior of the foundation. The thermo-mechanical model with bedding on all sides provided fairly good results in comparison with the other models and successfully close the overestimation factor to 4-26 with the field data. Another attempt of combining both inclined piles and the bedding on all three surfaces in the foundation along the thermo-mechanical analysis helped to mitigate the formation of the crack in the numerical model. Although the steel stresses in the top reinforcements are about 50% higher than the model with bedding on all sides, the crack widths remain the same. This might happen due to the stress distribution during the numerical simulation. After conducting all these analyses, increasing the stiffness to a higher value changes the factor of overestimation to 3-19 times between the model and the observed values in the field. Therefore, achieving a perfect match is difficult

and some variation will always exist between them. The cracks that are still present in the foundation can be eradicated by some additional effects such as relaxation and implementing proper cooling conditions in the numerical analysis.

One theory that can be added along with the hydration heat effect is the Relaxation effect. This theory can aid in redistributing stresses over time in the foundation which lowers stresses in critical areas and distributes the load more evenly. Additionally, relaxation also delays fatigue crack growth by reducing stress intensity near the crack tip, allowing reinforcements to withstand a larger number of load cycles. The Maxwell model can be used to include the relaxation effect in DIANA. Also, considering proper cooling methods during the analysis can help in reducing the heat and mitigating the cracks. In the current research, a proper soil model is ignored during the modeling of the foundation, the bedding as a boundary interface has effectively helped in achieving a better result especially when it is applied on all three sides. It should be noted that adding stiffness to the foundation bedding did not create any tensile stresses at the interface. If a proper soil model such as the Mohr-Coulomb model is used to model the soil properties which includes friction between the soil layers, a better result can be expected as discussed in [3] where the FEM calculations showed a good match with the experimental results even though it included a linear analysis.

Validating the stresses in the rebars can pose a few challenges since wind turbines are subjected to dynamic loads, and material behavior and the interaction between the foundation and the surrounding soil generate further complexities. Including these challenges guarantees that the validation process captures the true behavior of the foundation. Even modeling of bridges, offshore structures, tunnels, etc shows similar challenges during modeling in FEA.



Conclusion and Recommendations

This chapter includes the conclusions of the research thesis along with the answer to the research questions presented in chapter 1. The end of this chapter provides a brief overview of the primary recommendations for the future continuation of this research project.

8.1. Conclusion

In this research project, the stress behavior of the reinforcements in an onshore wind turbine foundation is analyzed with the help of finite element analyses. The beginning of the research involved some main and sub-research questions which are answered in this section.

Answer to main research questions

1. How do the steel stresses generated in the concrete foundation on site vary from the numerical analysis in the FE model?

The comparison between the stress measurements from the field and the FEA is important in order to determine the accuracy and reliability of the numerical analysis. The steel stresses obtained from the field measurement at a maximum overturning bending moment were within the elastic limit for all the measuring locations at each wind direction. It also showed no cracks in the measuring locations after comparing the measurement results of three years. However, this differed from a structural non-linear analysis using FEM that showed an over-approximation of steel stress. The obtained stress values from FEA vary for different measuring locations at 3 wind directions drastically. Significantly higher steel stress, up to 87 times, was observed at the bottom tangential near piles in the south (L08 C) while other locations showed a range of 5-30 times higher stress. These higher values of stress caused cracks in the foundation.

In order to study the heat effects in the DIANA model, transient heat analysis was performed along with the non-linear structural analysis. While doing so, the results of the thermo-mechanical model (Model 3) showed a reduction of up to 33% in the steel stresses when compared to the model that did not account for the thermal properties of the concrete (Model 0). The 33% reduction explains the extra effect of horizontal prestressing from hydration heat along with vertical prestressing already present in the foundation through anchors pretensioning. When Model 3 was compared with the field results, it was noticed that the location L08 C with an over-estimated outcome of 87 times higher steel stress was now reduced to 58 times. The other prevailing locations had also shown an improvement in decreasing the stresses in the steel bars but, this reduction was not yet sufficient to obtain a closer match with the field measurements. Especially, two locations of radial bars- top (L02) and bottom (L05) in the North (A) and South (C) directions respectively showed steel stresses that were still higher, approximately 10 and 29 times respectively than the observed field results.

The model showed relatively better results when the effects of bedding were provided on all sides, following an iterative method of consecutive changes in the thermo-mechanical analysis. Compared with the model with hydration heat (Model 3), the variant with both thermo-mechanical analysis and bedding on all sides (Model 6) showed a reduction in steel stresses from 3% to 92% depending on the location of the reinforcement. Model 6 also successfully reduced the gap between the FEM analysis and the field results. The over-approximation of the stresses had reduced from 58 to a factor of 11 at the same location (L08 C). In the case of the other locations, the stresses vary within

a factor of 0.03-26 times than the field data. Where the stress in L02 A decreased to a factor of 4 and the stress in L05 C was 26 times higher than the experimental data.

When Model 6 was modified with inclined piles (Model 8), it did not show any improvements to the stresses in the rebars located on top compared to Model 6. But the bottom bars did show a reduction of up to 15% resulting in lowering the factor to 22 times higher than the field results in the L05 C location.

The sensitivity study in Model 9 with fictitiously high stiffness values showed a closer match with the field results for all the locations. For example, the steel stress in the top radial (L02 A) was 3 times higher than the field results, while the stress in the bottom radial (L05 C) decreased its overestimation from 22 to 17 times from the previous model, and the stress in the bottom tangential (L08 C) was overestimated by 4 times. Hence, achieving a perfect match between the FEM model and measurements is an arduous task, and it is inevitable that numerical simulations will always have some degree of overestimation.

2. What is the best way to model the wind turbine foundation in the DIANA which will represent the real structure adequately?

During the research, several FE models were analyzed in DIANA FEA 10.5. The FE model in DIANA represents the actual wind turbine foundation located at Riemst, Belgium. The structure's geometry and reinforcement must follow the drawings and layout and the material properties must adhere to standard codes. It was noted that the behavior of the foundation was greatly affected by the characteristics of the soil and piles that uphold the structure. Hence, it was important to model the stiffness offered by them in the FE model. Along with this, time-dependent properties must be added to the concrete during the curing process to get a closer match with the experimental results. Therefore, for the numerical simulation to mimic the behavior of the operational wind turbine foundation, it was necessary to consider possible effects such as maturity and hydration heat. During the current numerical analyses, some simplifications have been considered such as no proper soil model, ignoring the effects of relaxation, etc. that did not allow to achieve a closer match with the field measurement. Despite not including all the effects, the current project achieved a match with the field results with an overestimation of an average factor of 5. Hence, to perform a non-linear FEM simulation effectively, the best way is to minimize simplifications and assumptions in FE software to obtain an adequate match with field results and avoid over-approximation.

Answer to the sub-research questions

1. How does the hydration heat develop over time?

Through the thermal analysis, it was observed that the heat of hydration inside the foundation follows a parabolic curve. During concrete pouring, the temperature peaked at 61 °C on day 3. After which, it gradually decreased and reached an equilibrium with the external temperature after 60 days. During the heating phase, thermal cracks occurred due to the temperature gradient between the innermost and outermost surfaces. The area near the foundation core reached the maximum temperature, while the top surface attained the lowest temperature due to the constant interaction with the air. During the cooling phase of the foundation, the steel bars developed compressive stresses from the hydration heat, providing extra horizontal prestressing to the foundation. The representation of temperature graphs is presented in Figure 6.5.

2. To what extent does the hydration heat emission, which provides the prestressing to the foundation, affect the steel stresses?

When the model with structural analysis (Model 0) and the model that include both mechanical and hydration heat analysis (Model 3) were compared to determine the resultant steel stress due to the applied wind load, it was observed that the final stress in Model 3 is lesser than Model 0. Although the decrease percentage varied in a range of 4-33% for each rebar group due to the stress distribution pattern in the reinforcements, it has been observed that at every location, the inclusion of hydration heat lowered the stresses in the model. In the case of top radial bars, the decrease percentage was 29% whereas bars located at the bottom radial showed a reduction of 26%. Additionally, from Figure 7.9-Figure 7.14 it was evident that the presence of hydration heat results in compressive stresses in the foundation which reduces the tensile stresses and helps in bridging the gap between the field measurement and the numerical simulation. The steel stresses that were overestimated to a factor of 11 in Model 0 reduced to a factor of 10 in Model 3 when compared with the experimental results, whereas an overestimation of 31 decreased to 29 times higher steel stress after the inclusion

of the hydration heat.

8.2. Recommendations

Based on the current research project some recommendations have arisen in order to investigate the same or any other wind turbine foundation for the future. They are presented below:

- The FBG sensors present in the foundation are the strain-measuring sensors and they did not monitor the temperature within the foundation. In case, the sensors are to be placed for structural health monitoring purposes, it is advisable to measure temperature along with the strains. Temperature monitoring can be very helpful, especially during the hardening stages.
- The current sensors are placed on the top and bottom locations in the foundation. It is advisable to place a sensor in the middle portion as well since that location experience the highest temperature during concrete hardening and it would be interesting to know the stresses in those rebars.
- During the modeling of the bedding in the concrete foundation in the DIANA, the soil is not modeled with any type of soil model. Hence, a suggestion would be to consider a soil model like the Mohr-Coulomb model in order to include the effects of friction between the soil layers.
- For further continuing this research, it is advisable to conduct a detailed investigation on the relaxation effect along with the heat of hydration and study the combined analysis of both these effects.
- In order to design such complex structures, FEM is always recommended since it not only helps in design optimization but also reduces the requirement for time-consuming and expensive physical prototyping by analyzing the behavior of structures under various conditions.

References

- [1] W. Cao. *Wind Turbine Generator Technologies*. (2012). URL: <https://www.intechopen.com/chapters/38933> (visited on 06/26/2023).
- [2] O. S. B. Al-Amoudi, W. A. Al-Kutti, S. Ahmad, and M. Maslehuddin. "Correlation between compressive strength and certain durability indices of plain and blended cement concretes". In: *Cement and Concrete Composites* 31.9 (2009), pp. 672–676.
- [3] Y. Zhou, X. Liu, Z. Deng, and Q.-F. Gao. "Field Monitoring and Numerical Analysis of the Reinforced Concrete Foundation of a Large-Scale Wind Turbine". In: *Advances in Materials Science and Engineering 2021* (2021).
- [4] M. He, X. Bai, R. Ma, and D. Huang. "Structural monitoring of an onshore wind turbine foundation using strain sensors". In: *Structure and Infrastructure Engineering* 15.3 (2019), pp. 314–333.
- [5] Q.-F. Gao, H. Dong, Z.-W. Deng, and Y.-Y. Ma. "Wind-induced dynamic amplification effects on the shallow foundation of a horizontal-axis wind turbine". In: *Computers and Geotechnics* 88 (2017), pp. 9–17.
- [6] Z.-W. Deng, Q.-F. Gao, H. Dong, and L.-X. Li. "Dynamic responses of the shallow foundation of an onshore wind turbine". In: *International Journal of Physical Modelling in Geotechnics* 19.5 (2019), pp. 247–260.
- [7] O. Kabus, O. OKulaienko, A. Ryabushko, V. Sopov, and O. Usherov-Marshak. "Temperature-time monitoring of concrete hardening of a wind farm foundation". In: *IOP Conference Series: Materials Science and Engineering*. Vol. 907. 1. IOP Publishing. (2020), p. 012037.
- [8] Y. Ju and H. Lei. "Actual temperature evolution of thick raft concrete foundations and cracking risk analysis". In: *Advances in Materials Science and Engineering 2019* (2019), pp. 1–11.
- [9] M. Perry, G. Fusiek, P. Niewczas, T. Rubert, and J. McAlorum. "Wireless concrete strength monitoring of wind turbine foundations". In: *Sensors* 17.12 (2017), p. 2928.
- [10] X. Liu, C. Zhou, and X. Chang. "Simulation of mass concrete temperature cracking propagation process". In: *Rock and Soil Mechanics* 31.8 (2010), pp. 2666–2671.
- [11] S. Li and S. Chen. "Structural health monitoring of maglev guideway PC girders with distributed long-gauge FBG sensors". In: *Structural Control and Health Monitoring* 25.1 (2018), e2046.
- [12] M. Currie, M. Saafi, C. Tachtatzis, and F. Quail. "Structural integrity monitoring of onshore wind turbine concrete foundations". In: *Renewable energy* 83 (2015), pp. 1131–1138.
- [13] T. A. Berkoff, M. A. Davis, and A. D. Kersey. "Fiber optic sensors for distributed vibration monitoring". In: *Vibration Monitoring and Control*. Vol. 2264. SPIE. 1994, pp. 148–154.
- [14] R. Rajinikumar, M. Suesser, K. Narayankhedkar, G. Krieg, and M. Atrey. "Fiber Bragg grating sensors for measuring temperature and strain simultaneously at cryogenic temperature". In: *AIP Conference Proceedings*. Vol. 985. 1. American Institute of Physics. (2008), pp. 383–390.
- [15] C. E.-I. du Béton. *CEB-FIP model code 1990: Design code*. Thomas Telford Publishing, (1993).
- [16] X. Wang and S.-j. Fang. "Comparison of Fatigue Design Code Requirements for Wind Turbine Foundations". In: *Special Publication* 348 (2021), pp. 145–158.
- [17] D. N. Veritas. "DNV-OS-J101-Design of offshore wind turbine structures". In: *Copenhagen, Denmark: DNV* (2014).

- [18] F. Z. Kachkouch, C. C. Noberto, L. F. d. A. L. Babadopulos, A. R. S. Melo, A. M. L. Machado, N. Sebaibi, F. Boukhelf, and Y. El Mendili. "Fatigue behavior of concrete: A literature review on the main relevant parameters". In: *Construction and Building Materials* 338 (2022), p. 127510.
- [19] F. Vidal, M. Navarro, C. Aranda, and T. Enomoto. "Changes in dynamic characteristics of Lorca RC buildings from pre-and post-earthquake ambient vibration data". In: *Bulletin of Earthquake Engineering* 12.5 (2014), pp. 2095–2110.
- [20] F. Omori. *The semi-destructive earthquake of April 26, 1922*. Imperial earthquake investigation committee, (1922).
- [21] G. M. Calvi, R. Pinho, and H. Crowley. "State-of-the-knowledge on the period elongation of RC buildings during strong ground shaking". In: *Proceedings of the 1st European conference of earthquake engineering and seismology, Geneva, Switzerland, paper*. Vol. 1535. (2006).
- [22] O. Salawu. "Detection of structural damage through changes in frequency: a review". In: *Engineering structures* 19.9 (1997), pp. 718–723.
- [23] N. Pugno, C. Surace, and R. Ruotolo. "Evaluation of the non-linear dynamic response to harmonic excitation of a beam with several breathing cracks". In: *Journal of sound and vibration* 235.5 (2000), pp. 749–762.
- [24] C. R. Farrar, S. W. Doebling, and D. A. Nix. "Vibration-based structural damage identification". In: *Philosophical Transactions of the Royal Society of London. Series A: Mathematical, Physical and Engineering Sciences* 359.1778 (2001), pp. 131–149.
- [25] P. Jiao, W. Borchani, H. Hasni, and N. Lajnef. "A new solution of measuring thermal response of prestressed concrete bridge girders for structural health monitoring". In: *Measurement Science and Technology* 28.8 (2017), p. 085005.
- [26] M. Hassanzadeh. *Cracks in Onshore Wind Power Foundations Causes and Consequences*. (2012).
- [27] Y. Huang, G. Liu, S. Huang, R. Rao, and C. Hu. "Experimental and finite element investigations on the temperature field of a massive bridge pier caused by the hydration heat of concrete". In: *Construction and Building Materials* 192 (2018), pp. 240–252.
- [28] G. De Schutter. "Finite element simulation of thermal cracking in massive hardening concrete elements using degree of hydration based material laws". In: *Computers & Structures* 80.27-30 (2002), pp. 2035–2042.
- [29] S. Kim. "Effect of heat generation from cement hydration on mass concrete placement, Civil Engineering, Iowa State University, Master of Science Thesis. 2010. 126 p". In: (2010).
- [30] Z. Li, D. Lu, and X. Gao. "Analysis of correlation between hydration heat release and compressive strength for blended cement pastes". In: *Construction and Building Materials* 260 (2020), p. 120436.
- [31] K. van Breugel, C. Braam, and E. Koenders. "Concrete structures under imposed thermal and shrinkage deformations: theory and practice". In: *TU Delft* (2011).
- [32] F.-J. Ulm and O. Coussy. "What is a "massive" concrete structure at early ages? Some dimensional arguments". In: *Journal of engineering mechanics* 127.5 (2001), pp. 512–522.
- [33] Y. Lee, M.-S. Choi, S.-T. Yi, and J.-K. Kim. "Experimental study on the convective heat transfer coefficient of early-age concrete". In: *Cement and Concrete Composites* 31.1 (2009), pp. 60–71.
- [34] A. Saul. "Principles underlying the steam curing of concrete at atmospheric pressure". In: *Magazine of Concrete Research* 2.6 (1951), pp. 127–140.
- [35] M. Hendriks and M. Roosen. *RTD 1016–1: 2020 Guidelines for Nonlinear Finite Element Analysis of Concrete Structures*. Tech. rep. Technical Report, 2020.
- [36] *DIANA User's Manual*. (2022). URL: <https://manuals.dianafea.com/d105/Diana.html> (visited on 06/26/2023).
- [37] B. Standard. "Eurocode 2: Design of concrete structures—". In: *Part 1.1* (2004), p. 230.

-
- [38] N. T. Chuc and A. Nikolay. "The effect of formworks on the temperature regime in the mass concrete". In: *Magazine of civil Engineering* 7 (99) (2020), p. 9911.

A

Appendix-A

A.1. Graphs for steel measurements from 2017

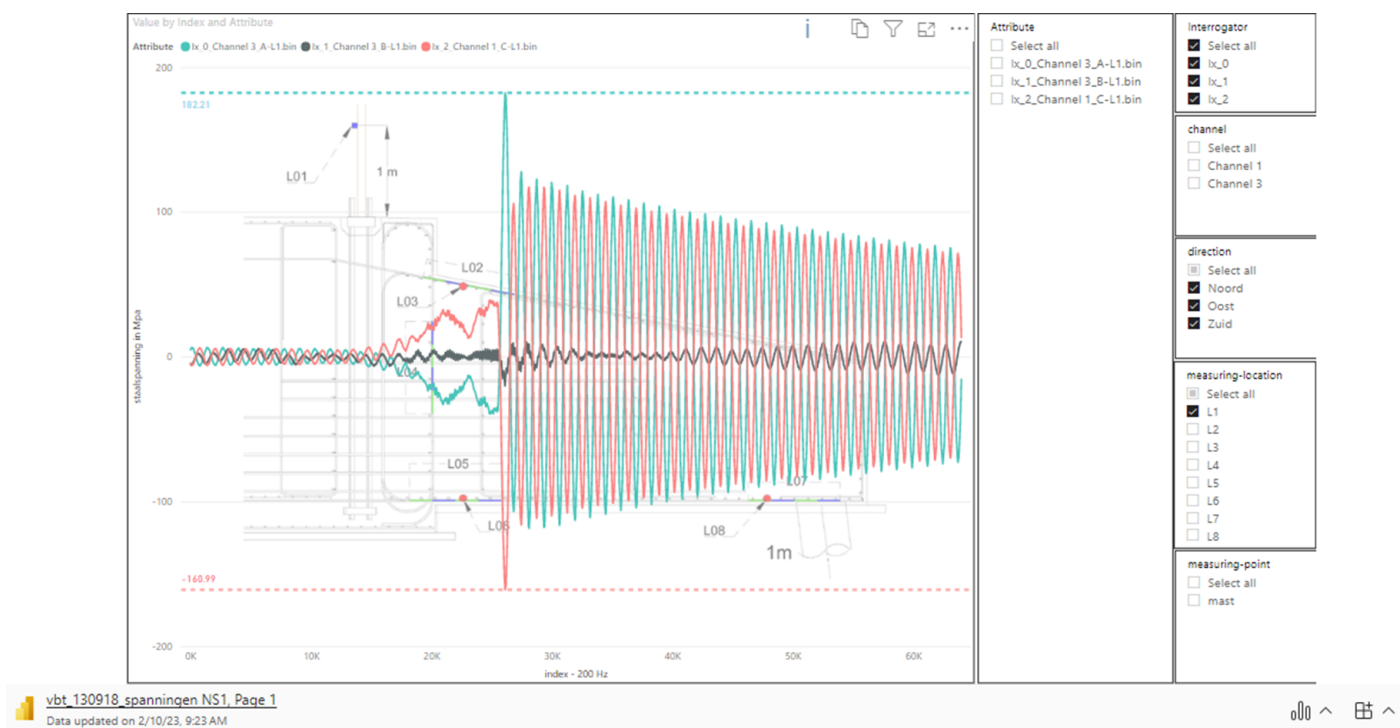


Figure A.1: Steel stress for L01 position

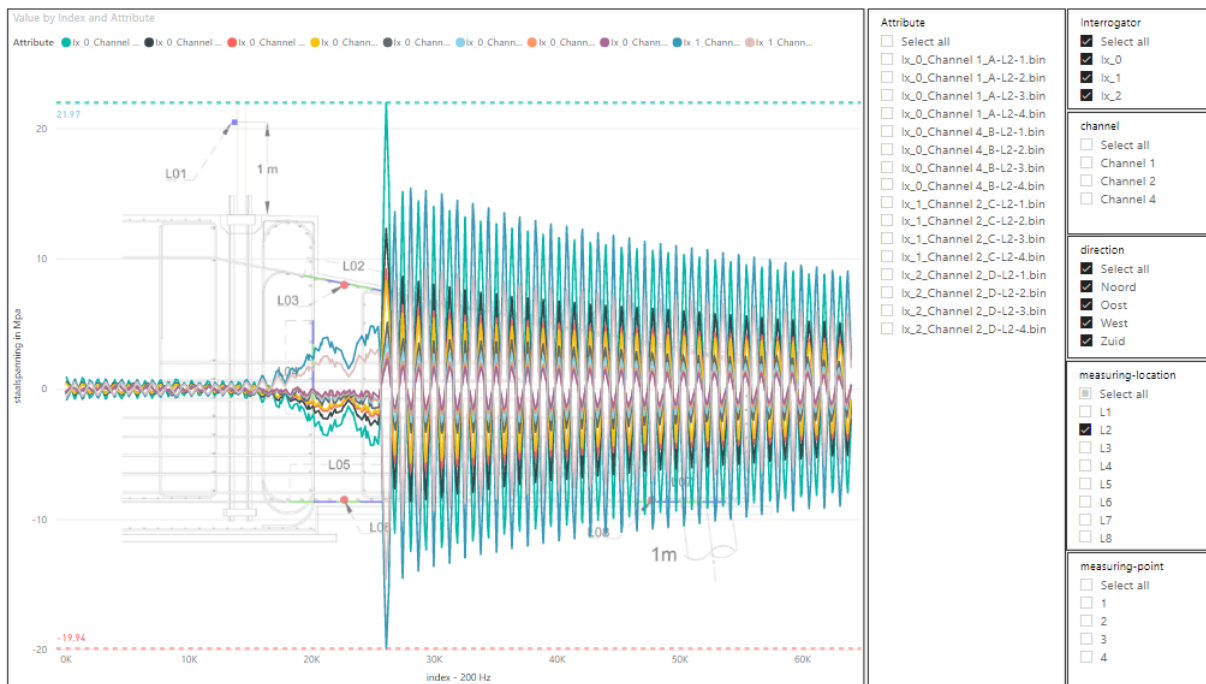


Figure A.2: Steel stress for L02 position

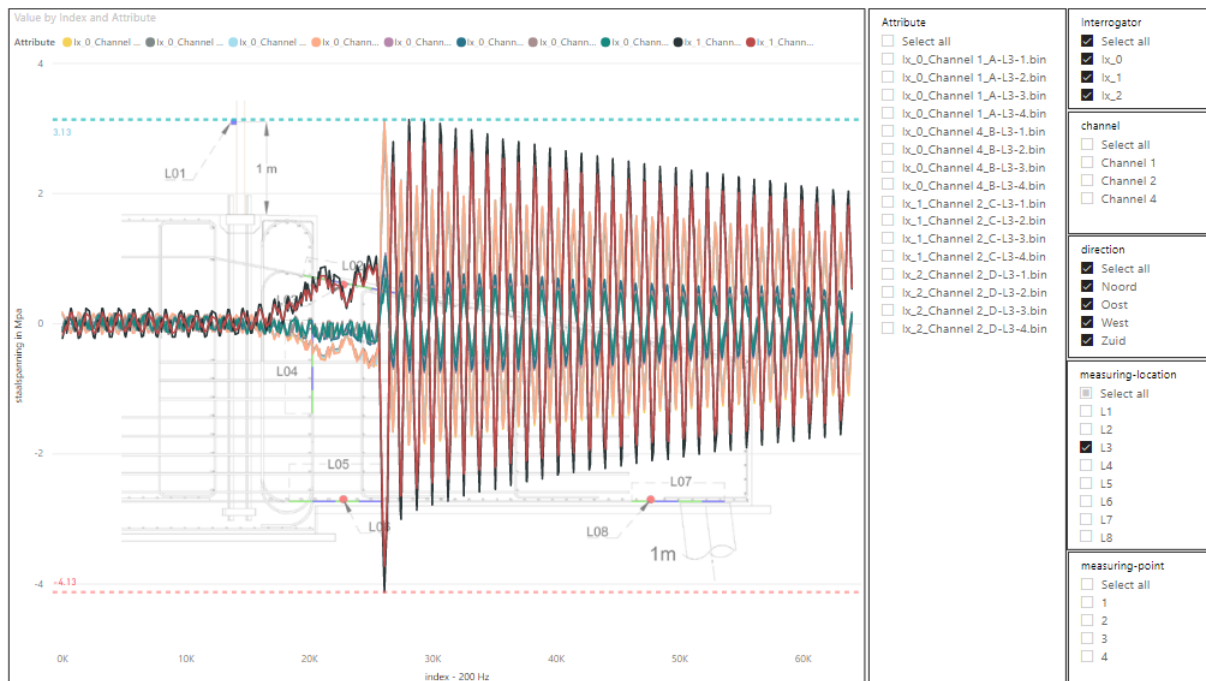


Figure A.3: Steel stress for L03 position

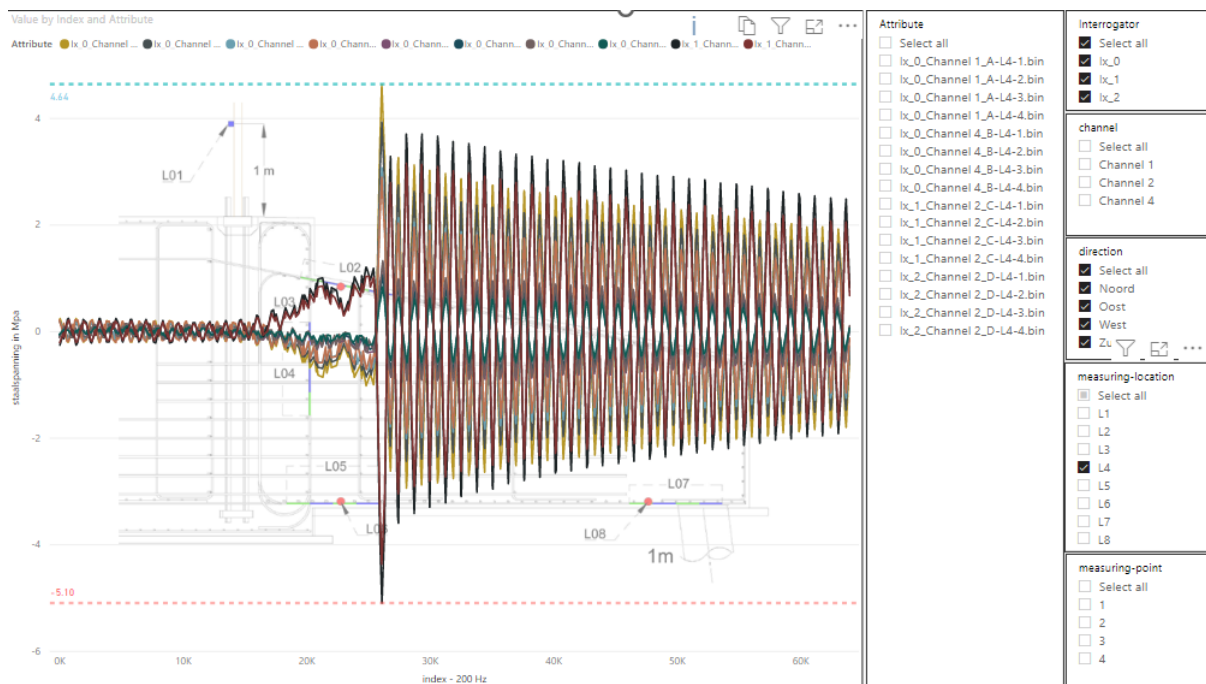


Figure A.4: Steel stress for L04 position

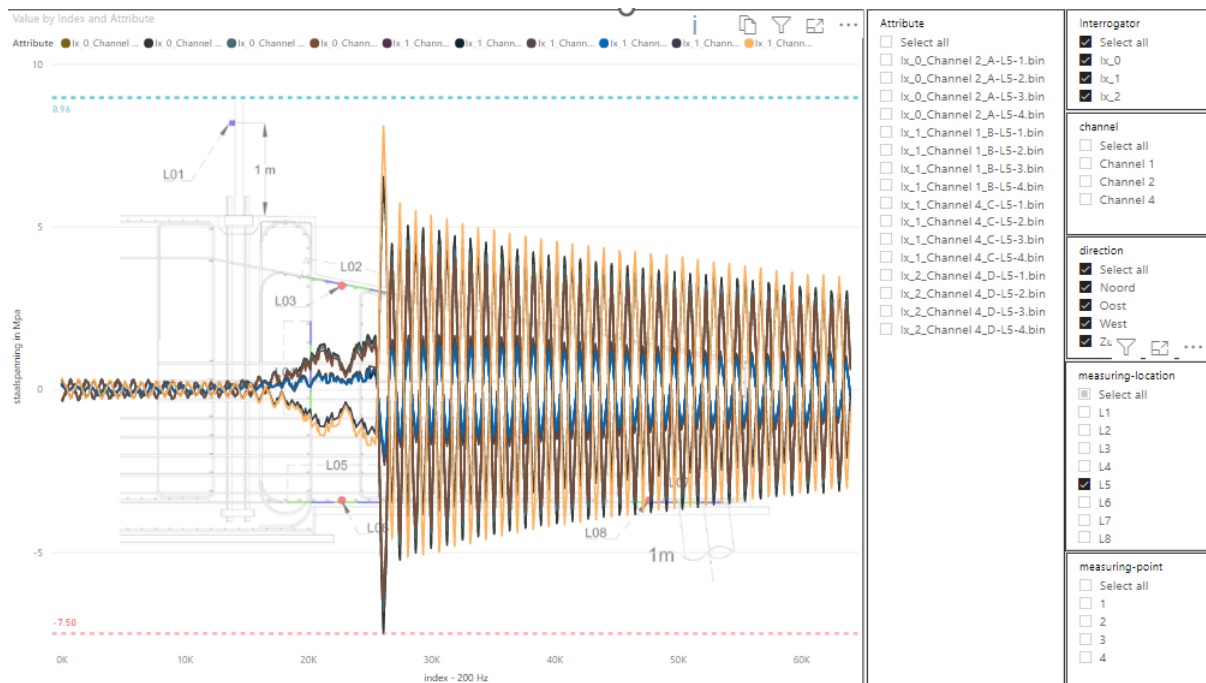


Figure A.5: Steel stress for L05 position

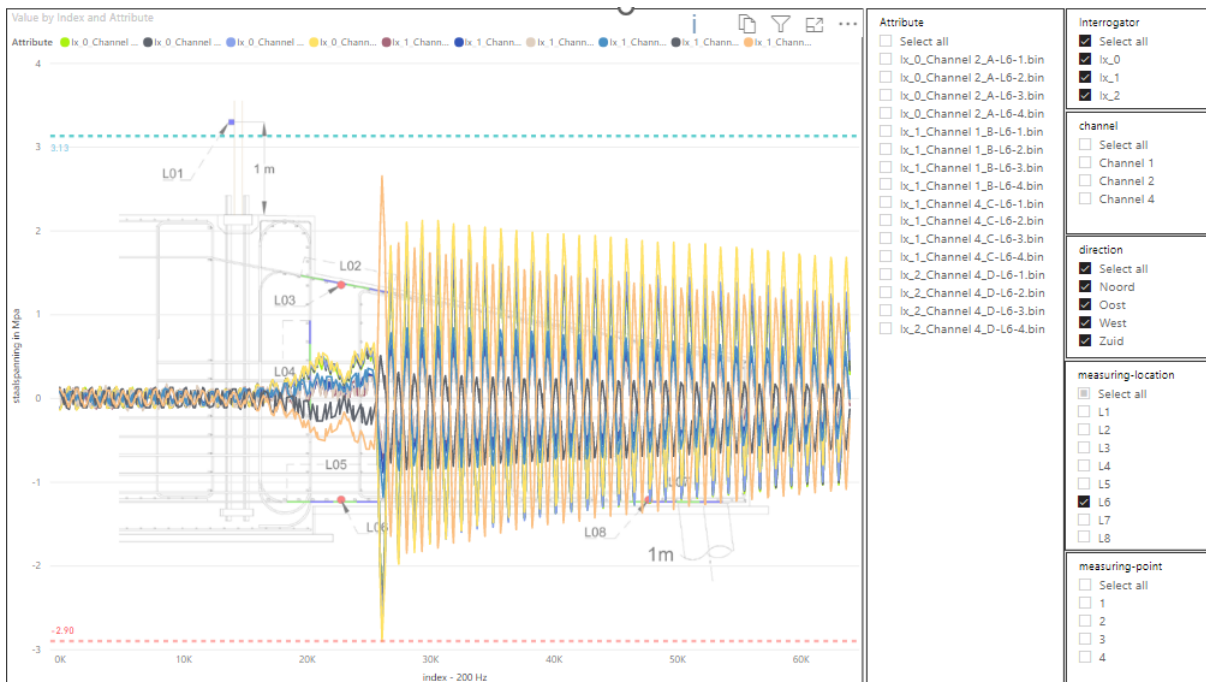


Figure A.6: Steel stress for L06 position

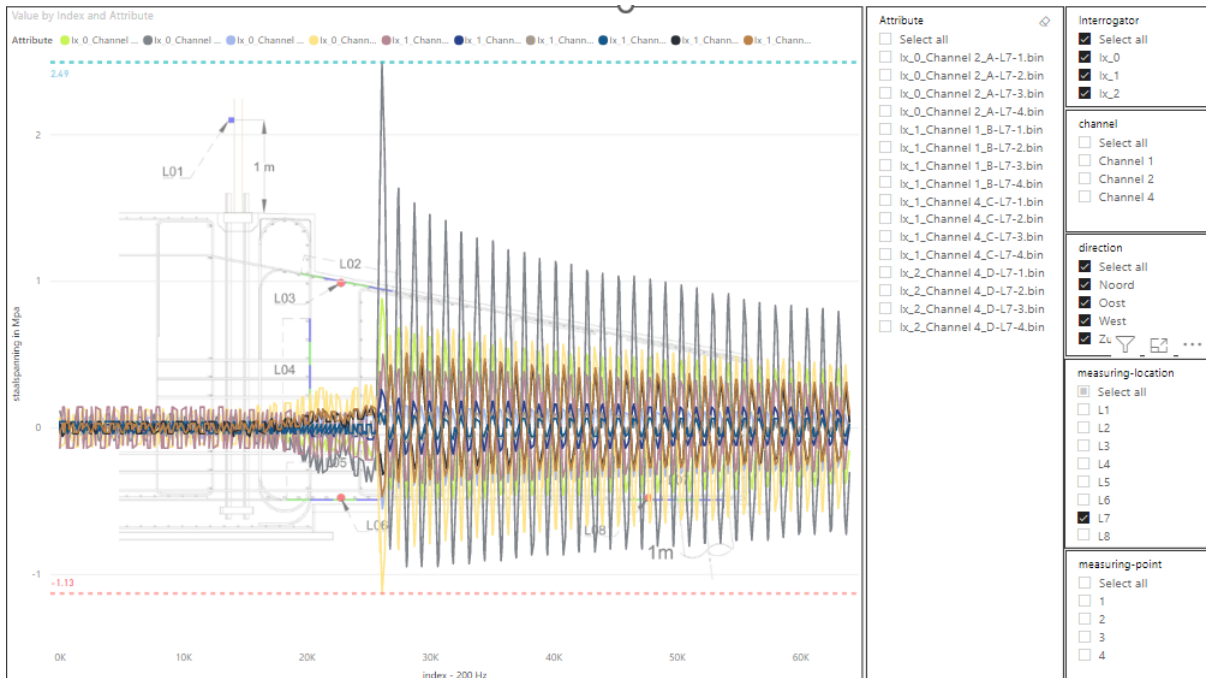


Figure A.7: Steel stress for L07 position

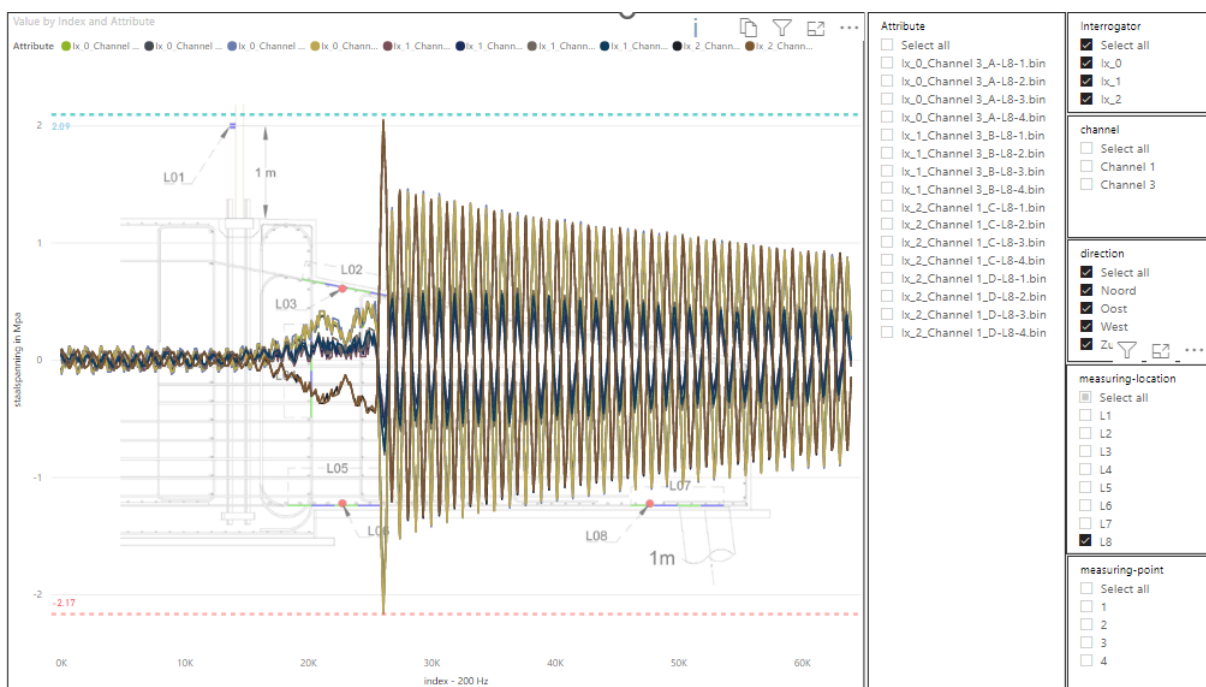


Figure A.8: Steel stress for L08 position

A.2. Graphs for steel measurements from 2022

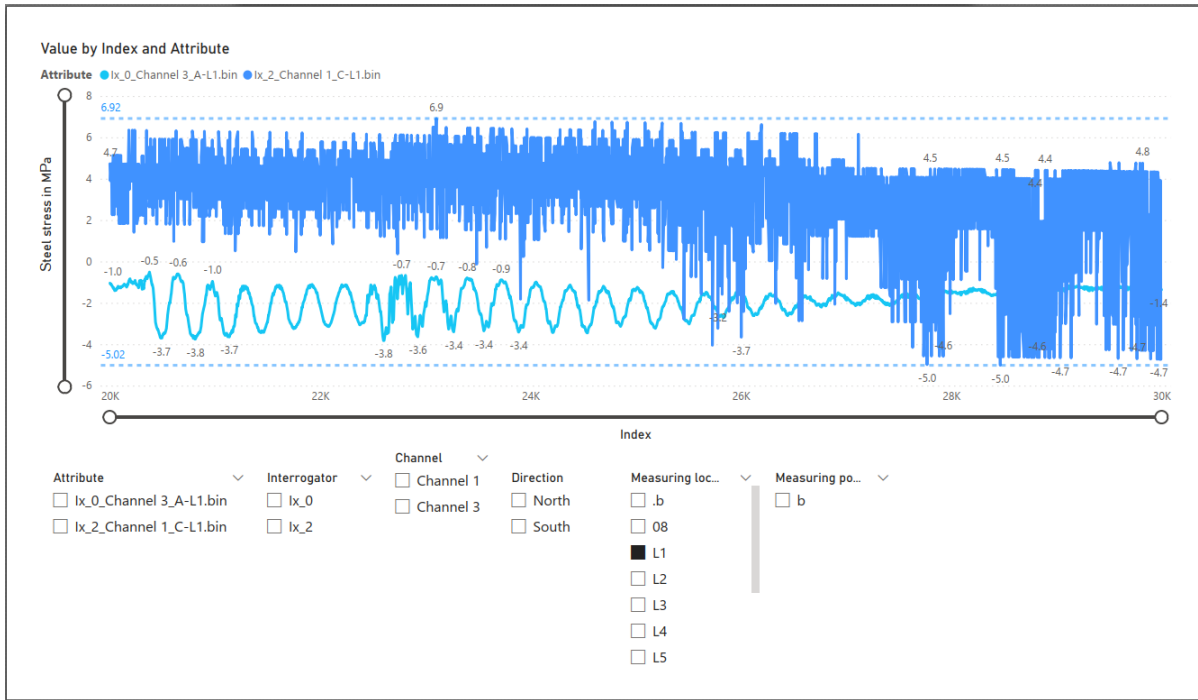


Figure A.9: Steel stress for L01 position

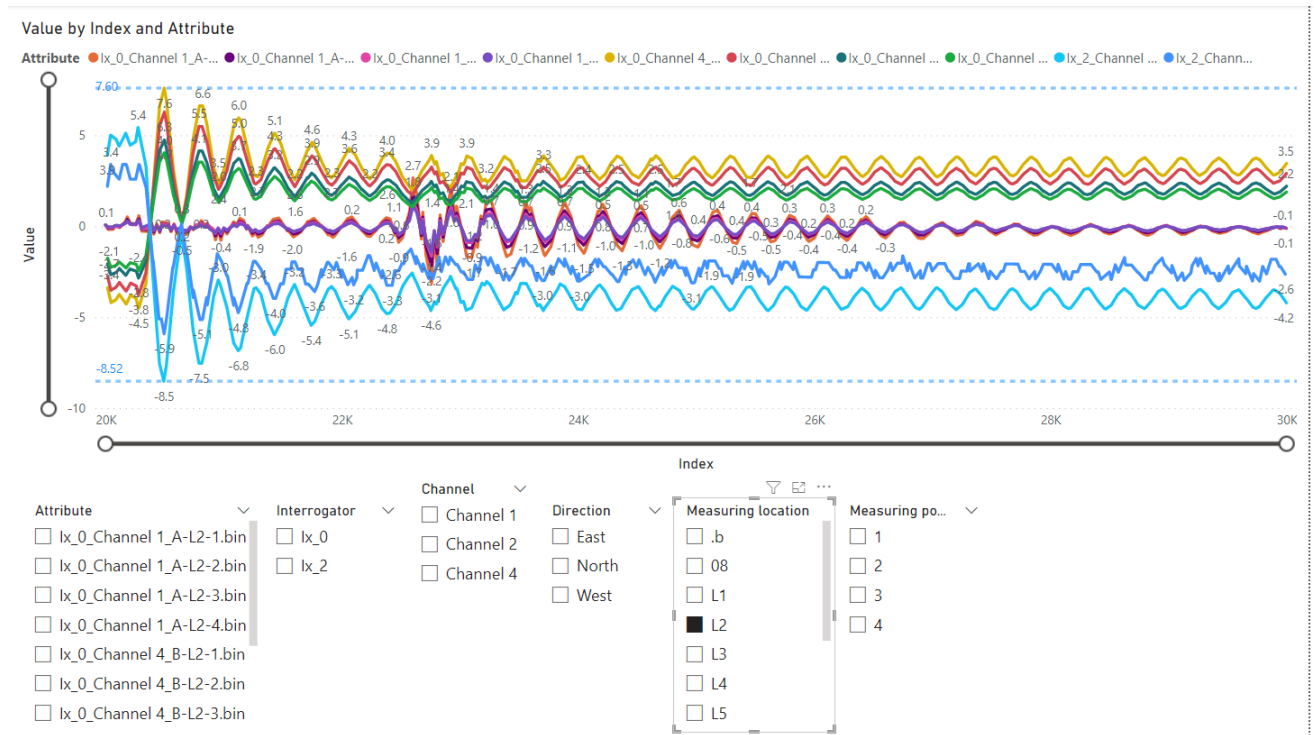


Figure A.10: Steel stress for L02 position

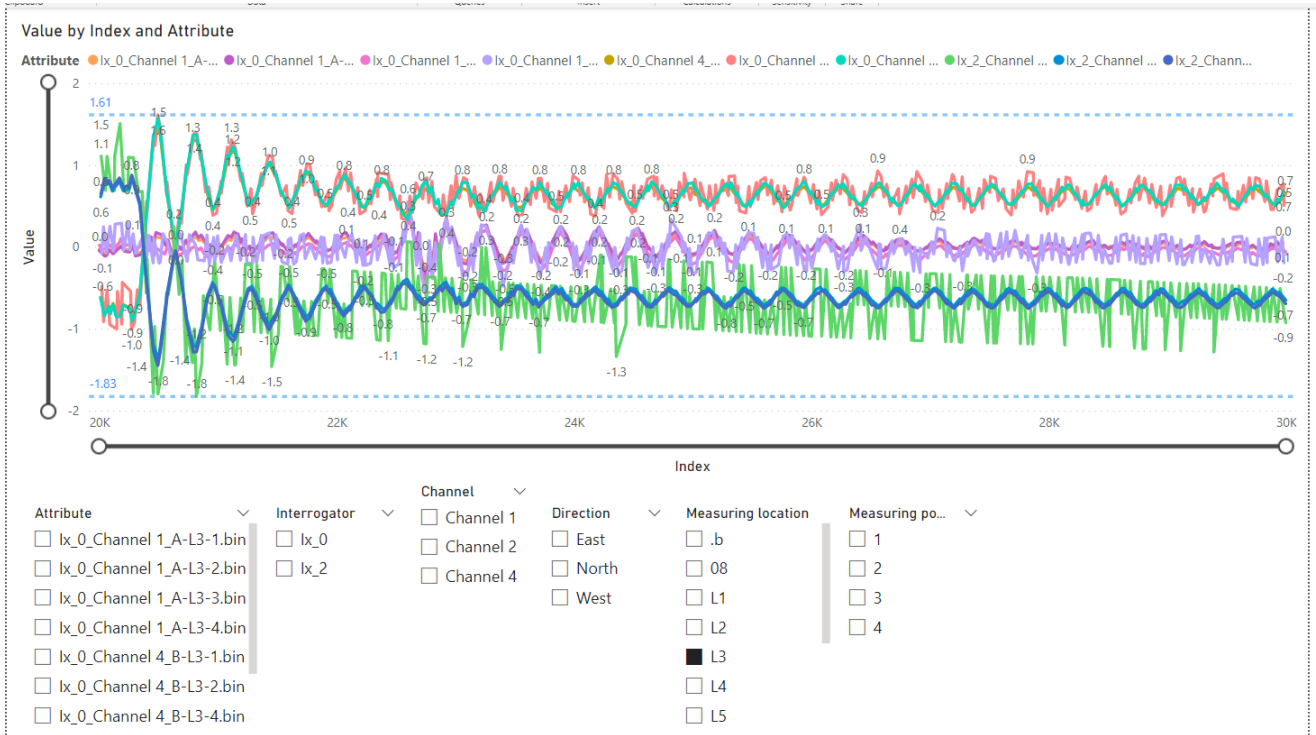


Figure A.11: Steel stress for L03 position

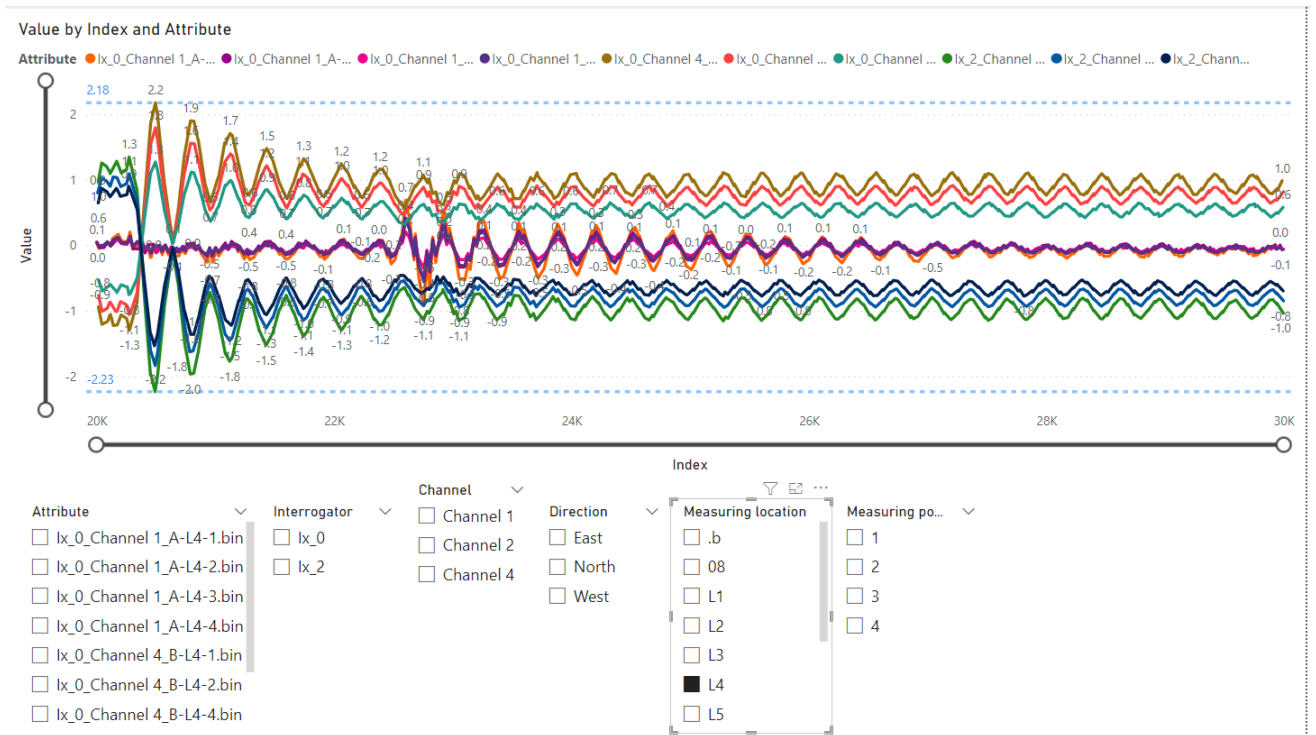


Figure A.12: Steel stress for L04 position

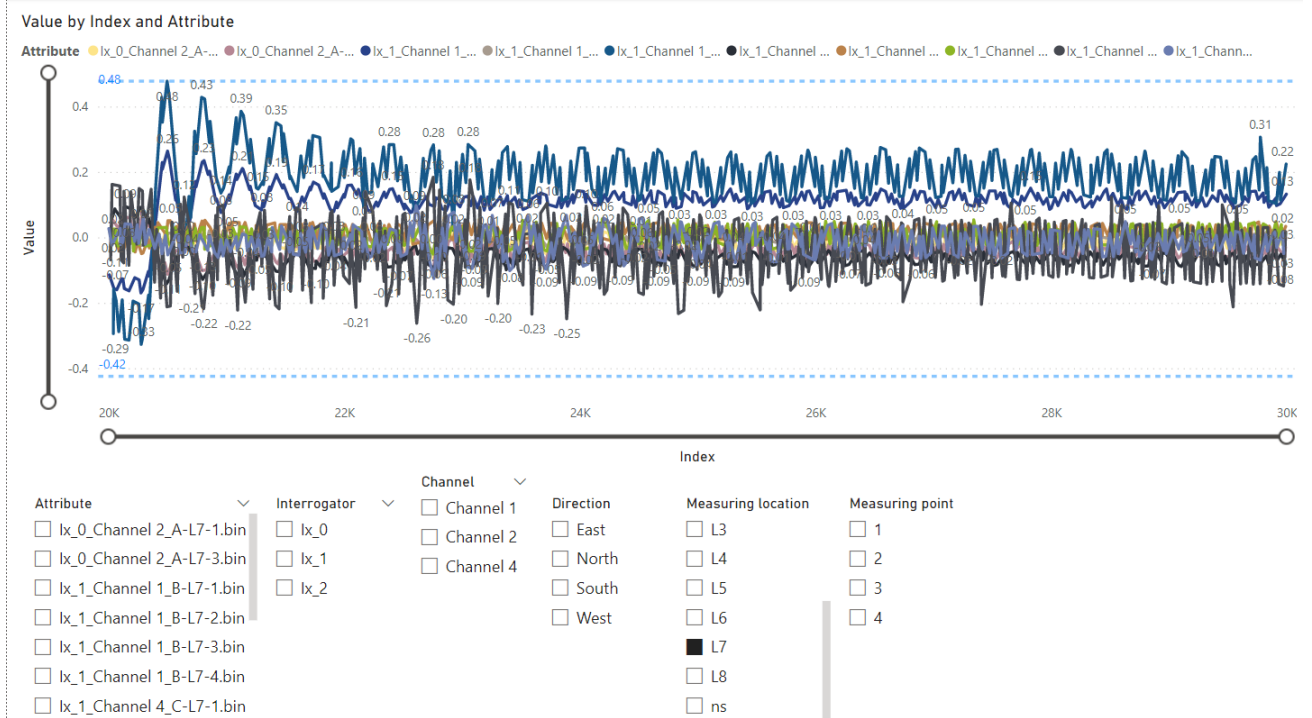


Figure A.15: Steel stress for L07 position

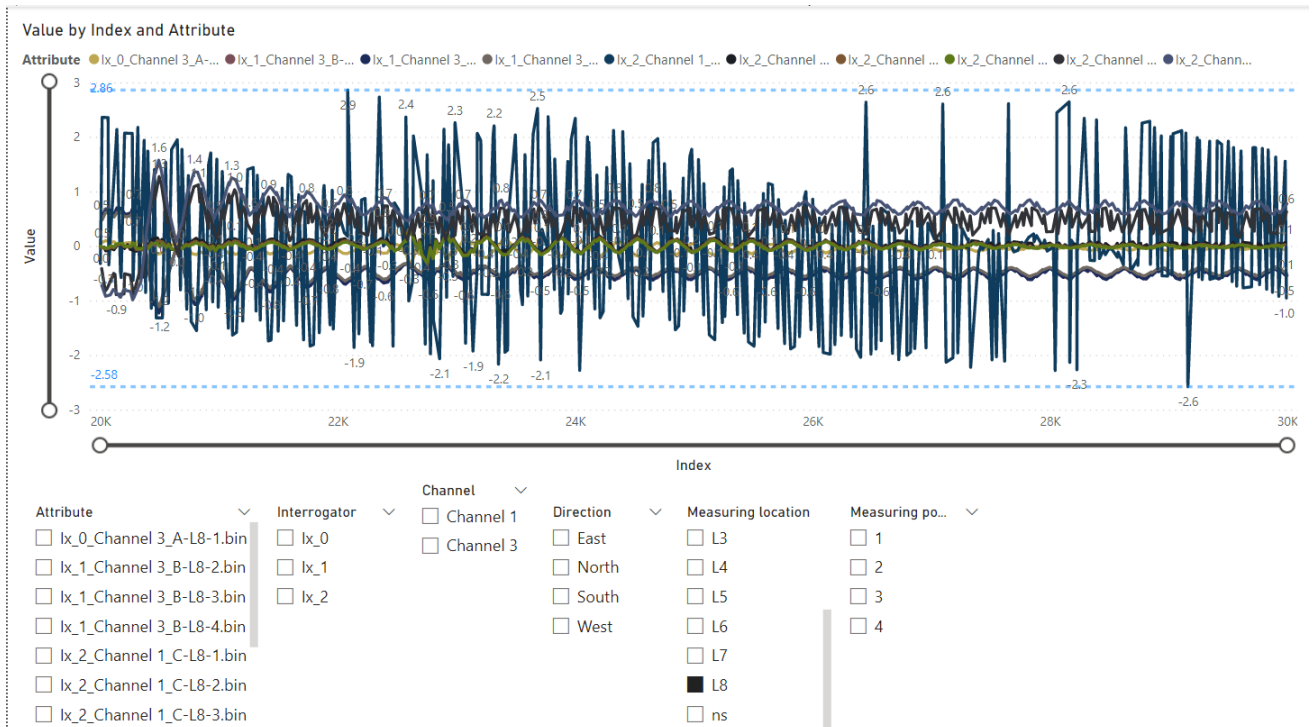


Figure A.16: Steel stress for L08 position

A.3. Graphs for steel measurements from 2023

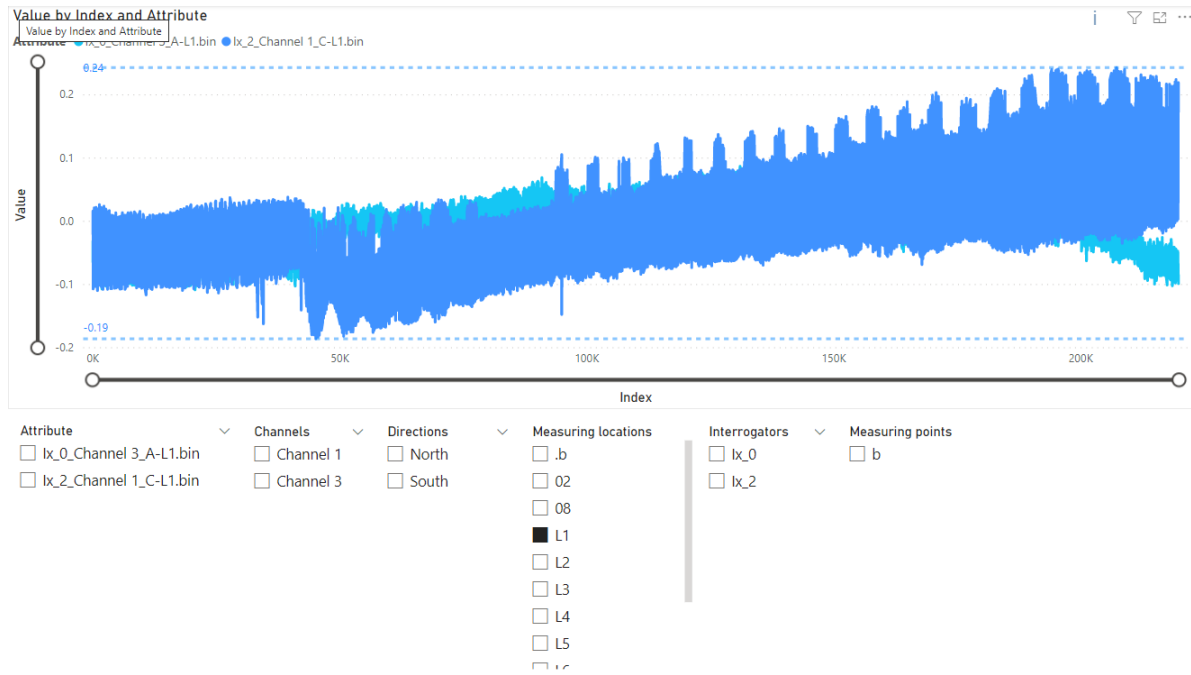


Figure A.17: Steel stress for L01 position



Figure A.18: Steel stress for L02 position



Figure A.19: Steel stress for L03 position

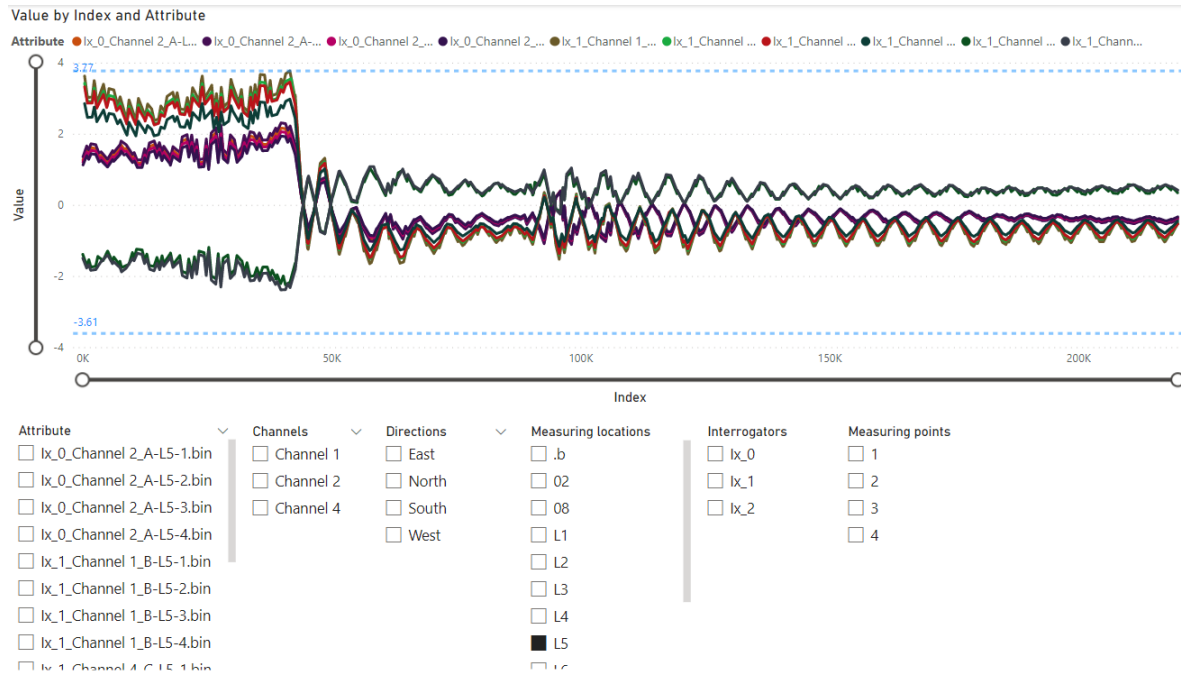


Figure A.20: Steel stress for L05 position

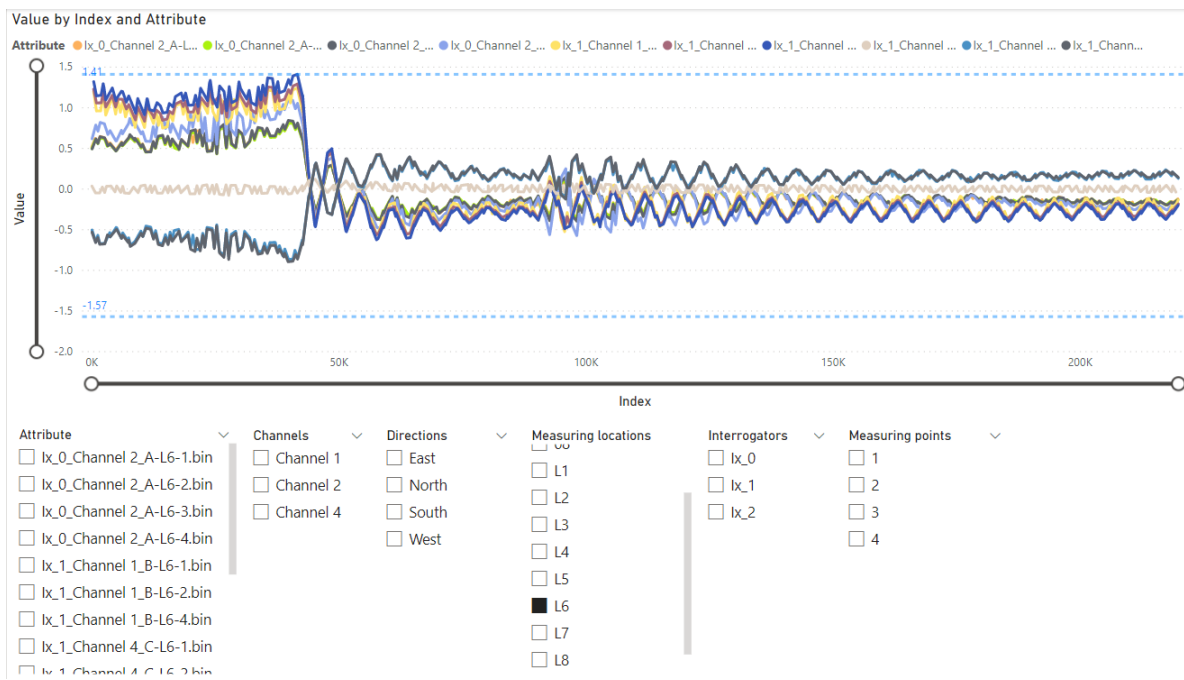


Figure A.21: Steel stress for L06 position

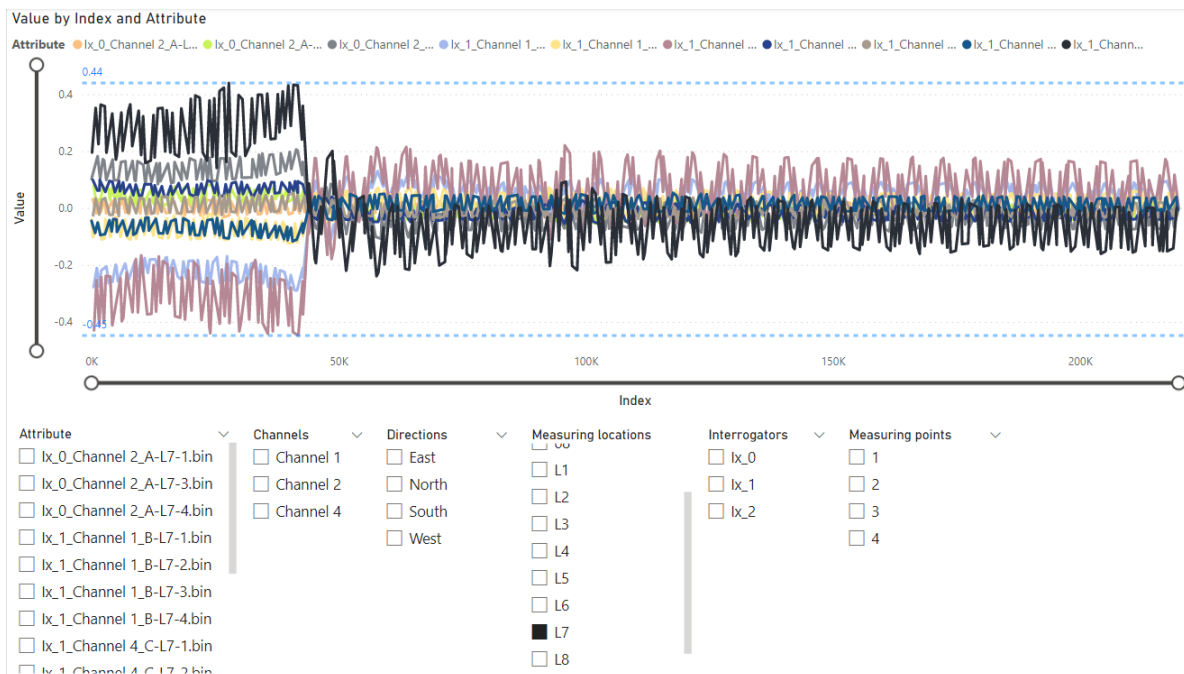


Figure A.22: Steel stress for L07 position

A.4. Determination of cracks

```

> restart;
> L := 150 : Lf := 22 :  $\Phi_{outer}$  := 6 :  $\Phi_{inner}$  := 5.9 : E := 2.1e+11 : Inertia := 2.6264 :
> E·Inertia;
                                     5.51544 × 1011
(1)
=
>  $\rho$  := 7850 : A := 0.6 :
> m :=  $\rho$ ·A;
                                     m := 4710.0
(2)
=
> Mtop := 114000 :
> f :=  $\frac{1}{2 \cdot 3.14} \left( \text{sqrt} \left( \frac{3.04 \cdot E \cdot \text{Inertia}}{(0.227 \cdot m \cdot (L + Lf) + Mtop) \cdot (L + Lf)^3} \right) \right)$ ;
                                     f := 0.1592356688
(3)
=
>

```

Figure A.23: Frequency analytical calculation

B

Appendix-B

B.1. Steel stresses due to the Nonlinear structural analysis only

Analysis1
Phase 11 - wind_ref, Loadstep 29, Loadfactor 1.0000
Reinforcement Couchy Total Stresses Sxx layer 1
min: 25.84N/mm² max: 176.33N/mm²

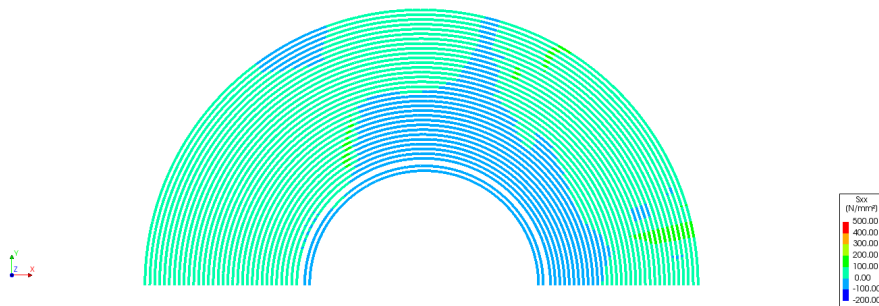


Figure B.1: Steel stress at top tangential-L3 position

Analysis1
Phase 11 - wind_ref, Loadstep 29, Loadfactor 1.0000
Reinforcement Couchy Total Stresses Sxx layer 1
min: -0.00N/mm² max: 253.69N/mm²

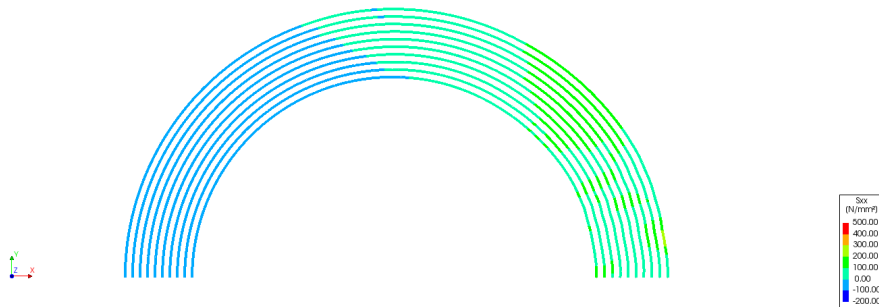


Figure B.2: Steel stress at bottom tangential-L6 position

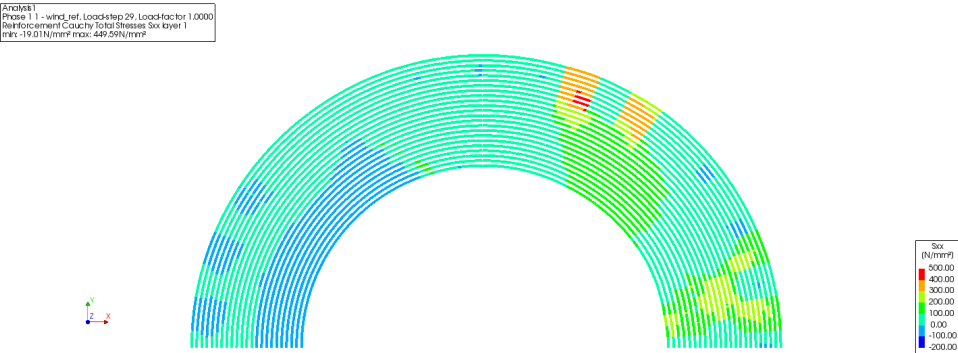


Figure B.3: Steel stress at bottom tangential near piles-L8 position

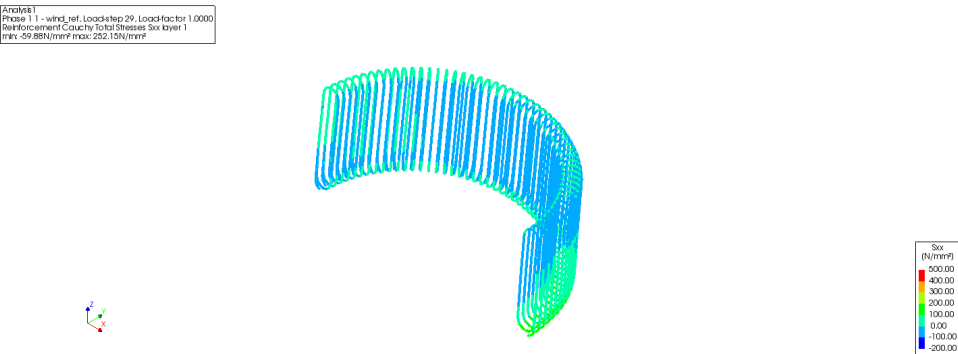


Figure B.4: Steel stress at stirrup-L4 position

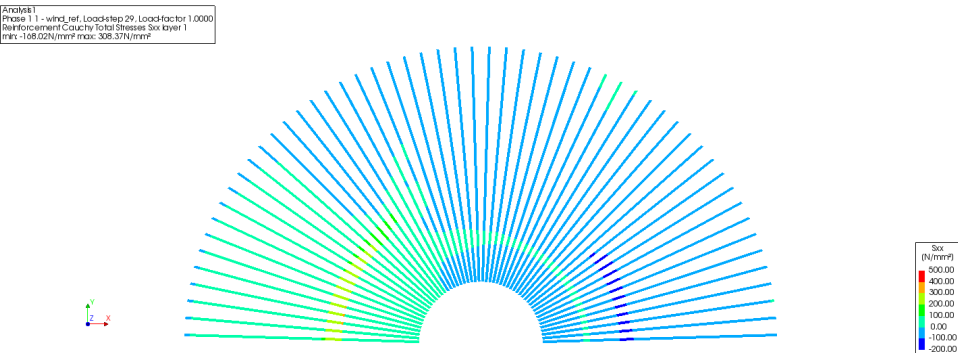


Figure B.5: Steel stress at top radial-L2 position

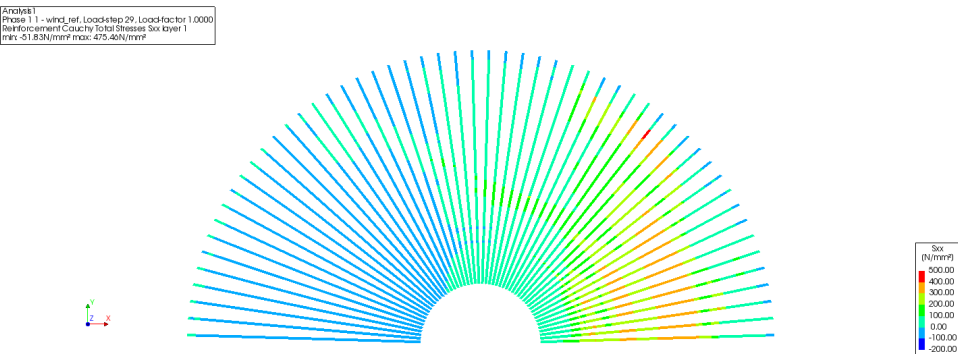


Figure B.6: Steel stress at bottom radial-L5 position

B.2. Effects of Maturity effect

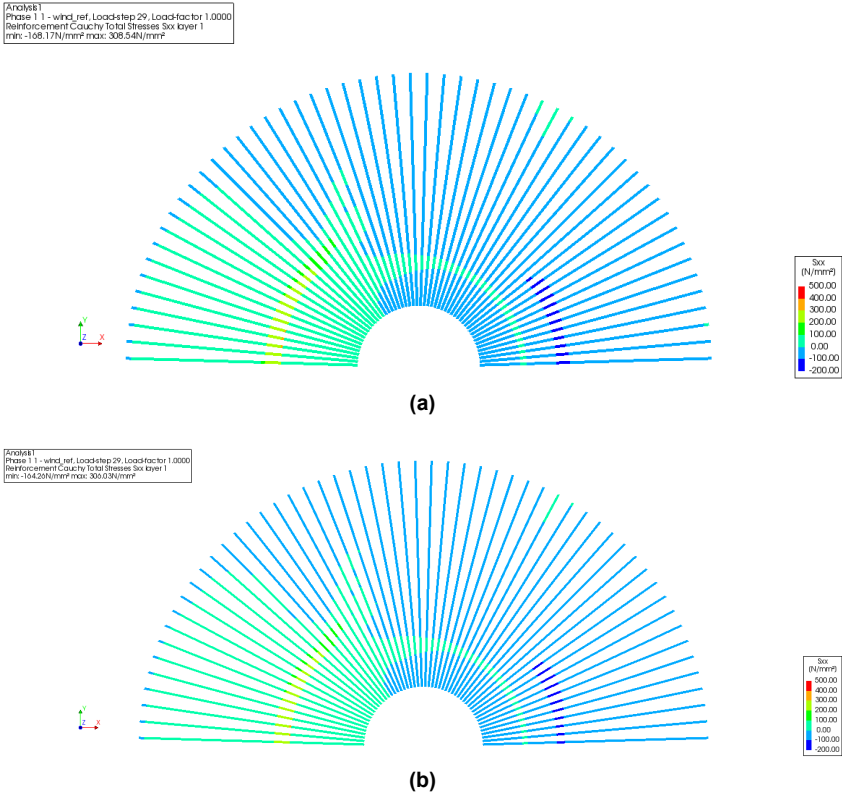


Figure B.7: Top radial bars a) without maturity effect, b)with maturity effect

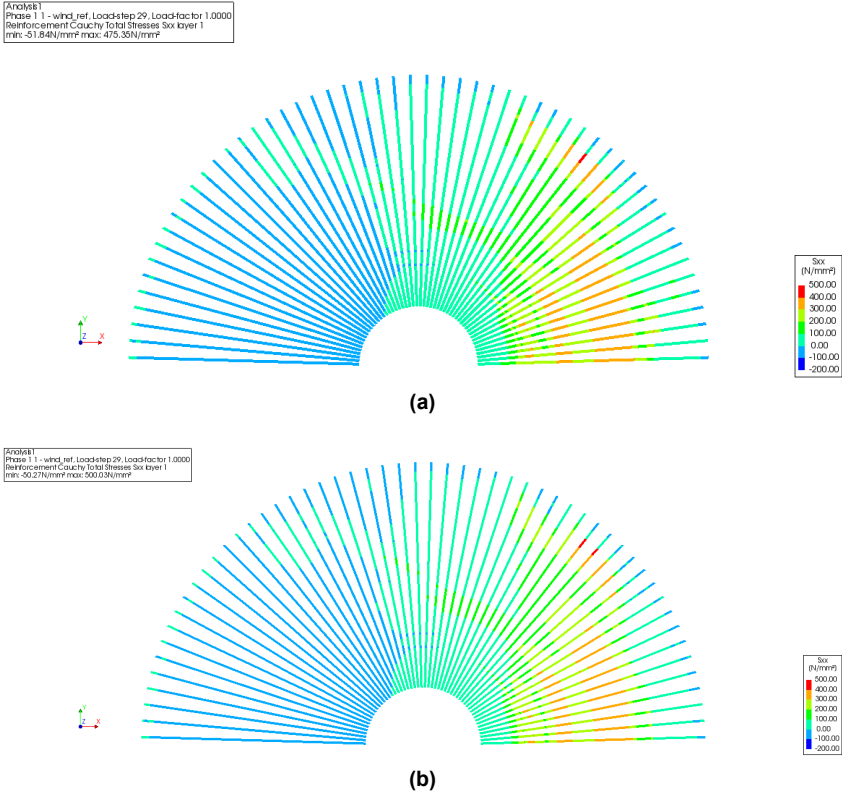


Figure B.8: Bottom radial bars a) without maturity effect, b)with maturity effect

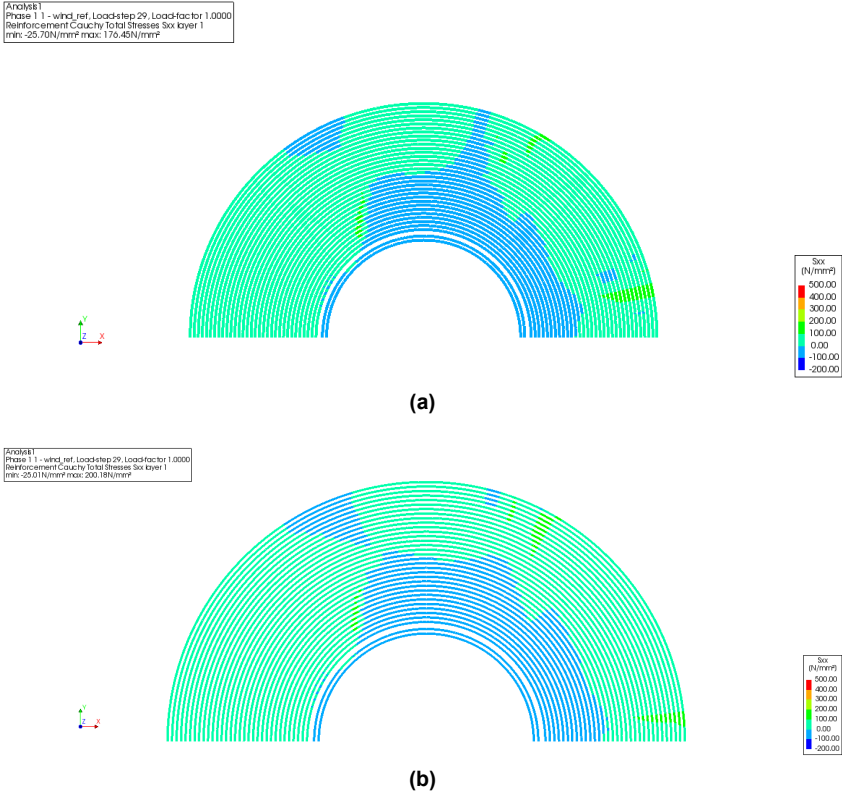


Figure B.9: Top tangential bars a) without maturity effect, b)with maturity effect

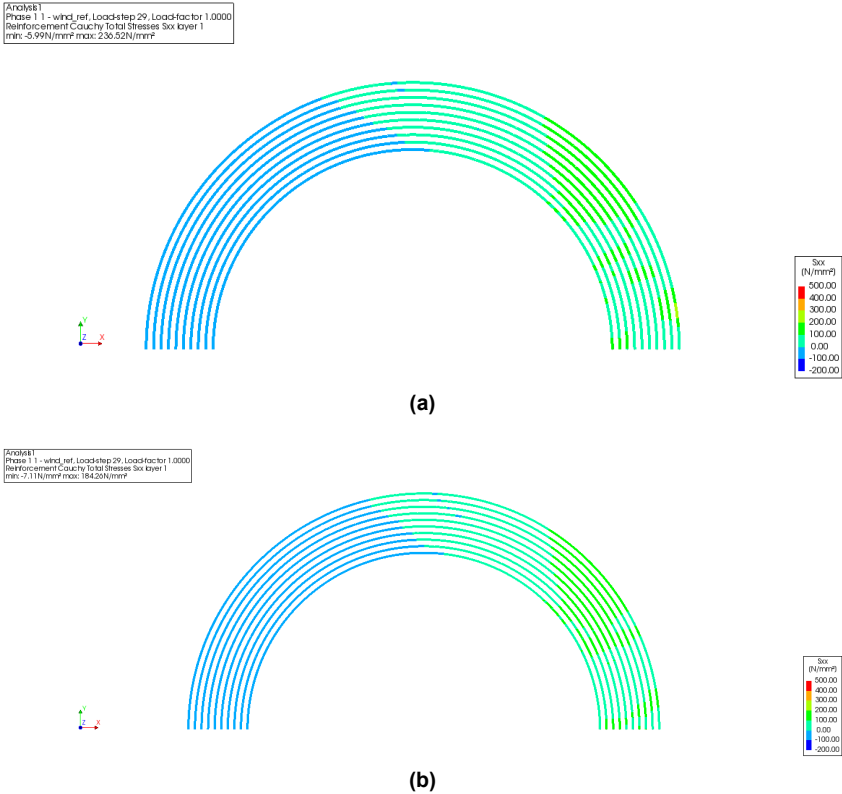


Figure B.10: Bottom tangential bars a) without maturity effect, b)with maturity effect

B.3. Steel stresses generated due to the Hydration heat effect

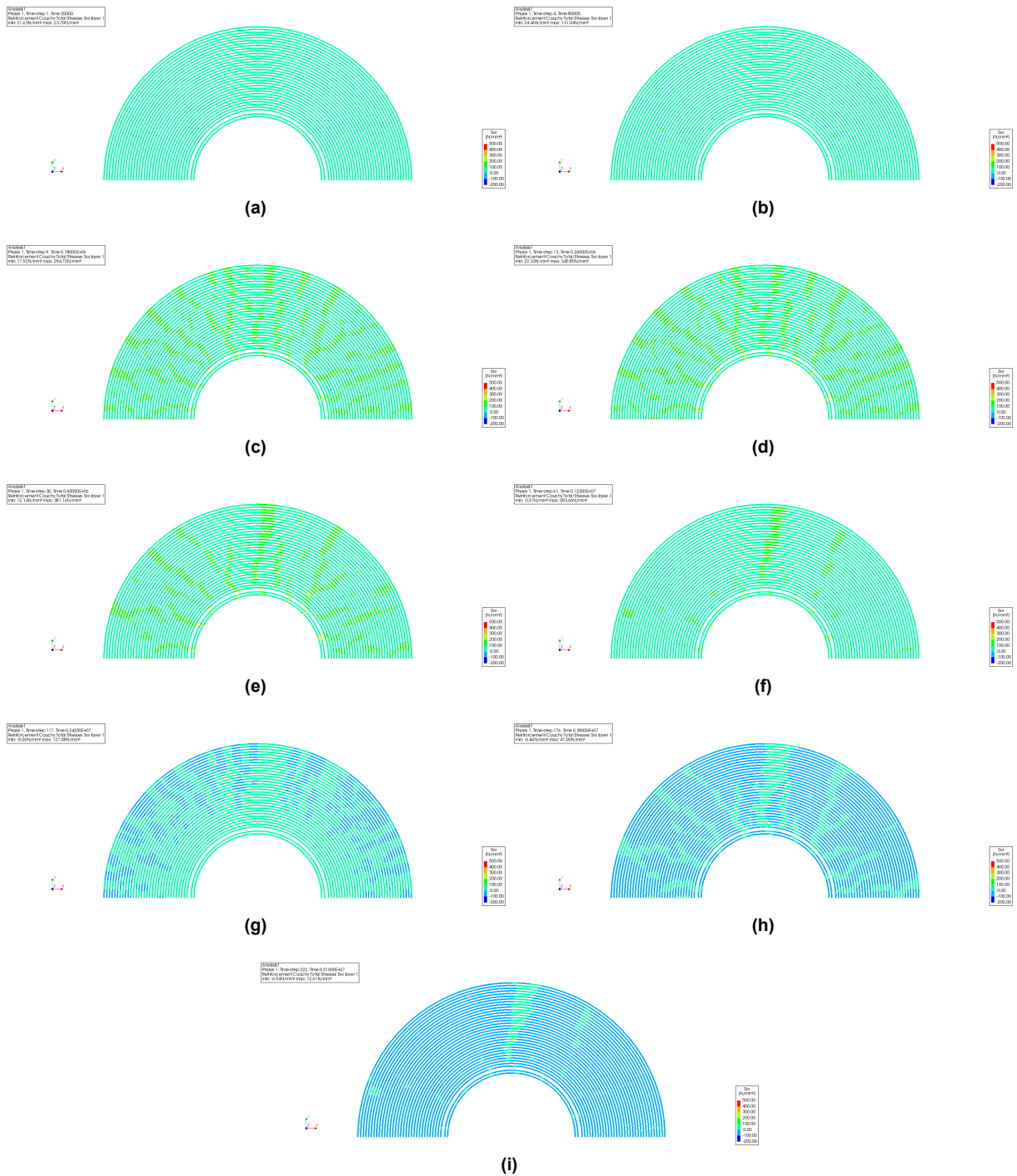


Figure B.11: Steel stress in the Top tangential rebars a) Day 0, b) Day 1, c) Day 2, d) Day 3, e) Day 7, f) Day 14, g) Day 28, h) Day 45, i) Day 60



Figure B.12: Steel stress in the Bottom tangential rebars a) Day 0, b) Day 1, c) Day 2, d) Day 3, e) Day 7, f) Day 14, g) Day 28, h) Day 45, i) Day 60

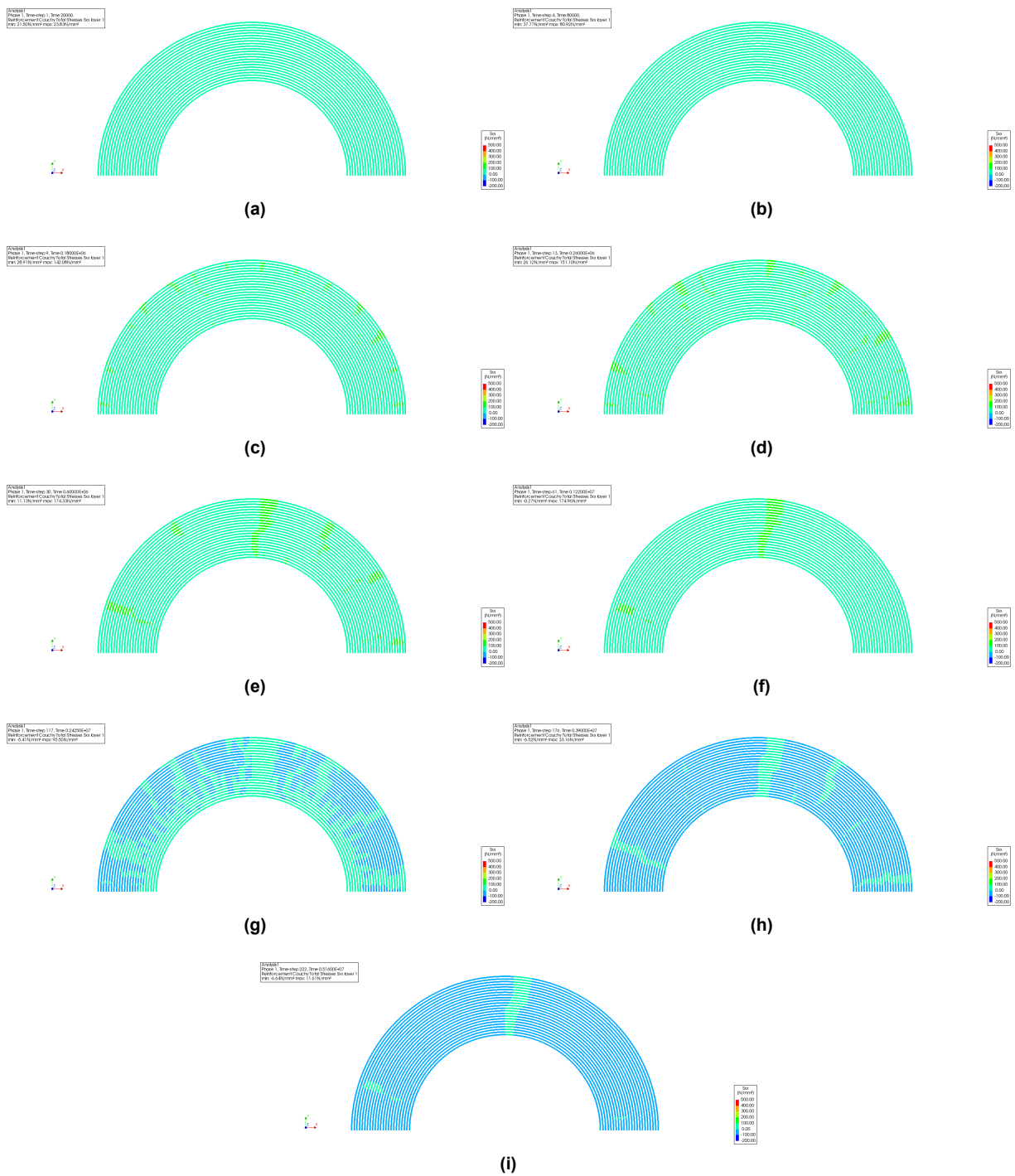


Figure B.13: Steel stress in the Bottom tangential rebars near the piles a) Day 0, b) Day 1, c) Day 2, d) Day 3, e) Day 7, f) Day 14, g) Day 28, h) Day 45, i) Day 60

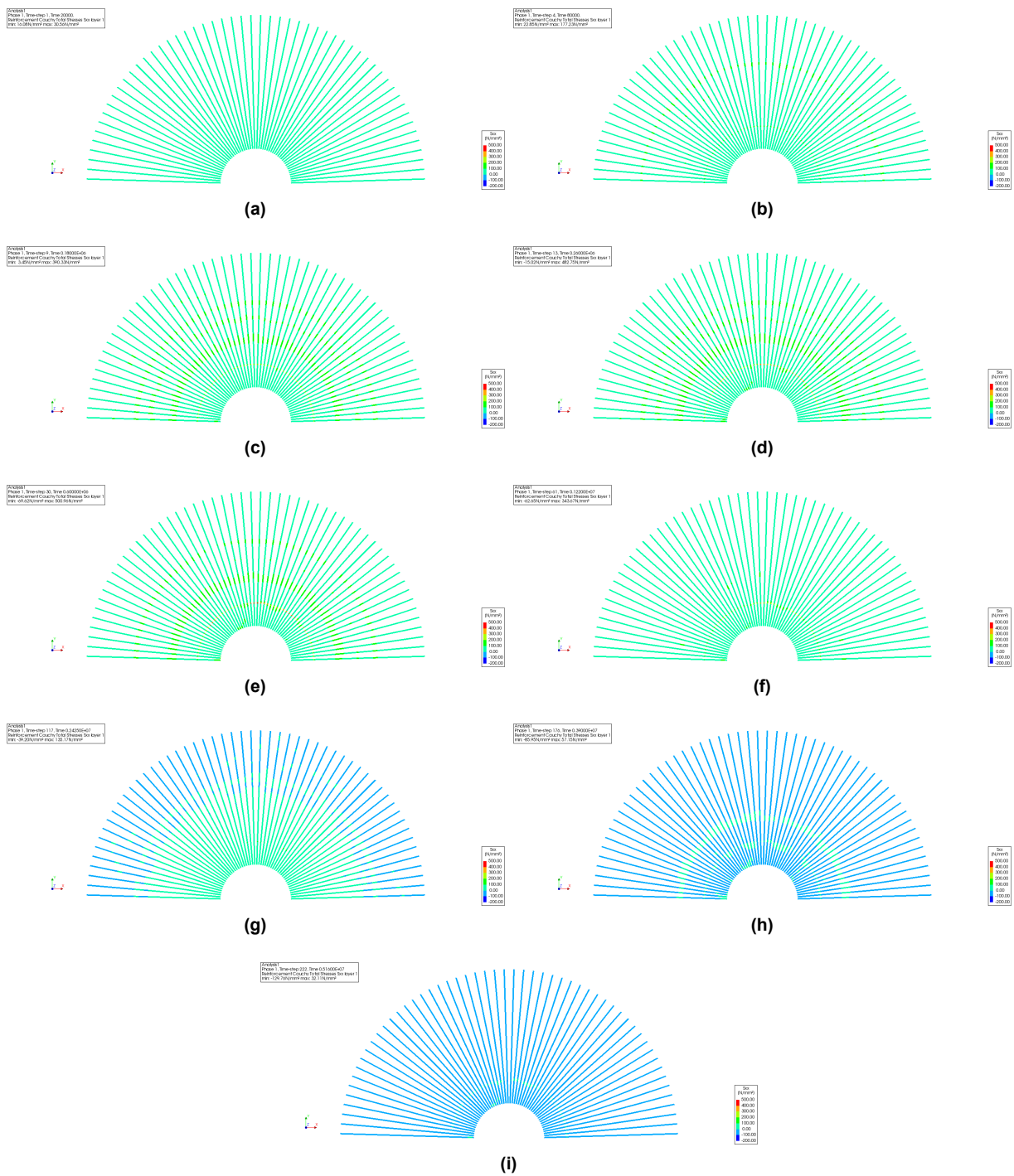


Figure B.14: Steel stress in the Top radial rebars a) Day 0, b) Day 1, c) Day 2, d) Day 3, e) Day 7, f) Day 14, g) Day 28, h) Day 45, i) Day 60

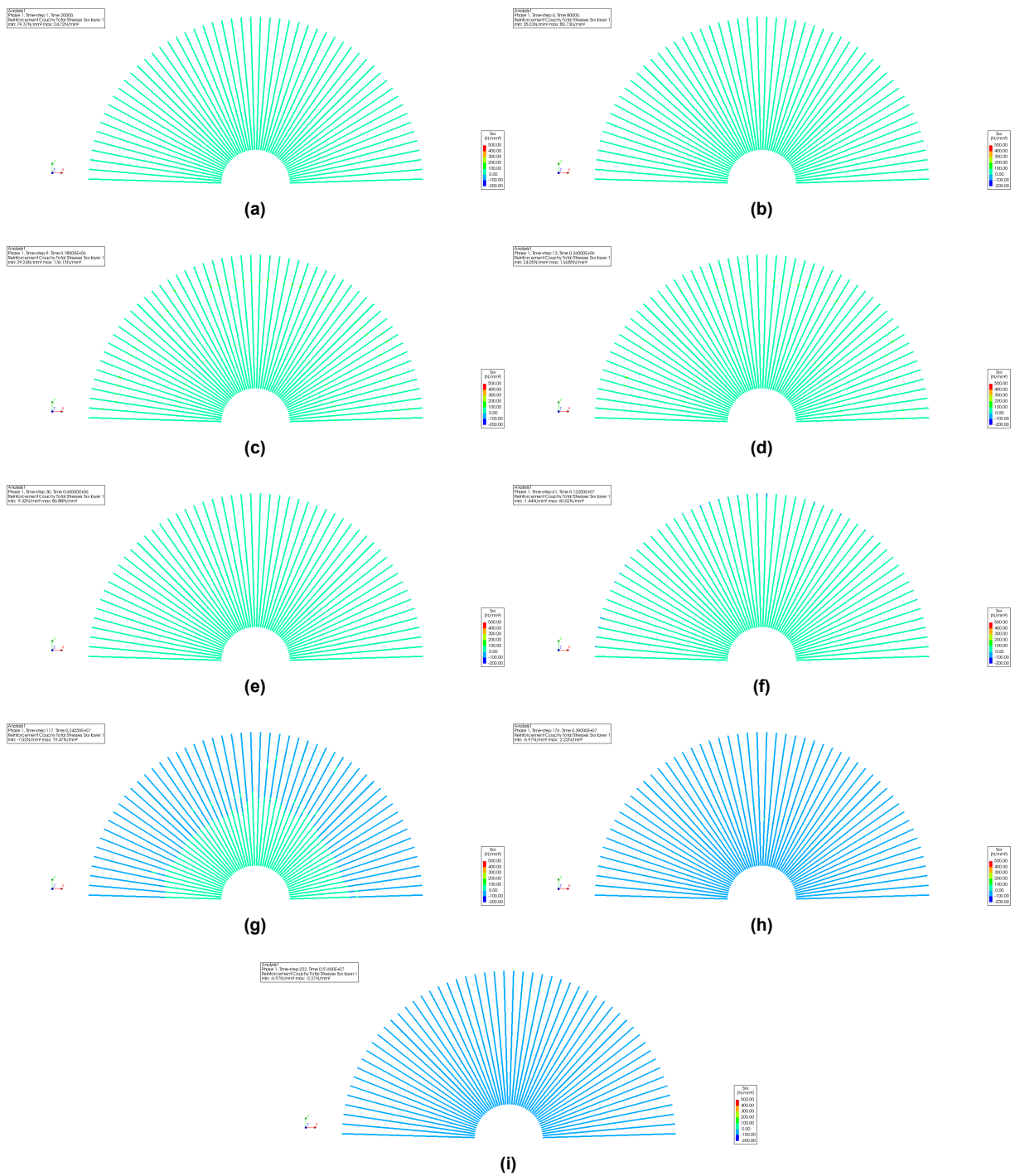


Figure B.15: Steel stress in the Bottom radial rebars a) Day 0, b) Day 1, c) Day 2, d) Day 3, e) Day 7, f) Day 14, g) Day 28, h) Day 45, i) Day 60

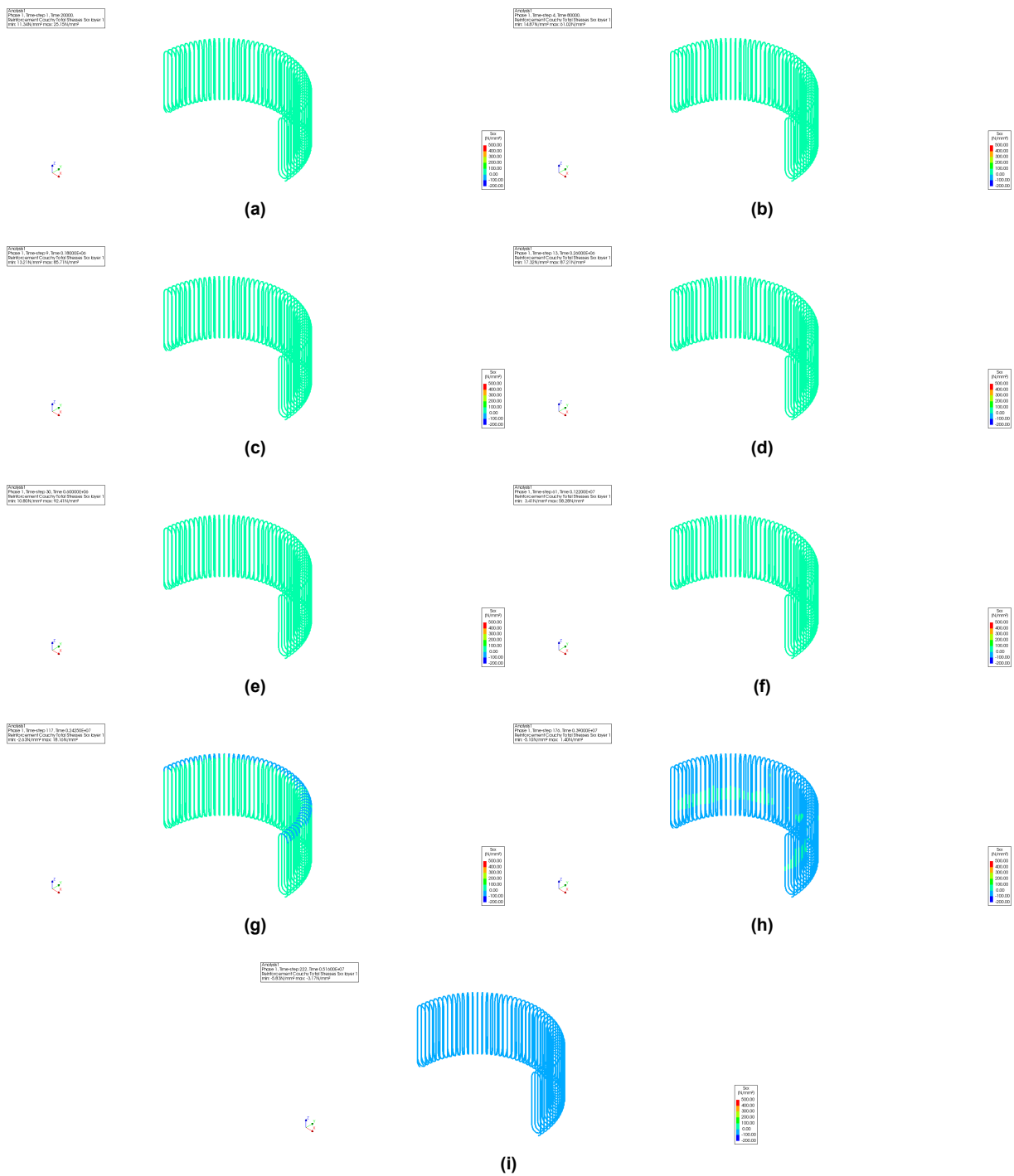


Figure B.16: Steel stress in the side stirrups a) Day 0, b) Day 1, c) Day 2, d) Day 3, e) Day 7, f) Day 14, g) Day 28, h) Day 45, i) Day 60

B.4. Steel stress due to the combined analysis

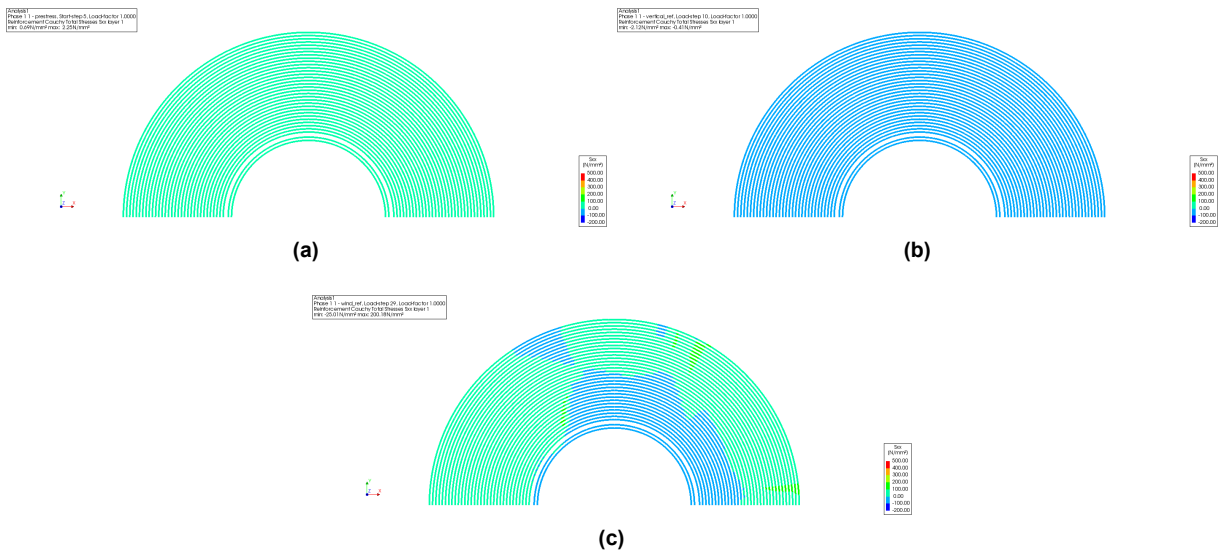


Figure B.17: Steel stress in the Top tangential rebars a) After prestress, b) After vertical load, c) After wind load

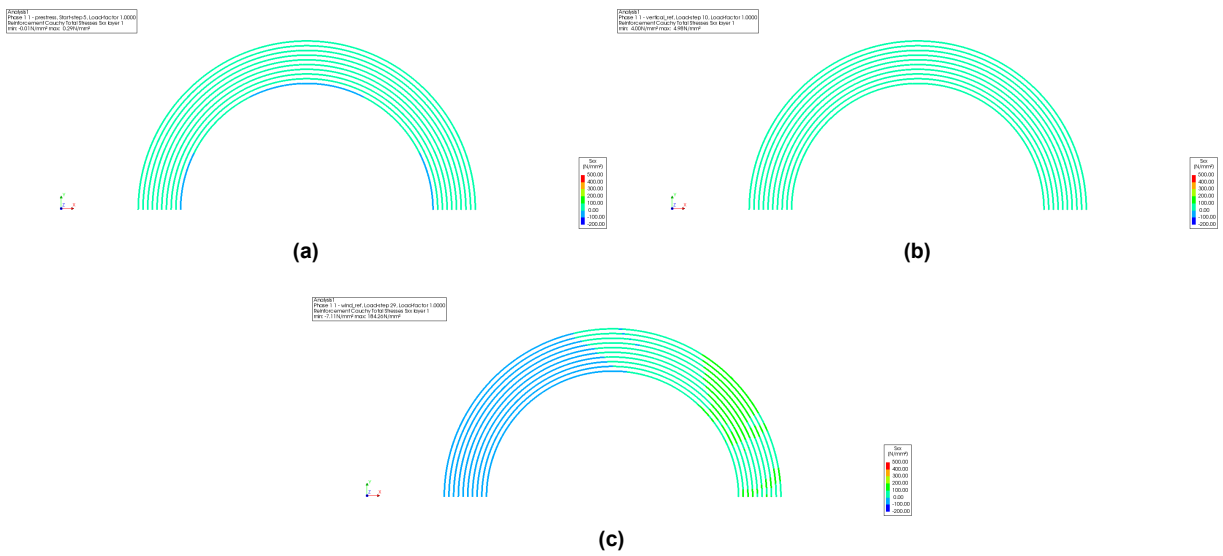


Figure B.18: Steel stress in the Bottom tangential rebars a) After prestress, b) After vertical load, c) After wind load

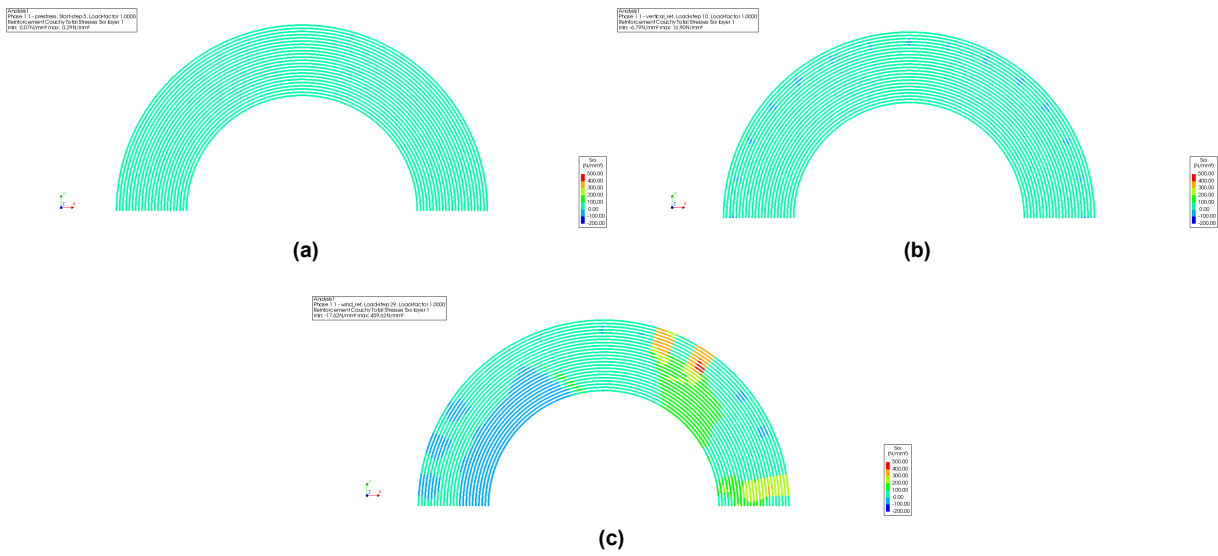


Figure B.19: Steel stress in the Bottom tangential rebars near piles a) After prestress, b) After vertical load, c) After wind load

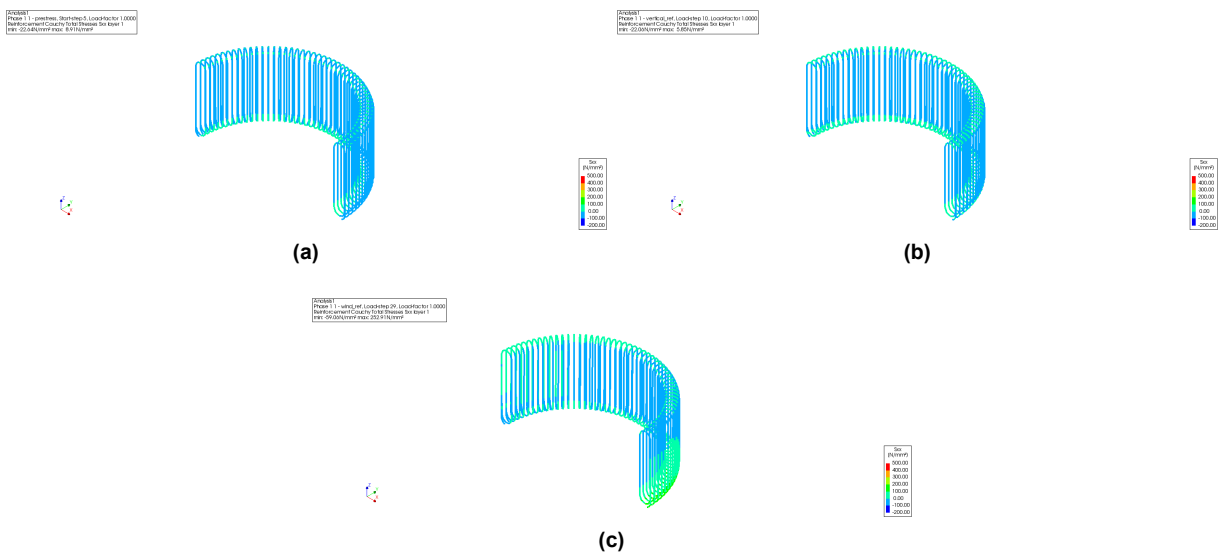


Figure B.20: Steel stress in the stirrups a) After prestress, b) After vertical load, c) After wind load

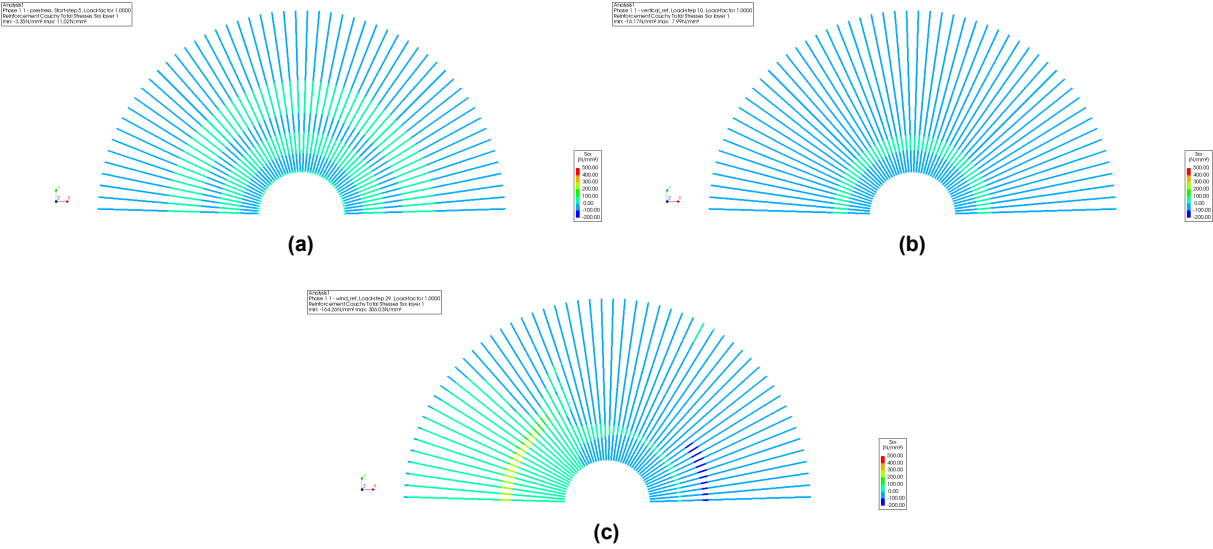


Figure B.21: Steel stress in the Top radial rebars a) After prestress, b) After vertical load, c) After wind load

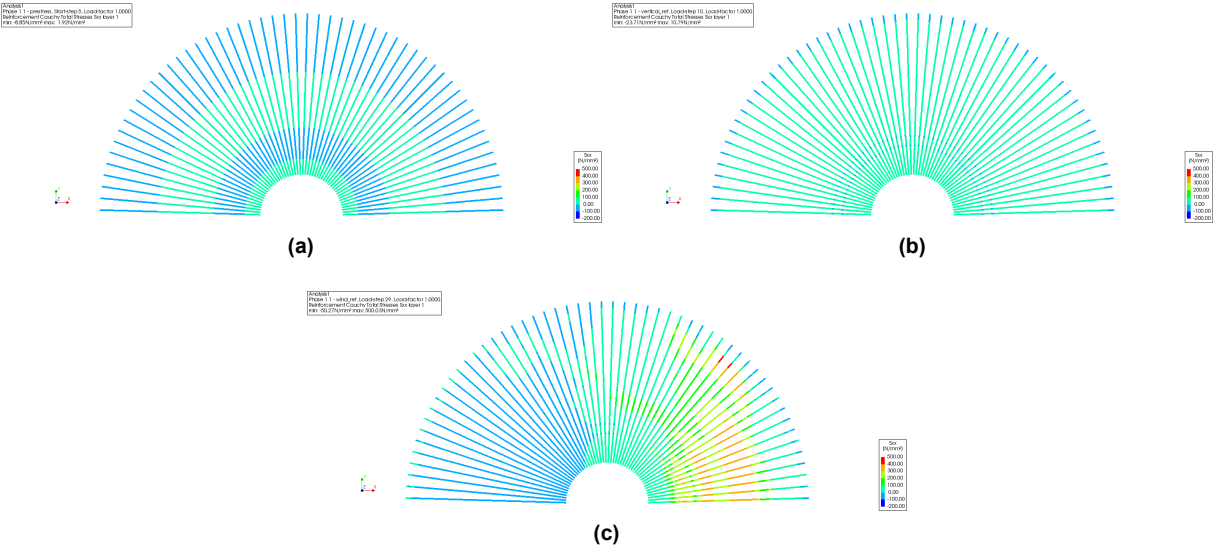
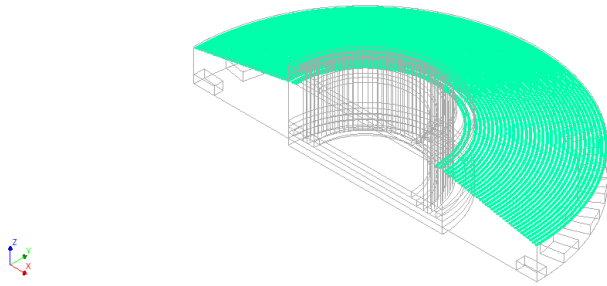
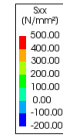


Figure B.22: Steel stress in the Bottom radial rebars a) After prestress, b) After vertical load, c) After wind load

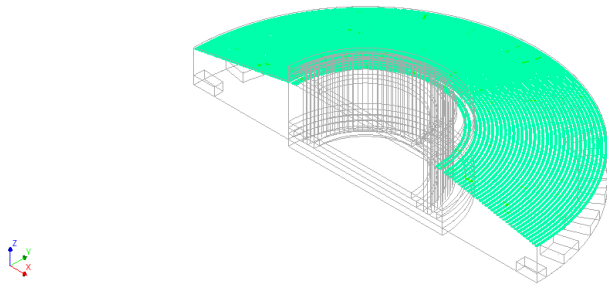
Analysis 1
Phase 1, Time-step 1, Time 20000.
Reinforcement Cauchy Total Stresses Six layer 1
min: 21.49N/mm² max: 23.74N/mm²



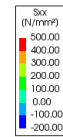
(a)



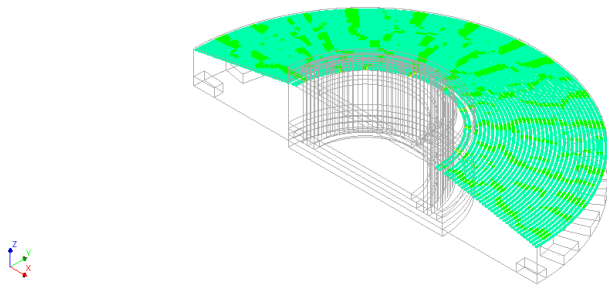
Analysis 1
Phase 1, Time-step 4, Time 80000.
Reinforcement Cauchy Total Stresses Six layer 1
min: 19.35N/mm² max: 139.19N/mm²



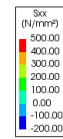
(b)



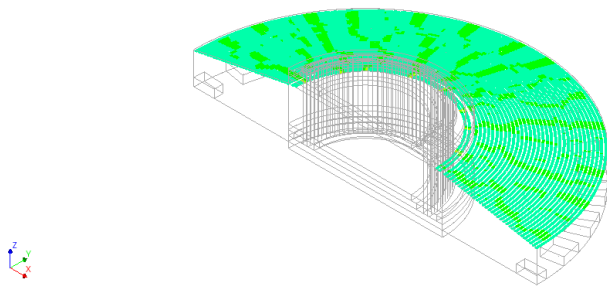
Analysis 1
Phase 1, Time-step 9, Time 0.18000E+06
Reinforcement Cauchy Total Stresses Six layer 1
min: 10.14N/mm² max: 305.00N/mm²



(c)



Analysis 1
Phase 1, Time-step 13, Time 0.24000E+06
Reinforcement Cauchy Total Stresses Six layer 1
min: 18.88N/mm² max: 302.31N/mm²



(d)

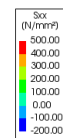
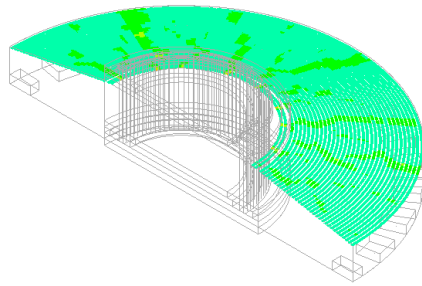


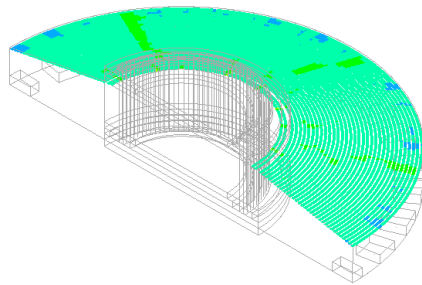
Figure B.23: Steel stress in the Top tangential rebar a) Day 0, b) Day 1, c) Day 2, d) Day 3

Analysis 1
Phase 1, Time-step 30, Time 0.60000E+06
Reinforcement Cauchy Total Stresses Six layer 1
min: 0.45N/mm² max: 401.97N/mm²



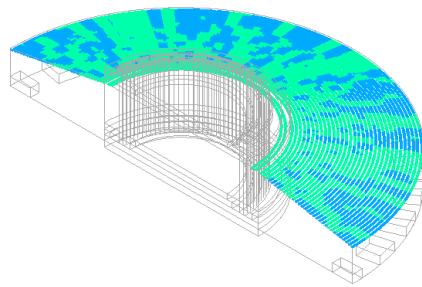
(e)

Analysis 1
Phase 1, Time-step 61, Time 0.12200E+07
Reinforcement Cauchy Total Stresses Six layer 1
min: -2.33N/mm² max: 279.95N/mm²



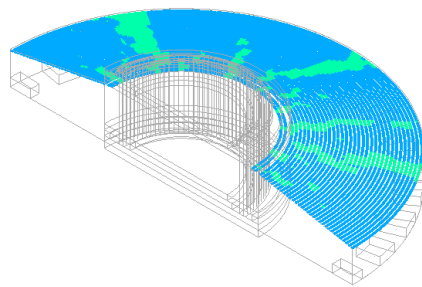
(f)

Analysis 1
Phase 1, Time-step 117, Time 0.24290E+07
Reinforcement Cauchy Total Stresses Six layer 1
min: -5.74N/mm² max: 113.35N/mm²



(g)

Analysis 1
Phase 1, Time-step 176, Time 0.39000E+07
Reinforcement Cauchy Total Stresses Six layer 1
min: -0.62N/mm² max: 31.29N/mm²



(h)

Figure B.23: Steel stress in the Top tangential rebars e) Day 7, f) Day 14, g) Day 28, h) Day 45

Analysis
Phase 1, Time-step 222, Time 0.51600E+07
Reinforcement Cauchy Total Stresses Six layer 1
min: -0.64N/mm² max: 7.35N/mm²

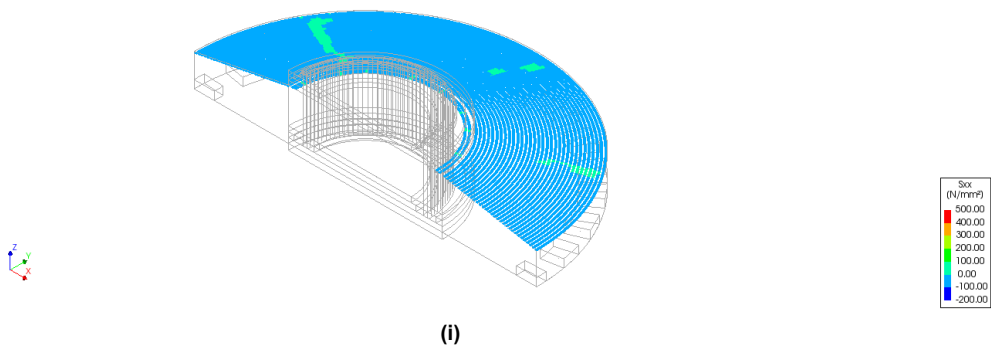
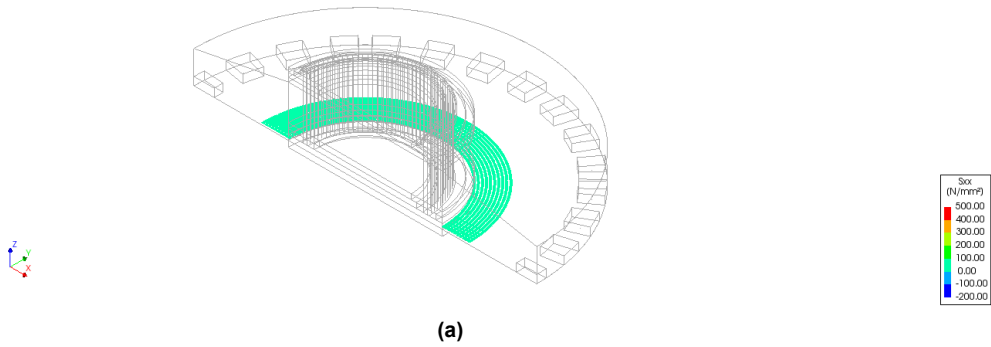


Figure B.23: Steel stress in the Top tangential rebars i) Day 60

Analysis
Phase 1, Time-step 1, Time 20000
Reinforcement Cauchy Total Stresses Six layer 1
min: 22.17N/mm² max: 22.01N/mm²



Analysis
Phase 1, Time-step 4, Time 80000
Reinforcement Cauchy Total Stresses Six layer 1
min: 41.42N/mm² max: 0.490N/mm²

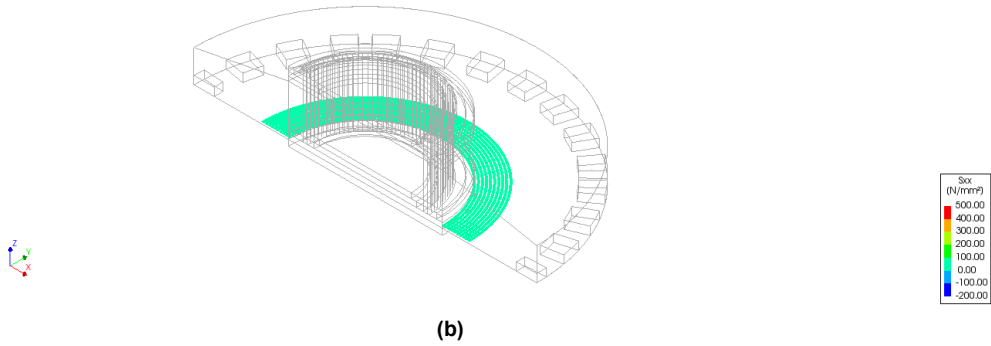
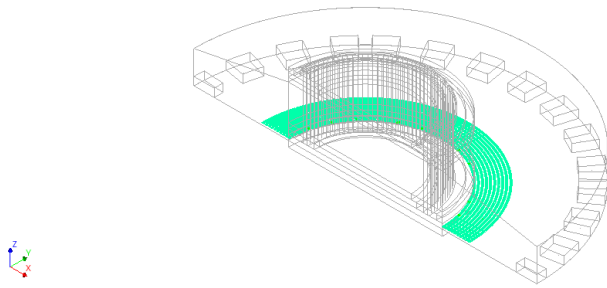
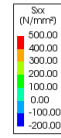


Figure B.24: Steel stress in the Bottom tangential rebars a) Day 0, b) Day 1

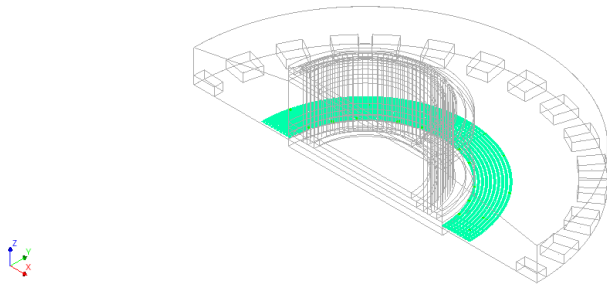
Analysis 1
Phase 1, Time-step 9, Time 0.18000E+00
Reinforcement Cauchy Total Stresses Six layer 1
min: 39.59N/mm² max: 130.25N/mm²



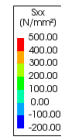
(c)



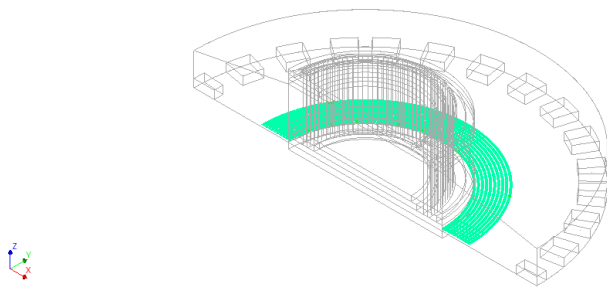
Analysis 1
Phase 1, Time-step 13, Time 0.26000E+00
Reinforcement Cauchy Total Stresses Six layer 1
min: 36.44N/mm² max: 143.72N/mm²



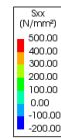
(d)



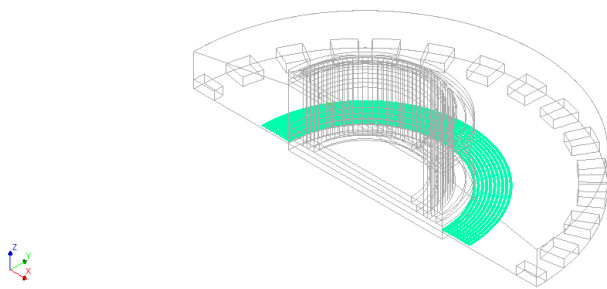
Analysis 1
Phase 1, Time-step 30, Time 0.60000E+00
Reinforcement Cauchy Total Stresses Six layer 1
min: 22.58N/mm² max: 135.29N/mm²



(e)



Analysis 1
Phase 1, Time-step 61, Time 0.12200E+07
Reinforcement Cauchy Total Stresses Six layer 1
min: 8.17N/mm² max: 110.80N/mm²



(f)

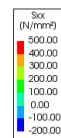
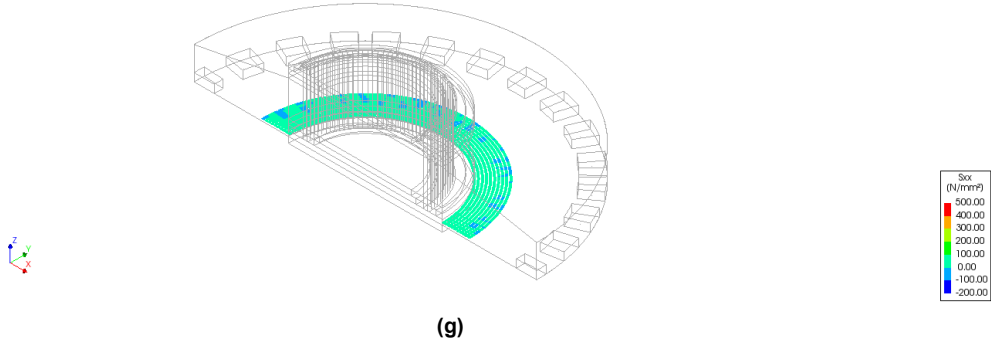
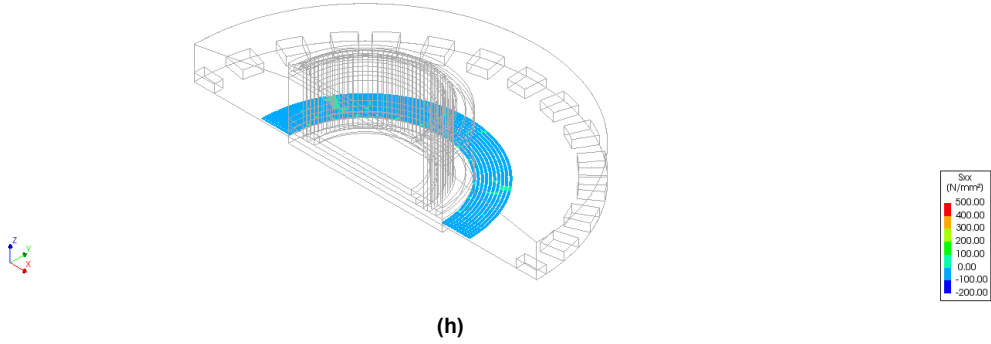


Figure B.24: Steel stress in the Bottom tangential rebars c) Day 2, d) Day 3, e) Day 7, f) Day 14

Analysis 1
Phase 1, Time-step 117, Time 0.24250E+07
Reinforcement Cauchy Total Stresses Six layer 1
min: -1.89N/mm² max: 51.72N/mm²



Analysis 1
Phase 1, Time-step 176, Time 0.39000E+07
Reinforcement Cauchy Total Stresses Six layer 1
min: -5.21N/mm² max: 14.35N/mm²



Analysis 1
Phase 1, Time-step 222, Time 0.51600E+07
Reinforcement Cauchy Total Stresses Six layer 1
min: -0.01N/mm² max: 3.04N/mm²

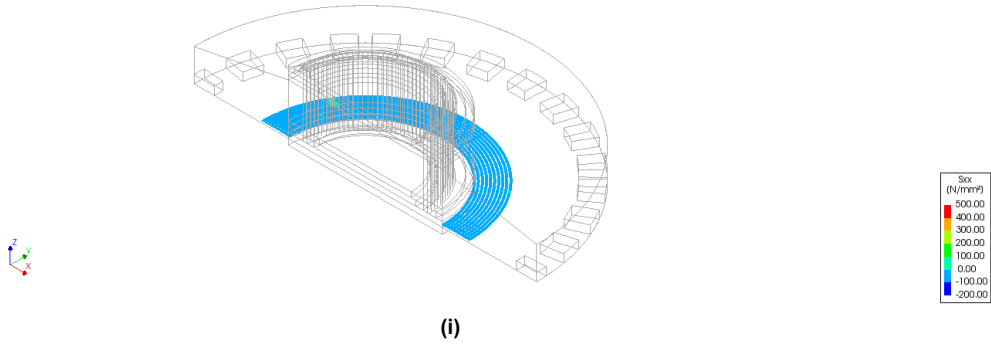
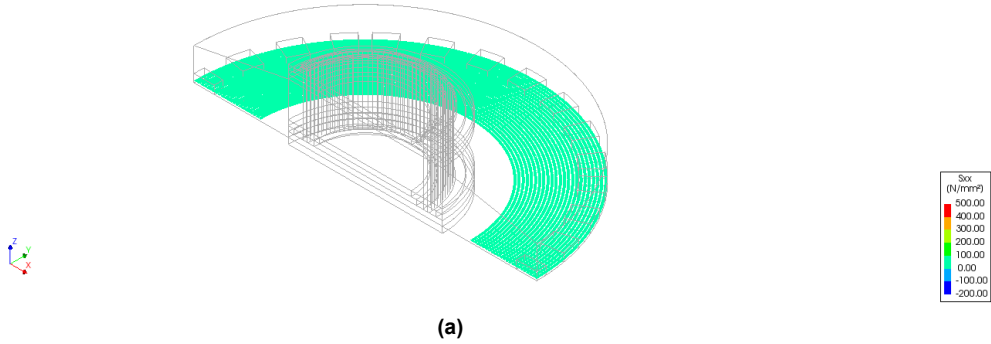
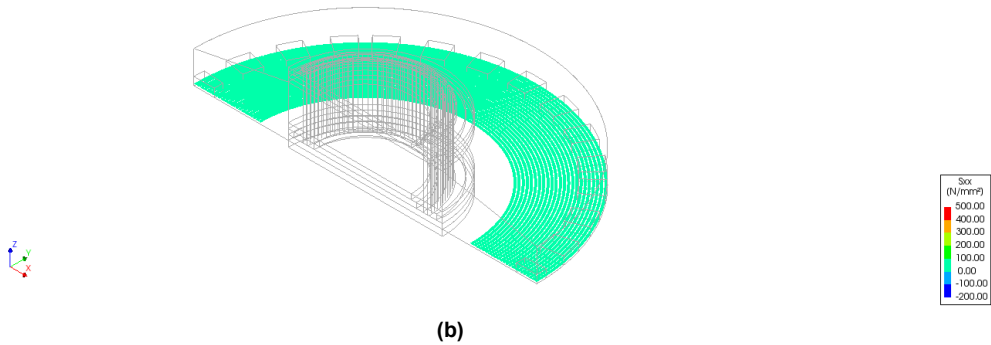


Figure B.24: Steel stress in the Bottom tangential rebars g) Day 28, h) Day 45, i) Day 60

[Analysis]
Phase 1, Time-step 1, Time 20000.
Reinforcement Cauchy Total Stresses Six layer 1
min: 20.06N/mm² max: 24.42N/mm²



[Analysis]
Phase 1, Time-step 4, Time 80000.
Reinforcement Cauchy Total Stresses Six layer 1
min: 33.68N/mm² max: 79.91N/mm²



[Analysis]
Phase 1, Time-step 9, Time 0.18000E+06
Reinforcement Cauchy Total Stresses Six layer 1
min: 24.59N/mm² max: 146.27N/mm²

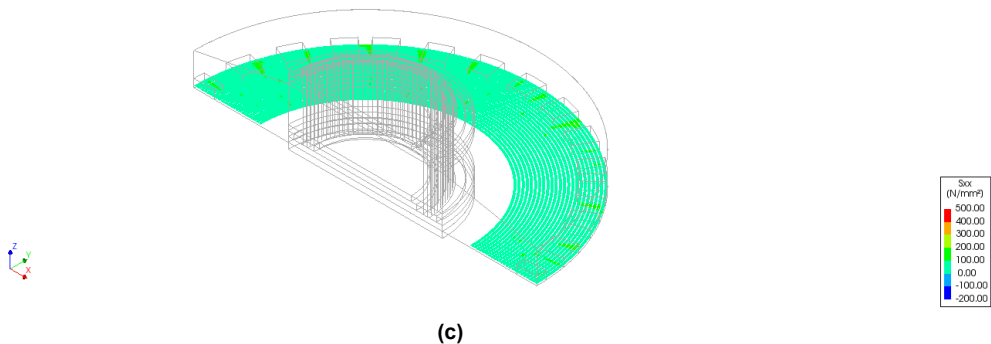
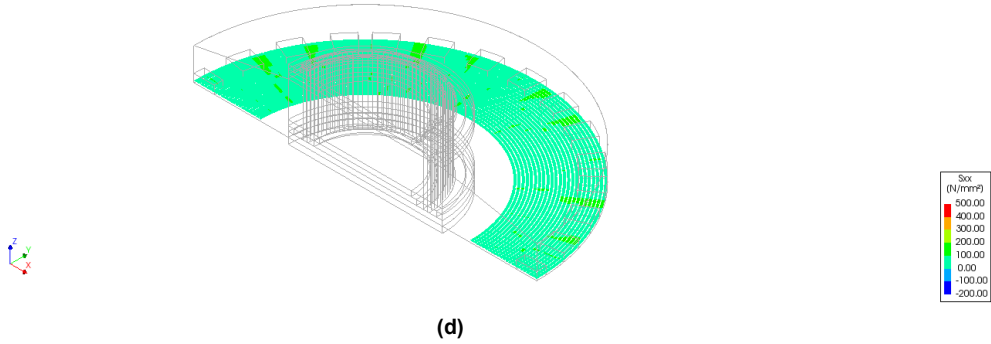
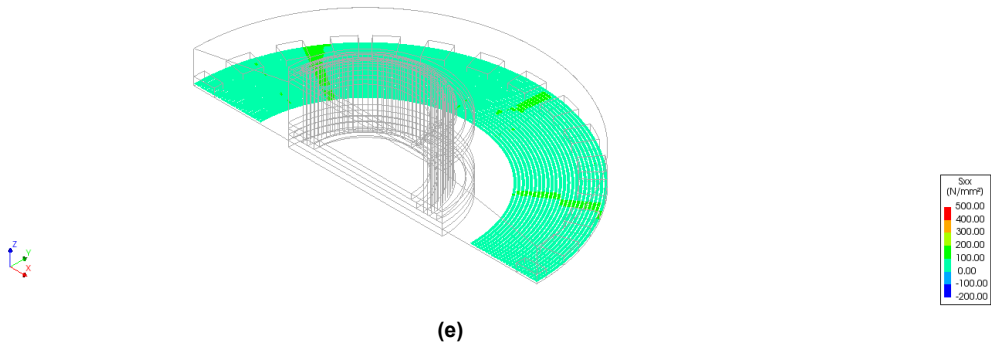


Figure B.25: Steel stress in the Bottom tangential rebar near the piles a) Day 0, b) Day 1, c) Day 2

[Analysis]
Phase 1, Time-step 13, Time 0.26000E+06
Reinforcement Cauchy Total Stresses Six layer 1
min: 20.58N/mm² max: 149.30N/mm²



[Analysis]
Phase 1, Time-step 30, Time 0.60000E+06
Reinforcement Cauchy Total Stresses Six layer 1
min: 0.71N/mm² max: 182.13N/mm²



[Analysis]
Phase 1, Time-step 61, Time 0.12200E+07
Reinforcement Cauchy Total Stresses Six layer 1
min: -2.45N/mm² max: 137.30N/mm²

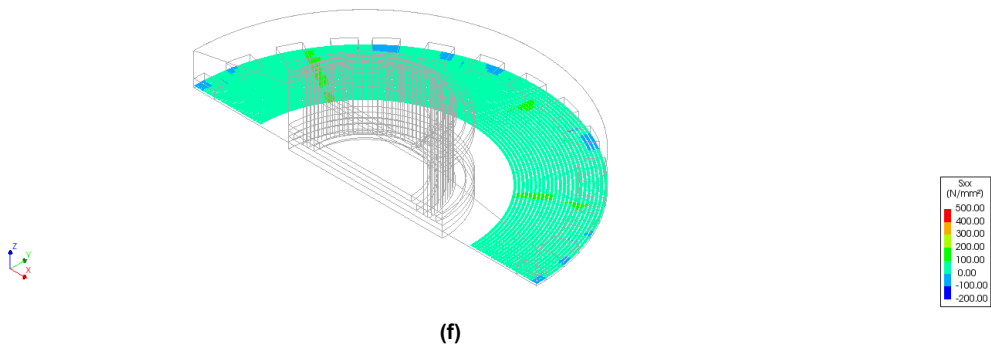
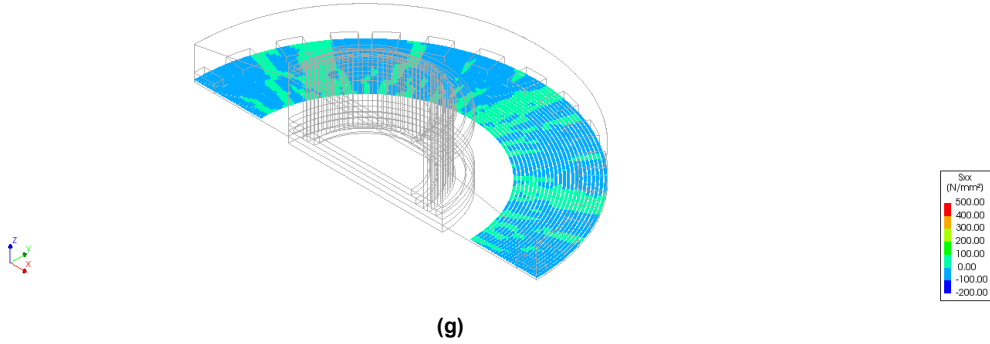
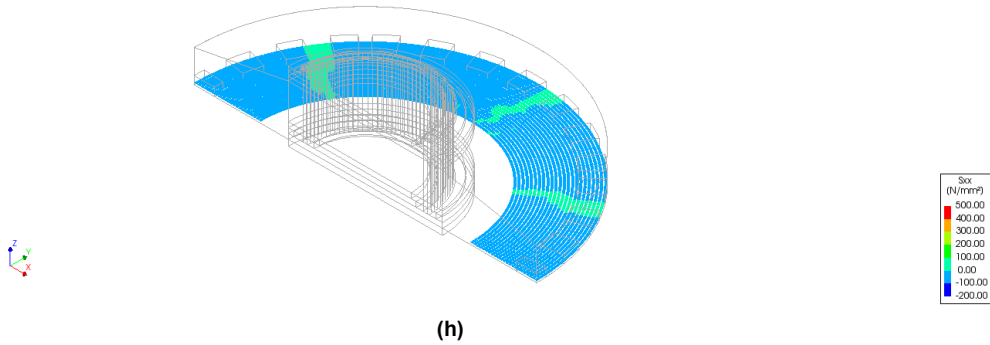


Figure B.25: Steel stress in the Bottom tangential rebars near the piles d) Day 3, e) Day 7, f) Day 14

Analysis 1
Phase 1, Time-step 117, Time 0.24250E+07
Reinforcement Cauchy Total Stresses Six layer 1
min: -5.94N/mm² max: 62.31N/mm²



Analysis 1
Phase 1, Time-step 176, Time 0.39000E+07
Reinforcement Cauchy Total Stresses Six layer 1
min: -0.78N/mm² max: 17.58N/mm²



Analysis 1
Phase 1, Time-step 222, Time 0.51600E+07
Reinforcement Cauchy Total Stresses Six layer 1
min: -0.86N/mm² max: 4.42N/mm²

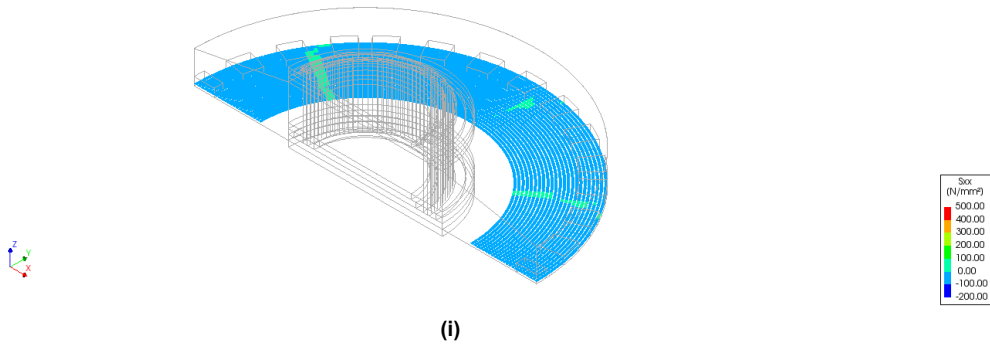
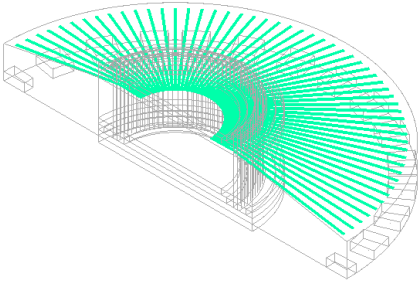


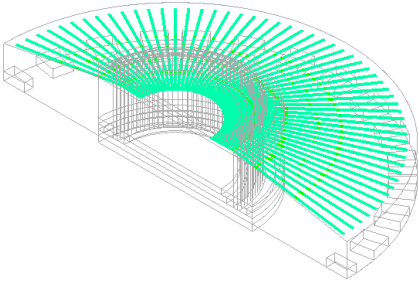
Figure B.25: Steel stress in the Bottom tangential rebars near the piles g) Day 28, h) Day 45, i) Day 60

[Analysis]
Phase 1, Time-step 1, Time 20000.
Reinforcement Couchy Total Stresses Six layer 1
min: 15.44N/mm² max: 31.79N/mm²



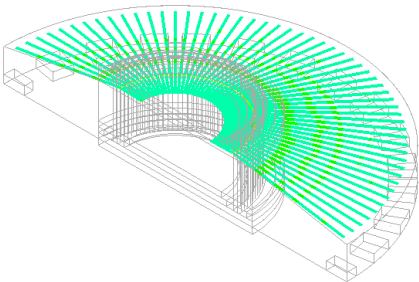
(a)

[Analysis]
Phase 1, Time-step 4, Time 80000.
Reinforcement Couchy Total Stresses Six layer 1
min: 20.38N/mm² max: 182.91N/mm²



(b)

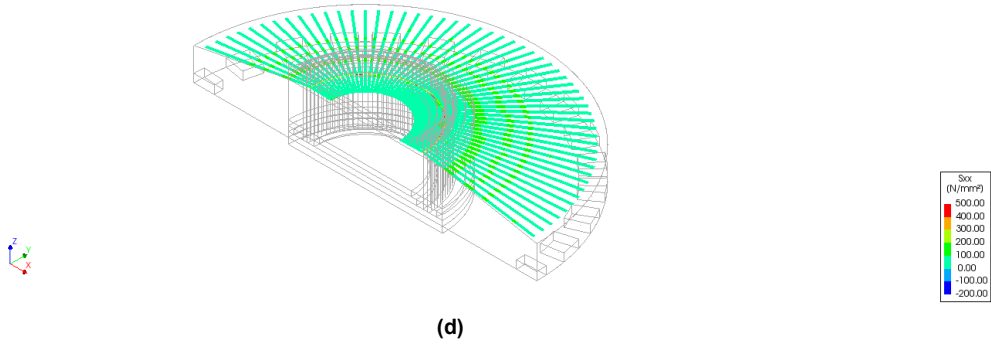
[Analysis]
Phase 1, Time-step 9, Time 0.18000E+06
Reinforcement Couchy Total Stresses Six layer 1
min: 1.22N/mm² max: 350.89N/mm²



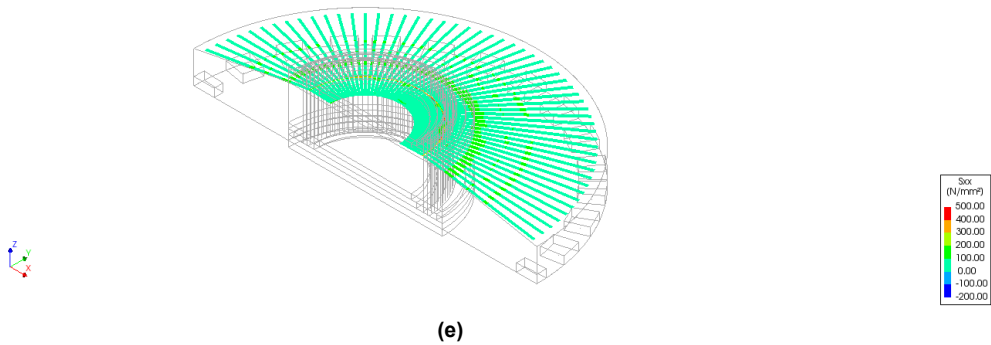
(c)

Figure B.26: Steel stress in the Top radial rebars a) Day 0, b) Day 1, c) Day 2

[Analysis]
Phase 1, Time-step 13, Time 0.26000E+06
Reinforcement Cauchy Total Stresses Sxx layer 1
min: -19.75N/mm² max: 500.08N/mm²



[Analysis]
Phase 1, Time-step 30, Time 0.60000E+06
Reinforcement Cauchy Total Stresses Sxx layer 1
min: -50.93N/mm² max: 491.93N/mm²



[Analysis]
Phase 1, Time-step 61, Time 0.12200E+07
Reinforcement Cauchy Total Stresses Sxx layer 1
min: -61.67N/mm² max: 326.46N/mm²

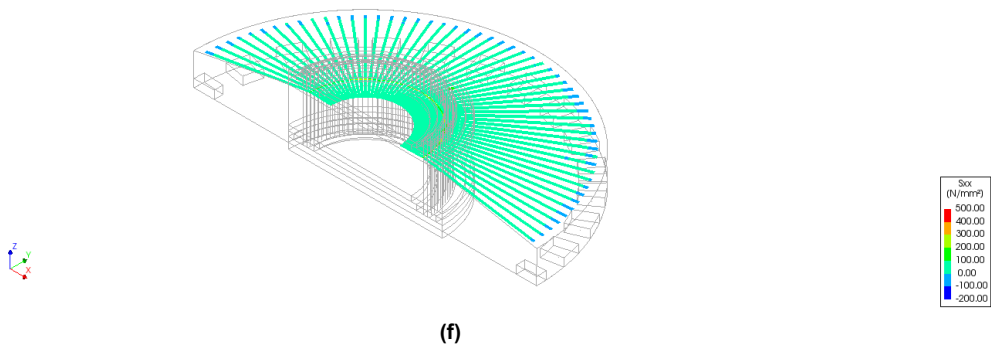
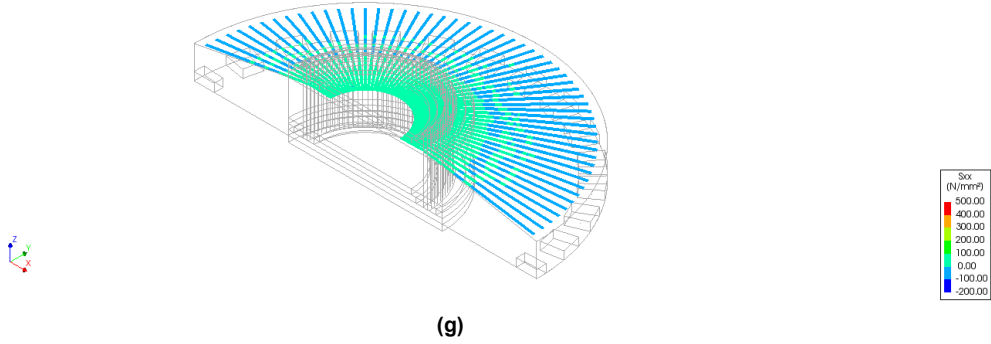
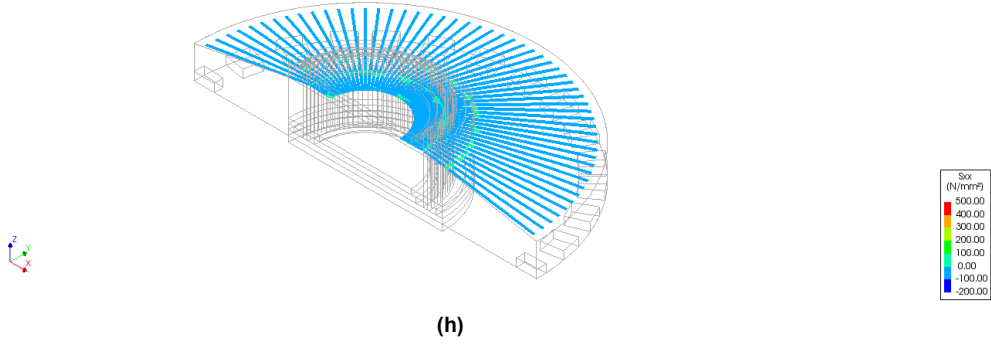


Figure B.26: Steel stress in the Top radial rebars d) Day 3, e) Day 7, f) Day 14

[Analysis]
Phase 1, Time-step 117, Time 0.24250E+07
Reinforcement Cauchy Total Stresses Sxx layer 1
min: -22.97N/mm² max: 122.56N/mm²



[Analysis]
Phase 1, Time-step 176, Time 0.39000E+07
Reinforcement Cauchy Total Stresses Sxx layer 1
min: -35.00N/mm² max: 33.69N/mm²



[Analysis]
Phase 1, Time-step 222, Time 0.51000E+07
Reinforcement Cauchy Total Stresses Sxx layer 1
min: -64.26N/mm² max: 10.96N/mm²

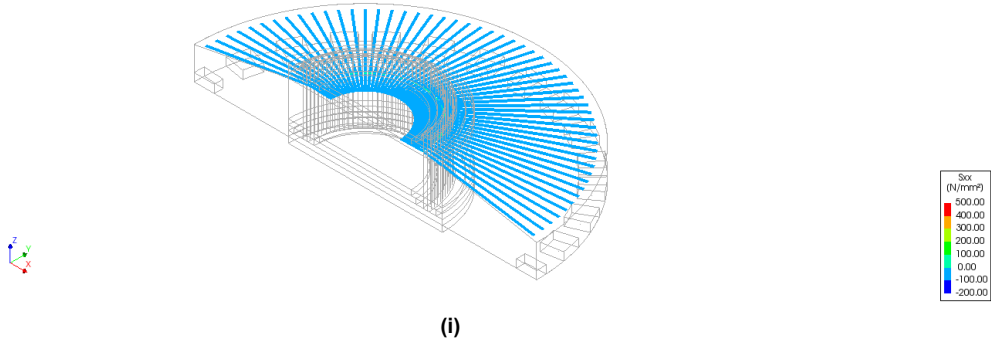
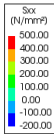
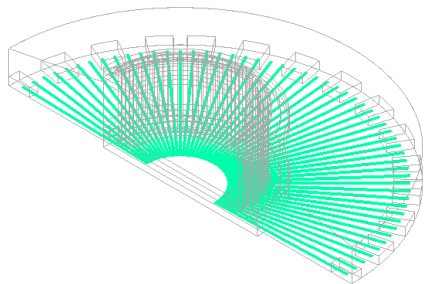


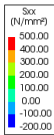
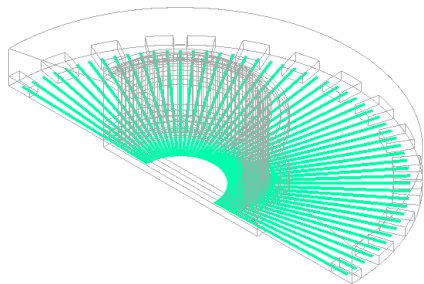
Figure B.26: Steel stress in the Top radial rebar g) Day 28, h) Day 45, i) Day 60

[Analysis]
Phase 1, Time-step 1, Time 20000.
Reinforcement Cauchy Total Stresses Six layer 1
min: 18.19N/mm² max: 25.57N/mm²



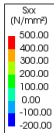
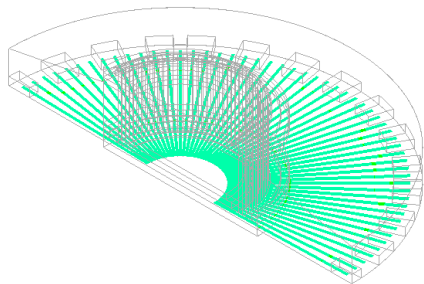
(a)

[Analysis]
Phase 1, Time-step 4, Time 80000.
Reinforcement Cauchy Total Stresses Six layer 1
min: 31.15N/mm² max: 84.67N/mm²



(b)

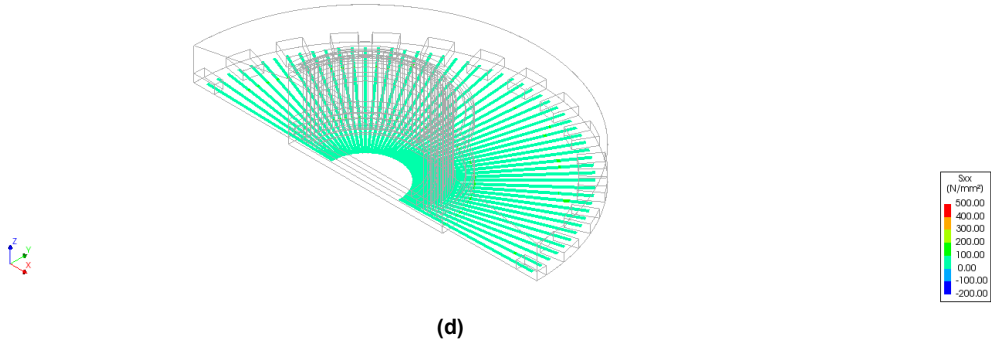
[Analysis]
Phase 1, Time-step 9, Time 0.18000E+06
Reinforcement Cauchy Total Stresses Six layer 1
min: 23.78N/mm² max: 146.15N/mm²



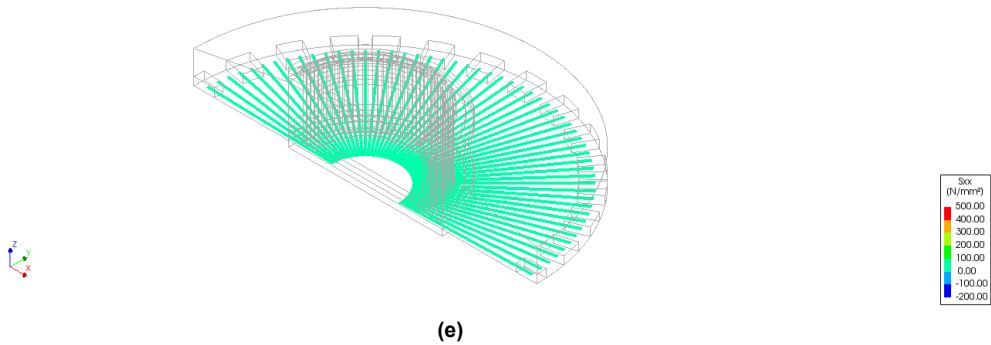
(c)

Figure B.27: Steel stress in the Bottom radial rebar a) Day 0, b) Day 1, c) Day 2

[Analysis]
Phase 1, Time-step 13, Time 0.26000E+06
Reinforcement Cauchy Total Stresses Sxx layer 1
min: 18.60N/mm² max: 131.73N/mm²



[Analysis]
Phase 1, Time-step 30, Time 0.60000E+06
Reinforcement Cauchy Total Stresses Sxx layer 1
min: 5.02N/mm² max: 98.08N/mm²



[Analysis]
Phase 1, Time-step 61, Time 0.12200E+07
Reinforcement Cauchy Total Stresses Sxx layer 1
min: -3.29N/mm² max: 54.84N/mm²

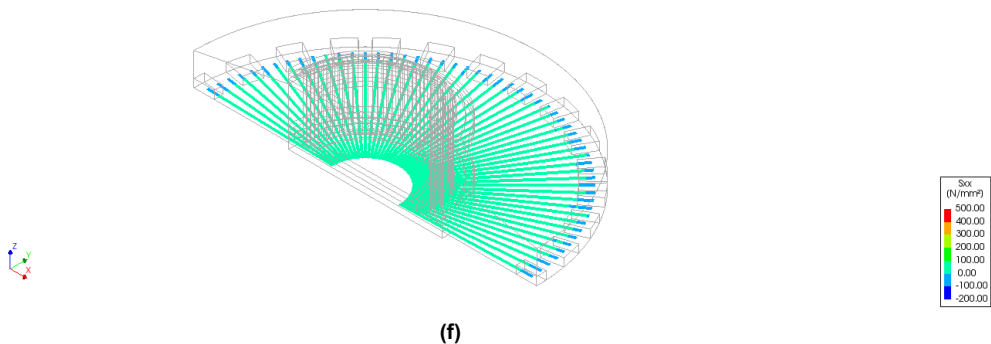
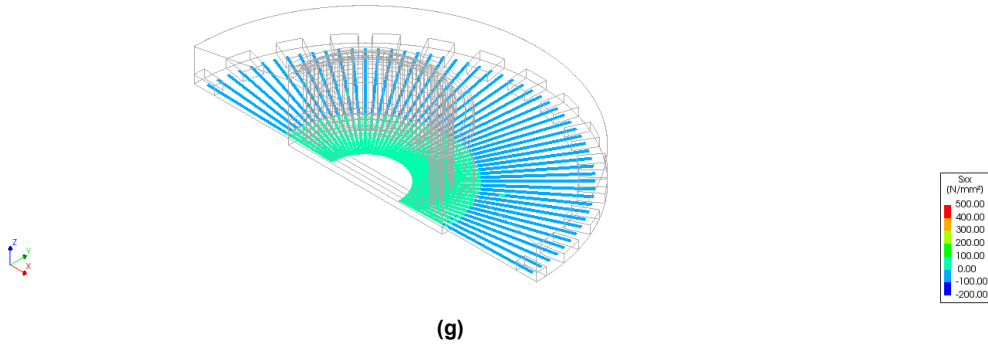
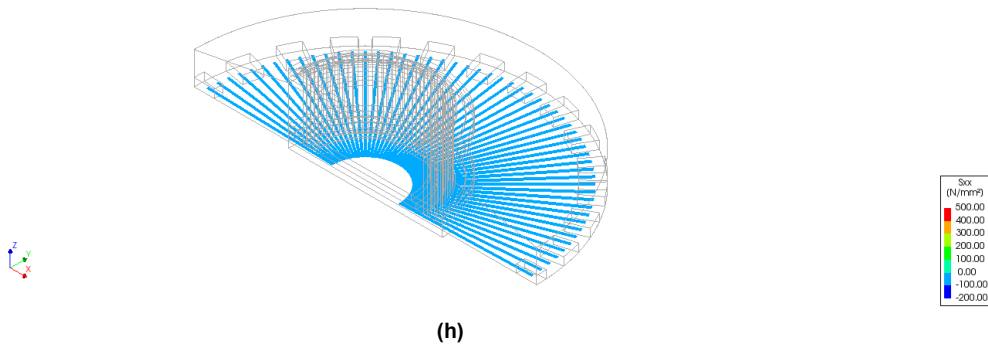


Figure B.27: Steel stress in the Bottom radial rebars d) Day 3, e) Day 7, f) Day 14

Analysis 1
Phase 1, Time-step 117, Time 0.24250E+07
Reinforcement Cauchy Total Stresses Six layer 1
min: -7.17N/mm² max: 12.91N/mm²



Analysis 1
Phase 1, Time-step 176, Time 0.39000E+07
Reinforcement Cauchy Total Stresses Six layer 1
min: -0.81N/mm² max: -0.70N/mm²



Analysis 1
Phase 1, Time-step 222, Time 0.51600E+07
Reinforcement Cauchy Total Stresses Six layer 1
min: -0.55N/mm² max: -3.44N/mm²

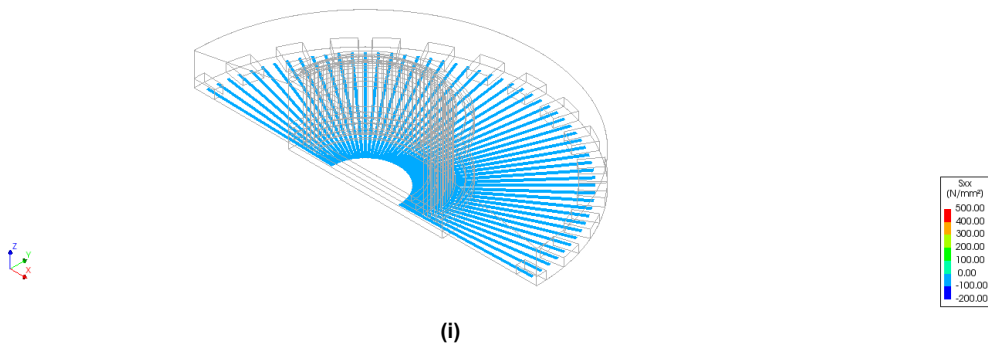
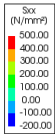
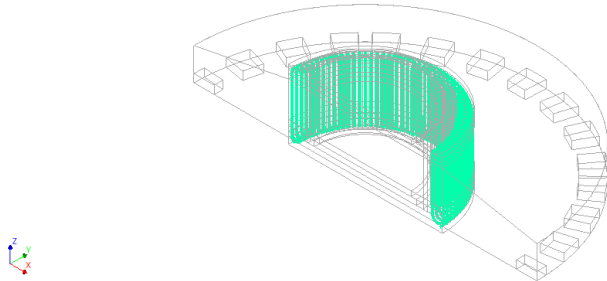


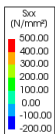
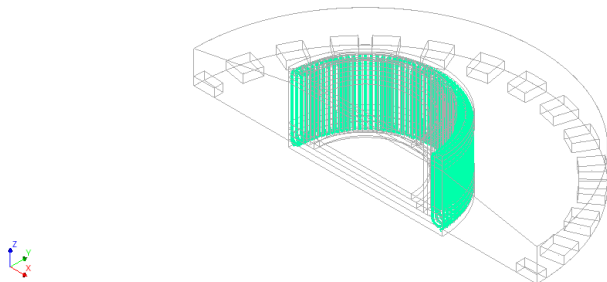
Figure B.27: Steel stress in the Bottom radial rebars g) Day 28, h) Day 45, i) Day 60

[Analysis]
Phase 1, Time-step 1, Time 20000.
Reinforcement Cauchy Total Stresses Sxx layer 1
min: 10.16N/mm² max: 25.31N/mm²



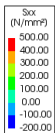
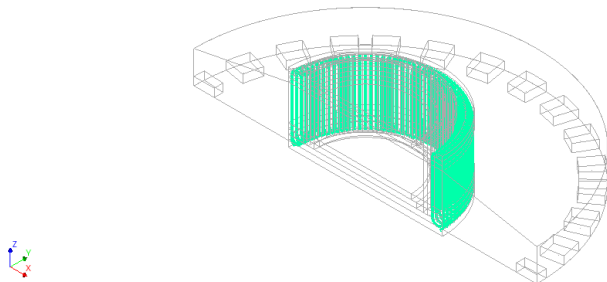
(a)

[Analysis]
Phase 1, Time-step 4, Time 80000.
Reinforcement Cauchy Total Stresses Sxx layer 1
min: 12.20N/mm² max: 61.67N/mm²



(b)

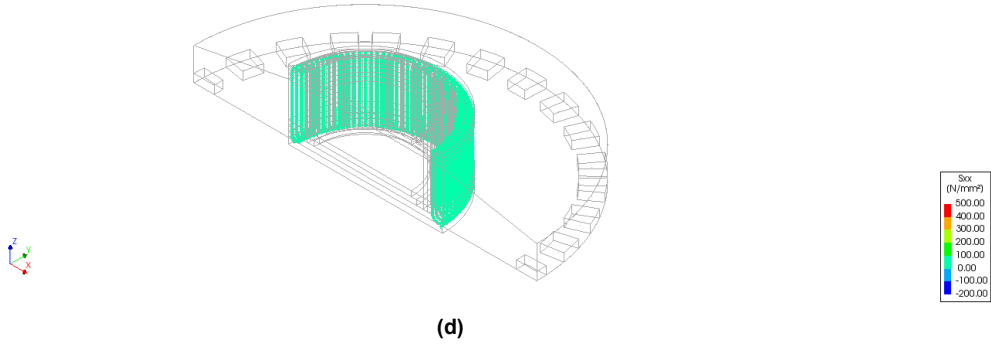
[Analysis]
Phase 1, Time-step 9, Time 0.18000E+06
Reinforcement Cauchy Total Stresses Sxx layer 1
min: 10.45N/mm² max: 93.20N/mm²



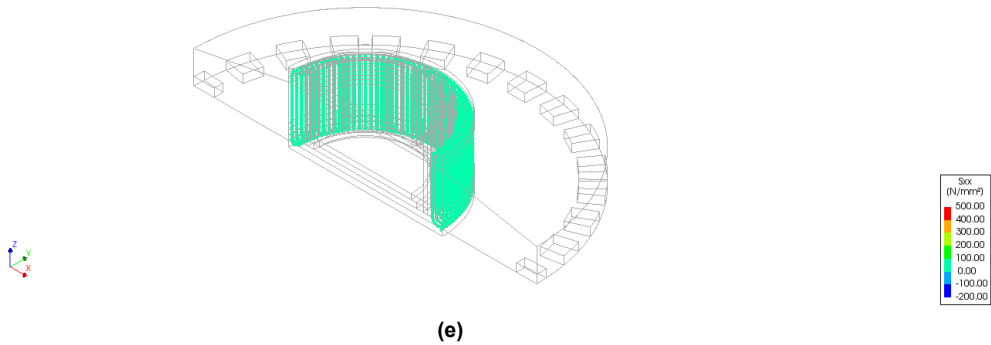
(c)

Figure B.28: Steel stress in the side stirrups a) Day 0, b) Day 1, c) Day 2

[Analysis]
Phase 1, Time-step 13, Time 0.26000E+06
Reinforcement Cauchy Total Stresses Sxx layer 1
min: 12.95N/mm² max: 85.41N/mm²



[Analysis]
Phase 1, Time-step 30, Time 0.60000E+06
Reinforcement Cauchy Total Stresses Sxx layer 1
min: 0.46N/mm² max: 83.44N/mm²



[Analysis]
Phase 1, Time-step 61, Time 0.12200E+07
Reinforcement Cauchy Total Stresses Sxx layer 1
min: 0.48N/mm² max: 47.93N/mm²

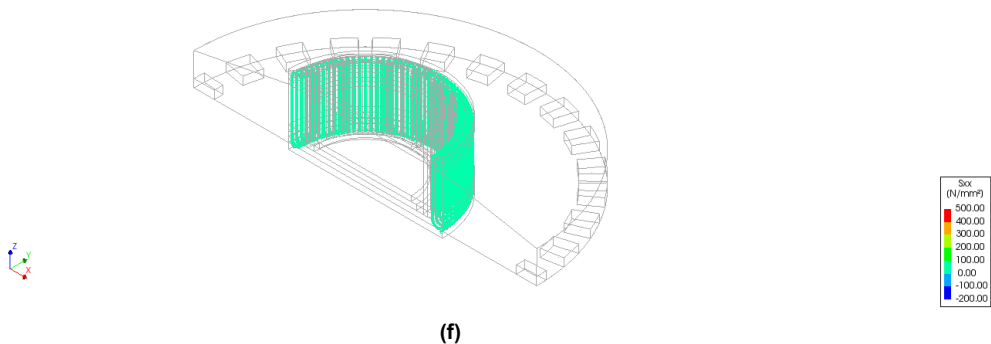
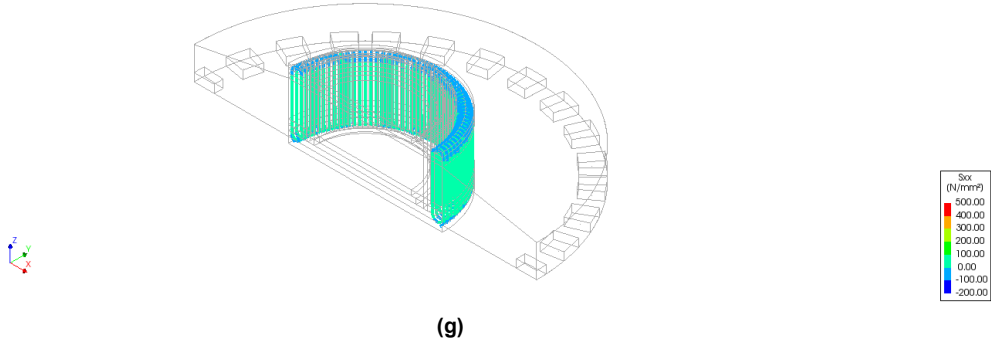
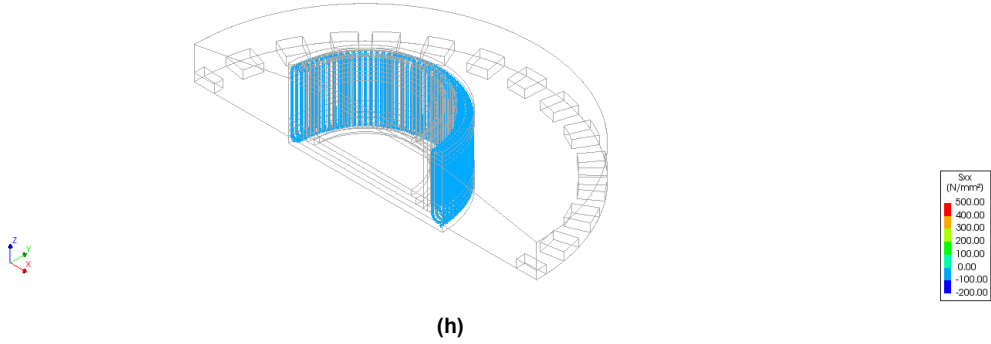


Figure B.28: Steel stress in the side stirrups d) Day 3, e) Day 7, f) Day 14

Analysis 1
Phase 1, Time-step 117, Time 0.24250E+07
Reinforcement Cauchy Total Stresses Six layer 1
min: -3.99N/mm² max: 11.72N/mm²



Analysis 1
Phase 1, Time-step 176, Time 0.39000E+07
Reinforcement Cauchy Total Stresses Six layer 1
min: -5.60N/mm² max: -1.12N/mm²



Analysis 1
Phase 1, Time-step 222, Time 0.51600E+07
Reinforcement Cauchy Total Stresses Six layer 1
min: -6.01N/mm² max: -4.26N/mm²

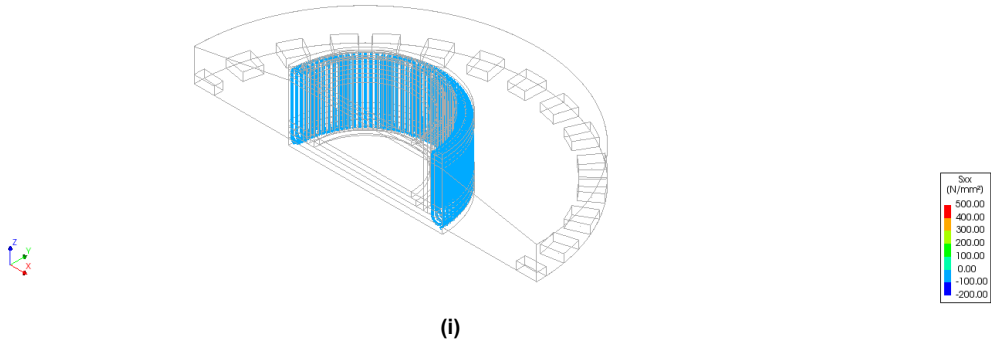


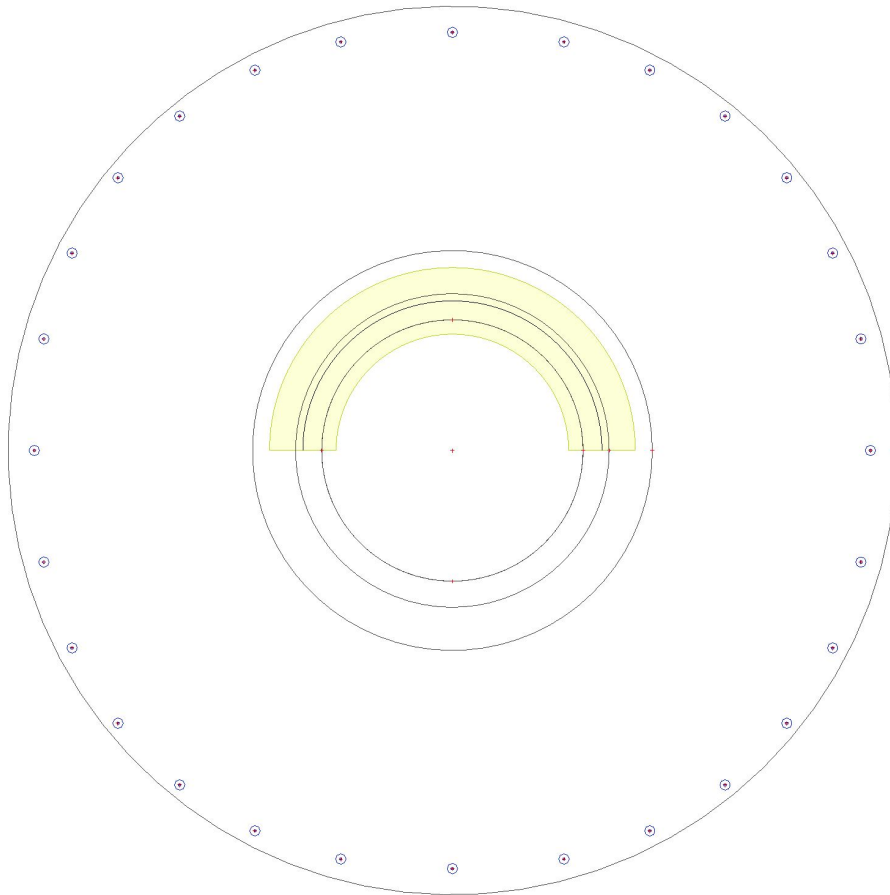
Figure B.28: Steel stress in the side stirrups g) Day 28, h) Day 45, i) Day 60

C

Appendix-C

C.1. SCIA Report

2. input (geometry)
2.1. Main Geometry



2.2. @{ProjectESA.IDS_MATERIAL}

Steel EC3

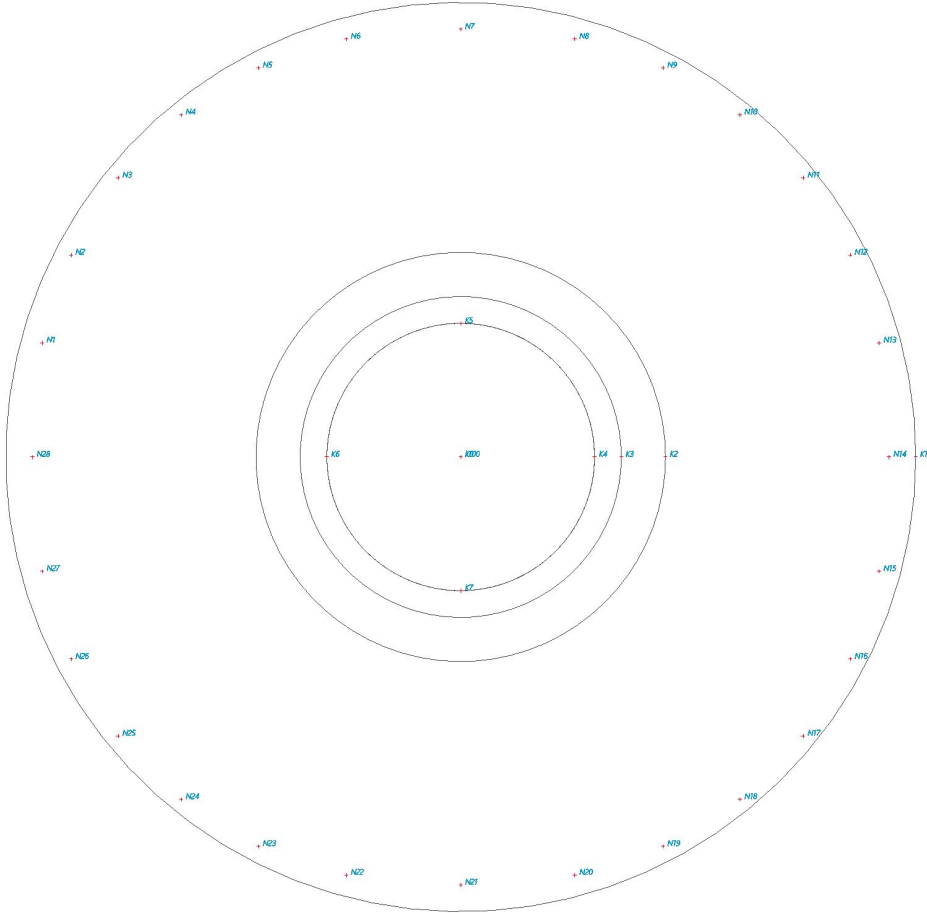
Name	ρ [kg/m ³]	E_{mod} [MPa] G_{mod} [MPa]	μ α [m/mK]	Lower limit [mm]	Upper limit [mm]	F_y [N/mm ²]	F_u [N/mm ²]	Colour
S 235	7850.0	2.1000e+05 8.0769e+04	0.3 0.00	0 40	40 80	235.00 215.00	360.00 360.00	■

Name	Type	ρ [kg/m ³]	Density in fresh state [kg/m ³]	E_{mod} [MPa]	μ	α [m/mK]	$f_{c,k,28}$ [MPa]	Colour
BetonAlg	Concrete	2500.0	2600.0	8.0000e+03	0.15	0.00	30.00	■
BetonMidden	Concrete	2500.0	2600.0	3.0000e+03	0.15	0.00	30.00	■

Explanations of symbols

Density in fresh state	The value in the density in fresh state property is used only in case a composite deck is input and its self-weight load is taken into account.
------------------------	-------------------------------------------------------------------------------------------------------------------------------------------------

2.3. nodes



2.4. @EP_StructureESAM.IDS_NODE

Name	Coord X [mm]	Coord Y [mm]
K1	8500	0
k100	0	0
K2	3825	0
K3	3000	0
K4	2500	0

Name	Coord X [mm]	Coord Y [mm]
K5	0	2500
K6	-2500	0
K7	0	-2500
K0	0	0
N1	-7817	2135

Name	Coord X [mm]	Coord Y [mm]
N2	-7277	3778
N3	-6399	5218
N4	-5218	6399
N5	-3778	7277
N6	-2135	7817

Name	Coord X [mm]	Coord Y [mm]
N7	0	8000
N8	2135	7817
N9	3778	7277
N10	5218	6399
N11	6399	5218

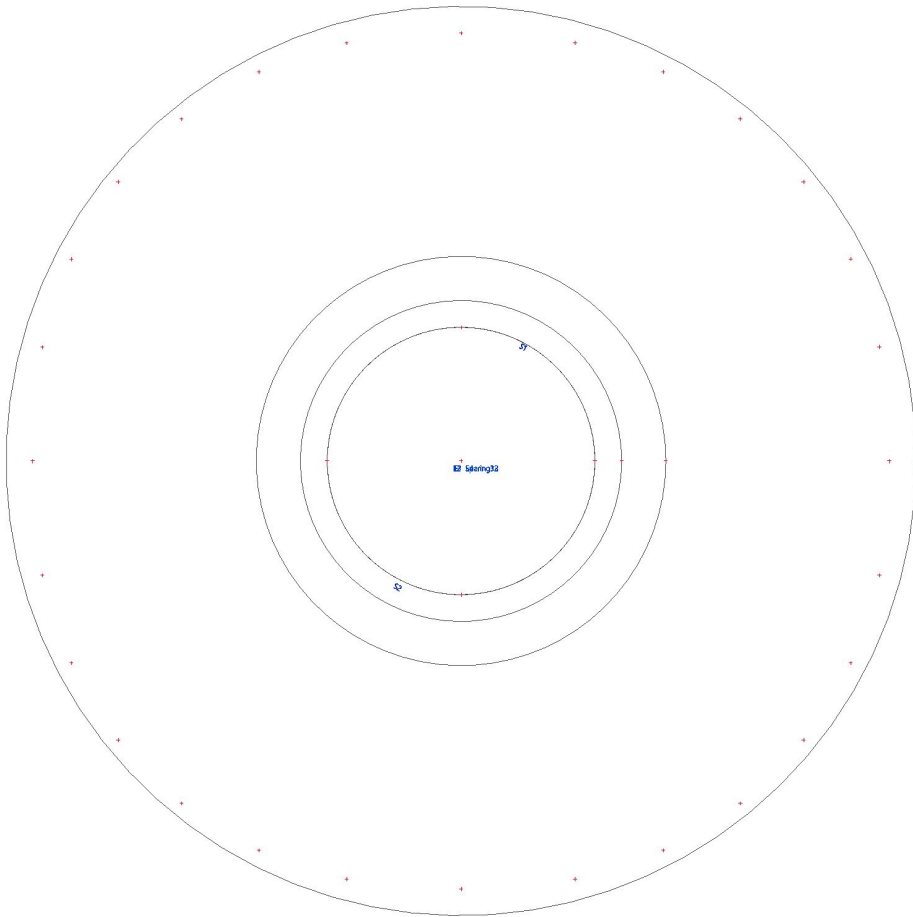
Name	Coord X [mm]	Coord Y [mm]
N12	7277	3778
N13	7817	2135
N14	8000	0
N15	7817	-2135
N16	7277	-3778

Name	Coord X [mm]	Coord Y [mm]
N17	6399	-5218
N18	5218	-6399
N19	3778	-7277
N20	2135	-7817
N21	0	-8000

Name	Coord X [mm]	Coord Y [mm]
N22	-2135	-7817
N23	-3778	-7277
N24	-5218	-6399
N25	-6399	-5218
N26	-7277	-3778

Name	Coord X [mm]	Coord Y [mm]
N27	-7817	-2135
N28	-8000	0

2.5. elements

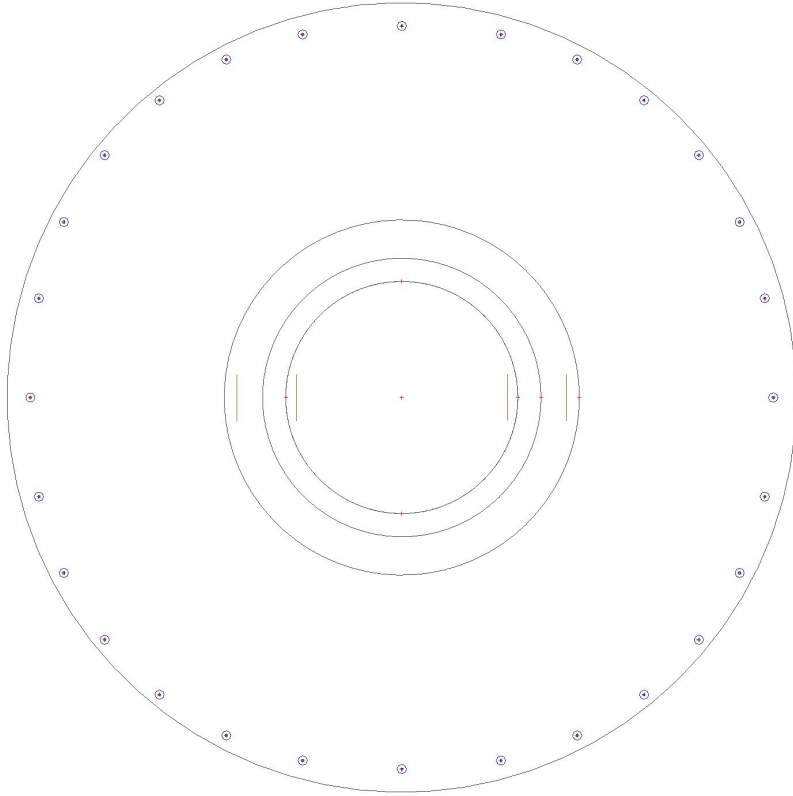


2.6. @{{EP_StructureESAM.IDS_SLAB}}

Name	Layer	Type	Element type	Material	Thickness type	Centre thickness [mm]
E1	foundation	plate (90)	Standard	BetonAlg	variable	3130 1600
E2	foundation	plate (90)	Standard	BetonAlg	constant	3430
E3	foundation	plate (90)	Standard	BetonAlg	constant	3430
E4	foundation	plate (90)	Standard	BetonMidden	constant	3430

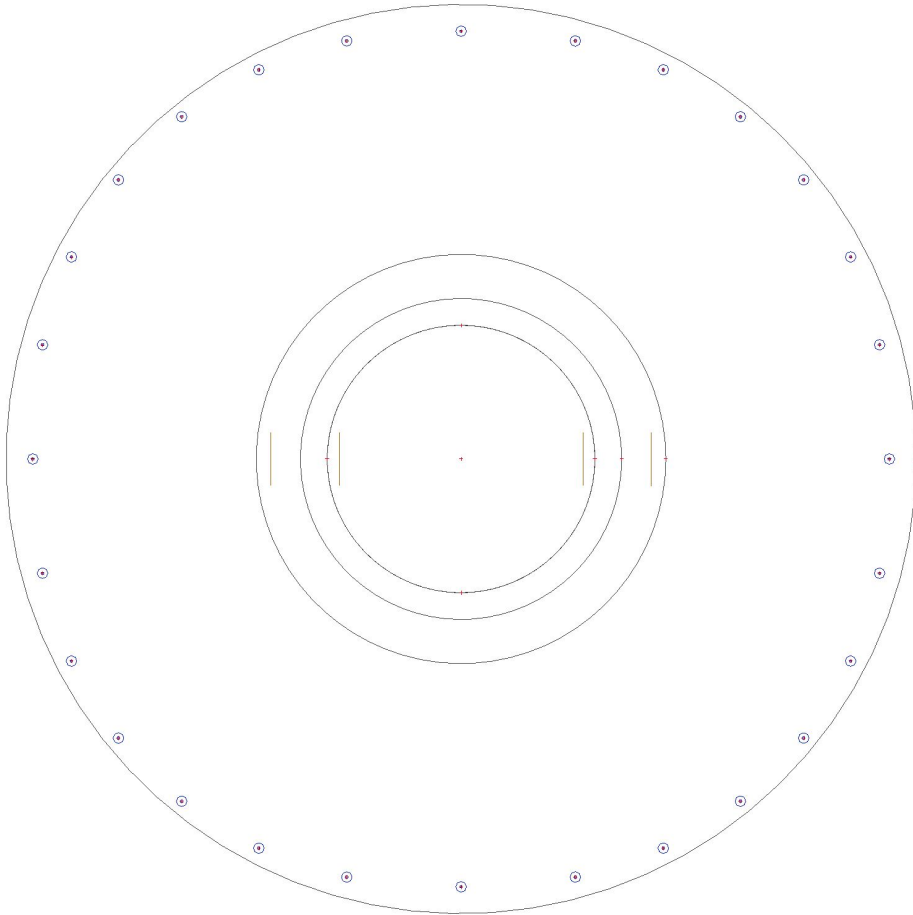
2.7. height crosssection

Not supported task. Please switch to V16 and older post-processing environment (available in 32-bit version).



2.8. E modulus

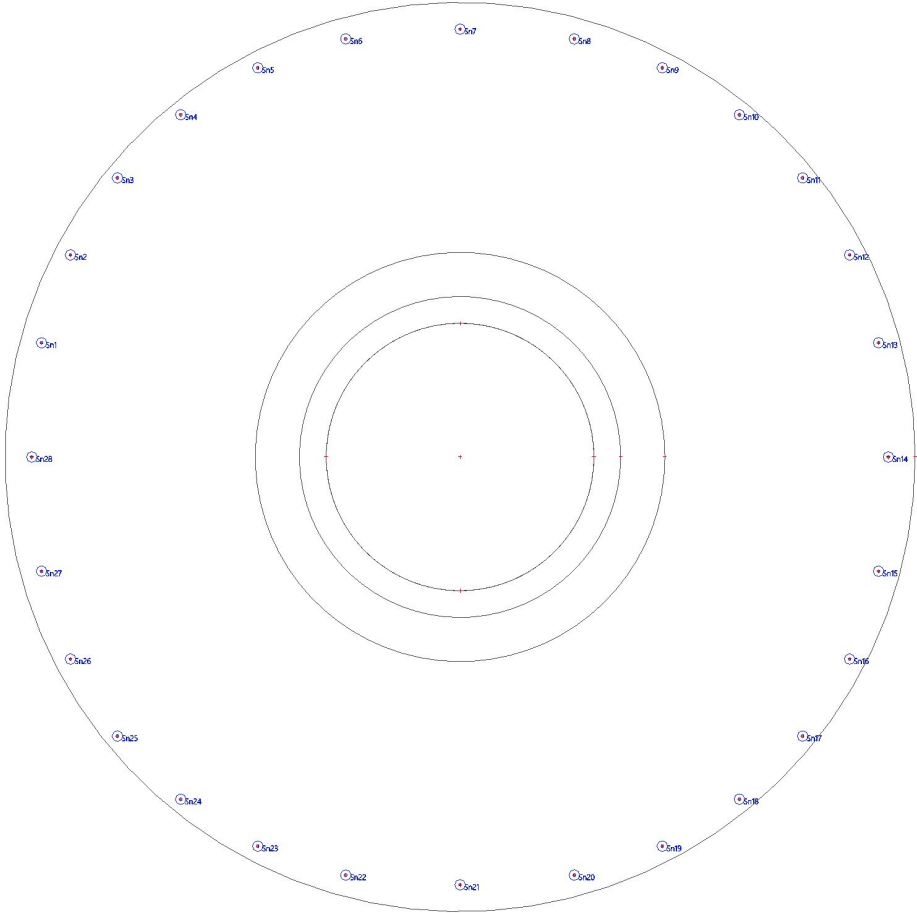
Not supported task. Please switch to 'V16 and older' post-processing environment (available in 32-bit version).



2.9. @EP_StructureESAM.IDS_SLAB_OPEN}

Name	2D member
Sparing1	E1
Sparing32	E2
Sparing33	E3

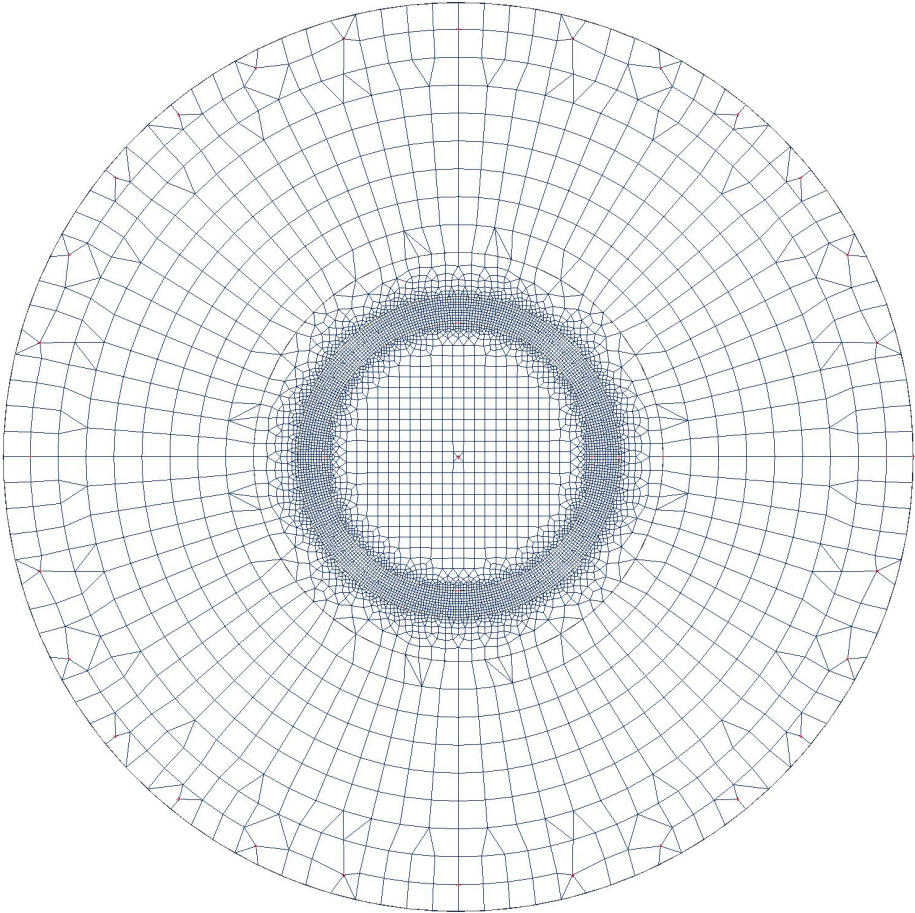
2.10. supports



2.11. @{EP_StructureESAM.IDS_NODAL_SUPPORT}

Name Node	System User UCS	Type Angle [deg]	Z		
			Stiffness Z [MN/m]	Stiffness Rx [MNm/rad]	Stiffness Ry [MNm/rad]
Sn1 N1	GCS	Standard	Flexible 1.5000e+02	Free	Free
Sn2 N2	GCS	Standard	Flexible 1.5000e+02	Free	Free
Sn3 N3	GCS	Standard	Flexible 1.5000e+02	Free	Free
Sn4 N4	GCS	Standard	Flexible 1.5000e+02	Free	Free
Sn5 N5	GCS	Standard	Flexible 1.5000e+02	Free	Free
Sn6 N6	GCS	Standard	Flexible 1.5000e+02	Free	Free
Sn7 N7	GCS	Standard	Flexible 1.5000e+02	Free	Free
Sn8 N8	GCS	Standard	Flexible 1.5000e+02	Free	Free
Sn9 N9	GCS	Standard	Flexible 1.5000e+02	Free	Free
Sn10 N10	GCS	Standard	Flexible 1.5000e+02	Free	Free
Sn11 N11	GCS	Standard	Flexible 1.5000e+02	Free	Free
Sn12 N12	GCS	Standard	Flexible 1.5000e+02	Free	Free
Sn13 N13	GCS	Standard	Flexible 1.5000e+02	Free	Free
Sn14 N14	GCS	Standard	Flexible 1.5000e+02	Free	Free
Sn15 N15	GCS	Standard	Flexible 1.5000e+02	Free	Free
Sn16 N16	GCS	Standard	Flexible 1.5000e+02	Free	Free
Sn17 N17	GCS	Standard	Flexible 1.5000e+02	Free	Free
Sn18 N18	GCS	Standard	Flexible 1.5000e+02	Free	Free
Sn19 N19	GCS	Standard	Flexible 1.5000e+02	Free	Free
Sn20 N20	GCS	Standard	Flexible 1.5000e+02	Free	Free
Sn21 N21	GCS	Standard	Flexible 1.5000e+02	Free	Free
Sn22 N22	GCS	Standard	Flexible 1.5000e+02	Free	Free
Sn23 N23	GCS	Standard	Flexible 1.5000e+02	Free	Free
Sn24 N24	GCS	Standard	Flexible 1.5000e+02	Free	Free
Sn25 N25	GCS	Standard	Flexible 1.5000e+02	Free	Free
Sn26 N26	GCS	Standard	Flexible 1.5000e+02	Free	Free
Sn27 N27	GCS	Standard	Flexible 1.5000e+02	Free	Free
Sn28 N28	GCS	Standard	Flexible 1.5000e+02	Free	Free

2.12. mesh



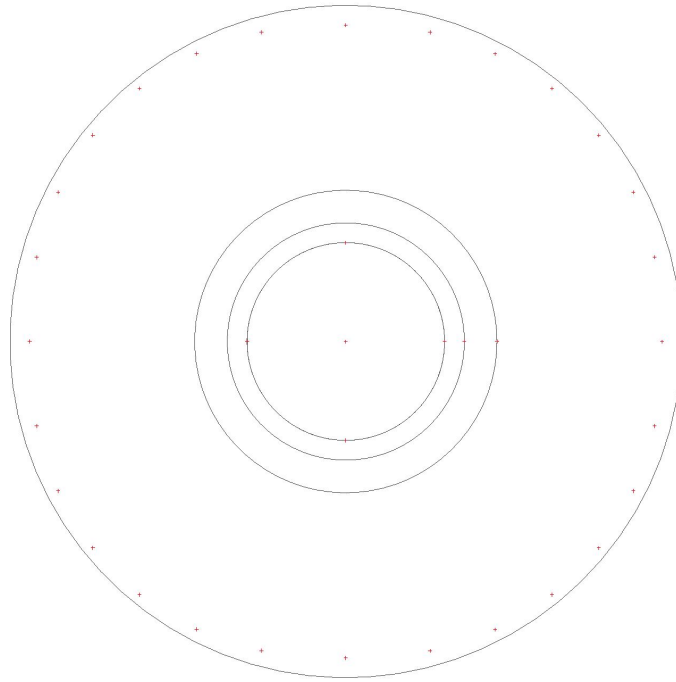
3. input (loads and loadcombinations)

3.1. @ProjectESA.IDS_LOADCASE}

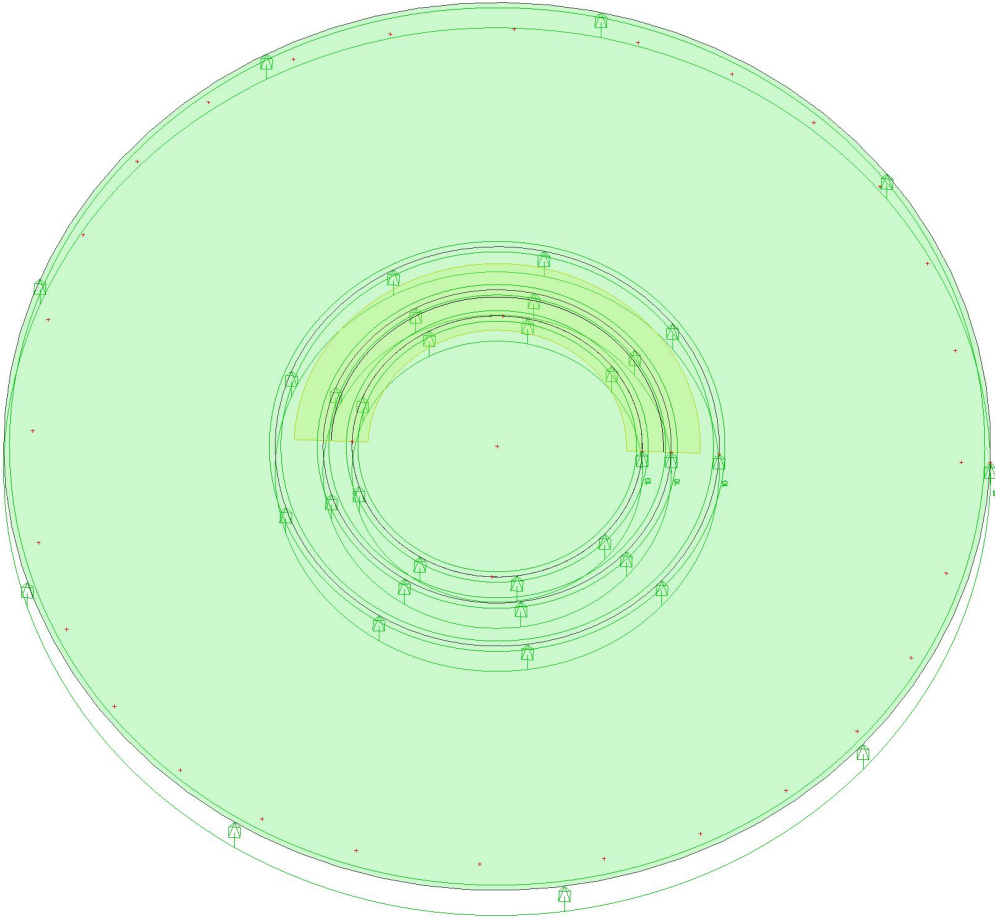
Name	Description	Action type	Load group	Duration	Master load case
	Spec	Load type			
BG01	selfweight concrete	Permanent Standard	LG1		
BG02	mound	Permanent Standard	LG1		
BG03	ground water	Permanent Standard	LG1		
BG101	unit load vertical (1.000kN) Standard	Variable Static	LG2	Short	None
BG102	unit load moment (100.000kNm) Standard	Variable Static	LG2	Short	None

3.2. BG01 - self weight

Not supported task. Please switch to 'V16 and older' post-processing environment (available in 32-bit version).

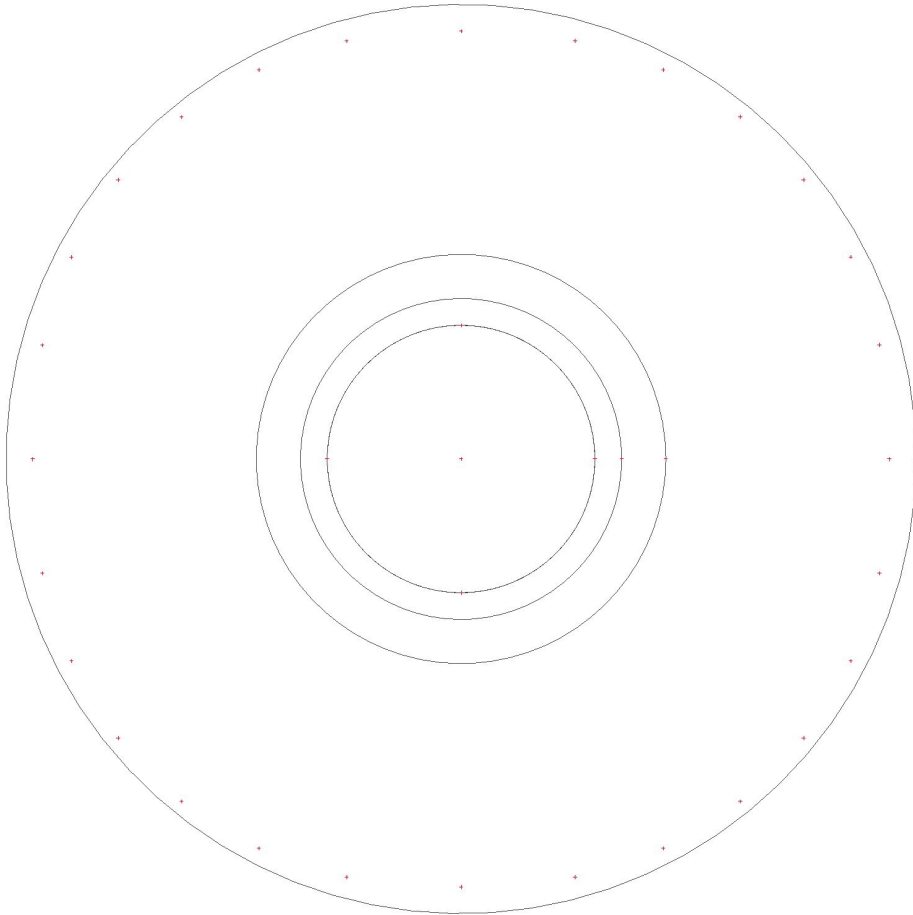


3.4. BG03 - ground water



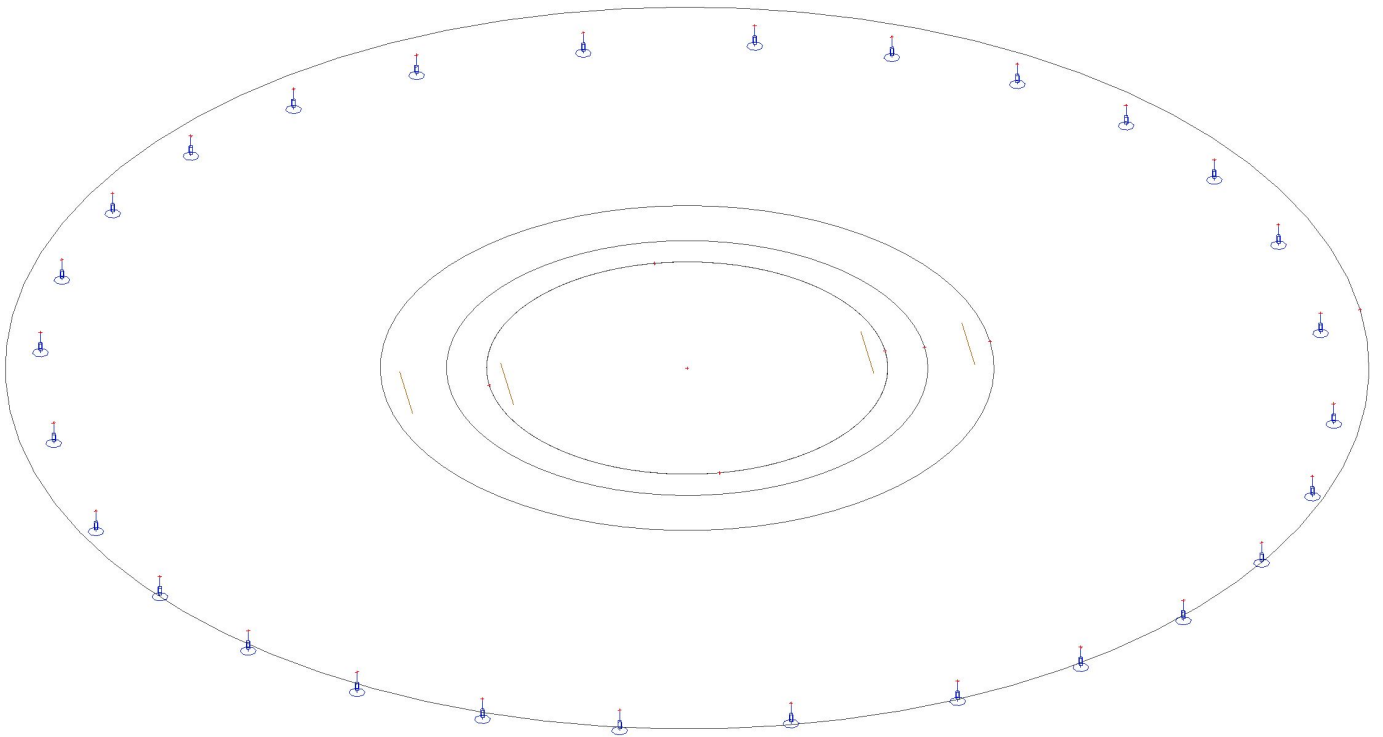
3.5. BG101: Unit load vertical (1.000kN)

Not supported task. Please switch to 'V16 and older' post-processing environment (available in 32-bit version).



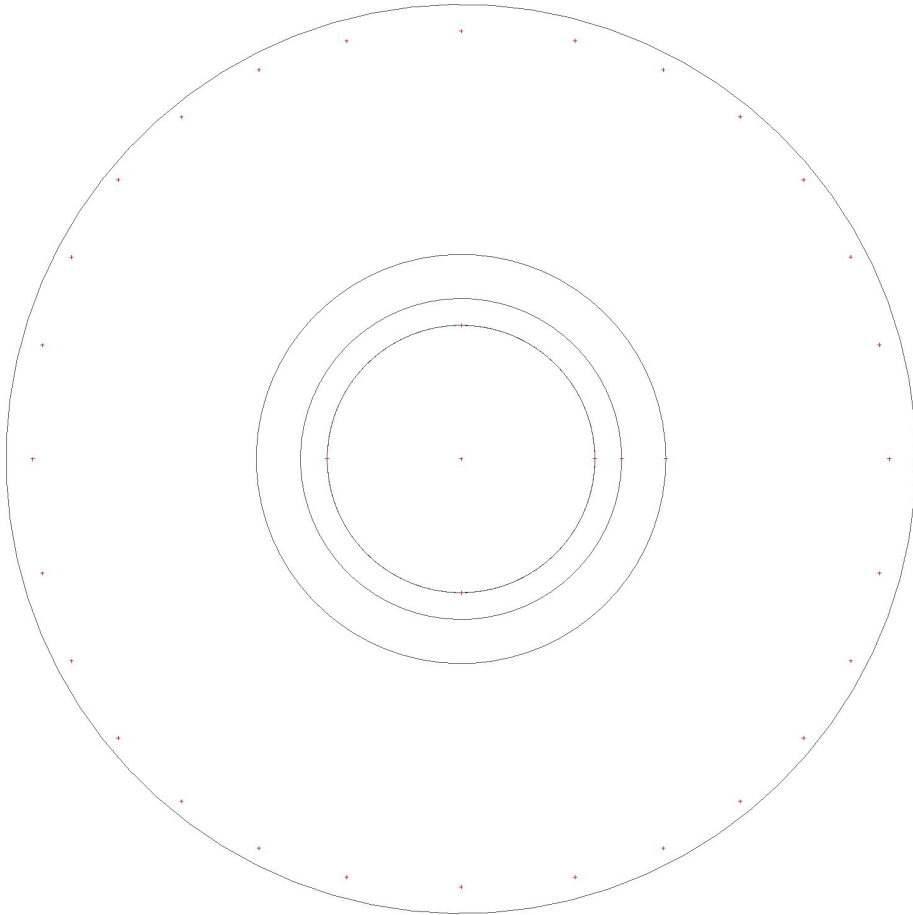
3.6. BG101: result vertical load

Not supported task. Please switch to 'V16 and older' post-processing environment (available in 32-bit version).



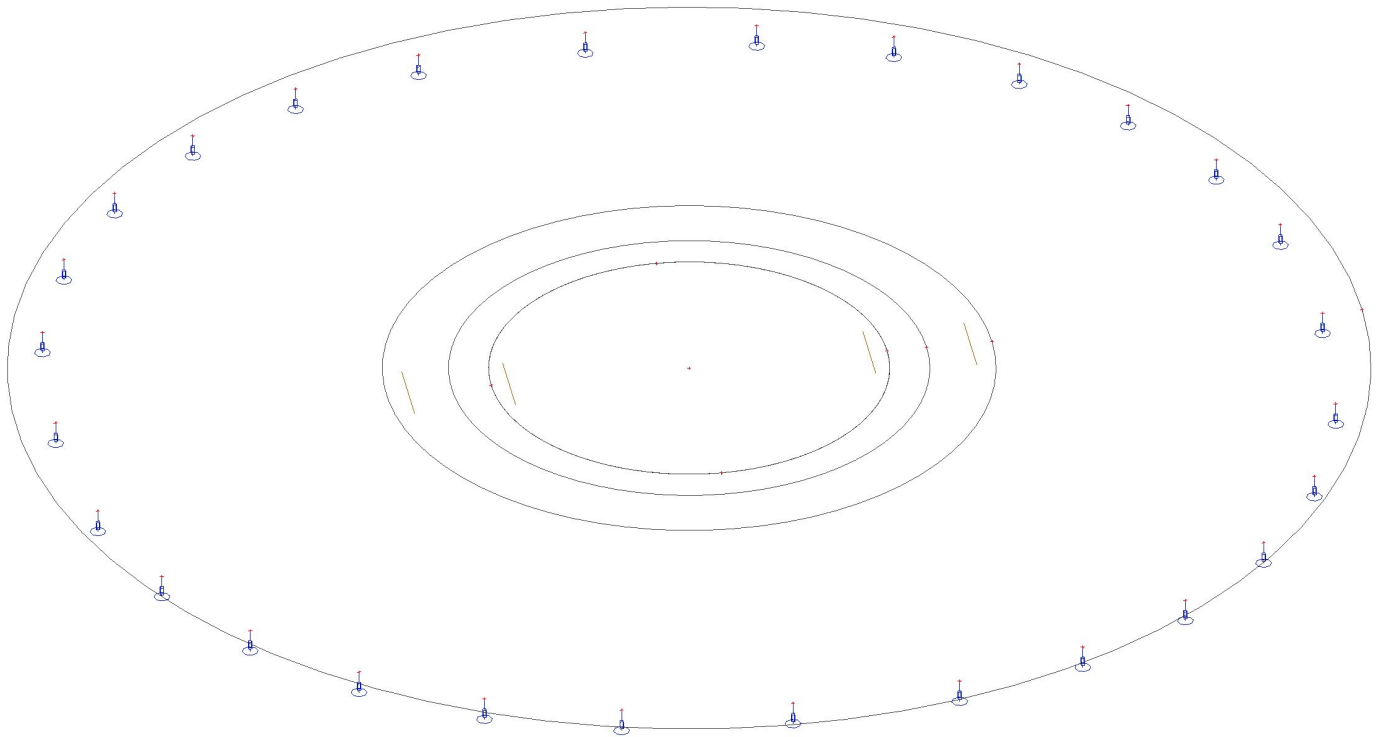
3.7. BG102: Unit load moment(100.000kN)

Not supported task. Please switch to 'V16 and older' post-processing environment (available in 32-bit version).



3.8. BG102: result bending moment

Not supported task. Please switch to 'V16 and older' post-processing environment (available in 32-bit version).



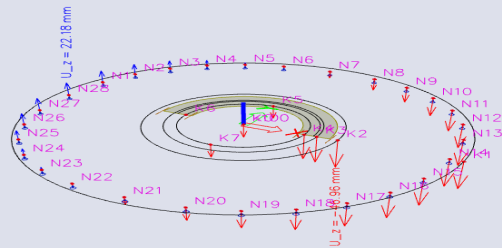
Displacement of nodes

Nonlinear calculation
 NonLinear Combi: NC_Combi 1
 Extreme: Global
 Selection: All

Name	Case	U _x [mm]	Φ _x [mrad]	Φ _y [mrad]	U _{max} [mm]
K2	NC_Combi 1	-46.96	0.0	3.7	46.96
N28	NC_Combi 1	22.18	0.0	3.3	22.18
N18	NC_Combi 1	-32.25	-3.7	1.3	32.25
N10	NC_Combi 1	-32.25	3.7	1.3	32.25
N14	NC_Combi 1	-46.29	0.0	-0.9	46.29
K7	NC_Combi 1	-21.55	-0.8	7.3	21.55

Displacement of nodes

Values: U_x
 Nonlinear calculation
 NonLinear Combi: NC_Combi 1
 Extreme: Global
 Selection: All



3D displacement

Nonlinear calculation

NonLinear Combi: NC_Combi 1

Selection: All

Location: In nodes avg. on macro. System: LCS mesh element

Results on 1D member:

Extreme 1D: Global

Name	dx [mm]	Fibre	Case	u _x [mm]	u _y [mm]	u _z [mm]	φ _x [mrad]	φ _y [mrad]	φ _z [mrad]	U _{total} [mm]
S1	7854	6	NC_Combi 1	0.00	0.00	-0.83	-6.1	-0.1	0.0	0.83
S2	7854	5	NC_Combi 1	0.07	-6.92	-42.24	4.6	0.0	0.0	42.81

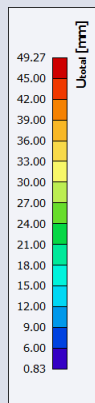
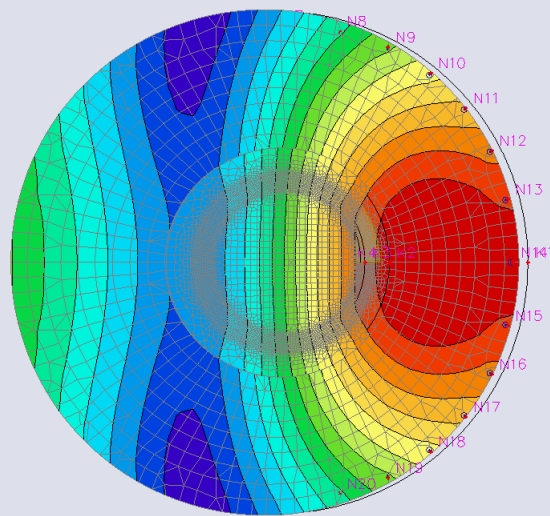
Results on 2D member:

Extreme 2D: Global

Name	Mesh	Position [mm]	Case	ux+ [mm] ux- [mm]	uy+ [mm] uy- [mm]	uz+ [mm] uz- [mm]	φ _x [mrad]	φ _y [mrad]	φ _z [mrad]	U total+ [mm] U total- [mm]
E1	Element: 247 Node: 405 0	7478 1	NC_Combi 1	-0.79 0.79	0.00 0.00	-47.51 -47.51	0.0	-0.9	0.0	47.52 47.52
E3	Element: 2912 Node: 2989 0	-536 -2442 1	NC_Combi 1	12.72 -12.72	0.72 -0.72	-16.70 -16.70	-0.4	7.4	0.0	21.01 21.01
E1	Element: 521 Node: 682 0	3782 5206 1	NC_Combi 1	2.53 -2.53	-3.35 3.35	-35.34 -35.34	3.4	2.6	0.0	35.59 35.59
E1	Element: 577 Node: 738 0	3782 -5206 1	NC_Combi 1	2.53 -2.53	3.35 -3.35	-35.34 -35.34	-3.4	2.6	0.0	35.59 35.59
E1	Element: 349 Node: 510 0	5391 1	NC_Combi 1	1.11 -1.11	0.00 0.00	-49.25 -49.25	0.0	1.0	0.0	49.27 49.27
E1	Element: 67 Node: 3 0	-8500 0 1	NC_Combi 1	-2.74 -2.74	0.00 0.00	23.99 23.99	0.0	3.3	0.0	24.15 24.15
E1	Element: 115 Node: 198 0	5142 -6128 1	NC_Combi 1	1.08 -1.08	3.11 -3.11	-33.51 -33.51	-3.7	1.3	0.0	33.68 33.68
E1	Element: 19 Node: 893 0	5142 6128 1	NC_Combi 1	-1.08 -1.08	-3.11 3.11	-33.51 -33.51	3.7	1.3	0.0	33.68 33.68
E1	Element: 1 Node: 20 0	8000 1	NC_Combi 1	-0.76 0.76	0.00 0.00	-46.29 -46.29	0.0	-0.9	0.0	46.29 46.29
E1	Element: 93 Node: 159 0	-2851 -8008 1	NC_Combi 1	-3.99 -3.99	0.67 -0.67	0.81 0.81	-0.8	4.9	0.0	4.13 4.13

3D displacement

Values: U_{total}
NonLinear calculation
NonLinear Combi: NC_Combi 1
Selection: All
Location: In nodes avg. on macro.
System: LCS mesh element



3D stress

Nonlinear calculation

NonLinear Combi: NC_Combi 1

Selection: All

Location: In nodes avg. on macro. System: LCS mesh element

Basic magnitudes

Results on 1D member

Extreme 1D: Global

Name	dx [mm]	Fibre	Case	σ_x [N/mm ²]	τ_{xy} [N/mm ²]	τ_{xz} [N/mm ²]	τ_{yz} [N/mm ²]
S2	5989-	3	NC_Combi 1	-333.61	0.00	0.00	0.00
S2	5989-	1	NC_Combi 1	333.61	0.00	0.00	0.00

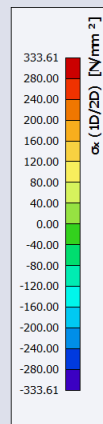
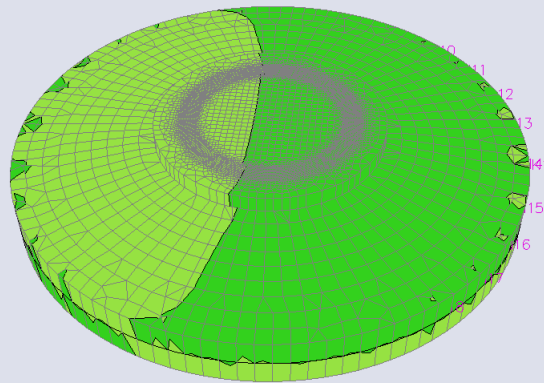
Results on 2D member

Extreme 2D: Global

Name	Mesh	Position [mm]	Case	σ_{xx} [N/mm ²] σ_{yy} [N/mm ²]	σ_{zz} [N/mm ²] σ_{xy} [N/mm ²]	τ_{xyx} [N/mm ²] τ_{xyz} [N/mm ²]	τ_{xzx} [N/mm ²]	τ_{yzy} [N/mm ²]
E1	Element: 223 Node: 378	3622 1230 0	NC_Combi 1	-21.31 21.31	-9.89 9.89	-2.05 2.05	4.15	0.34
E3	Element: 4223 Node: 4528	-2019 1867 0	NC_Combi 1	11.72 -11.72	4.02 -4.02	-0.19 0.19	-1.72	0.57
E3	Element: 4464 Node: 4769	2122 1827 0	NC_Combi 1	-19.16 12.12	-12.12 19.16	1.11 -1.11	4.07	0.23
E3	Element: 5035 Node: 5340	-2128 -1895 0	NC_Combi 1	11.39 -4.13	4.13 -11.39	0.09 -0.09	4.12	1.36
E1	Element: 208 Node: 353	746 3752 0	NC_Combi 1	-7.96 7.96	-6.56 6.56	-6.69 6.69	-1.61	2.08
E1	Element: 153 Node: 262	746 -3752 0	NC_Combi 1	-7.82 7.82	-6.63 6.63	6.85 -6.85	-1.61	-2.37
E3	Element: 2940 Node: 3045	-1733 -1802 0	NC_Combi 1	10.22 -10.22	2.24 -2.24	-0.44 0.44	-13.88	-8.64
E3	Element: 2485 Node: 1229	2240 1995 0	NC_Combi 1	-17.73 17.73	-11.63 11.63	1.25 -1.25	10.85	6.37
E3	Element: 2770 Node: 944	1995 -2240 0	NC_Combi 1	-18.15 18.15	-9.97 9.97	-0.50 0.50	2.46	-13.14
E3	Element: 2492 Node: 1222	1995 2240 0	NC_Combi 1	-18.15 18.15	-9.97 9.97	0.50 -0.50	2.46	13.14

3D stress

Values: σ_x (1D/2D)
Nonlinear calculation
NonLinear Combi: NC_Combi 1
Selection: All
Location: In nodes avg. on macro.
System: LCS mesh element
Basic magnitudes

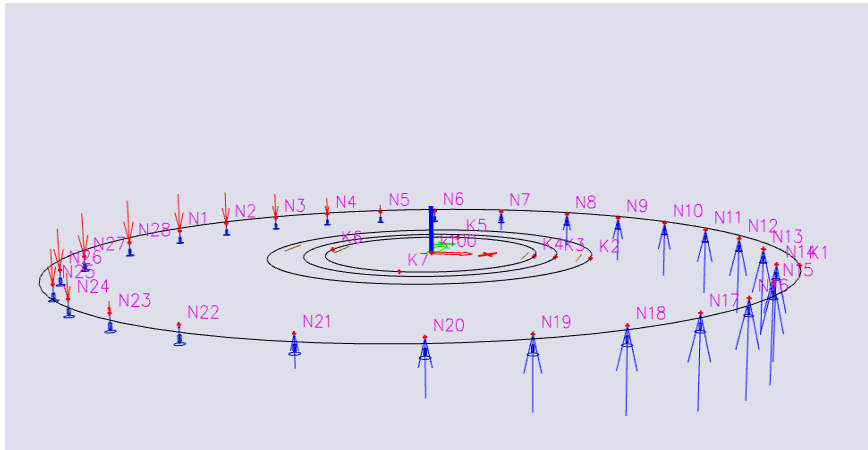


Reactions

Nonlinear calculation
NonLinear Combi: Load nonlinear combinations
System: Global
Extreme: Global
Selection: All

Nodal reactions

Name	Case	R _z [kN]	M _x [kNm]	M _y [kNm]	e _x [mm]	e _y [mm]
Sn28/N28	Load nonlinear combinations	-1018	0	0	0.00	0.00
Sn14/N14	Load nonlinear combinations	2329	0	0	0.00	0.00



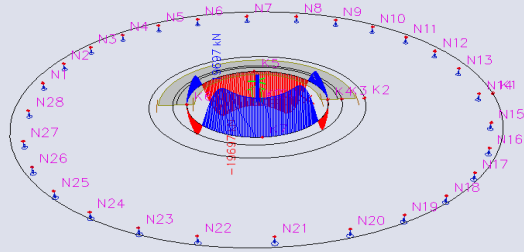
1D internal forces

Nonlinear calculation
NonLinear Combi: NC_Combi 1
Coordinate system: Member
Extreme 1D: Global
Selection: All

Name	dx [mm]	Case	V _z [kN]	M _x [kNm]	M _y [kNm]
S1	5154	NC_Combi 1	-19697	0	-3732
S2	2700	NC_Combi 1	19697	0	-3731
S1	3878	NC_Combi 1	-16984	0	7629
S2	3976	NC_Combi 1	16984	0	7630
S1	5989	NC_Combi 1	-5383	0	-10645
S2	5989	NC_Combi 1	5383	0	25021

1D internal forces

Values: V_z
Nonlinear calculation
NonLinear Combi: NC_Combi 1
Coordinate system: Member
Extreme 1D: Global
Selection: All



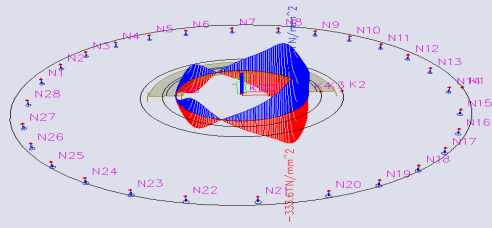
1D stresses

Nonlinear calculation
NonLinear Combi: NC_Combi 1
Coordinate system: Principal
Extreme 1D: Global
Selection: All

Name	dx [mm]	Fibre	Case	σ_x [N/mm ²]	T_{xy} [N/mm ²]	T_{xz} [N/mm ²]	T_{yz} [N/mm ²]
S2	5989	3	NC_Combi 1	-333.61	0.00	0.00	0.00
S2	5989	1	NC_Combi 1	333.61	0.00	0.00	0.00

1D stresses

Values: σ_x
Nonlinear calculation
NonLinear Combi: NC_Combi 1
Coordinate system: Principal
Extreme 1D: Global
Selection: All



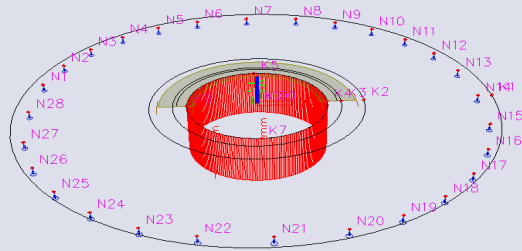
1D deformations

Linear calculation
Load case: BG01
Coordinate system: Global
Extreme 1D: Global
Selection: All

Name	dx [mm]	Case	u_x [mm]	ϕ_x [mrad]	ϕ_y [mrad]	U_{total} [mm]
S1	3878	BG01	-4.75	0.1	0.0	4.75
S2	3927	BG01	-4.75	-0.1	0.0	4.75
S1	0	BG01	-4.75	0.0	-0.1	4.75
S1	7854	BG01	-4.75	0.0	0.1	4.75

1D deformations

Values: u_x
Linear calculation
Load case: BG01
Coordinate system: Global
Extreme 1D: Global
Selection: All



2D internal forces

Nonlinear calculation
 NonLinear Combi: NC_Combi 1
 Extreme: Global
 Selection: All
 Location: In nodes avg. on macro. Rotation of the planar system: LCS-Member 2D

Principal magnitudes

Name	Mesh	Position [mm]	Case	m_1 [kNm/m] m_2 [kNm/m]	α_1 [deg]	R_{1max} [kNm/m]	R_{2max} [kN/m]	β_1 [deg]
E3	Element: 5035 Node: 5340	-2120 -1895 0	NC_Combi 1	-9095 -22332	-89.26	7118	9922	-161.74
E3	Element: 4063 Node: 4368	1983 -1833 0	NC_Combi 1	38538 23033	7.89	7753	8588	-25.31
E3	Element: 4223 Node: 4528	-2019 1867 0	NC_Combi 1	-7877 -22994	88.61	7559	4140	-18.34
E3	Element: 4465 Node: 4770	2091 1862 0	NC_Combi 1	38130 23465	-7.97	7332	6435	-161.77
E1	Element: 181 Node: 6	-3825 0 0	NC_Combi 1	-2534 -9598	-90.00	3532	2597	180.00
E1	Element: 1 Node: 1	8500 0 0	NC_Combi 1	1436 58	90.00	689	2579	0.00
E4	Element: 6552 Node: 44	0 0 0	NC_Combi 1	3783 3735	89.98	24	7420	0.00
E3	Element: 2899 Node: 2963	98 -2498 0	NC_Combi 1	20235 -2647	-39.17	11441	16521	3.02
E1	Element: 645 Node: 806	-2150 -6616 0	NC_Combi 1	2082 -1721	-60.00	1901	62	-49.25
E3	Element: 2942 Node: 3049	-1802 -1733 0	NC_Combi 1	-4566 -20637	84.86	8036	37933	33.91
E1	Element: 133 Node: 4	3825 0 0	NC_Combi 1	20121 8990	0.00	5565	5851	-180.00
E1	Element: 389 Node: 550	-5391 0 0	NC_Combi 1	-1928 -5095	-90.00	1584	2356	180.00

2D internal forces

Values: m_1

Nonlinear calculation

NonLinear Combi: NC_Combi 1

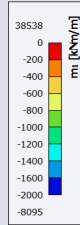
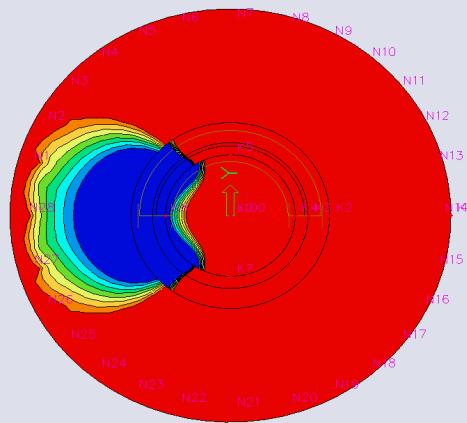
Extreme: Global

Selection: All

Location: In nodes avg. on macro.

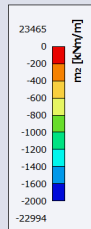
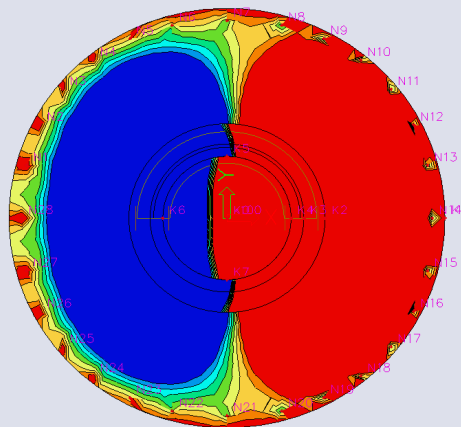
Rotation of the planar system:

LCS-Member 2D



2D internal forces

Values: m_2
Nonlinear calculation
NonLinear Combi: NC_Combi 1
Extreme: Global
Selection: All
Location: In nodes avg. on macro.
Rotation of the planar system:
LCS-Member 2D



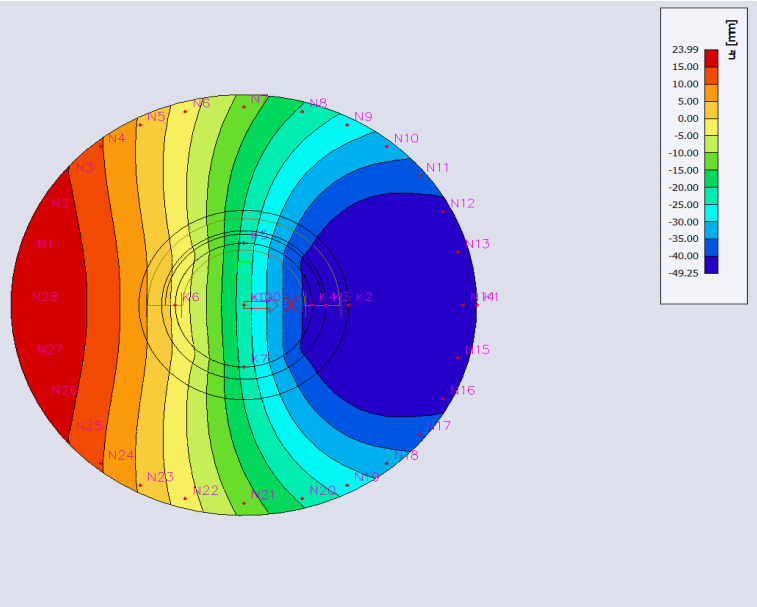
2D displacement

Nonlinear calculation
 NonLinear Combi: NC_Combi 1
 Extreme: Global
 Selection: All
 Location: In nodes avg. on macro. System: LCS mesh element

Name	Mesh	Position [mm]	Case	u_x [mm]	ϕ_x [mrad]	ϕ_y [mrad]	U_{max} [mm]
E1	Element: 349 Node: 510	5391 0 0	NC_Combi 1	-49.25	0.0	1.0	49.25
E1	Element: 67 Node: 3	-8500 0 0	NC_Combi 1	23.99	0.0	3.3	23.99
E1	Element: 115 Node: 198	5142 -6128 0	NC_Combi 1	-33.51	-3.7	1.3	33.51
E1	Element: 19 Node: 893	5142 6128 0	NC_Combi 1	-33.51	3.7	1.3	33.51
E1	Element: 1 Node: 20	8000 0 0	NC_Combi 1	-46.29	0.0	-0.9	46.29
E3	Element: 2912 Node: 2989	-536 -2442 0	NC_Combi 1	-16.70	-0.4	7.4	16.70
E2	Element: 1215 Node: 1052	-2614 -1471 0	NC_Combi 1	0.00	0.1	6.2	0.00

2D displacement

Values: u_x
 Nonlinear calculation
 NonLinear Combi: NC_Combi 1
 Extreme: Global
 Selection: All
 Location: In nodes avg. on macro.
 System: LCS mesh element



2D stress/strain

Nonlinear calculation
 NonLinear Combi: NC_Combi 1
 Etienne: Global
 Selection: E1
 Location: In node avg. on macro. System: LCS mesh element
 Principal stress - Standard result

Name	Mesh	Position [mm]	Case	σ_{11} [N/mm ²]	σ_{22} [N/mm ²]	σ_{33} [N/mm ²]	σ^+ [deg]	τ_{max} [N/mm ²]
E2	Element: 220 Node: 373	3313 1913 0	NC_Combi 1	-10.12	-21.83	18.92	-75.52	4.68
E1	Element: 172 Node: 293	-3313 -1913 0	NC_Combi 1	10.98	3.83	9.87	6.44	2.87
E1	Element: 219 Node: 371	3035 2329 0	NC_Combi 1	-9.77	-21.93	19.03	-73.17	5.32
E1	Element: 171 Node: 295	-3035 -2329 0	NC_Combi 1	11.26	2.41	10.26	7.32	3.25
E1	Element: 72 Node: 125	-8157 -2390 0	NC_Combi 1	0.19	-0.05	0.22	-61.45	0.51
E1	Element: 645 Node: 806	-2150 -6616 0	NC_Combi 1	3.55	-3.57	5.66	30.00	0.05
E1	Element: 118 Node: 23	6399 -5218 0	NC_Combi 1	1.90	0.09	1.85	-70.30	15.62

Principal stress - Results on sections and edges:

Name	Mesh	Position [mm]	Case	σ_{11} [N/mm ²]	σ_{22} [N/mm ²]	σ_{33} [N/mm ²]	σ^+ [deg]	τ_{max} [N/mm ²]
E1/Edge 1	Element: 3	8445 967 0	NC_Combi 1	-0.32	-5.51	5.76	5.50	0.23
E1/Edge 1	Element: 69	-8445 -967 0	NC_Combi 1	3.57	0.14	1.50	-84.14	0.21
E1/Edge 1	Element: 131	8445 -967 0	NC_Combi 1	-0.32	-5.91	5.76	-5.80	0.23
E1/Edge 1	Element: 115	5372 -6587 0	NC_Combi 1	1.68	-3.81	4.88	-65.41	3.44
E1/Edge 1	Element: 72	-8157 -2390 0	NC_Combi 1	0.19	-0.05	0.22	-61.45	0.51
E1/Edge 1	Element: 59	-7832 3303 0	NC_Combi 1	1.12	-0.09	1.16	65.04	0.20
E1/Edge 1	Element: 21	4988 6883 0	NC_Combi 1	0.43	-4.41	4.64	57.50	3.58

2D stress/strain

Nonlinear calculation
 NonLinear Combi: NC_Combi 1
 Etienne: Global
 Selection: E1, E2
 Location: In node avg. on macro. System: LCS mesh element
 Principal stress - Standard result

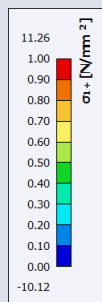
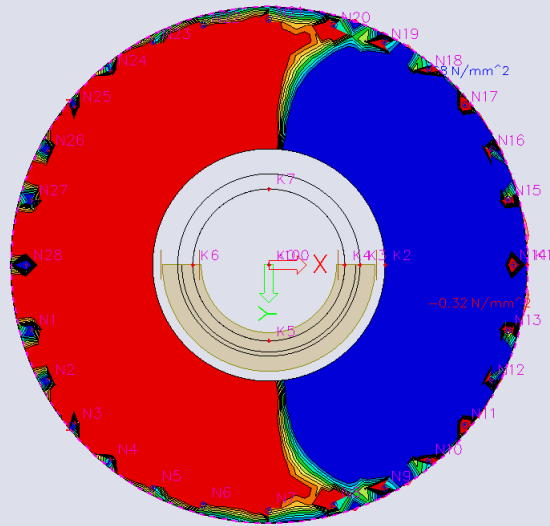
Name	Mesh	Position [mm]	Case	σ_{11} [N/mm ²]	σ_{22} [N/mm ²]	σ_{33} [N/mm ²]	σ^+ [deg]	τ_{max} [N/mm ²]
E2	Element: 1429 Node: 1230	-2273 1958 0	NC_Combi 1	-11.47	-17.71	17.71	-77.21	15.58
E2	Element: 1199 Node: 1040	-2273 -1958 0	NC_Combi 1	9.97	3.89	-9.97	8.70	-1.98
E1	Element: 219 Node: 371	3035 2329 0	NC_Combi 1	-9.77	-21.93	19.03	-73.17	5.32
E1	Element: 171 Node: 295	-3035 -2329 0	NC_Combi 1	11.26	2.41	10.26	7.32	3.25
E1	Element: 72 Node: 125	-8157 -2390 0	NC_Combi 1	0.19	-0.05	0.22	-61.45	0.51
E1	Element: 645 Node: 806	-2150 -6616 0	NC_Combi 1	2.95	-3.57	5.66	30.00	0.05
E1	Element: 118 Node: 23	6399 -5218 0	NC_Combi 1	1.90	0.09	1.85	-70.30	15.62

Principal stress - Results on sections and edges:

Name	Mesh	Position [mm]	Case	σ_{11} [N/mm ²]	σ_{22} [N/mm ²]	σ_{33} [N/mm ²]	σ^+ [deg]	τ_{max} [N/mm ²]
SE104	Element: 1959	3050 11 0	NC_Combi 1	-10.61	-11.03	10.83	-65.66	2.43
E2/Edge 3	Element: 975	-3313 -1913 0	NC_Combi 1	6.19	2.85	-6.19	5.37	-10.66
E2/Edge 3	Element: 926	2705 2705 0	NC_Combi 1	-8.20	-14.25	12.39	-71.86	3.88
E2/Edge 3	Element: 980	-2705 -2705 0	NC_Combi 1	7.01	1.93	6.37	-7.30	2.40
E1/Edge 1	Element: 72	-8157 -2390 0	NC_Combi 1	0.19	-0.05	0.22	-61.45	0.51
E1/Edge 1	Element: 59	-7832 3303 0	NC_Combi 1	1.12	-0.09	1.16	65.04	0.20
E2/Edge 3	Element: 922	3035 2329 0	NC_Combi 1	-9.05	-13.86	13.19	61.32	3.92

2D stress/strain

Values: σ_1
Nonlinear calculation
NonLinear Combi: NC_Combi 1
Extreme: Global
Selection: E1
Location: In nodes avg. on macro.
System: LCS mesh element



2D stress/strain

Values: $T_{max,b}$

Nonlinear calculation

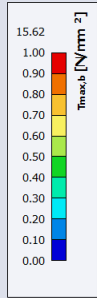
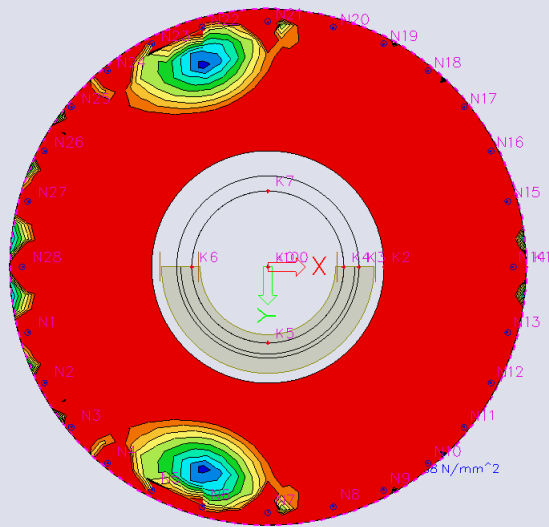
NonLinear: Combi: NC_Combi 1

Extreme: Global

Selection: E1

Location: In nodes avg. on macro.

System: LCS mesh element



2D stress/strain

Values: σ_2+
Nonlinear calculation
NonLinear Combi: NC_Combi 1
Extreme: Global
Selection: E1
Location: In nodes avg. on macro.
System: LCS mesh element

